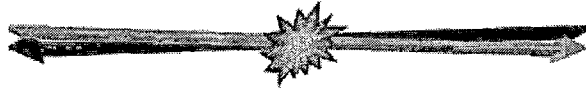
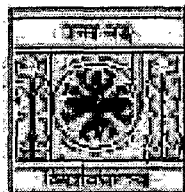


Some Aspects of Multiparticle Production in ^{32}S -Ag/Br Interactions at 200A GeV/c



A dissertation submitted for the degree of
Doctor of Philosophy (Science)

By
Malay Kumar Ghosh



Department of Physics, University of North Bengal
Raja Rammohunpur, Darjeeling -734013
West Bengal, India

Ref. —
539.7
G412s

212070
02 FEB 2009

STOCK TAKING-2011 |

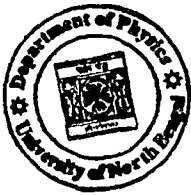


Ref. No.

Dated 17.03.2008

To whom it may concern

This is to certify that the present thesis entitled, "Some Aspects of Multiparticle Production in ^{32}S -Ag/Br Interactions at 200A GeV/c", is a Ph.D. (Science) dissertation submitted by Mr. Malay Kumar Ghosh (Registration no. AE11723 of 1992-'93). The research work presented in the thesis, is to some extent collaborative in nature. But major part of it has been carried out under my supervision at the Department of Physics, of the University of North Bengal. No part of the thesis has ever been submitted for obtaining a Ph.D. degree from this department. Mr. Ghosh has made significant contribution to every stage of the investigation, and he has fulfilled all the requirements to submit a Ph.D. thesis. To the best of my understanding, in character and disposition, Mr. Malay Kumar Ghosh is fit to submit his thesis for Ph.D. (Science) degree.



Amitabha Mukhopadhyay

Amitabha Mukhopadhyay

Reader
Department of Physics
University of North Bengal

Preface

The history of heavy-ion physics dates back to the early 1970's, when a group of physicists at the Lawrence Berkeley Laboratory (LBL) used the Bevalac facility to study shock compression within nuclear matter. Since that time the scope of the subject has expanded enormously, with many different issues emerging and new dimensions continuously being added to them. During the past three decades or so, technology has allowed us to construct bigger accelerators capable of producing ions moving with ultra-relativistic speed, and the focus of heavy-ion physics has also shifted to a large extent. At present, the subject stands at the interface between nuclear and particle physics, whose central research objective is to create and characterize a new state of matter comprised of isolated quarks and gluons within a limited region of space-time. This new state is similar to the ordinary plasma in the sense that, like free electrical charges in the latter, colour degrees of freedom can break loose out of their usual confinement within hadrons, in the former. However, this can be achieved only if local thermal equilibrium is established. Indications from the latest RHIC results are strongly in favour. People call it the Quark-gluon Plasma (QGP), a state that perhaps filled up the universe only after a few micro-seconds after its birth, may still be available at the core of very compact stars, and may possibly be created in the laboratory by colliding two nuclei at high-energy. Over the period of time for which high-energy heavy-ion physics has been seriously taken as a frontier area of research, there have been claims and counter claims about the formation and observation of such an exotic state of matter in the laboratory. However, it is safe only to say that the situation is far from conclusive, and with the installation of the Large Hadron Collider (LHC) at CERN (Geneva), we are probably standing at the doorstep of achieving the ultimate goal of QGP creation under the controlled conditions of a laboratory.

A relativistic heavy-ion collision is a dynamical process that takes place within a typical space-time scale of 10 fm. A state like the QGP, even if it is created, cools down very rapidly to undergo a QCD phase transition and fragments into colour neutral hadrons, several other species of particles and radiation. One has to critically examine these remnants of the interaction, and undertake the tedious journey to trace back history to the initial stage of the collision. It's tempting to draw a parallel with the "big bang" theory of the birth of our universe and its connection with the observation of cosmic microwave

background. Often therefore, a high-energy collision between two nuclei in laboratory is termed as a "little bang".

Beside the fact that in a high-energy interaction two colliding nuclei fragment into smaller pieces, many new particles are also produced. To the physicists working in this area the mechanism of multiparticle production has remained a topic of investigation for a long period of time. For this purpose it is necessary to analyze the distributions of these particles in terms of their number, energy, momentum, rapidity etc.. However, it has also been a long tradition to perform such analysis, globally. During mid 80's the priorities changed drastically, and in stead of global distributions, local structures of particle distribution within limited regions of phase-space started to draw more attention. If the final state particles are an outcome of a phase transition, one expects various time integrated patterns of clusters within narrow regions of phase-space, as well as sharp voids in the distribution. This may also happen even without invoking any phase transition, as observed in normal hadronic interactions. As a result, sharply fluctuating phase-space distribution of particle densities should be observed. On many occasions the study of fluctuations in physical variables (or quantities) has initiated new frontiers of scientific research. However, it's absolutely essential to figure out whether the fluctuations arise out of trivial statistical noise, or do they have any dynamical origin. Various statistical methods to study the dynamical component of fluctuation in multiparticle distribution have been suggested. Efforts have been made to associate self-similar geometrical structure, like fractals, to the observed fluctuations. In the present investigation we have collected and analyzed a set of data on the angular distribution of singly charged particles produced in ^{32}S -Ag/Br interactions at an incident momentum of 200A GeV/c. Nuclear emulsion technique has been employed to collect the data, and the data have been analyzed in terms of the intermittency, multifractality and erraticity techniques. Over the past two decades the validity of these statistical methods, suggested by others, has been tested on several other data sets on high-energy interaction. We do not claim any originality regarding the data analysis techniques adopted in the present investigation.

The thesis starts with a brief review of the subject namely, nucleus-nucleus (AB) interaction at high-energy. We have tried to emphasize the broad experimental aspects of the subject, avoiding mathematical intricacies as they do not fall within the scope of present

investigation. While organizing chapter one, the following sequence has been maintained. Salient features of two body kinematics, the roll of geometry in collision between two nuclei, and some other general characteristics of AB interaction have been outlined. A semi-qualitative description of the space-time evolution of AB interaction in terms of Landau's and Bjorken's hydrodynamical models has been incorporated. Deconfinement of colour degree of freedom and formation of QGP in AB interaction has been discussed in terms of the MIT Bag model. Both the high temperature and high pressure scenario have been addressed. Thereafter, the experimental status of AB interactions at high-energy has been described. We have concentrated mainly on experiments performed during the BNL-AGS, CERN-SPS and BNL-RHIC era. The physics of various signatures that have already been suggested to identify the creation of a QGP like state has been outlined, and the major experimental observations corresponding to each of these signatures have been depicted. As the present investigation mainly deals with fluctuation in particle number within narrow intervals of phase-space, the phenomenological and experimental issues related to this particular area have been elaborated with a little more details than the other signatures. The first chapter ends with a brief qualitative description of several models on particle production in high-energy AB collision.

Chapter two is a compilation of three different aspects namely, the nuclear emulsion technique, the microscopy associated with it, and some gross features of the data sample used. Since 1940's the nuclear emulsion has remained as an accepted technique for studying interaction between particles. Beside its low cost and easy to handle properties, the unique feature that makes nuclear emulsion still a useful tool, is its high spatial resolution. Particularly if one is trying to investigate the structure of particle distribution within narrow spatial intervals, then nuclear emulsion can certainly be a preferred choice over its costlier, larger and more glamorous electronic counterparts. However, the technique also has certain limitations. With the collider type of experiments becoming more and more dominant over the fixed target ones, it's probably not a very distant future when the application nuclear emulsion technique is going to be limited only to cosmic ray experiments. In chapter two we have tried to address most of the important issues pertaining to nuclear emulsion and its associated microscopy. This chapter also includes a section covering certain kinematic, and statistical features of the ^{32}S -emulsion data sample used

for further analysis and presented in subsequent chapters. This is important, because it provides the reader with a fair idea about where do our results stand with respect to those obtained from similar other investigations.

In chapter three, four and five, issues related respectively to intermittency, multifractality and erraticity have been discussed, and our results on these three different aspects of particle production have been described. There are certain common features among these apparently differing phenomena. All three techniques involve studying fluctuation of produced particle density in limited phase-space intervals. In each of them, one type of power law scaling behaviour or the other has been used. The scaling laws describe variations of certain moments of particle distribution as functions of phase-space interval size. There also exist close connections between intermittency and multifractality, as well as that between intermittency and erraticity. In the first case, several intermittency and multifractal parameters that result from the corresponding scaling law, can be related to one another as both the phenomena deals with the same underlying self-similar structure of particle distribution. Whereas in the second case, the erraticity technique analyzes the event-to-event fluctuation of fluctuation of particle density in a single event the latter being characterized by the moments of intermittency. We have tried to make our analysis as comprehensive as possible, but scopes of improvement are not ruled out. The thesis ends with a short summary of the major conclusions of the present investigation, with a few remarks on what else can be done in future.

I would like to end this preface with some personal remarks. It was October 2001 when as a Junior Research Fellow, I started to work in the field of high-energy heavy-ion interaction in the Department of Physics of the University of North Bengal. For the past six years or so, we tried to utilize our limited resources, and could ultimately bring the thesis out in its present form. The thesis is based mainly on the works published in the following papers by our group:

1. Erraticity analysis of particle production in $^{32}\text{S-Ag/Br}$ interaction at 200A GeV/c - Malay Kumar Ghosh and Amitabha Mukhopadhyay, *Physical Review C* **68**, 034907 (2003).
2. Erraticity analysis of multiparticle production in nucleus-nucleus interactions at relativistic energies - Dipesh Chanda, Malay Kumar Ghosh, Amitabha Mukhopadhyay and

Gurmukh Singh, Physical Review C **71**, 034904 (2005).

3. Multifractal moments of particles produced in ^{32}S -Ag/Br interaction at 200A GeV/c - Malay Kumar Ghosh, Amitabha Mukhopadhyay and Gurmukh Singh, Journal of Physics G: Nuclear and Particle Physics **32**, 2293 (2006).

4. Intermittency and multiplicity moments of charged particles produced in ^{32}S -Ag/Br interaction at 200A GeV/c - Malay Kumar Ghosh, Amitabha Mukhopadhyay and Gurmukh Singh, Journal of Physics G: Nuclear and Particle Physics **34**, 177 (2007).

I have been fortunate to have Dr. A. Mukhopadhyay as the supervisor of my Ph.D. thesis, whose tireless efforts helped me learn many new things. I am grateful to Dr. Mukhopadhyay for his involvement at every stage of the investigation, for his continuous support to follow the necessary technicalities of the subject, and for his encouragement particularly at the low points of my brief research career. Being located at a remote area of the country, we lacked some of the basic facilities required for any frontier area of research. We take this opportunity to express our gratitude to Prof. D. Ghosh, who was kind enough to allow us to use his laboratory infrastructure in the Physics Department of Jadavpur University, Kolkata. In the year 2003 we could start a collaboration with Dr. G. Singh, who at that time was in the Physics Department of SUNY at Buffalo. Dr. Singh was generous enough to share some of the emulsion data on heavy-ion interaction collected in their laboratory. This was an immense help to our group at North Bengal University, and the collaboration with Dr. Singh is still successfully continuing. We are also thankful to Prof. P. L. Jain, leader of the Buffalo group, who spared some of the emulsion plates exposed to various heavy-ion beams. During the first two years of my research tenure, the financial support that I received from the Govt. of West Bengal in the form of a Junior Research Fellowship, is gratefully acknowledged. Last but not the least I must also acknowledge the constant moral support, that I received from my family and from all the members of the Physics Department of the University of North Bengal.

Malay Kumar Ghosh
17/03/08
Malay Kumar Ghosh
Raja Rammohunpur.

Contents

1	High-energy Nucleus-Nucleus Collision: An Overview	9
1.1	Introduction	10
1.2	Kinematics of Two Body Interaction	11
1.3	General Characteristics of AB Interaction	15
1.3.1	Centrality of Collisions	16
1.3.2	p_t Distribution of Produced Particles	17
1.3.3	Central and Fragmentation Regions	18
1.3.4	Coherent and Incoherent Collisions	20
1.4	AB Interaction and the QGP	20
1.4.1	Landau's Hydrodynamical Picture	24
1.4.2	Bjorken's Estimation of Energy Density	26
1.4.3	Deconfinement and the Bag Model	27
1.4.4	Quark-Gluon Plasma at High Temperature	29
1.4.5	Quark-Gluon Plasma at High Baryon Density	30
1.5	The Experimental Scenario	31
1.5.1	Experiments at the BNL AGS	33
1.5.2	Experiments at the CERN-SPS	37
1.5.3	Experiments at BNL RHIC	45
1.6	Signatures of QGP in Heavy-ion Interactions	48
1.6.1	Dilepton Production	50
1.6.2	Production of Direct Photons	54
1.6.3	Suppression of J/ψ Production	59
1.6.4	Bose-Einstein Interferometry	62
1.6.5	Strangeness Production	66

1.6.6	Elliptic flow of hadrons	68
1.6.7	Charged Particle Ratio Fluctuations	74
1.7	Particle Density Fluctuations	77
1.7.1	Intermittency	78
1.7.2	Self-affinity	81
1.7.3	Factorial Correlators	83
1.7.4	Multifractality	85
1.7.5	Takagi's Multifractal Moments	89
1.7.6	Erraticity	91
1.8	Models of AB interaction	94
1.8.1	LEXUS	95
1.8.2	Lund Model - Fritiof	96
1.8.3	Dual Parton Model	98
1.8.4	HIJING	99
1.8.5	UrQMD	100
2	The Emulsion Technique and Data Characteristics	109
2.1	Nuclear Emulsion Technique	110
2.1.1	Nuclear Emulsion	110
2.1.2	Latent Image Formation	113
2.1.3	Emulsion Processing	114
2.1.4	Track Structure	117
2.2	The Microscopy	122
2.2.1	Counting and statistics	124
2.2.2	Geometric Measurements in Emulsion	126
2.2.3	Scanning in Emulsion	130
2.3	Advantages and Disadvantages of Emulsion Technique	131
2.4	General Characteristics of the Data	134
3	Intermittency in $^{32}\text{S-Ag/Br}$ interaction at 200A GeV/c	144
3.1	Introduction	145
3.2	Methodology and Results	146

3.2.1	Intermittency in 2-d	156
3.2.2	Factorial Correlators	162
3.2.3	Oscillatory Multiplicity Moments	165
3.3	Discussion	167
4	Multifractality in $^{32}\text{S-Ag/Br}$ interaction at 200A GeV/c	172
4.1	Introduction	173
4.2	Hwa's Multifractal Moments	174
4.3	Takagi's Multifractal Moments	182
4.4	Discussion	186
5	Erraticity in $^{32}\text{S-Ag/Br}$ interaction at 200A GeV/c	190
5.1	Introduction	191
5.2	Erraticity of particle distribution	193
5.3	Results on Erraticity of particle distribution	196
5.4	Erraticity of gap distribution	203
5.5	Results on Erraticity of Gap Distribution	205
5.6	Discussion	208
6	Concluding Remarks	213

Chapter 1

High-energy Nucleus-Nucleus Collision: An Overview

In this chapter we shall briefly review different aspects of AB collision at high-energy, emphasizing the experimental scenario in particular. The prospect of observing a phase transition from normal nuclear matter to the Quark-gluon Plasma (QGP), where colour degrees of freedom become deconfined, followed by a subsequent freeze out to the final state particles, lies at the heart of the subject. In the beginning, kinematics of two body interaction and some general features of AB interaction have been discussed. A brief outline of nuclear matter under extreme conditions of temperature and pressure in the background of the MIT bag model, follows next. Subsequently, the status of major experiments on high-energy AB interaction has been reviewed to the extent possible. Different signatures, that have been proposed to identify a possible formation of QGP like state, have also been summarized qualitatively in terms of the physics problems associated with each of them. Major experimental observations related to these signatures have also been incorporated. A section has been devoted to review the experimental observations on dynamical fluctuations in the density distribution of produced particles. The chapter ends with a brief and qualitative description of some phenomenological models on particle production in high-energy AB interactions.

1.1 Introduction

A high-energy AB collision is a complicated dynamical process, where in present day experiments, the typical number of nucleons involved is $10^2 - 10^3$, and where the nucleon-nucleon (NN) center of mass energy, denoted by $\sqrt{s_{NN}}$, typically lies within a range of $10^1 - 10^2$ GeV. This particular area of research has already a more than three decade old history behind it. It all started in the early 1970's with an objective to study the shock compression wave in extended nuclear matter at the Lawrence Berkeley Laboratory. At that time the topic could inspire only about 30 odd physicists. Since then this number has grown by a factor $\sim 10^2$ in this particular area of research, and at present high-energy AB interaction deserves the status of a separate subject [1, 2].

The processes through which an AB collision evolves in space-time have till date remained a debatable issue, because everything happens at a typical space-time scale of ~ 10 fm. A nucleus is an extended object, and one can expect that the geometry more specifically the impact parameter of a collision, plays a crucial role in deciding this evolution process. In general it may however be speculated that, depending on the collision energy involved, as the two colliding nuclei meet they would try to stop each other with varying degrees. Because of this stopping, the colliding nucleons suffer substantial loss in their kinetic energies, that gives rise to new degrees of freedom [3]. The constituents of normal nuclear matter, the valence quarks and the wee partons, are compressed very hard. As a result a region of very high-energy / matter density, sometimes called a 'fireball', is formed [4]. Depending on the initial conditions, this fireball may subsequently come to a local thermal and/or a chemical equilibrium. If the energy density and/or the matter density exceeds certain critical values, one expects a transition [5, 6] from the normal nuclear matter to a colour deconfined state containing quarks and gluons moving freely within a region, that is several to many times larger than the confinement of a typical hadron (~ 1 fm). It is generally believed that a few microseconds after the initial 'big bang', the universe was filled up with such a state of matter. Since the high-energy AB interactions can possibly replicate that state of the universe under controlled conditions of a laboratory, it is tempting to call such AB interactions as 'little bang'. After the initial compression and subsequent equilibration, the fireball probably undergoes an isentropic expansion stage [7], that is accompanied with an obvious loss in the temperature. Ultimately, a freeze out

temperature is reached when another phase transition leads the fireball to fragment into the final state particles, mostly hadrons. As mentioned above, the number of hadrons emanating from a typical AB interaction in present day experiments is $\sim 10^2 - 10^3$ per event. From the debris of hundreds (even thousands on some occasions) of produced particles it is therefore, not a very easy task to trace back the correct signals for any kind of phase transition, that may not or may have taken place during the course of evolution of the collision process. Often the signal is lost into a large number of unwanted background particles and radiation [8].

In this chapter we have briefly reviewed the current scenario of high-energy AB interaction with an emphasis on the experimental aspects of the subject. The natural unit system ($\hbar = c = k_B = 1$) has been used. Chapter I has been organized in the following way. The kinematics pertaining to a two body high-energy interaction and emission of final state particles have been described. Some of the general characteristics of AB interaction along with the effects of collision geometry have been discussed. The transition from normal nuclear matter to a colour unconfined state under extreme conditions of pressure and temperature have been outlined in the framework of the MIT bag model [9]. Within the limited scope of the present thesis, experimental investigations on high-energy AB interaction performed in the recent past have been reviewed. Different signatures proposed to identify the formation of a QGP like state have been qualitatively explained, where mathematical intricacies have been avoided. The present status of experimental observations against each such signature has also been described. As the present thesis primarily deals with nonstatistical fluctuation in the density of produced particles, we have therefore, incorporated a separate section to review the experimental results on this particular topic. Finally, several models of particle production in high-energy AB interactions have also been briefly outlined.

1.2 Kinematics of Two Body Interaction

The collision between two objects (nuclei) may be analyzed either in the target rest frame (equivalent to the laboratory frame for a target fixed in the laboratory), or in the center of mass frame, where total momentum of the colliding objects is equal to zero. Therefore,

at the very beginning it is necessary to identify the kinematic variables relevant to the two body interaction, and also to find out relationships between these variables in both frames of reference mentioned above [1, 10]. Let us consider a collision between two nuclei A and B, respectively, of mass numbers A and B and masses m_1 and m_2 . Let us also define a Lorentz invariant (scalar) quantity s one of the Mandelstam variables as,

$$s = (P_1 + P_2)^2 = (P_1 + P_2)^\mu (P_1 + P_2)_\mu,$$

where $P_1(P_2)$ is the four-momentum of A(B) in the laboratory system (ls). They can also be denoted by, $P_1 = (E_1, \mathbf{P}_1)$ and $P_2 = (E_2, \mathbf{P}_2)$, where $E_1(E_2)$ and $\mathbf{P}_1(\mathbf{P}_2)$ are respectively, the energy and ordinary three momentum of A(B). The relativistic energy-momentum relation $E_2^2 = |\mathbf{P}_2|^2 + m_2^2$ holds for B , which one may consider to be the projectile. If A is considered to be the target fixed in the ls , then $\mathbf{P}_1 = \mathbf{0}$ and $E_1 = m_1$. Thus, $P_2 = (E_2, \mathbf{P}_2)$ and $P_1 = (m_1, \mathbf{0})$. The Mandelstam variable s in ls is therefore,

$$s = (P_1 + P_2)^2 = (E_2 + m_1)^2 - |\mathbf{P}_2|^2 = m_1^2 + m_2^2 + 2m_1 E_2.$$

Variables in the center of mass system (cms) should be distinguished from those in the ls . This is done by using an extra superscript c with each variable. According to the definition of the cms $\mathbf{P}_1^c + \mathbf{P}_2^c = \mathbf{0}$. Hence, $-\mathbf{P}_1^c = \mathbf{P}_2^c = \mathbf{P}^c$ say. The corresponding energy values for A and B are given, respectively by,

$$E_1^c = \sqrt{|\mathbf{P}^c|^2 + m_1^2} \text{ and } E_2^c = \sqrt{|\mathbf{P}^c|^2 + m_2^2}.$$

The individual four-momentum, respectively for A and B are therefore, $P_1^c = (E_1^c, -\mathbf{P}^c)$ and $P_2^c = (E_2^c, \mathbf{P}^c)$. Once again the Mandelstam variable s in the cms will be,

$$s = (P_1^c + P_2^c)^2 = (E_1^c + E_2^c)^2 = (E^{cm})^2, \text{ say.}$$

The total cms energy E^{cm} is thus related to s as, $\sqrt{s} = E^{cm}$. Since s is a Lorentz invariant quantity, $m_1^2 + m_2^2 + 2m_1 E_2 = (E^{cm})^2$, and at relativistic energies where $E_2 \gg m_1, m_2$,

$$E^{cm} \approx \sqrt{2m_1 E_2}.$$

The cms velocity $\beta_{cm} = |\mathbf{P}_1 + \mathbf{P}_2|/(E_1 + E_2)$ in the ls can be obtained by using the Lorentz transformation relations. $\mathbf{P}_1 = \mathbf{0}$ for a target (A) fixed in the ls , and $\beta_{cm} = |\mathbf{P}_2|/(E_1 + E_2)$. The corresponding Lorentz factor is,

$$\gamma_{cm} = \frac{1}{\sqrt{1 - \beta_{cm}^2}} = \frac{E_1 + E_2}{\sqrt{s}}.$$

Consider now that, a particle of rest mass m is produced in the collision between A and B and it comes out with a four-momentum $p(E, \mathbf{p})$, making an angle θ in the ls with respect to the beam (B) direction. In the cms let the corresponding four-momentum be $p^c(E^c, \mathbf{p}^c)$, while the angle of emission is denoted by θ^c . If the longitudinal and the transverse components of the momentum of the particle are denoted respectively, by (p_l, p_t) in the ls , and by (p_l^c, p_t^c) in the cms , then once again through Lorentz transformation the following relations can be obtained,

$$\begin{aligned} p_l^c &= \gamma_{cm}(p_l - \beta_{cm} E), & E^c &= \gamma_{cm}(E - \beta_{cm} p_l), \\ p_t &= \mathbf{p} \sin \theta = p_t^c = \mathbf{p}^c \sin \theta^c, & p_l &= \mathbf{p} \cos \theta = \gamma_{cm}(\beta_{cm} E^c + p_l^c), \\ \text{and } E &= \gamma_{cm}(E^c + \beta_{cm} p_l^c) = \gamma_{cm}(E^c + \beta_{cm} \mathbf{p}^c \cos \theta^c). \end{aligned}$$

The transverse mass of the particle is defined as, $m_t = \sqrt{m^2 + p_t^2}$. In most cases the cms is a better choice than the ls to study a two body interaction. Of all reference frames it is the cms where the energy available is at its minimum value, and therefore, it can provide the threshold value of production of particle(s). Moreover, as in the cms the total momentum of colliding objects is zero, unlike the ls in this frame there is no preferential direction of particle emission other than those imposed by the kinematic conditions. If now any preferential emission pattern is observed in the cms , then it must be due to some underlying dynamics. To describe the kinematic conditions of a particle produced in a high-energy interaction, we need suitable variables. Components of the four-momentum $p^\mu = (p^0, p^1, p^2, p^3)$ can serve the purpose. These components are constrained by the relativistic energy-momentum relation, that reduces the number of independent variables from four to three. However, as it is often necessary to compare results in different frames of references, one must always keep track of the proper transformation relations between them. If in a reaction many particles are produced, then one often is actually concerned with the distribution of these particles in terms of one or more variables. Under such a situation it would be convenient to choose the kinematic variables in such a way, that the overall shape of the distribution function remains unchanged as one moves from one frame to the other. The rapidity (y) of a particle, a parameter of finite special Lorentz transformation (also called the Lorentz boost), can be defined in several ways e.g,

$$\text{space-time: } \tanh y = \beta, \quad y = \frac{1}{2} \ln \left(\frac{1 + \beta}{1 - \beta} \right), \quad (1.1)$$

$$\text{energy-momentum: } p_l = m_t \sinh y, \quad E = m_t \cosh y, \quad y = \frac{1}{2} \ln \left(\frac{E + p_l}{E - p_l} \right). \quad (1.2)$$

Rapidity is a dimensionless quantity and is related to the longitudinal motion (along the beam axis) of the particle. As one can see from the above relations, at $\beta \ll 1$ the rapidity of a particle traveling in the longitudinal direction is almost equal to the velocity of the particle. Recall that the total energy in the *cms* is \sqrt{s} . The energy and momentum of the *cms* in the *ls* are given, respectively by, $\gamma_{cm} \sqrt{s}$ and $\beta_{cm} \gamma_{cm} \sqrt{s}$. The rapidity of the *cms* in the *ls* is therefore,

$$y_{cm} = \frac{1}{2} \ln \frac{\gamma_{cm} \sqrt{s} + \beta_{cm} \gamma_{cm} \sqrt{s}}{\gamma_{cm} \sqrt{s} - \beta_{cm} \gamma_{cm} \sqrt{s}} = \frac{1}{2} \ln \frac{1 + \beta_{cm}}{1 - \beta_{cm}}. \quad (1.3)$$

The rapidity of a particle in the *cms* is denoted by y^c ,

$$y^c = \frac{1}{2} \ln \left(\frac{E^c + p_l^c}{E^c - p_l^c} \right). \quad (1.4)$$

Through Lorentz transformation one can see that,

$$y = \frac{1}{2} \ln \frac{\gamma_{cm}(E^c + \beta_{cm} p_l^c) + \gamma_{cm}(\beta_{cm} E^c + p_l^c)}{\gamma_{cm}(E^c + \beta_{cm} p_l^c) - \gamma_{cm}(\beta_{cm} E^c + p_l^c)}$$

$$y = \frac{1}{2} \ln \frac{E^c + p_l^c}{E^c - p_l^c} + \frac{1}{2} \ln \frac{1 + \beta_{cm}}{1 - \beta_{cm}}$$

Thus under the Lorentz boost one gets a simple additive relation between the rapidities in the *ls* and in the *cms*,

$$y = y^c + y_{cm}. \quad (1.5)$$

This simple additive property of the rapidity variable is of utmost importance, because in both frames the shape of the rapidity distribution remains unaltered in either of the frames. To determine the rapidity of a particle, actually two variables E and p have to be measured. In some experiments only the angle of emission (θ) of the particle with respect to the beam axis can be measured. In such cases the pseudorapidity (η) variable defined by,

$$\eta = -\ln \left[\tan \left(\frac{\theta}{2} \right) \right] \quad (1.6)$$

is used. At high-energies where $p \gg m$ one can see that,

$$y = \frac{1}{2} \ln \left(\frac{E + p_l}{E - p_l} \right) = \frac{1}{2} \ln \left(\frac{\sqrt{p^2 + m^2} + p_l}{\sqrt{p^2 + m^2} - p_l} \right)$$

$$\begin{aligned}\implies y &\approx \frac{1}{2} \ln \left(\frac{p + p_l}{p - p_l} \right) = \frac{1}{2} \ln \left(\frac{1 + \cos \theta}{1 - \cos \theta} \right) \\ y &\approx -\ln \left[\tan \left(\frac{\theta}{2} \right) \right] = \eta.\end{aligned}$$

Pseudorapidity is a very convenient variable because, there is no need to measure the momentum of a particle and therefore, no need to apply a magnetic field. Using the exact relations between y and η it can be shown that, in terms of these two variables the normalized number densities of a particular type of particle (of rest mass m say) are related to each other,

$$\frac{dn}{dy dp_t} = \sqrt{1 - \frac{m^2}{m_t^2 \cosh^2 y}} \frac{dn}{d\eta dp_t}. \quad (1.7)$$

Any discrepancy in the magnitudes of the density (due to the factor within square root) is insignificant for most of the particles produced in high-energy interactions. The differential cross section for particle production expressed in the form of

$$\frac{d^3\sigma}{dp_x dp_y dp_z}$$

is not invariant under Lorentz boost. If the longitudinal direction is chosen to coincide with the z -direction, then $p_z = m_t \sinh y$ and $dp_z = m_t \cosh y dy$. Therefore, $dp_z/E = dy$, which is invariant under Lorentz boost, and one may define the invariant cross section as,

$$E \frac{d^3\sigma}{d^3p} = \frac{d^3\sigma}{dp_x dp_y dy}.$$

Using, $p_t = \sqrt{p_x^2 + p_y^2}$, and $\tan \varphi = p_y/p_x$ the invariant cross section can also be expressed as,

$$E \frac{d^3\sigma}{d^3p} = \frac{d^3\sigma}{p_t dp_t d\varphi dy}.$$

1.3 General Characteristics of AB Interaction

Consider a two body reaction like: $A + B \rightarrow X + \text{anything}$,

where X belongs to a definite species of particles. If one is interested to investigate the issues related only to the production of X , then it is called an inclusive analysis. On the other hand, in a high-energy interaction, e.g, nucleus-nucleus (AB) interaction, one may have different types of particles in the final state e.g, fragments of the incident nucleus (projectile), fragments of the target nucleus, and newly produced particles most of which are different types of mesons. Such a reaction can be expressed as,

Projectile + Target \rightarrow Fragments of the colliding nuclei + Produced particles.

If without making any distinction among its different constituent species, we concentrate our study to one particular category of particles then the analysis is semi-inclusive in nature. It is to be understood that, each category e.g, the category of produced particles can be further subdivided like, the neutral, positive and negative π -mesons, strange mesons, leptons, photons etc. The number of particles in each category is called the multiplicity of that particular category of particles.

1.3.1 Centrality of Collisions

At high-energy two colliding nuclei look like two Lorentz contracted discs/pancakes in their *cms*, the contraction being along the direction of motion of each nucleus [10]. If the impact parameter (b) of collision is as large as the sum of the radii of two nuclei involved, then such a collision is called an extreme peripheral collision. There will hardly be any nuclear interaction, and the interaction between the two nuclei will predominantly be electromagnetic in nature. Either or both of the nuclei will absorb energy through giant resonances, proton-neutron clusters, $\Delta(1231)$ resonances, higher lying nucleon resonances or through decay by emission of one or more nucleons. Only a small fraction of the total number of nucleons belonging to each nuclei are actually affected in peripheral interactions, while most other remain as spectators. On the other hand, if the nuclei experience a head on collision with an impact parameter $b \approx 0$, then the collision is called a central collision. In such a situation the smaller nucleus actually makes a cylindrical hole into the larger nucleus, and in principle all nucleons of the smaller nucleus and most nucleons of the larger nucleus participate in the reaction. Thus one can see that the range over which b can vary is $0 \leq b \leq (R_1 + R_2)$, where R_1 and R_2 are the radii of two nuclei, and the total geometrical cross-section is given by $\sigma_g = \pi r_0^2 (A^{1/3} + B^{1/3})^2$.

Based on the fact that the number of nucleons actually participating in an interaction depends on the impact parameter, the centrality of a collision is determined following certain assumptions. They are, (i) on an average the energy released in a collision is proportional to the number of participating nucleons, (ii) the average multiplicity of particles produced is proportional to the number of participating nucleons, and (iii) average number of produced particles is proportional to the energy released, and hence proportional to

the impact parameter of the collision. The impact parameter/ the centrality of a nuclear collision however, can be and has been decided from other considerations as well. The energy flow in the forward direction is denoted by E_{ZD} and is often measured by setting a zero degree calorimeter (ZDC). The net charge flow within the extreme forward cone is denoted by Q_{ZD} . Both these quantities can serve the purpose of measuring the centrality of a collision [11]. As the impact parameter decreases, the magnitude of E_{ZD} or Q_{ZD} will be smaller. Correspondingly, the transverse energy E_t defined by,

$$E_t = \sum_{i=1}^n E_i \sin \theta_i$$

will be larger in central than in the peripheral collisions. Here n is the number of particles produced in an event, and E_i , θ_i are respectively, the energy and emission angle associated with the i th particle. E_t is a suitable measure of the energy available in the *cms* for production of particles, which increases with increasing centrality of the collision. Therefore, E_t can also be used to determine the centrality of a collision. In chapter two, we shall try to illustrate the issues related to AB collision discussed in this section in detail specifically in terms of nuclear emulsion experiments.

1.3.2 p_t Distribution of Produced Particles

As the nucleons belonging to the two colliding nuclei stop each other they lose substantial fraction of their kinetic energies, creating a central fireball stationary at the *cms* of the colliding nuclei, that subsequently cools down to fragment into new final state particles, most of which ($\sim 80-90\%$) are pions. In the *cms* there should not be any preferential direction of emission of the final state particles, except those restricted by the kinematic conditions, and unless there is some dynamics involved in the particle production process. Any new degree of freedom like for example, the transverse momentum component is therefore, a result of the thermodynamic characteristics of the central fireball. With decreasing impact parameter the longitudinal energy is increasingly converted into transverse energy radiated in a direction transverse to the beam direction in the form of produced particles and their kinetic energies. Hence the p_t or E_t distribution of produced particles belonging to different species from the AB collisions may provide important and useful information, that is necessary for to identify the thermodynamical state of the source from which they



are coming out, particularly so because of a possible phase transition from normal nuclear matter to the QGP [10].

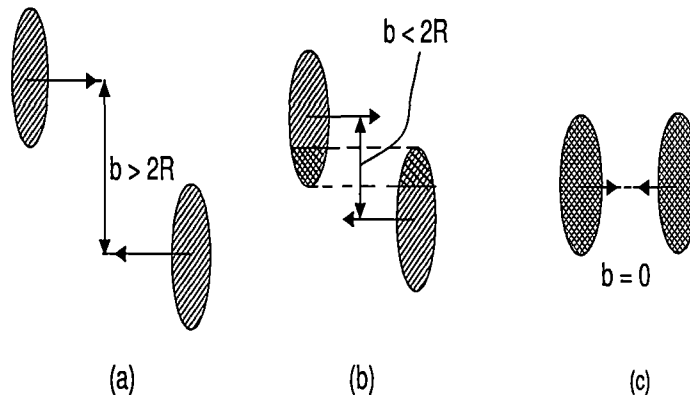


Figure 1.1: The geometry of an AB interaction between two nuclei of same size: (a) extreme peripheral, (b) semi-central and (c) extreme central collision.

The average transverse momentum $\langle p_t \rangle$ is taken as a measure of the temperature, whereas, the charge particle multiplicity density either globally or restricted to a limited rapidity interval is taken as a measure of entropy and/or energy density. While for most of the pions the $\langle p_t \rangle \approx 0.35$ GeV/c, in some high-energy cosmic ray interactions and in various high-energy AB interactions carried out in laboratories, it has been found that on some occasions $\langle p_t \rangle$ is significantly larger than its average value 0.35 GeV/c. $\langle p_t \rangle$ may be plotted against the energy density ϵ , or the particle density which is also a measure of entropy density ($s_e = A_{part}^{-2/3} dn/dy$). If it is observed that after a monotonic rise there is a plateau and again there is sharp increase in the $\langle p_t \rangle$ value, then the behaviour can be related to some kind of phase transition. It may be speculated that, perhaps the rapid increase of $\langle p_t \rangle$ after the plateau is due to the formation of QGP and the plateau region indicates the possible phase transition from QGP to normal nuclear matter.

1.3.3 Central and Fragmentation Regions

From simple geometrical considerations it is also possible to estimate the average number of binary collisions (inelastic collisions between two nucleons one each from the A and B),

and the number of participating nucleons in each of the projectile and target nuclei [12]. These numbers are given by,

$$\text{Average projectile participants } \langle P_B \rangle = B \sigma_{pA} / \sigma_{AB},$$

$$\text{Average target participants } \langle P_A \rangle = A \sigma_{pB} / \sigma_{AB},$$

$$\text{and the average number of binary collisions } \langle N_{BC} \rangle = AB \sigma_{pp} / \sigma_{AB},$$

where σ_{pp} is the proton-proton (pp), σ_{pA} , σ_{pB} are the respective proton-nucleus, and σ_{AB} is the AB cross-sections. One can see that the average numbers of participating nucleons for one nucleus can be obtained by taking the ratio of the geometrical cross-section of the other nucleus and σ_g . Therefore, the average number of participating protons for A is,

$$\langle Z_A^{part} \rangle \approx Z_A \frac{\pi r_0^2 B^{2/3}}{\sigma_g} = \frac{Z_A B^{2/3}}{(A^{1/3} + B^{1/3})^2},$$

whereas, the average number of spectator protons in A is,

$$\langle Z_A^{spec} \rangle = Z_A - \langle Z_A^{part} \rangle \approx \frac{Z_A (A^{2/3} + 2A^{1/3} B^{1/3})}{(A^{1/3} + B^{1/3})^2},$$

with similar expressions for $\langle Z_B^{part} \rangle$ and $\langle Z_B^{spec} \rangle$. The total number of participating protons will therefore be,

$$\langle Z^{part} \rangle = \langle Z_A^{part} \rangle + \langle Z_B^{part} \rangle \approx \frac{Z_A B^{2/3} + Z_B A^{2/3}}{(A^{1/3} + B^{1/3})^2}.$$

As the two nuclei collide with each other, the incoming nucleons lose their kinetic energies through binary collisions, and new degrees of freedom evolve. The amount of energy lost during such collisions depends on the thickness of the nuclei, and on the collision energy. The degree of energy lost is called the nuclear stopping power. The nuclear stopping results in a shift in the rapidity values of incoming nucleons toward the central or mid-rapidity region. Thus rapidity distribution provides key information regarding the extent of nuclear stopping. At an incident energy of \sim a few tens of GeV/nucleon (typical of BNL AGS), there would be sufficient stopping between the two colliding nuclei, and the central region will be rich in its net baryon content. If a produced particle belongs to the kinematic region, where the target nucleus was initially at rest then it is said to be in the target fragmentation region. Similarly if the produced particle belongs to the kinematic region near that of the projectile, then the particle is said to belong to the projectile fragmentation region. At sufficiently high-energy there is a saturation in the

nuclear stopping, and to a great extent the colliding nuclei are transparent to each other. The two fragmentation regions are then well separated, leaving in between a very hot and dense central region, that is high in energy density and low in its net baryon content. In any high-energy interaction most of the particles produced belong to the central region.

1.3.4 Coherent and Incoherent Collisions

It is difficult to decide whether in an AB interaction each of the colliding nuclei interact as a whole, or the AB collision can be treated as a superposition of a series of independent nucleon-nucleon (NN) collisions [10]. If the two nuclei interact as a whole and there is a collective effect, then the collision is said to be coherent. On the other hand, if the AB collision is a superposition of many independent NN collisions then the collision is said to be incoherent. The total *cms* energy for a coherent collision is not same as that for an incoherent collision. It is therefore, important to find out the degree of coherence, because the way the interaction evolves, depends on the total energy available in the *cms*. Once again in the next chapter we shall see, how the total *cms* energy varies if the events under consideration are assumed to be coherent or incoherent collisions. There are certain theoretical models based on the assumption that the AB collisions are coherent, and there are also models that consider the AB interaction as a combination of series of independent NN interactions. The models based on coherent type of collisions make use of thermodynamics to determine how quantities like energy and temperature are exchanged. They also use hydrodynamics to decide the mechanical compression and expansion of the nuclear matter. The energy density of the hot hadronic matter produced in the central region can be estimated only by assuming that the AB collisions are coherent. Whereas, models based on incoherent type of collisions assume that, through the course of interaction two nucleons are excited, and the excited nucleons exchange a string of quark-antiquark pair, from which hadrons originate.

1.4 AB Interaction and the QGP

The density of normal nuclear matter is, $\rho_0 = \frac{A}{\frac{4}{3}\pi R^3}$ nucleons, where A is the mass number, $R = r_0 A^{1/3}$ is the radius of the nucleus, and $r_0 \approx 1.1$ fm is the nuclear radius parameter.

Thus $\rho_0 \approx 0.15$ nucleons/fm³. The corresponding energy density is,

$$\epsilon_0 \approx 0.15 \times 940 \text{ MeV/fm}^3 \approx 0.14 \text{ GeV/fm}^3.$$

Often the temperature is expressed in units of MeV, the relationship being given by the Boltzmann constant ($k_B = 8.6173 \times 10^{-14}$ GeV/K). Thus, in natural unit system, where $k_B = 1$,

$$1 \text{ GeV} \approx 1.16 \times 10^{13} \text{ K}.$$

Similarly the time required to travel a distance of 1 fm at the speed of light is often referred to as 1 fm ($\approx 3.3 \times 10^{-24}$ sec).

An important property of the QCD is its large coupling constant at low temperature, which is a result of chiral symmetry breaking, first recognized by Nambu and Jona-Lasinio [13]. Due to this, quarks, antiquarks and gluons are confined inside a nucleon. If the QCD vacuum is heated, then at comparatively lower temperatures new colour neutral hadrons like pions, kaons etc., are thermally excited. As the temperature is further raised, at a certain critical temperature T_c the hadronic matter may start to dissolve or melt down from the individual hadrons into a system of unconfined quarks, antiquarks and gluons filling up a volume, that is several to many units of the characteristic length scale of the hadrons. It is expected that the quarks and antiquarks are excited with equal probability. Therefore, such a state of colour deconfined (gluonic) plasma will be less in its net baryon content. Different model calculations and Monte Carlo lattice QCD simulation indicates that $T_c \geq 150 \sim 200$ MeV. On the other hand, if a large number of baryons are subjected to an extremely high pressure, they can be isothermally compressed to such an extent that, the baryons start to overlap and attain a critical baryon density $\rho_c \approx (5 - 10)\rho_0$. Under such a situation, one may also expect that the system of baryons will dissolve into a state of deconfined quark matter, which unlike the previous case is rich in its net baryon content. Thus one can see that a new state of coloured plasma consisting of free (weakly coupled) quarks, antiquarks and gluons, called the Quark-gluon plasma (QGP) can be created under a high temperature and/or high pressure situation [15]. One can look for such a state of matter in three possible places.

(i) The entire universe was probably filled up with the QGP just a few to several microseconds after its birth. The universe might have undergone a QCD phase transition at $T = 150 - 200$ MeV at a time scale $\sim 10^{-5}$ sec or so after the big bang.

(ii) At the core of very dense compact stars such as the neutron stars or the strange (quark) stars such a state of matter can be found. If the central density of these compact stars is $> (5 - 10)\rho_0$, then there is a fair possibility that their constituent hadrons will melt into cold quark matter.

(iii) And lastly, the QGP can possibly be created in laboratory by allowing two heavy nuclei to collide with each other at an extremely high-energy [5], which one may be tempted to call "a little bang".

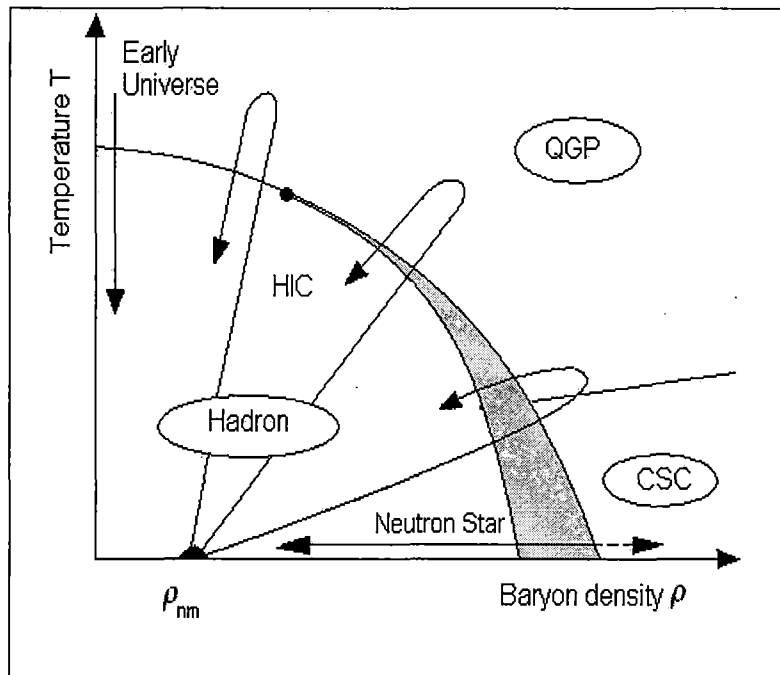


Figure 1.2: Phase diagram showing the hadronic, QGP and colour superconducting (CSC) phases. ρ_{nm} denotes the density of normal nuclear matter. QGP can be created in heavy-ion collisions (HIC).

As mentioned earlier at an incident energy of a few hundred GeV/nucleon one may expect a hot central region of high-energy density filled up predominantly with gluonic plasma, low in net baryon content. Whereas, at a few tens of GeV/nucleon incident energy one expects a high baryon density, high-energy density central region [14]. To produce a well thermalized state of QGP in the laboratory, high-energy collisions between two heavy nuclei have certain advantages over the ordinary hadron-hadron (hh), NN or pA collisions

due to the following reasons:

- (i) The average multiplicity of produced particles in high-energy AB collision is larger; hence high-energy density results on the average.
- (ii) Larger spatial size of the nuclei enables the produced particles to rescatter several times before being emitted from the collision region. This may allow enough time for thermal and chemical equilibrium to be established in the central region.
- (iii) For higher multiplicities statistical fluctuations are smaller and collective phenomena will be easier to observe.

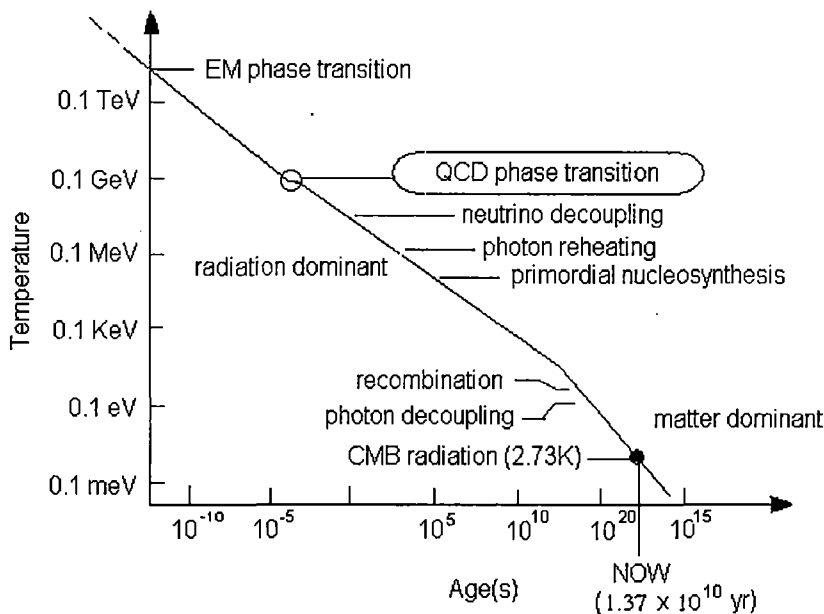


Figure 1.3: Evolution of the universe since electro-weak phase transition. Note the QCD phase transition occurring at a temperature of $\sim 10^2$ MeV.

The exact space-time evolution of a high-energy AB collision is still in a speculative stage. One possible way of looking into the process may be summarized in the following manner. The initial conditions immediately after the first instant of nuclear contact is not precisely known. The colour glass condensate, a coherent, highly excited gluonic configuration, can be a possible candidate for this stage but not the only one. Through frequent interactions among the constituent partons and their rescattering, the excited quanta materialize into new particles. The system evolves through a pre-equilibrium stage to a thermalized era

of QGP. The locally thermalized plasma is treated as a perfect fluid (no viscosity, no thermal conductivity), and the system expands isentropically according to the laws of relativistic hydrodynamics. Eventually it undergoes a chemical and thermal freeze-out producing the final state particles such as, colour neutral hadrons, leptons, photons etc. If we want to know the exact evolution process, then it is necessary to define a few initial parameters such as the initial energy density, thermalization time and freeze-out temperature. Then by solving the hydrodynamical equations it may be possible to relate those initial conditions to the experimentally observed final state particles.

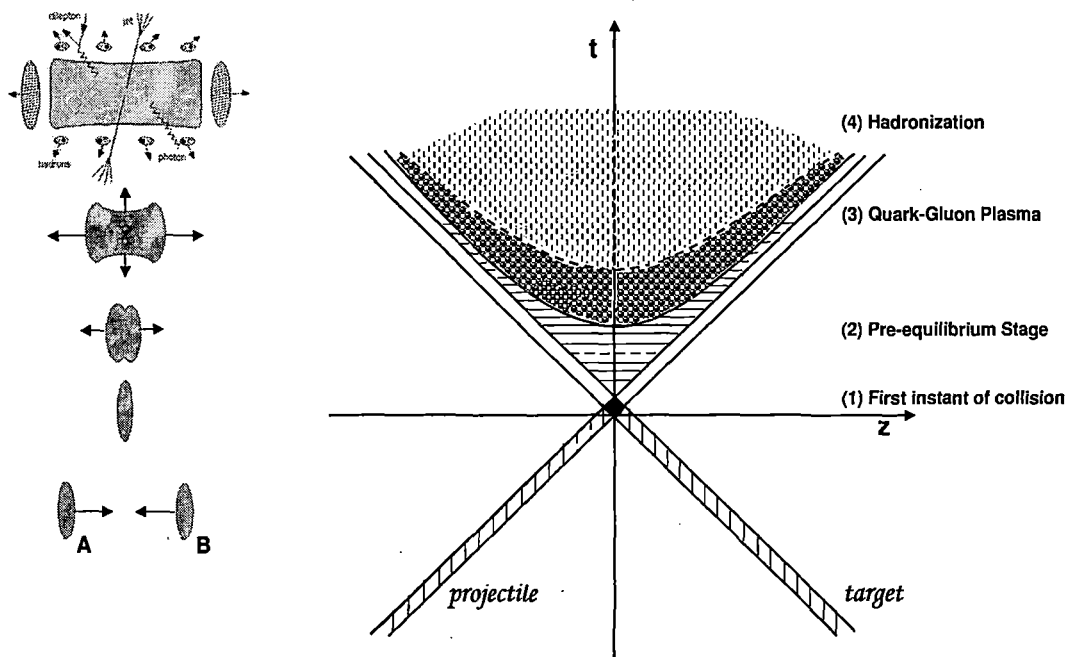


Figure 1.4: A speculative diagram of the space-time evolution of high-energy collision between two nuclei. On the left two Lorentz contracted nuclei meet, collide and then recede from each other leaving a central particle producing region in between. On the right notice the forward and backward light cones and different stages of the evolution.

1.4.1 Landau's Hydrodynamical Picture

As mentioned above, in high-energy AB collisions the baryonic matter is slowed down and loses a large fraction of its initial energy during the collision process. This energy is

deposited around the vicinity of the center of mass of the colliding objects. Considering simple picture of a head-on central collision (zero impact parameter) between two nuclei of equal mass number (say A) in Landau picture [16], where both the nuclei stop each other in the cms and as a result lose all their kinetic energies. The resulting energy density at and around the center of mass at the time of collision may be estimated. As discussed above the total energy in the cms

$$E^{cm} = \sqrt{s} = 2A m_N \gamma_{cm},$$

where m_N is the rest mass of individual nucleons. The initial energy density will therefore be,

$$\epsilon = \frac{\sqrt{s}}{V} = \frac{2A m_N \gamma_{cm}}{V_0/\gamma_{cm}} = 2\epsilon_0 \gamma_{cm}^2,$$

where V_0 is the volume of the nucleus at rest, and $\epsilon_0 \approx 0.15 \text{ GeV}/\text{fm}^3$ is the energy density of normal nuclear matter. Similarly, the initial baryon number density is,

$$\rho = \frac{2A}{V} = 2\rho_0 \gamma_{cm},$$

where $\rho_0 \approx 0.16/\text{fm}^3$ is the baryon density of normal nuclear matter. Landau and Belensky treated the intermediate expanding state of the matter as a perfect fluid, and applied relativistic hydrodynamics to estimate the initial (shortly after the impact) entropy density (s_e) and the temperature (T) as,

$$s_e \propto \epsilon^{3/4}, \text{ and } T_e \propto \epsilon^{1/4}.$$

Since initial energy density $\epsilon \propto \gamma_{cm}^2 \propto (E^{cm})^2$, the initial entropy density is,

$$s_e \propto \epsilon^{3/4} \propto (E^{cm})^{3/2}.$$

Due to the perfect fluid assumption made by Landau and Belensky, total entropy of the system (S_e) remains constant during hydrodynamical expansion stage, and since the number density of produced pions is proportional to s_e , one can estimate the total number of pions as,

$$N_\pi \propto s_e V \propto (E^{cm})^{3/2} V_0/\gamma_{cm} \propto A (E^{cm})^{1/2} \propto A E^{1/4},$$

where E is the laboratory energy. Two points can be noted from the hydrodynamical calculation of Landau, (i) one is that, the number of pions scale with the mass number

of the nuclei; hence in comparison with NN interaction in AB interactions more particles result in the final state, and (ii) at ultra-relativistic energies (SPS or RHIC) total stopping of the two colliding nuclei is too unrealistic, and hence untenable.

1.4.2 Bjorken's Estimation of Energy Density

Once again let us consider a head-on collision between two nuclei at ultra-relativistic energy in their *cms*, where each experiences substantial Lorentz contraction. The energy is so high that the longitudinal thickness of each nucleus can be neglected, and to a great extent the nuclei are transparent to each other. It may be assumed that the two nuclei are coming respectively, from $z = +\infty$ and $z = -\infty$, and they meet at $z = 0$ at time $t = 0$. Due to transparency, after the colliding nuclei recede from each other, leaving a region with high-energy density and low net baryon content around $z \sim 0$, which one may call to be the reaction volume. According to Bjorken [17], thereafter, the space-time evolution of the reaction volume is guided by the laws of hydrodynamics. In the first approximation the reaction volume experiences strong expansion in the longitudinal (say z) direction, and one may drop the transverse dimensions to treat the problem in $(1 + 1)$ dimension. Let us recall the definition of the rapidity variable, that allows us to determine the longitudinal velocity near the origin ($z \approx 0, t \approx 0$) as, $\beta_z = z/t = \tanh y$. The space-time rapidity defined by,

$$z = \tau \sinh y, \quad t = \tau \cosh y, \quad y = \frac{1}{2} \ln \frac{t+z}{t-z}$$

are now useful. Here τ is the proper time ($\tau = \sqrt{t^2 - z^2}$). Consider a longitudinal length of thickness Δz at $z = 0$ and let the transverse overlapping area of the two colliding nuclei be \mathcal{A} . The volume of our interest is therefore, $\mathcal{A}\Delta z$. Fixing our attention to the proper time τ_0 at which the QGP may have been formed and equilibrated, the number density of hadrons produced within the considered volume at $z = 0$ and $\tau = \tau_0$ is,

$$\frac{\Delta n}{\mathcal{A}\Delta z} = \frac{1}{\mathcal{A}} \left. \frac{dn}{dy} \frac{dy}{dz} \right|_{y=0}$$

The corresponding energy density at $t = 0$ is therefore,

$$\epsilon = m_t \cosh y \frac{\Delta n}{\mathcal{A}\Delta z}$$

Averaging over the transverse area \mathcal{A} at proper time τ_0 one gets,

$$\epsilon = \frac{m_t}{\tau_0 \mathcal{A}} \left. \frac{dn}{dy} \right|_{y=0} \approx \frac{m_t}{\tau_0 \mathcal{A}} \left. \frac{dn}{d\eta} \right|_{\eta=0},$$

which is the well known Bjorken's estimation of the energy density.

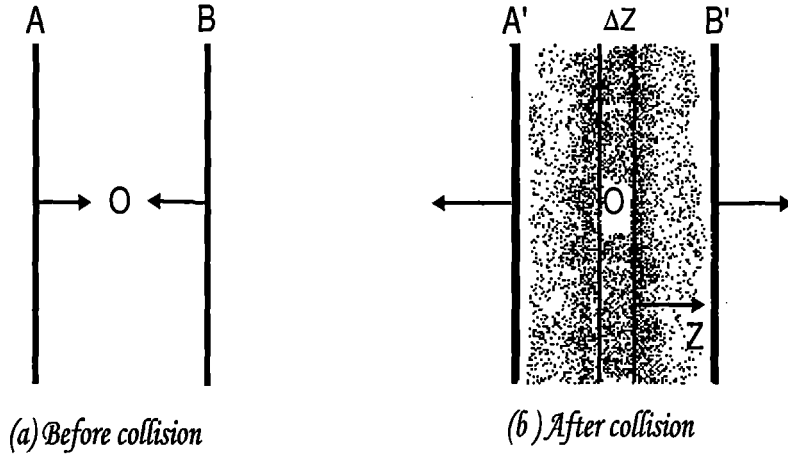


Figure 1.5: Bjorken's estimation of energy density in the central rapidity region.

1.4.3 Deconfinement and the Bag Model

Due to the asymptotic nature of the force that binds the quarks and antiquarks (if any) inside a hadron, it is impossible for the quarks or antiquarks to break free and exist independently. Quarks, gluons and antiquarks are always confined within the hadrons. Values of parameters like the pressure, energy density, temperature etc. at which one may expect a deconfined state like the QGP, may be obtained from different theoretical considerations, one of which is the MIT bag model. The method of calculation within the frame work of this model has been outlined in [1], short summary of which is also presented here. In the MIT bag model the quarks are treated as massless, non-interacting fermions inside a bag of finite dimension, and they are infinitely massive outside the bag. Confinement in this model is a result of the balance between a bag pressure B directed inwards, and an outward stress arising from the kinetic energy of the quarks. Quarks and gluons are confined within the bag, and the total colour charge contained inside the bag

is zero. An estimation of the bag pressure can be made with the help of Dirac equation for massless non-interacting fermions in a spherical cavity of radius R ,

$$\gamma^\mu p_\mu \psi = 0,$$

where ψ is a four component spinor. Confinement of quarks within the bag is described in terms of a vector current, $J_\mu = \bar{\psi} \gamma_\mu \psi$ the normal component of which vanishes at the bag surface. This condition is same as the requirement that the scalar density $\bar{\psi} \psi$ of the quarks also vanishes at the boundary say, $r = R$. The lowest energy solutions ($s_{1/2}$ -state) of the Dirac's equation for massless fermions restricted by the above mentioned boundary conditions will lead to,

$$p_0 = \frac{2.04}{R}.$$

Considering the bag pressure as due to the energy difference between the vacuum inside and outside the bag, the total energy for an N-quark system becomes,

$$E = \frac{2.04N}{R} + \frac{4\pi}{3} R^3 B.$$

The equilibrium radius of the system located at the radius R , is determined by,

$$\left. \frac{dE}{dr} \right|_{r=R} = 0,$$

which leads to a bag pressure constant,

$$B^{1/4} = \left(\frac{2.04N}{4\pi} \right)^{1/4} \frac{1}{R}.$$

Taking $R \approx 0.8$ fm as the radius for a three quark bound system (a baryon), an estimate of the bag pressure constant can be obtained. Generally, the value of the bag pressure $B^{1/4}$ is taken within a range between 145 MeV and 235 MeV. Now it is clear that if the pressure of the quark matter inside the bag is increased, there will be a point when the pressure directing outward will be greater than the inward bag pressure. When this happens, the bag pressure can not balance the outward pressure and the bag can not contain the quark matter inside the baryon. A new phase of matter consisting of quarks, antiquarks and gluons in a deconfined state is then possible. There can be two possibilities when a high pressure is generated, (i) the temperature of the matter is high, and/or (ii) the baryon number density is large.

1.4.4 Quark-Gluon Plasma at High Temperature

Consider the case of a quark-gluon system in thermal equilibrium at a high temperature T , within a volume V . Once again treat the quarks and gluons as non-interacting massless particles. It is also assumed that the total number of quarks and total number of antiquarks are equal so that the net baryon number in the system is zero. Considering the Fermi-Dirac distribution for quarks and antiquarks, and Bose-Einstein distribution for gluons one can estimate the partial pressure arising due to the quarks, the antiquarks and the gluons separately. Taking together all these contributions the total pressure (P) of an ideal QGP comes out as,

$$P = \left[g_g + \frac{7}{8}(g_q + g_{\bar{q}}) \right] \frac{\pi^2}{90} T^4 = 37 \frac{\pi^2}{90} T^4,$$

where $g_q (= g_{\bar{q}})$ is the degeneracy factor of the quark (antiquark) states and g_g is the degeneracy factor of the gluonic states. The energy density of the quark-gluon matter at a temperature T is,

$$\epsilon = 37 \frac{\pi^2}{30} T^4.$$

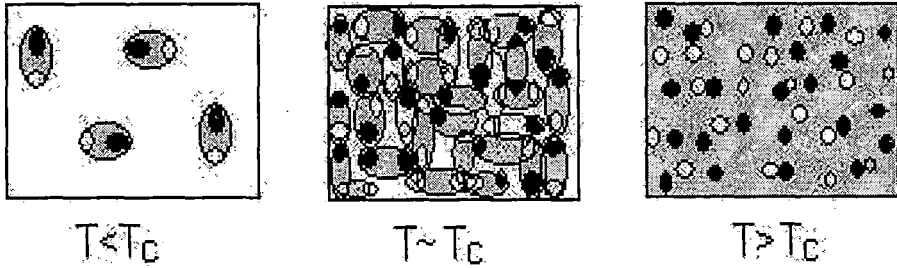


Figure 1.6: A volume enclosing colour neutral hadrons when heated above the critical temperature T_c , undergoes a phase transition to a state comprising of free quarks, antiquarks and gluons.

As the total internal pressure P due to the quark matter increases with increasing temperature, there exists a critical value of temperature at which the internal pressure will be equal to the bag pressure B . The critical temperature T_c is also related to the bag constant as,

$$T_c = \left(\frac{90}{37\pi^2} \right)^{1/4} B^{1/4}.$$

For $B^{1/4} = 215$ MeV we have $T_c \approx 150$ MeV. If the quark matter in a bag is heated up to a temperature greater than this critical temperature, the quark matter inside the bag will experience a pressure greater than the bag pressure. When this happens the bag will not be able to hold the quark matter within the bag and the quark matter will be deconfined.

1.4.5 Quark-Gluon Plasma at High Baryon Density

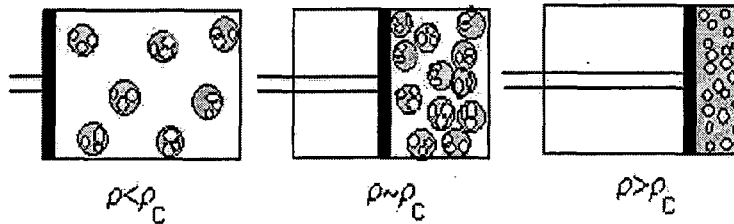


Figure 1.7: A volume enclosing colour neutral hadrons when subjected to extreme pressure, undergoes a similar phase transition beyond the critical density ρ_c .

Let us now look into the possibility of deconfinement at high baryon density at $T = 0$. Because of the Pauli's exclusion principle, an individual quark must populate a single state associated with a definite set of quantum numbers. Due to this, when the number density of quarks increases the quarks must populate states of higher momentum, where the degeneracy of the states are high. Due to this degeneracy the quark gas acquires a pressure, which increases with the increasing quark density. When this pressure exceeds the value of bag pressure, the confinement of quarks within the bag becomes impossible, and a state of deconfined quark matter may then be achieved.

To determine the pressure arising from relativistic quark gas at which the deconfinement occurs at temperature $T = 0$, one may assume for simplicity that the contributions comes only from the quarks. If μ_q is the Fermi momentum i.e. highest possible value of momentum for the quarks at temperature $T = 0$, the energy density of a quark gas can be written as,

$$\epsilon_q = \frac{g_q}{8\pi^2} \mu_q^4.$$

Corresponding pressure density is,

$$P_q = \frac{g_q}{24\pi^2} \mu_q^4.$$

At critical point this quark pressure will be equal to the bag pressure B . This leads to,

$$\mu_q = \left(\frac{24\pi^2}{g_q} \right)^{1/4},$$

which corresponds to a critical quark number density

$$n_q = 4 \left(\frac{g_q}{24\pi^2} \right)^{1/4} B^{3/4}$$

while the corresponding baryon number density is,

$$n_B = \frac{4}{3} \left(\frac{g_q}{24\pi^2} \right)^{1/4} B^{3/4}.$$

For a bag pressure of $B^{1/4} = 215$ MeV, the critical baryon number density at which the hadronic matter becomes a quark-gluon plasma with a high baryon content at $T = 0$ is $n_B = 0.8/fm^3$, which is more than five times larger than the normal nuclear matter density. When the baryon density exceeds the critical value, the bag pressure is not strong enough to withstand the pressure due to the degeneracy of quarks, and the confinement of quarks within the individual baryon bags will not be possible, leading to the formation of a state of deconfined quark matter. From the above discussion it is clear that at high temperature (> 144 MeV) and/or at high baryon density (> 5 times of nuclear matter density), an exotic state like the QGP may be created. It should however be mentioned that the critical values of temperature as well as the baryon density are model dependent, and so they not unique. It is generally accepted that a phase transition should occur if the baryon density becomes $n_B \approx (10$ to $15)$ times the normal nuclear density, and the temperature is so high that the energy density reaches a value like $\epsilon \approx (2$ to $3)$ GeV/fm³.

1.5 The Experimental Scenario

To start it is worthwhile to look back into history, and summarily follow how the heavy-ion accelerator facilities has evolved with time (Table 1.1). The first serious attempt to study nuclear matter under extreme conditions was made at the Lawrence Berkeley Laboratory (LBL) by using the Bevalac facility. Heavy nuclei like Iron ($A = 56$), Krypton

($A = 84$) and Uranium ($A = 238$) were accelerated with an incident energy of a few GeV per nucleon for fixed target experiments. Among other observables in the experiments performed at the Bevalac the central aim was to study the shock compression in extended volume of nuclear matter. Soon the Russians also jumped into the fray and established their synchrophasotron facility at the Joint Institute of Nuclear Research (JINR) at Dubna near Moscow. It was possible for them to accelerate lighter ions like Carbon ($A = 12$), Neon ($A = 20$), Magnesium ($A = 24$) and Silicon ($A = 28$), at slightly higher incident momentum per nucleon ($4 - 5$ GeV/c) than that in the Bevalac. The JINR facility became available in the early 1980's. Using this facility various aspects of particle production in AB collisions like for example, the multiplicity distribution, the y/η distribution, a few particle correlation, azimuthal anisotropy etc. were investigated in fixed target experiments.

Table 1.1. History of Heavy-ion Accelerators

Accelerator	Year	Beam species	Circumference	$\sqrt{s_{NN}}$ GeV
Berkeley - Bevalac	1973	^{16}O , ^{56}Fe , ^{84}Kr , ^{238}U	$\sim 10^2$ mt.	2
Synchrophasotron JINR - Dubna	1985	^{12}C , ^{16}O , ^{20}Ne , ^{24}Mg , ^{28}Si	207.3 mt.	3
BNL - AGS	1987	^{28}Si	0.8 km.	5
	1992	^{197}Au		4
CERN - SPS	1986	^{16}O	6.9 km.	20
	1987	^{32}S		20
	1994	^{208}Pb		17
BNL - RHIC	2000	$^{197}\text{Au} + ^{197}\text{Au}$	3.8 km.	200
CERN - LHC	2008(?)	$^{208}\text{Pb} + ^{208}\text{Pb}$	26.7 km.	5600

With the advent of the Super Proton Synchrotron at the CERN and the Alternating Gradient Synchrotron (AGS) at the Brookhaven National Laboratory (BNL), the prospect of achieving a deconfined QGP like state over an extended volume became brighter. These machines at first started producing lighter ions like Oxygen ($A = 16$), Sulfur ($A = 32$) at CERN and Silicon ($A = 28$) at BNL, and at a later stage heavy nuclei like Lead ($A = 208$) at CERN and Gold ($A = 197$) at BNL. The SPS facility for accelerating nuclei

came first at the late 1980's and the AGS in the early 1990's. In both places many fixed target experiments were carried out, with typical incident ion energy \sim a few hundred GeV per nucleon at the SPS, and ~ 10 GeV per nucleon at the AGS. Several indicators to identify a probable phase transition, have been thoroughly examined by analyzing the data available from the experiments performed both at SPS and AGS. They were compared with models based on numerical simulations, the theories were modified and the data were reexamined. But no concrete evidence of a colour deconfined state was available, thus eluding the expectation of a large number of researchers working in this area. In a bid to achieve a higher *cms* energy the Relativistic Heavy-ion Collider (RHIC) was installed at the BNL, that started functioning in the year 2000. Instead of using fixed targets two beams of Gold nuclei with equal momentum were allowed to impinge upon each other from two opposite directions, resulting in a much higher value of *cms* energy, $\sqrt{s_{NN}} = 200$ GeV. New features have been observed in the RHIC data. However, there is enough indication, that some of the signatures proposed during the AGS-SPS era have still stood the test of time. The lesson of RHIC experiments is that, though the development is proceeding in the right direction, to achieve the ultimate goal of creating and identifying a QGP like state, one has to wait until sometime in the current decade, when the Large Hadron Collider (LHC) at CERN starts to accelerate Lead ions at $\sqrt{s_{NN}} = 5600$ GeV. In the next subsection the experimental arrangements of some of the collaborative experiments performed in the BNL AGS, the CERN SPS and also in the BNL RHIC have been briefly outlined [1, 8, 10, 18]. The experimental results obtained from these experiments have been incorporated in section 1.7, where each signature to identify QGP formation has preceded corresponding experimental results. Within the limited scope of the present thesis it is practically impossible to discuss all experiments performed till date, and any omission though unintentional is regretted.

1.5.1 Experiments at the BNL AGS

Since 1960, the Alternating Gradient Synchrotron (AGS) has been one of the world's premiere particle accelerators, well known for three Nobel Prizes won as a result of researches performed there. The AGS name is derived from the concept of alternating gradient focusing, in which the field gradients of the accelerator's 240 magnets are suc-

cessively alternated inward and outward, permitting particles to be propelled and focused both in the horizontal and vertical planes at the same time. Capable of accelerating 25 trillion protons with every pulse, and heavy-ions such as silicon, gold and iron, the AGS during its most productive period (1992-1993) was annually used by 850 users from 180 institutions from around the world. The AGS receives protons from Brookhaven's 200 MeV linear accelerator (LINAC). The AGS Booster, constructed in 1991, further augmented the capabilities of the AGS, enabling it to accelerate protons and heavy-ions to higher energies. ^{28}Si ions at 14.6A GeV in 1987 and ^{197}Au ions at 10.6A GeV in 1993 were available from the BNL AGS for different fixed target experiments. Currently the AGS is being used as an injector for the Relativistic Heavy-Ion Collider (RHIC). Short description of three experiments performed in the BNL-AGS has been given in Table 1.2.

Table 1.2. Three Experiments at BNL AGS

Experiment	Main Detector(s)	Observables
E802	Zero degree calorimeter (ZDC), Pb-glass Calorimeter (PBGL) Target multiplicity array (TMA), Magnetic spectrometer	E_{ZD} , $\rho(\eta)$, p , \bar{p} , d , π^\pm , K^\pm spectrum
E810	Time projection chamber (TPC)	Momenta and angles of charged particles
E814	NaI + U calorimeter, Target calorimeter (TCAL), Silicon multiplicity counter, Participant calorimeter (PCAL), Forward spectrometer and calorimeter	Transverse energy E_t , multiplicity of n and p in the forward direction

The E802 Experiment: The E802 Experiment experiment is the first heavy-ion programme at BNL. This collaboration studied the production of K^\pm and π^\pm and their ratios, in Si + Au central collisions at 14.5A GeV/c. The layout of the BNL E802 experiment is shown in Fig. 1.8. To identify whether the collisions are central or peripheral, three devices namely Target Multiplicity Array (TMA), Lead Glass Electromagnetic Calorimeter (PBGL) and Zero-degree Hadronic Calorimeter (ZDC) are used. The TMA is made of

tabular counters operated in the proportional mode. In order to determine the tracking of the produced particles two sets of drift chambers (T_1, T_2) are placed in front, and two other sets (T_3, T_4) behind a magnet. This experiment has a powerful identification system for charged particles. The particle identification system consists of 160 flat plastic scintillator time of flight walls (TOF), a 96 segment aerogel Cerenkov counter (AEROC), a 40 segment high pressure gas Cerenkov counter (GASC), and an array of three gas Cerenkov counters (CC) with their associated scintillators (S_1, S_2) and tracking chambers (T_5, T_7).

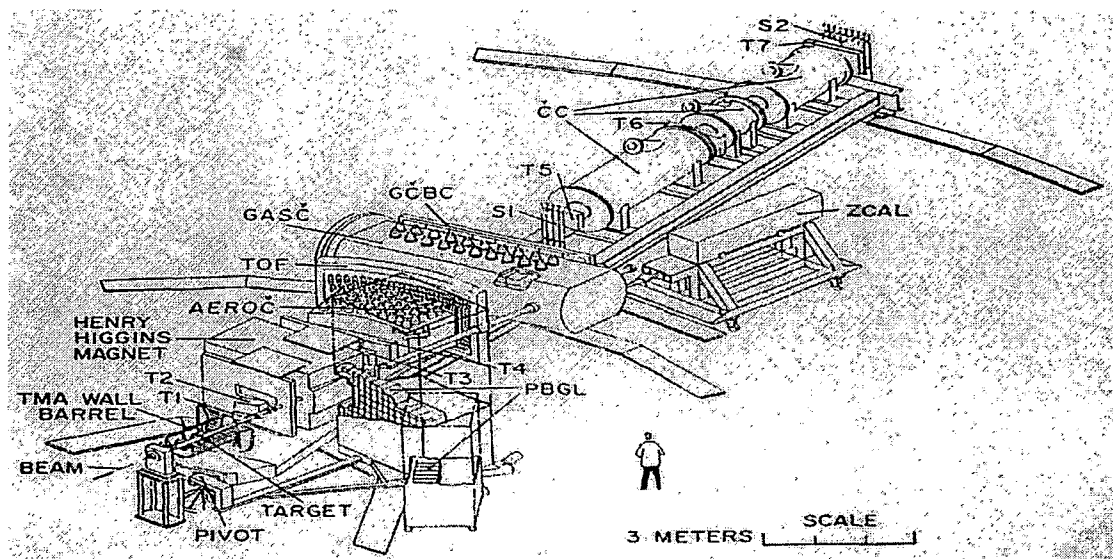


Figure 1.8: The E802 experimental set up.

The E810 Experiment: The main intention of the E810 Experiment was to measure the angles and momenta of charged tracks, using the time projection chambers (TPC's) and trigger detectors. This program allowed the experimenters to look for anomalous behaviour in the y/η , multiplicity, p_t distributions of the produced particle and the participating nucleons. Three TPC modules downstream of the target are used to measure the momenta and angles of the produced charged particles. The ability of the E810 apparatus to detect particles in a relatively large solid angle allowed the researchers to systematically study the correlation among various possible signals. These observations were on an event-by-event basis so that particularly interesting classes of events could be selected and added together to search for new effects (like strangelets) implying a QGP, or

other new states of matter in a manner which tends to maximize signal - to - background ratios.

The E814 Experiment:

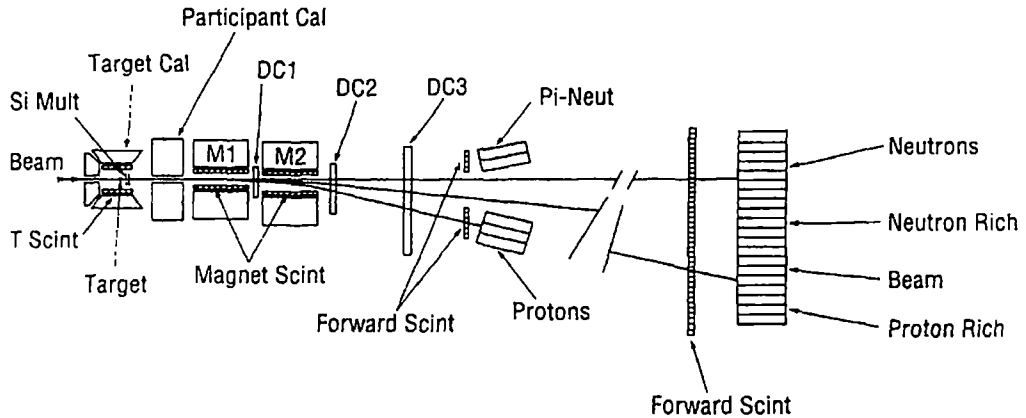


Figure 1.9: The E814 experimental set up.

The E814 collaboration studied $^{28}\text{Si} + \text{Al}$, Cu and Pb collisions at $E_{lab} = 14.6 \text{ GeV/nucleon}$ at the BNL AGS. The experimental setup used in the E814 Experiment is shown in Fig. 1.9. The detectors used in this experiment may be divided into two groups. The upstream set of detectors mainly consists of a target calorimeter, target scintillators, participant calorimeter, and the Silicon multiplicity detector. This set of detectors were mainly designed for detecting the reaction products and target fragments at large angles, such as those produced in more central collisions. A drift chamber, Uranium calorimeters, forward scintillators and magnet scintillators are the constituent components of the downstream detector. The target is surrounded by participant calorimeter (PCAL) and target calorimeter (TCAL). PCAL covers the forward hemisphere ($0.83 \leq \eta \leq 4.20$), and TCAL covers the backward hemisphere ($-0.9 \leq \eta \leq 0.8$). The beam enters through a hole in the back wall of the target calorimeter. Forward going particles pass through the PCAL opening and magnets M1 and M2, which provide the deflection for the forward spectrometer. Track positions are measured in drift chambers DC1, DC2 and DC3. Charge is measured in the forward scintillators and energy is measured in U/Cu calorimeters. The charged

particle multiplicity is measured with the two silicon pad detectors located downstream of the target and inside the TCAL.

1.5.2 Experiments at the CERN-SPS

The Super Proton Synchrotron (SPS) is the second largest of the CERN accelerators, soon going to loose its long lasting glory to the Large hadron Collider, that will start to function sometime in 2008. The SPS has about 7 km circumference, has 1317 conventional (room temperature) electromagnets including 744 dipoles to bend the beams round the ring. A proton beam of 400 GeV energy was first extracted from the SPS in 1976 with a proton flux of 5×10^{12} per pulse. The SPS was later modified to accelerate heavy-ions like ^{16}O at 60 and 200A GeV/c, ^{32}S at 200A GeV/c (year: 1986-'87) and ^{208}Pb at 158A GeV/c (year: 1994). The ions partially stripped of their electrons, originate from an electron cyclotron resonance, pass through a radio frequency quadrupole, and then they are injected to the linear accelerator (LINAC), where they are accelerated to an energy of 4.2A MeV. To get rid of the remaining electrons the ions are then allowed through a stripper foil (0.5 mm thick Al), and then successively accelerated by the proton synchrotron booster (PSB) and proton synchrotron (PS). They come out of the PS with an energy of 4.2A GeV, and then passes through another stripper, that completely ionizes the ions. These ions are then injected into the SPS, where they are accelerated at their highest energies. The ions are extracted at seven different points located at the CERN West and North Area experimental sites. Various experiments were performed in CERN using the accelerator namely Super Proton Synchrotron. Almost 22 years have passed since the CERN ion programme started. All the experiments carried out up to present may be divided into two ages. One is the Oxygen-Sulfur age experiments (1986-1993) and another is the lead age experiments (1994-present). Short summary of some of the CERN heavy-ion experiments is given below with a list of the same in Table 1.3.

The NA34 Experiment: The detector used in the NA34 experiment has two targets. One of them, target 1, consists of the wires of a multiwire proportional chamber. It is surrounded by a Uranium-scintillator calorimeter (U/Sc). Along the beam line there are, a transition radiator detector (TRD) to identify electrons, target 2, a Uranium-liquid Argon calorimeter (U/LA), a Uranium-scintillator calorimeter (U/Sc) followed by a muon

spectrometer consisting of a magnet and multiwire proportional chambers. Another part of the detector called the External Spectrometer sees target 1 through a slit made into the front of U/Sc calorimeter and was designed to detect photons. It consists of a multiwire proportional chamber followed by an iron plate for γ conversion (PC/Conv), and two drift chambers one on each side of a magnet. Photons produced in target 1, when crossing the iron plate, are converted into electron-positron pairs whose trajectories are curved in the magnetic field and detected by the drift chambers.

Table 1.3. Small experiments at CERN SPS: Oxygen - Sulfur age (1986 - 1993)

Experiment	Detector	Observables
EMU01	Nuclear Emulsion, Emulsion Chamber	Shower multiplicity (n_s), Fluctuation, η distribution $\rho(\eta)$, Projectile (<i>target</i>) fragmentation: PF (TF)
EMU02	Plastic	Electromagnetic Dissociation (ED), PF and Fractional charges,
EMU03	Nuclear Emulsion	n_s , PF, $\rho(\eta)$
EMU04	Nuclear Emulsion	Cross-section: direct e^-e^+ pairs
EMU05	Emulsion chamber with magnetic field	n_s , $\rho(\eta)$, K/π ratio, p_t for \pm particles, Boson interferometry
EMU07	Nuclear Emulsion	n_s , $\rho(\eta)$, Fluctuation
EMU08	Nuclear Emulsion	ED, n_s , $\rho(\eta)$, PF and TF, Fluctuation
NA39	Mercury tank	Search for free quarks
NA40	Au-target, γ -spectroscopy	ED, $^{197}\text{Au}(B,X)^{196}\text{Au}$
NA41	Au-target, Si-telescopes	Spallation, Multifragmentation
WA86	Plastic	Calibration for magnetic monopole search at Gran Sasso
WA87	Plastic	ED, Fractional charges
WA88	Plastic	Test of Bubble damage detectors

The NA35 Experiment: The NA35 detector has a streamer chamber placed within a magnetic field, which allows the measurement of charged particles trajectories, momenta,

sign of the charge and multiplicities. It detects also secondary particles coming of some decays, among them the important Λ , $\bar{\Lambda}$ and K_s^0 decays. A veto calorimeter (a zero-degree calorimeter) placed downstream along the beam line defines central and peripheral collisions. It has an electromagnetic calorimeter (PPD) and a hadronic calorimeter (Ring Cal + Intermediate Cal) both covering the η interval $2.2 \leq \eta \leq 3.9$.

1.4. Large Experiments at CERN SPS: Oxygen - Sulfur age (1986 - 1993)

Experiment	Detector	Observables
NA34	U-calorimeter, Liquid Ar-calorimeter Si-pad detectors, External spectrometer	$E_t, \rho(\eta), \pi^-, \gamma$ Low mass muon pairs
NA35	ZDC, Ring calorimeter Photon position detector Streamer chamber, Vertex magnet	$E_{ZD}, E_t, \rho(y),$ $\pi^-, p, K_s^0, \Lambda, \bar{\Lambda}$
NA36	TPC	$K_s^0, \Lambda, \bar{\Lambda}, \Xi, \Omega$
NA38	Electromagnetic calorimeter, Di-muon spectrometer	$E_t, \text{Muon pair}, J/\psi$
WA80	ZDC, Mid-rapidity calorimeter (MIRAC), Mid-rapidity multiplicity detector (MIRAM), Large angle multiplicity detector (LAM) Pb-glass photon detector (SAPHIR)	$E_{ZD}, E_t, \text{Multiplicity of}$ $\text{charged particles } (n_{ch}),$ $\rho(\eta), \gamma, \pi^0$
WA85	Ω -spectrometer Butterfly MWPC	$K^+, K^0, \Lambda, \bar{\Lambda}, \Xi^\pm$

The NA38 Experiment: The NA38 experiment consists essentially of a multiple active target made of 10 thin subtargets surrounded by cylindrical scintillators, an electromagnetic calorimeter made of scintillator fibers embedded in lead and divided into 30 cells, and a multi-muon spectrometer. The spectrometer has a beam dump to absorb hadrons, consisting of a Carbon part in which the muons propagate and a Tungsten-Uranium central core to kill the part of the beam which dose not interact in the target. There are

magnets for the measurement of the particle momentum and sign of the charge, four scintillator hodoscopes for the trigger, and eight multiwire proportional chambers for the measurement of trajectories, four placed before the magnet and four after. There is no arrangement for particle identification and multiplicity measurement. By definition a muon is a particle which leaves the target and reaches one of the hodoscope at the far end.

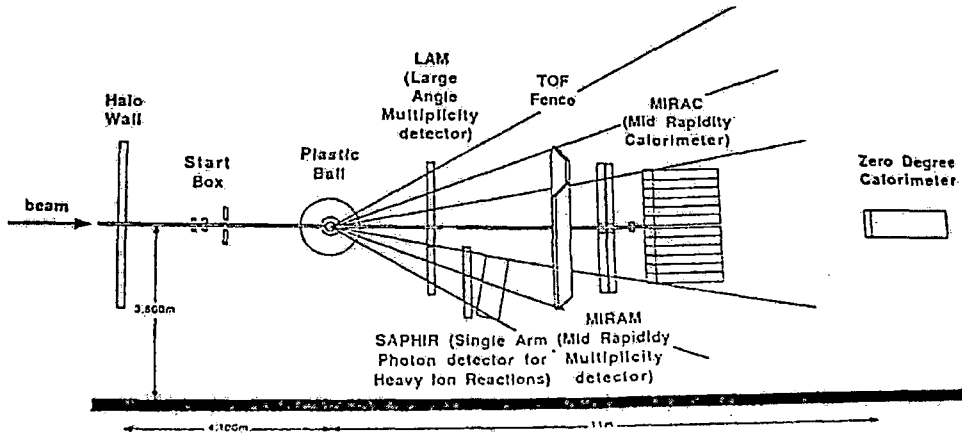


Figure 1.10: Layout of the WA80 detector.

The WA80 Experiment: The lay out of the detector used in WA80 Experiment is shown in Fig. 1.10. It consists of an array of 665 plastic scintillators (plastic ball). Three calorimeters, (a) Uranium-scintillators Zero-Degree Calorimeter (ZDC), (b) Electromagnetic Calorimeter (SAPHIR) and (c) Midrapidity Calorimeter (MIRAC) are used to measure the different energy. All the plastic ball scintillators are used to identify baryons and to measure their energy in the target fragmentation region of $-1.7 \leq \eta \leq 1.3$. The ZDC detector is placed at the end of the detector along the beam line and it is used to decide whether the collisions are central or peripheral. In case of central collisions a small portion of the beam reaches the calorimeter that measures a small energy. To measure the energy and direction of the direct photons the SAPHIR detector is used. This detector consists of 1280 Lead-glass modules. MIRAC is a hadron calorimeter and is very useful to measure the transverse energy flux with a large coverage. Multiplicity of charge particles are measured by the sets of Iarocci streamer tubes called LAM (Large Angle Multiplicity

detector), SAM (Single Arm Multiplicity detector), and MIRAM (Mid-rapidity Multiplicity detector), which cover a wide range of η ($-1.7 \leq \eta \leq 4.4$).

The WA85 Experiment: In this experiment an Ω spectrometer is installed. The Target T is placed inside the Ω magnetic field. Seven multiwire proportional chamber (MWPC) are placed within the magnetic field and four other chambers outside the magnetic field are used to trace the tracks. Two hodoscope HZ0 and HZ1 and the sensitive region of the chambers are matched to detect the charged particles with their transverse momentum above a certain minimum value chosen as ~ 0.6 GeV/c. There is a good detector of multiplicities consisting of two arrays of $50\mu\text{m}$ pitch silicon microstrips, each with 512 channels, placed above and below the beam 15 cm downstream from the target. They measure multiplicities in the η range $2.1 \leq \eta \leq 3.4$. A hadron calorimeter placed along the beam line 25 meter downstream of the target defines central and peripheral collisions (a zero-degree calorimeter).

The NA49 Experiment: NA49 has a large acceptance magnetic and tracking spectrometer, detecting about 70% of all created charged particles simultaneously in each event. It is associated with a large volume gas-filled high-resolution time projection chambers (TPC). Two vertex TPC's are placed inside huge dipole magnets with superconducting coils. From the bending of the trajectories in the magnetic field one derives the particle momentum. Two larger TPC's are placed behind the magnets to measure very accurately the ionization energy loss of the particles in the chamber gas and therefrom deduce the particle velocity. The time-of-flight (TOF) measurement between the target and two walls of scintillation counters tiles provides another independent determination of the velocity for a significant fraction of the particles. The combined knowledge of the momentum and the velocity allows us to identify the mass of the particles. The tracking of charged particles is performed by time projection chambers (TPC). Each main TPC has a readout surface at the top of 3.9×3.9 m², and a depth of the field cage of about 1.1 m. It is filled with a gas mixture of Argon/Carbon Dioxide/Methane in the proportion 91/4.5/4.5. The track signals are read out by 25 proportional chambers providing up to 90 measured points and ionization samples on each particle trajectory. The accuracy of the measurement of the average ionization energy loss for a particle is about 4%. Downstream of the TPC's NA49 has a Ring Calorimeter and a Veto Calorimeter. The Ring Calorimeter is of

sampling type composed of sandwiched layers of Lead or Iron absorbers and scintillator plates. The summed light signal from the scintillator plates is proportional to the energy of the particles absorbed in the calorimeter. The device has a cylindrical structure, coaxial with the incident beam, and its sensitive area is circular with an outer diameter of 3.0 m and a 56 cm central hole. It is segmented into 240 cells, 24 sectors in azimuth and 10 rings radially. The Ring Calorimeter was used to measure the energy flow due to the particles produced in Pb+Pb collisions. The Veto Calorimeter is also of similar type. It is placed behind an iron collimator with a hole around the beam line designed to let pass only those fragments of the beam nuclei which have not interacted in the target foil. The recorded energy tells us which part of the beam nucleus interacted and thus how close the centers of the colliding nuclei approached during the collision.

1.5. Lead age experiments at CERN SPS: 1994 - present

Experiment	Detector	Particles	y_{lab}	p_t (GeV/c)
NA44	Focusing Spectrometer, TOF	K^+	2.5 – 3.5	0.0 – 1.6
NA49	TPC	$\phi, K^+, K^0, \Lambda, \bar{\Lambda}, \Xi$	3.0 – 5.0	> 0.5
NA50	Dimuon spectrometer	ϕ	3.0 – 4.0	> 1.0
NA52	Beam spectrometer	K^+	1.4 – 6.0	≈ 0
WA97	Silicon telescope	$K^+, K^0, \Lambda, \bar{\Lambda}, \Xi^-,$ $\bar{\Xi}^+, \Omega^-, \bar{\Omega}^+$	2.4 – 3.4	> 0.5

The NA45/CERES Experiment: CERES is one of the second generation heavy-ion experiments at the CERN SPS. It is dedicated to the study of e^+e^- pairs in relativistic nuclear collisions. CERES has taken data for about 10 years. The CERES spectrometer is optimized to measure electron pairs from 50 MeV/c up to 2 GeV/c at mid-rapidity $2.1 < \eta < 2.63$ with 2π azimuthal coverage. NA45 consists of two ring imaging Cherenkov detectors (RICH) with methane gas radiator ($\gamma_{th} \sim 32$, which makes it blind to most of the hadrons) to identify electrons. A pad chamber (PC) behind the two RICH detectors, in conjunction with all other detectors, is used to track the particles. Furthermore a Silicon Drift chamber (SiDC) before the first RICH allows particle tracking to the interaction point and hence determine the vertex (interaction point) of a collision. A Silicon Pad

detector is used for a coarse multiplicity evaluation, which is the bases for the centrality trigger.

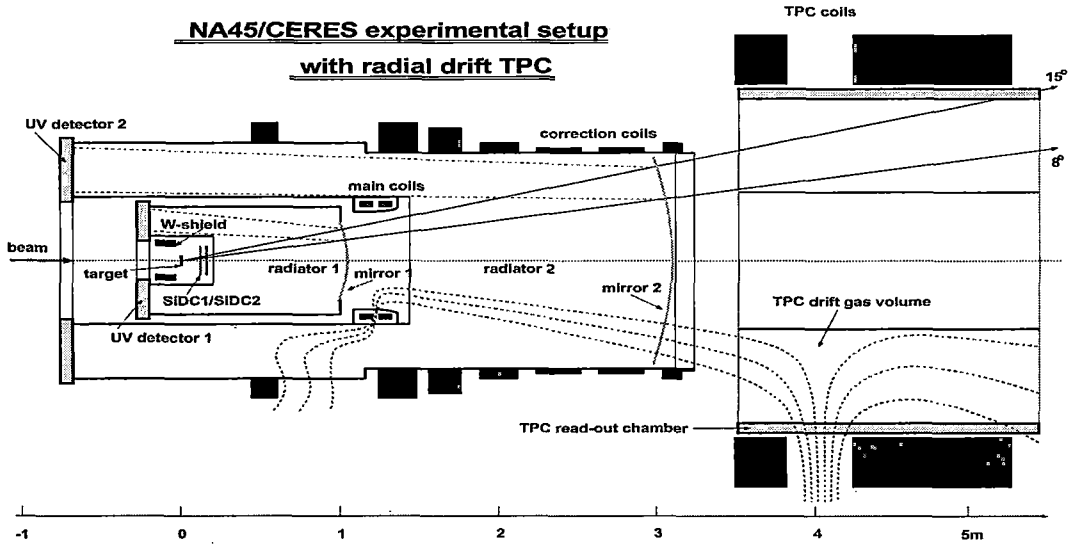


Figure 1.11: CERES detector system has been schematically depicted.

The CERES spectrometer has been upgraded by the addition of radial-drift time projection chamber (TPC) with an additional magnetic field behind the RICH detectors. The TPC was added to CERES in 1998. The new experimental setup is shown in Fig. 1.11. The TPC has a cylindrical geometry as all the other detectors in the experiment and covers the same angular acceptance in θ . Electrons produced by ionization due to the passage of charged particles in the TPC are drifted in a radial electric field defined by an inner cylindrical electrode and 16 read-out chambers at out side. The read-out chambers are multiwire proportional chambers with cathode pad read-out. There are 20 pad-rows in the beam direction with 16×48 pads in azimuthal direction, each sampling the radial (drift) direction in $256 \times$ bins. A magnetic field is provided by two large coils surrounding the TPC with currents running in opposite direction. The measurement of track curving through the magnetic field will provide momentum of the track. The TPC in conjunction with the two SDC's will significantly improve the dielectron mass resolution less than 2%

of the ω mass.

The NA50 Experiment: A dimuon spectrometer designed for the study of the production of J/ψ and high mass lepton pairs. The target is followed by the multiplicity detector and the transverse energy calorimeter, providing information on the centrality of the events, and by an absorber where all the particles except the muons are stopped. A "zero degree" hadron calorimeter for the measurement of the beam spectators is embedded in the absorber. The muons emerging from the absorber pass through a spectrometer that allows the measurement of their momentum. The spectrometer consists of a series of Multi-Wire Proportional Chambers (MWPC) placed before and after a magnet. Scintillator hodoscopes placed between the spectrometer chambers and behind an iron wall at the end of the layout provide the information used to define the dimuon trigger.

The NA57 Experiment: The NA57 setup is designed to measure the decays of strange baryons and antibaryons in the high ultrarelativistic AB collisions at the SPS. The principal aim of NA57 experiment is to investigate of strangeness enhancement effect at the variation of the energy and centrality i.e. the number of participants, of the nucleus-nucleus collisions. NA57 took the data with a Pb beam both at 158A GeV/c and at 40A GeV/c. In such a high-energy a huge number of particles are produced. To reconstruct the decay of Λ , Ξ , Ω , and K in such an environment NA57 used granularity telescope in silicon pixel plane. This detector had the capability to collect a large statistics. The main features of the telescope are:

- (a) The telescope is made of 13 silicon pixel detector planes, for a total of about 1.1×10^6 channels. Seven planes of them use Omega2 front end chip with a pixel size of $75 \times 500 \mu\text{m}^2$ and the rest six planes use Omega3 front end chip with a pixel size of $50 \times 500 \mu\text{m}^2$.
- (b) an array of six scintillator petals, placed 10 cm downstream of the target covering the η range $1 < \eta < 2$, used to trigger on the centrality of the collisions.
- (c) A set of silicon multiplicity detectors sampling the charged multiplicity produced in the region $2 < \eta < 4$, in order to measure the centrality of the nucleus-nucleus collisions. The telescope is placed above the beam line, inclined and aligned with the lower edge of the detector on a line pointing to the target. The centrality of the collision is measured by sampling the charge multiplicity at central rapidity, with two stations of Multiplicity Strip Detectors (MSD).

1.5.3 Experiments at BNL RHIC

The Relativistic Heavy-Ion Collider (RHIC) at BNL is the first machine in the world capable of colliding heavy-ions. RHIC primarily uses ions of ^{197}Au one of the heaviest common elements, because its nucleus is densely packed with particles. RHIC's 2.4 mile ring has six intersection points where its two rings of accelerating magnets cross, allowing the particle beams to collide. The collisions produce the fleeting signals that are captured by one of RHIC's experimental detectors. If RHIC's ring is thought of as a clock face, the four current experiments are at 6 o'clock (STAR), 8 o'clock (PHENIX), 10 o'clock (PHOBOS) and 2 o'clock (BRAHMS). There are two additional intersection points at 12 and 4 o'clock where future experiments may be placed. The main components of the RHIC are:

1. A Tandem Van de Graaff generator that uses static electricity to accelerate atoms removing some of their electrons, The Tandem gives billions of these ions a boost of energy, sending them on their way toward the Booster.
2. Tandem-to-Booster line (TTB) - From the Tandem, the bunches of ions enter the Tandem-to-Booster beam line, which carries them through a vacuum via a magnetic field to the Booster. At this point, they're traveling at about 5% the speed of light.
3. The Booster synchrotron - The Booster synchrotron is a powerful and compact circular accelerator that provides the ions more energy, by having them surf ride on the downhill slope of radio frequency electromagnetic waves. The ions are propelled forward at higher and higher speeds, getting closer and closer to the speed of light. The Booster then feeds the beam into the Alternating Gradient Synchrotron (AGS).
4. AGS - As the ions enter the AGS from the Booster, they are traveling at $\sim 37\%$ the speed of light. As they whirl around the AGS and are accelerated, until they are traveling at 99.7% the speed of light.
5. ATR - When the ion beam is traveling at top speed in the AGS, it is taken down another beam line called the AGS-To-RHIC (ATR) transfer line. At the end of this line, there is a fork in the road, where a switching magnet sends the ion bunches down one of two beam lines. Bunches are directed either left to the clockwise RHIC ring or right to travel counter-clockwise in the second RHIC ring. From here on, the counter-rotating beams are accelerated, as in the Booster and AGS, and then circulate in RHIC where

they will be collided into one another at as many as six interaction points.

The BRAHMS Experiment: One of the RHIC's two smaller detectors is the Broad Range Hadron Magnetic Spectrometer, or "BRAHMS". This device studies charged hadrons as they pass through its spectrometers. BRAHMS measures only a small number of particles emerging from a specific set of angles during each collision. The momentum, energy and other characteristics of the particles are measured very precisely.

The PHOBOS Experiment:

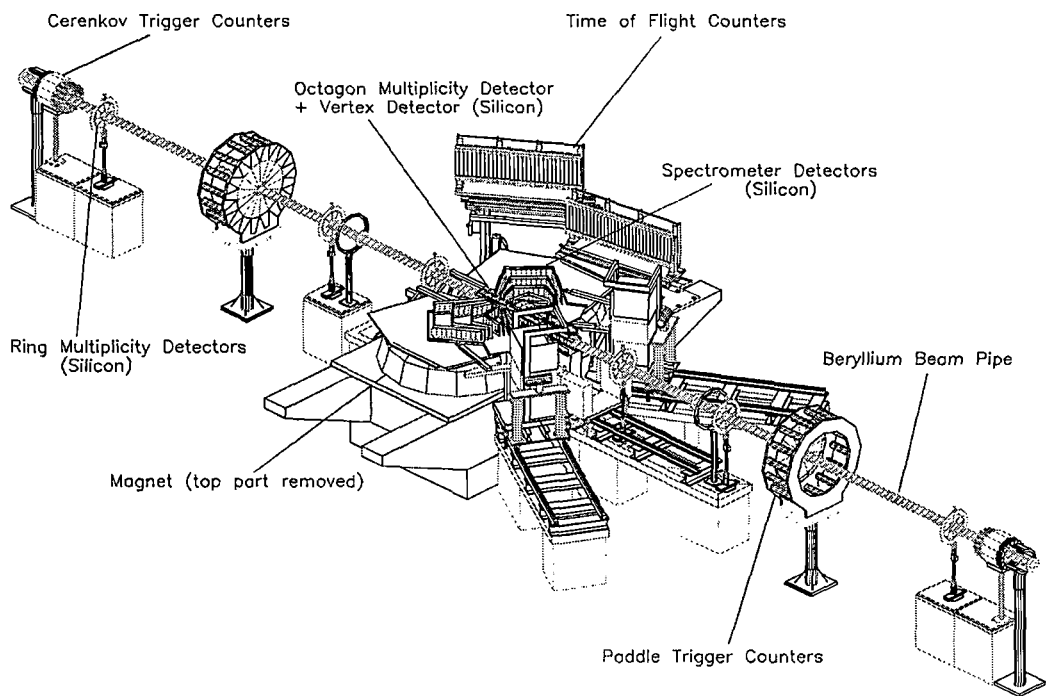


Figure 1.12: Layout of the PHOBOS experimental setup at RHIC.

The PHOBOS detector is comprised primarily of silicon pad sensors used in two separate detector subsystems, as illustrated in Fig. 1.12. The multiplicity array is a single layer of silicon that provides almost 4π coverage. This subsystem is used to measure the number of charged particles emitted from the collisions over a large pseudo-rapidity range $|\eta| \leq 5.4$. Two central double-layered sections of finer granularity Si pads above and below the *Be* beam pipe serve as a vertex detector. The second subsystem has two

spectrometer arms located near mid-rapidity, each consisting of a total of 16 layers of silicon. The spectrometer arms are used to track a fraction ($\sim 2\%$) of the total charged particles emitted in a 2 T magnetic field and to identify these particles by their specific energy loss (dE/dx). Scintillator time-of-flight (TOF) walls extend the particle identification capabilities to higher momenta in one arm. A minimum-bias event trigger is provided by a coincidence registered between two sets of 16 scintillator paddle counters located at ± 3.21 m from the nominal interaction point along the beam axis. The measured time difference is required to be consistent with the primary event vertex occurring between the paddle sets. The paddle counters, which cover $3 < |\eta| < 4.5$, are also used to estimate event centrality, by correlating the sum of their measured signals with the simulated event multiplicity within their acceptance. Each of the four RHIC experiments has zero-degree calorimeters (ZDCs) located ± 18.5 m from the nominal interaction points. The ZDCs provide a common means to measure luminosity and centrality using the beam-velocity neutrons from fragmentation and/or evaporation of the colliding nuclei. The event centrality determined with the paddle counters monotonically correlates with the estimated centrality from the ZDCs, providing an independent cross check of both methods. All the Si sensors in PHOBOS are AC-coupled single-sided, double-metal pad sensors with pad areas varying from 1 to 30 mm². Using this technology, all signals appear on bonding pads at one or two edges of the sensor, where the read-out chips are connected. The Si sensors are read out with VA-HDR-1 chips, providing an analog measurement with large dynamic range (up to 100 MIP) of the ionization charge deposited in each pad. The analog signals are multiplexed out for digitization by 12-bit ADCs. Integrated into the read-out chain is a gain calibration system, which is used to calibrate each individual channel. Latch-up circuitry that interlocks during single-event upset was included to protect against chip radiation damage.

The PHENIX Experiment: The PHENIX detector records many different particles emerging from RHIC collisions, including photons, electrons, muons, and hadrons. PHENIX weighs 4,000 tons and has a dozen detector subsystems. Three large steel magnets produce high magnetic fields to bend charged particles along curved paths. Tracking chambers record hits along the flight path to measure the curvature and thus determine each particle's momentum. Other detectors identify the particle type and/or measure the

particle's energy. Still others record where the collision occurred and determine whether each collision was "head-on" (central), a "near-miss" (peripheral), or something in between. The PHENIX detector is located at the 8 o'clock position on the RHIC ring. The PHENIX Experiment consists of a collection of detectors, each of which perform a specific role in the measurement of the results of a heavy-ion collision. The detectors are grouped into two central arms, which are capable of measuring a variety of particles including pions, protons, kaons, deuterons, photons, and electrons, and two muon arms which focus on the measurement of muon particles. There are also additional event characterization detectors that provide additional information about a collision.

The STAR Experiment: The Solenoidal Tracker at RHIC (STAR) is a detector which specializes in tracking the thousands of particles produced by each ion collision at RHIC. Weighing 1,200 tons and as large as a house, STAR is a massive detector. It is used to search for signatures of the form of matter that RHIC was designed to create: the quark-gluon plasma. It is also used to investigate the behaviour of matter at high-energy densities by making measurements over a large area. STAR's "heart" is the Time Projection Chamber, made of many electronic systems, which tracks and identifies particles emerging from heavy-ion collisions. As each collision occurs, STAR measures many parameters simultaneously to look for signs of the quark-gluon plasma. By using powerful computers to reconstruct the sub-atomic interactions which produce the particles emerging from each collision, the detector can, in a sense, run time backwards. This process can be compared to examining the final products which come out of a factory and trying to determine what kinds of machines produced them. The goal of STAR is to obtain a fundamental understanding of the structure of interactions between particles called hadrons, which are made of quarks and gluons. STAR is located at the 6 o'clock position on the RHIC ring.

1.6 Signatures of QGP in Heavy-ion Interactions

Relativistic heavy-ion collisions are dynamical processes characterized by typical length scale of ~ 10 fm and time scale ~ 10 fm/c. Even if the QGP or a QGP like state is created at any stage of the collision, it is an extremely difficult task to detect it. The

central region with high-energy density cools down very rapidly, and the outcome is only a large number of colour neutral hadrons in the final state. As it is the case for present day ultra-relativistic collisions between two heavy nuclei, from a debris of $\sim 10^2 - 10^3$ particles per collision it therefore, requires a high degree of theoretical insight as well as experimental skill to identify correct signals and trace back for the production of any exotic state like the QGP. As a result of the research efforts during last few decades several signatures for QGP production have been identified. Most of them have already been put to experimental test undertaken by small and big collaborations. While still none of them can claim to be an unambiguous candidate for the QGP, it is worthwhile to know where do we stand at present. A list of some of these signatures is furnished below,

- (i) Enhancement of thermal dileptons and photons
- (ii) Modification in the properties of heavy mesons such as J/ψ due to colour screening
- (iii) Measurement of the particle producing source size through boson interferometry
- (iv) Enhancement in heavier flavours such as, strangeness and charm production
- (v) Elliptic flow of hadrons and modification in the jet structure
- (vi) Suppression of event-by-event fluctuation of conserved charges.

In the following subsections qualitative arguments as to why a particular phenomenon among those listed above, can be treated as a probable QGP signature will be given within the limited scope of the present thesis. The probable physical processes involved in each case have been emphasized. As far as possible, mathematical intricacies, which are beyond the scope of the present thesis, have been avoided [1, 8].

Besides the above signatures, dynamical fluctuation in the phase-space density distributions of produced particles have also been extensively studied in many small and big experiments. Such fluctuations are guided by certain scaling laws, that have been examined by analyzing multiparticle production data as well as through numerical simulations. The origin of dynamical fluctuations is being debated, and it still remains an open issue whether or not such fluctuations are a result of some kind of phase transition. Efforts have been made to correlate the fluctuations with definite geometrical patterns such as fractals. In the present investigation, we too have examined several issues related to the dynamical fluctuation of produced charged particles in $^{32}\text{S-Ag/Br}$ interaction at an incident momentum of 200A GeV/c. No distinction in terms of charge sign or mass of the

particles have been made. While in chapters III to V these issues have been discussed in the perspective of present experimental investigation, in section 1.7 a brief review of other experimental results on dynamical fluctuation have been made.

1.6.1 Dilepton Production

A dilepton is simply a system of lepton-antilepton pair. Inside a volume where deconfined quarks and antiquarks are freely moving, a quark can interact with an antiquark to form a virtual photon (γ^*), that can subsequently decay into a lepton (l^-) and an antilepton (l^+). A dilepton may be characterized by a dilepton four momentum $p = p^- + p^+$, its invariant mass squared $M^2 = p^\mu p_\mu$, and a dilepton transverse momentum $p_t = p_t^- + p_t^+$, where $p^-(p^+)$ is the four momentum of $l^-(l^+)$.

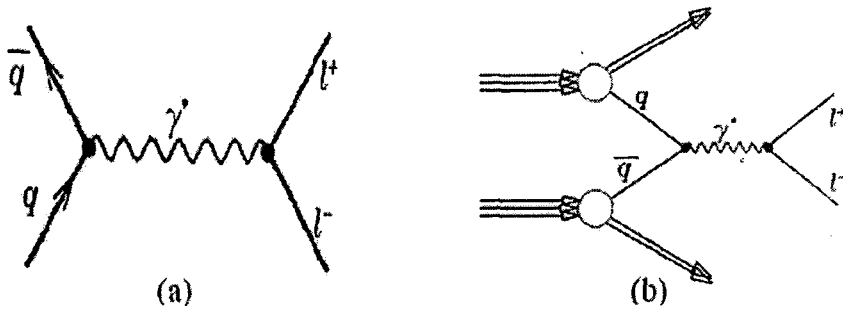


Figure 1.13: (a) Feynman diagram for $q\bar{q} \rightarrow l^-l^+$ process; (b) l^-l^+ production in the Drell-Yan process.

Leptons can be produced during the entire evolution of an AB collision. But they can be observed only when they can come out of the collision region to reach the detectors. Leptons can interact predominantly through electromagnetic and/or weak interactions. The interaction cross section of a lepton with another charged particle is $\sim (\alpha_e^2/s)$, where $\alpha_e (\approx 1/137)$ is the electromagnetic coupling constant, and \sqrt{s} is the center of mass energy of the lepton-charge particle system. In comparison with the reaction volume corresponding electromagnetic/weak mean free path is sufficiently large, so that the leptons are able to come out of the collision region suffering little interaction. Hence they are considered to carry information of all stages of the evolution of the collision. The production rate and

the momentum distribution of the produced dileptons should depend on the distributions of the quarks and the antiquarks inside the QGP, that are dictated by the thermodynamic conditions of the plasma. Therefore, dileptons coming out from the collision region can carry information about the thermodynamical state of the medium from which they originate [19, 20]. The dilepton number density distribution can be shown to approximately follow a relation like,

$$\frac{dN_{l^-l^+}(QGP)}{dM dy} \sim T_0^3 \left(\frac{M}{T_0}\right)^{1/2} \exp(-M/T_0).$$

The relation can be parametrized to obtain the initial temperature (T_0) of the plasma. The problem is solved by using the usual Feynman diagram technique of the perturbative quantum electrodynamics (QED). However, it has to be remembered that, in high-energy nucleus-nucleus interaction QGP formation is not the only source of l^-l^+ pairs. Other processes such as the Drell-Yan process, hadronic interactions, decay of resonances etc. also contribute to the dilepton production. The contribution from a possible QGP formation can be filtered out only when the contributions from other sources are properly accounted for.

Dilepton Production From Other Sources

A. Drell-Yan process: In a nucleus-nucleus interaction a valance quark of a nucleon of one of the nuclei may interact with a sea antiquark of a nucleon of the other nucleus and they annihilate. Due to this reaction a virtual photon comes out that subsequently decays into an l^-l^+ pair. This is the Drell-Yan (DY) process [21], and the dominant non-QGP contribution of dilepton production actually comes from the DY process. The calculation is based on a Glauber type of probability distribution with respect to the impact parameter between the colliding nuclei [22]. The DY cross-section for the NN system is determined with a suitable choice of functional representation of the parton distribution functions for a particular flavour,

$$xq(x, Q) = A_0 x^{A_1} (1-x)^{A_2} P(x)$$

corresponding to each nucleon. The choice of the smoothly varying function $P(x)$ differs considerably. For the heavy-ion collisions it can be assumed that, the net DY contribution comes from the DY contributions of a collection of independent nucleon-nucleon (NN)

interactions. In particular, for a head-on collision between two equal mass nuclei the number of l^-l^+ pairs coming from the DY process can be shown to scale with the mass number of colliding nuclei in the following way,

$$\frac{dN_{l^-l^+}(DY)}{dM dy} \sim A^{4/3} \frac{d\sigma_{DY}^{NN}}{dM dy}.$$

B. Hadronic decays: Hadrons and hadronic resonances are produced in nucleus-nucleus interactions. Dileptons may also come from hadronic interactions such as, $\pi + \pi \rightarrow l^-l^+$, and from the so called 'hadronic decay cocktail' consisting of the Dalitz decay of π^0 ($\pi^0 \rightarrow \gamma e^-e^+$), decay of hadron resonances e.g., ρ , ω , ϕ , and J/ψ particles. The contribution to dilepton production rate from known hadronic states can once again be estimated following Feynman diagram technique. The decays of hadron resonances show up as sharp peaks in the invariant mass spectrum of the l^-l^+ pairs. Charm mesons such as the $D^-(D^+)$ particle which are composite particles consisting of a charm quark (antiquark) and up, down or strange antiquarks (quarks), may also be produced by the interaction of a constituent of one nucleon with a constituent of the other. According to the lowest order QCD theory, particularly a quark of one nucleon interacts with the sea antiquark of other nucleon to form a virtual gluon which decays into a $c\bar{c}$ pair. The $c\bar{c}$ pair may also be produced as a result of the interaction of a gluon of one nucleon with a gluon of the other nucleon. Following the production of the $c\bar{c}$ pair in a NN hard scattering, the fragmentation of the c quark into a D^+ meson and the fragmentation of the \bar{c} antiquark into a D^- meson result in the production of a D^+D^- pair. D^+D^- pair decays subsequently through the interaction $D^\mp \rightarrow l^\mp \bar{K}^0 \bar{\nu}_l(\nu_l)$ and give rise to an l^-l^+ pair.

Some experimental observations on dilepton production

The NA45/CERES collaboration has studied the invariant mass spectra of low-mass e^-e^+ pairs in p+Be, p+Au interactions at 450 GeV/c, in S+Au interactions at 200A GeV/c, and also in Pb+Au interaction at 158A GeV/c [23]. For the proton induced interactions exclusive measurement of π^0 and η^0 , was compared with the inclusive $M_{e^-e^+}$ spectra. The observed spectra were well explained by the known decays of vector mesons and Dalitz decay of neutral mesons. However, considerable excesses in the e^-e^+ yield was observed both in the S+Au and Pb+Au interactions in the low mass region between π^0 -Dalitz and $\rho - \omega$ peaks ($M_{e^-e^+} \approx 0.4$ GeV). The yield was enhanced by a factor of $\sim 5(3)$

in S(Pb) -induced interaction, and in both cases the enhancements were quite similar in shape. Beside the low M region significant excesses were also observed above $M_{e^-e^+} \approx 1.0$ GeV. Such excess production could not be explained in terms of known hadronic sources. Annihilation of thermal pions ($\pi + \pi \rightarrow e^-e^+$), which itself is an indication of creation of hot and dense matter during the collision, can to a certain extent account for the excess production of e^-e^+ pairs, though not entirely.

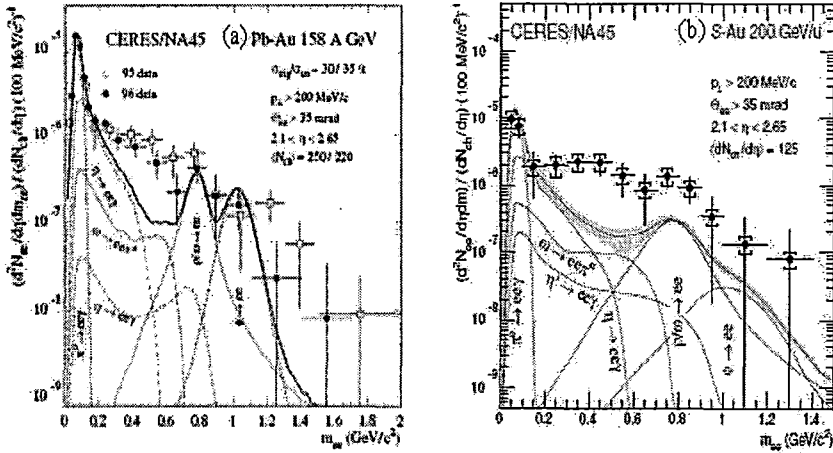


Figure 1.14: NA45/CERES result on excess e^-e^+ production in (a) Pb+Au interactions at 158A GeV/c, and (b) S+Au interactions at 200A GeV/c. The $M_{e^-e^+} = 0.2 - 0.8$ GeV region is to be noted.

In a similar analysis, data on dimuon invariant mass spectra from p+U interactions at 200 GeV/c collected by the NA38 group could be explained by lepton pairs from charm production and the DY mechanism. While the spectra obtained from S+U interaction at 200A GeV/c by the NA38 Collaboration [24], and from Pb+Pb interaction at 158A GeV/c by the NA50 Collaboration [25], showed excess $\mu^- \mu^+$ production around $M_{\mu^- \mu^+} \approx 2.0$ GeV and below the J/ψ mass region. The effects were pronounced more in the central than in the peripheral events. The observed discrepancies in dilepton yields have been interpreted in terms of modified meson properties within a hot/dense medium of interacting particles, thereby indicating an onset of chiral symmetry restoration at the phase boundary between hadronic matter and QGP.

1.6.2 Production of Direct Photons

In a QGP like state the different possible ways of photon production are, (i) annihilation process - a quark interacting with an antiquark to produce a photon and a gluon, ($q\bar{q} \rightarrow \gamma g$), (ii) Compton process - a gluon interacting with a quark (antiquark) to produce a photon, ($gq \rightarrow \gamma q$) and/or ($g\bar{q} \rightarrow \gamma\bar{q}$). Besides these two, a quark can annihilate with an antiquark also to produce a pair of photons, ($q\bar{q} \rightarrow \gamma\gamma$). However, the probability of occurrence for annihilation into 2γ is less by a factor of (α_e/α_s) , which is only a few percent of the other two, and therefore, can be easily neglected. Production of only a single photon in a $q\bar{q}$ annihilation is prohibited by the kinematic considerations. After a photon is produced, it must come out from the collision region in order to be detected. The photons interact only through electromagnetic interaction, and the corresponding mean free path is larger than the dimensions of the reaction volume. Therefore, the photons may not suffer any interaction as they make an exit from the collision zone, and hence they are considered to be clean signal for the state of the matter produced during the collision. The photon production rate and the photon momentum distribution will depend on the momentum distribution of the quarks, antiquarks and gluons present in the medium, which are governed by the thermodynamical conditions of the state. Therefore, photons produced inside the interaction region should carry information about the thermodynamical state of the medium at the moment at its production [26]. Kinematic differences between a sample of selected inclusive photons originating from high-energy AB interactions, and the photons that originate from known hadronic decays may serve as one of the possible tools to search for a QGP like state. It should however be remembered that, besides emission from the QGP photons can also be emitted through two other ways, e.g., from the hot hadron gas through hadronic decays, and through production by parton collisions. It is therefore, necessary to identify the contribution from different sources so as to extract the information on photon emission from the QGP. IF the net baryon density in the QGP is taken to be zero, the energy-momentum distribution of the quarks $f_q(p_q)$ will then be same as that of the antiquarks $f_{\bar{q}}(p_{\bar{q}})$. Both these distributions are of Fermi-Dirac type whereas, the gluons are guided by the Bose-Einstein type of distribution function. Using Feynman calculus, it is possible to find out the the invariant differential photon number distribution $\left(E_\gamma \frac{dN_\gamma}{dp_\gamma d^4x}\right)$ both for the annihilation and the Compton processes.

It is observed that the photons pick up the quark (antiquark) momentum distributions $f_q(p_q)$, and following Kapusta et al. [27] a relation for the differential number

$$E_\gamma \frac{dN_\gamma(QGP)}{dp_\gamma d^4x} \sim f_q(p_\gamma) T^2 \left\{ \ln \left(\frac{3.74 E_\gamma}{g^2 T} \right) \right\}$$

is obtained.

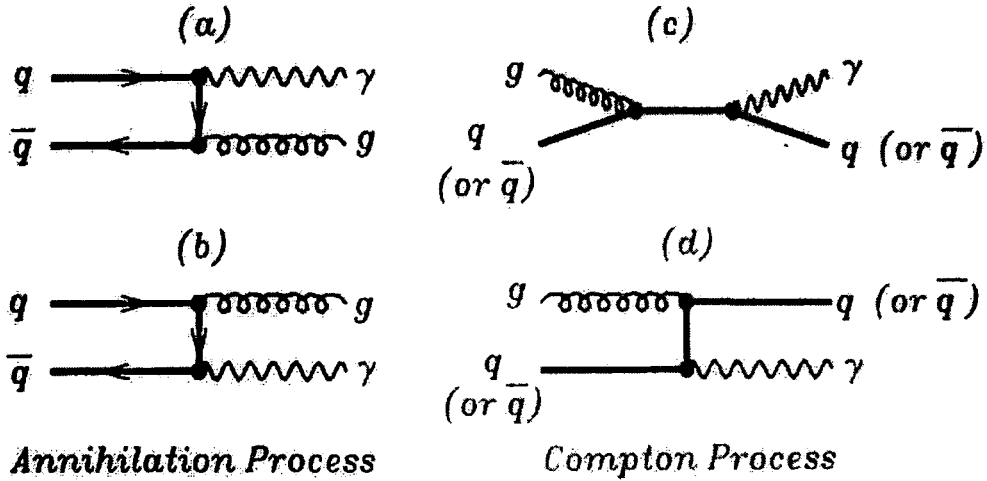


Figure 1.15: (a) and (b) Feynman diagram for photon production in annihilation process $q + \bar{q} \rightarrow g + \gamma$; (c) and (d) the same in Compton scattering process $q(\bar{q}) + g \rightarrow \gamma + q(\bar{q})$.

Photon Production From Other Sources

A. Hadronic interactions: Besides the QGP photons can be emitted by the hot hadronic gas following the annihilation of π mesons $\pi^+\pi^- \rightarrow \gamma\rho^0$, or through the interaction $\pi^\pm\pi^0 \rightarrow \gamma\rho^\pm$. Other possible interactions that may lead to photon production are, (i) $\pi^\pm\rho^0 \rightarrow \gamma\pi^\pm$, (ii) $\pi^\pm\rho^\mp \rightarrow \gamma\pi^0$, and (iii) $\pi^0 + \rho^\pm \rightarrow \gamma\pi^\pm$. Following the same procedure as that for the QGP photons one can determine the invariant differential number for the photons from hadronic decays, which has the following form,

$$E_\gamma \frac{dN_\gamma(\pi^i\pi^j \rightarrow \gamma\rho^k)}{dp_\gamma d^4x} \sim f_{\pi^i}(p_\gamma) \{ \ln E_\gamma + C \},$$

where C is a constant. Since $(\ln E_\gamma + C)$ is a slowly varying function of E_γ , the photon distribution from hadronic decays approximately follow the shape of the hadron distribution $f_\pi(p_\pi)$, and for high hadron energies this has a form $\sim \exp(-E/T_h)$, where T_h

is the temperature of the hadron gas. On the other hand, for photons from the QGP the distribution will be characterized dominantly by a function like $\sim T^2 f_q(p_\gamma)$, where $f_q(p_\gamma) \sim \exp(-E/T_q)$ and T_q is the characteristic temperature of the QGP. As $T_q > T_h$, it is expected that the two distributions for photon production will behave differently, and this difference can be utilized to distinguish between the sources of photon production.

B. Parton collisions: Photons may also be emitted by the initial state (much before a QGP like state is produced) collision of a constituent of one nucleon, with the constituent of other nucleon. For example, a quark of one nucleon can interact with a sea antiquark of the other nucleon to produce a photon and a gluon by the annihilation process and/or a gluon of one nucleon can interact with a quark or a sea antiquark of the other nucleon to produce a photon by the Compton process. Production of photons due to these parton collisions is similar to the production of photons from the QGP. The only significant difference between the two processes is the following. In the case of QGP the photons pick up the distribution function of the quark, antiquark and the gluons, whereas, in the case of parton collisions it is the structure functions, which play a similar role. Assuming same functional representation of the parton distribution as in the case of dilepton production, the characteristic temperature at which photons are produced from parton collisions comes out to be much larger than the characteristic QGP temperature. It is also observed that the effective photon temperature at $\sqrt{s} = 200$ GeV will be large in the case of parton collisions than in the case of QGP. This signifies that at large energies the photon yield from parton collision will be greater than the photon yield from the QGP. Besides the above photons may also be produced by the heavy-ion bremsstrahlung and decay of neutral mesons produced in the interaction such as the π^0 and ρ^0 mesons.

Some experimental observations on direct photon production

It is a difficult task to separate out the contributions from each source of photon production. Enhancement in direct photon production due to thermalization of QGP, considered as a signal, is likely to be shadowed behind a huge background of decaying hadrons such as $\pi^0 \rightarrow \gamma\gamma$ and $\eta \rightarrow \gamma\gamma$. Only a precise comparison of the inclusive photon spectra with contribution from all other known sources of photon production can provide the required information. The NA34 collaboration studied inclusive photon production in p+W, O+W, S+W and S+Pt interactions at 200A GeV/c within a rapidity range of

$1.0 < y < 1.9$ [28]. The photons were converted to e^-e^+ pairs by allowing them to pass through an iron plate, and drift chambers were used to measure their momenta. The sample size of reconstructed photons for each type of interactions was not very large. The major conclusions of this experiment were that, the p_t distribution of photons could be reproduced from known mesonic decays, and no significant difference in the inclusive spectra of photons produced in different types of interactions were observed. It was also observed that the ratio of number of γ 's to the number of π^0 's did not vary with the transverse energy E_t of the photons. The NA45 Collaboration once again measured the photon yields by the conversion method. The measurement covers a η range of $2.03 < \eta < 2.64$. Momenta of the e^-e^+ pairs were measured with a Cerenkov ring imaging spectrometer. Contribution to photon production from the $\pi^0 \rightarrow 2\gamma$ process was estimated from the measured distribution of the charged mesons. Results for central collision of S+Au at 200A GeV showed that, within a systematic error of 11%, there is no evidence of excess photons above the meson decay background.

The WA80 Collaboration studied inclusive photon spectra, $(\frac{1}{N_{ev}} \frac{dN}{dp_t})$ against p_t , covering a η range of $2.1 \leq \eta \leq 2.9$, in p+Au, O+C and O+Au central interactions at 60A and 200A GeV/c in 1986, and later in 1990 in S+Au interaction at 200A GeV/c [29]. Energy measured by a ZDC was used to classify the centrality of interactions. For all types of interactions the inclusive photon spectra were fitted with an analytical function like, $\sim \exp(-p_t/T_{eff})$. The resulting values of T_{eff} came out within a range of $\sim 200 - 235$ MeV. The WA80 experiment also studied the average $\langle p_t \rangle$ of the inclusive photons as a function of centrality as well as the entropy density $(\propto \frac{1}{A_{part}^{2/3}} \frac{dn}{d\eta})$, of the collisions. The $\langle p_t \rangle$ value increases with both centrality and entropy density of the collisions. The WA80 experiment was later upgraded to WA93 experiment with Pb-glass calorimeter arrays and photon multiplicity detector. Data on inclusive photons covering a region $3.3 < \eta < 4.3$ in S+Au interaction at 200A GeV/c were collected. While for peripheral events there did not seem to be any excess photon yield over and above that obtained from the normal mesonic decays, a non-significant excess of direct photon production was observed in the most central collisions. However the scenario was consistent with or without a phase transition being taken into account. Thus none of the above mentioned experiments observed any significant excess in direct photon production. The experimen-

tal results could be reproduced by using hadron and string cascading models without invoking the formation of QGP.

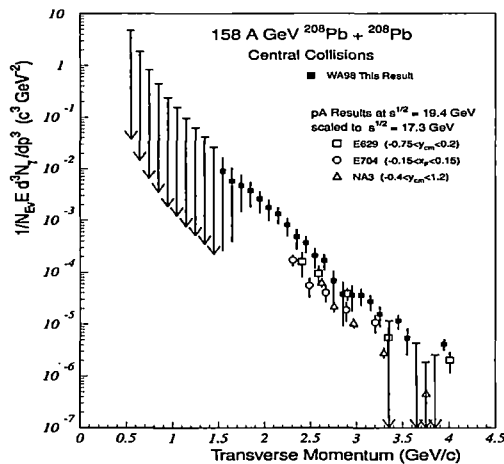


Figure 1.16: WA98 results on direct photon production in ^{208}Pb - ^{208}Pb interaction at 200A GeV/c.

The WA98 experiment at CERN SPS performed a high precision search for inclusive photons in Pb+Pb interaction at 158A GeV covering a range $2.3 \leq \eta \leq 2.95$ and $0.3 \leq p_t \leq 4.0$ GeV/c [30]. For the same data sample neutral meson yield, that forms the basis for background calculation, were extracted. A significant photon excess over the background was observed in the central collisions for $p_t > 1.5$ GeV/c. No significant excess was however found in the peripheral collisions. When WA98 results in photon spectra were scaled by those from fixed target proton induced interactions at similar \sqrt{s} value, the shape of the spectra did exhibit similarity, but the yield was enhanced in Pb+Pb collision. Even the model predictions that could successfully describe the Sulfur age results on inclusive photon yield, failed short by a factor $\sim 1 - 2$ in magnitude for the Pb+Pb collision. However, the global trend of the experimental γ -spectrum of WA98 could be reproduced by model calculations. Subsequent analysis showed that depending on the model assumptions, the initial temperature characterizing the photon spectrum can vary over a wide range ($205 \leq T \leq 270$ MeV), and the agreement between theory and experiment has always been reasonably good. Hence, while WA98 data can naturally be explained in a QGP scenario, it does not necessarily provide a concrete evidence for such

a phase transition.

The PHENIX experiment at RHIC made use of highly segmented electromagnetic calorimeters (Pb-scintillator type and Pb-glass Cherenkov type) to detect photons in high p_t region (upto ≈ 12 GeV/c), coming from Au+Au collisions at $\sqrt{s_{NN}} = 200$ GeV [31]. Ratio of measured inclusive photon spectrum and the expected photon spectrum from mesonic decays for central collisions did exhibit a clear signal beyond $p_t = 4$ GeV/c. When compared with the photon yield from pp collision at $\sqrt{s} = 200$ GeV, this ratio follows the expected scaling with respect to the number of binary collisions involved in Au+Au interactions. Calculation based on photon production due to interaction between partons from hard scattering with thermalized partons of the QGP shows that high p_t photons are not particularly suppressed.

1.6.3 Suppression of J/ψ Production

The evolution of QGP may be described in terms of four stages namely (i)pre-equilibrium, (ii) equilibrium, (iii) cooling, and (iv) hadronization. In the equilibrium state one actually studies the thermalized QGP. It is expected that within a thermalized QGP there would be enough energy density for the formation of heavier quarks and antiquarks in pairs (to conserve flavour) like for example the charm (c, \bar{c}) and strange (s, \bar{s}). It is also expected that while in most of the cases the quark and the antiquark fly apart in opposite directions, some of the quarks and antiquarks may form a quarkonium ($q\bar{q}$) bound state like for example the charmonium ($c\bar{c}$). Such heavy quarks can only be produced at an early stage of the collision when enough energy is available to the colliding partons. In a later stage, as and when the energy is distributed among hundreds of particles, no collision can provide sufficient energy to produce heavy quark flavours. The J/ψ meson is one such charmonium bound state with a mass of 3.1GeV. The potential $V(r)$ between c and \bar{c} can phenomenologically be assumed as a linear combination of a Coulomb part and a confining linear part given by,

$$V(r) = \frac{q_c}{4\pi r} + \kappa r,$$

where q_c is the colour charge of the quark and κ is the $c - \bar{c}$ string tension coefficient. The presence of other quarks, antiquarks and gluons in the QGP, screen the colour charge of the c and \bar{c} , thereby reducing the effect of the attractive Coulomb part of the potential.

The process is similar to the Debye screening in an ordinary electron plasma, and due to this effect the Coulomb potential is modified to a Yukawa type of potential given by

$$\frac{q_c \exp(-r/r_D)}{4\pi r}.$$

The range of this potential is given by the corresponding Debye screening length r_D . On the other hand, the string tension coefficient κ depends on temperature. If a deconfined state like the QGP is formed then $\kappa \rightarrow 0$, at the high temperature that characterizes the QGP formation (\sim a few hundred MeV), and the only way by which a $c\bar{c}$ bound system can be formed is through the Yukawa type of potential mentioned above. Moreover, as r_D changes inversely with temperature, the range of the attractive Yukawa type of force may be small compared to the Bohr radius of the $c\bar{c}$ system, and the formation of a $c\bar{c}$ bound state may not at all be possible. It should also be mentioned at this point that formation of similar quarkonium bound states for up, down and strange quarks are even less possible, simply because the corresponding Bohr radii are even more larger than r_D at characteristic QGP temperature. If any J/ψ state is formed in the initial stage of the AB collision, then in a QGP environment it should dissociate, and the charm quarks and antiquarks can only form open charm systems with lighter quarks such as, $D(c\bar{u}, c\bar{d})$, $\bar{D}(\bar{c}u, \bar{c}d)$, $D_s(c\bar{s})$ and $\bar{D}_s(\bar{c}s)$ mesons. Therefore, if a QGP like state is formed production of J/ψ particle will be highly suppressed, as was first suggested by Matsui and Satz [32] even before any experimental indication in this regard was available. This suppression of J/ψ production compared to the case when there is no possibility of creation of a QGP may, therefore, be used as a signature for the presence of QGP.

Some experimental observations on J/ψ production

The NA38 and NA51 collaborations at CERN carried out experimental investigation to study $\mu^- \mu^+$ production from the continuum, from vector meson decays and from the DY-process in several high-energy pA and AB interactions [33]. The experimental set up basically consisted of scintillators, an electromagnetic calorimeter and a multi-muon spectrometer. The J/ψ is detected via its decay $J/\psi \rightarrow \mu^- \mu^+$. The apparatus is triggered on by muon pairs and measures the electromagnetic energy released in the interaction. In this experiment the muon spectrometer is designed to accept $\mu^- \mu^+$ pairs within a rapidity range $2.8 < y_{lab} < 4.0$. The dimuon mass spectrum showed a continuum along

with a peak at 3.1 GeV that corresponds to the rest mass of J/ψ . One can obtain the number of J/ψ particles in the resonance peak region ($N_{J/\psi}$) and the number of $\mu^-\mu^+$ pairs in the continuum (N_{cont}) under the resonance peak. From pp to S+U, in all types of interactions studied, it has been found that the J/ψ production is suppressed and the ratio $N_{J/\psi}/N_{cont}$ decreases with increasing centrality. The centrality is measured either in terms of the transverse energy deposited, or in terms of number of participating nucleons in a particular interaction. However, in such early experiments induced by proton and light nuclei, the suppression of J/ψ was attributed to absorption of J/ψ in the nuclear matter, they had to traverse after production, and a simple absorption model can explain data up to central S+U collision at 200A GeV/c [34].

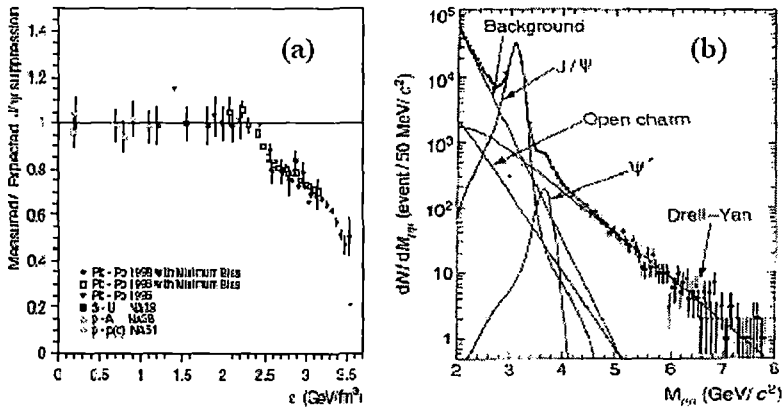


Figure 1.17: (a) Suppression of J/ψ production with increasing centrality (measured in terms of energy density); (b) The dimuon invariant mass spectrum showing the J/ψ peak at $M_{\mu\mu}c^2 = 3.1$ GeV [25].

Using a muon spectrometer, the NA50 collaboration studied the dimuon invariant mass spectrum at CERN SPS for various light ion induced interactions and also in Pb-Pb interaction at 200A GeV/c [25]. A diagram in this respect is given in Fig. 1.17(b). The continuous background of $\mu^-\mu^+$ pairs as well as those originating from different vector meson decays, were studied. Since the rate of DY process was found to remain same in all AB interactions, contribution of the DY process in AB interaction can be estimated from the corresponding value in pp interaction as,

$$\sigma_{DY}^{AB} = AB \sigma_{DY}^{pp}.$$

When the ratio $\sigma_{J/\psi}/\sigma_{DY}$ is normalized by the corresponding value expected from normal nuclear absorption, and the normalized ratio is plotted against the energy density ϵ achieved (Bjorken's formula), a clear suppression in J/ψ production is observed in Fig. 1.17(a) beyond $\epsilon = 2.3 \text{ GeV}/\text{fm}^3$. However, it remains to be seen, whether or not the observed suppression does necessarily require formation a colour deconfined medium, to effect a screening in the colour $c\bar{c}$ binding potential.

1.6.4 Bose-Einstein Interferometry

The interference phenomenon associated with detecting two bosons in coincidence at two different space-time / energy-momentum points, is called intensity interferometry. The probability of coincident detection depends on the transverse separation of the detectors, as well as on the angular separation of the emitting source [35]. This method has been applied in radio-astronomy to measure the angular diameter of a distant star, and is called the Hanbury-Brown-Twiss (HBT) effect [36]. In particle physics also the HBT effect can therefore, be used to estimate the size of the particle emitting source [37]. There is however, a difference in the interference process for photons in astronomy and for mesons in AB interaction. While in the former case the interference takes place near the detector (say telescopes), in the latter case the interference takes place near the source. Assume that two identical bosons are produced with a small momentum difference $(p, p + \Delta p)$ at a short time interval $(t, t + \Delta t)$ with random relative phases. Let (a, b) be the points of emission separated by a distance R of the two bosons from an extended source, and (A, B) be the positions of the detectors separated by a distance D as shown in Fig. 1.18. Let the distance between the source and the detector be r . Let us denote the angles D/r and R/r , respectively, by Θ and Φ , and the distances (aA, bA, bB, aB) , respectively by (x_1, x_2, y_1, y_2) . The probability amplitude for the boson to start at (\mathbf{x}, t) and detected at (\mathbf{x}', t') is given by,

$$\psi(k, x \rightarrow x') = \sum_{\text{all paths}} e^{iS(\text{path})},$$

the dominant contribution coming from the classical trajectory. It is therefore, reasonable to replace the sum by a single term like $\exp\{iS(\text{classical path})\}$. By simple algebraic maneuvering, it can be shown that, both for the nonrelativistic ($S = \int L dt$) and the

relativistic $\left(S = -m \int \sqrt{dt^2 - dx'^2}\right)$ cases,

$$S(\text{classical path}) \approx p.(x - x').$$

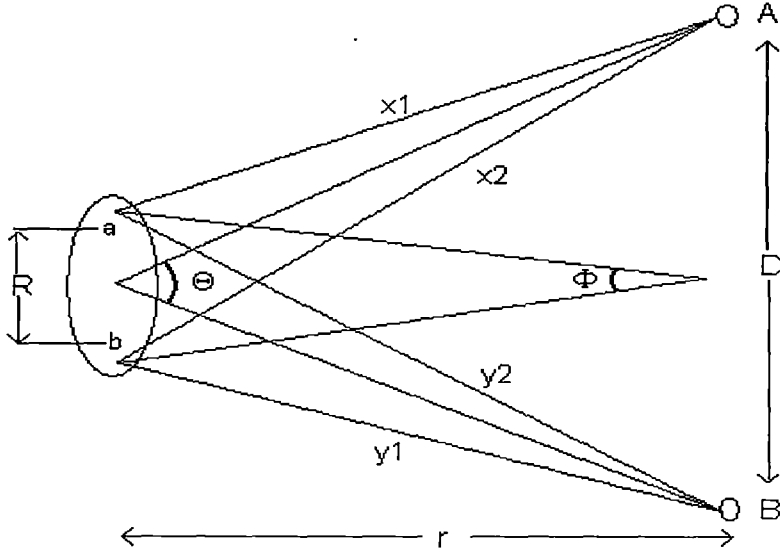


Figure 1.18: Schematic description of source size determination through Bose-Einstein correlation study.

There can be two distinct coincidence possibilities,

(i) A detects a particle coming from a and B detects a particle coming from b : the amplitude for this is given by, $\sim e^{ip.x_1} e^{ip.y_1}$ and

(ii) A detects a particle coming from b and B detects a particle coming from a : the amplitude for this is, $\sim e^{ip.x_2} e^{ip.y_2}$. The amplitude for coincidence is proportional to the sum of the above two amplitudes, which is,

$$\sim e^{ip.(x_1+y_1)} + e^{ip.(x_2+y_2)}.$$

The rate of coincidence is $\propto |\text{amplitude}|^2$, and is therefore,

$$\sim [2 + e^{ip.\{(x_2-x_1)+(y_2-y_1)\}} + e^{-ip.\{(x_2-x_1)+(y_2-y_1)\}}].$$

Note that, $(x_2 - x_1) + (y_2 - y_1) = \Phi D$, and the rate of coincidence is therefore, $\propto 2(1 + \cos pR\Theta)$. As the coincidence rate is measured as a function of Θ , from successive maxima occurring at $pR\Theta = 0, 1, 2 \dots$ one estimates R , the dimension of the source. The criterion for path ambiguity is decided by the uncertainty relation $\Delta p \Delta x \leq \hbar \approx 197 \text{ MeV fm}$. This means that to achieve a simultaneous detection of two identical mesons within $\Delta t \sim 1 \text{ fm/c}$, the mesons must not exceed each other in their momentum values by more than a few hundred MeV. Experimentally this condition may be achieved,

- (i) by studying the interference as a function of difference of a suitable phase-space variable, say momentum magnitudes of two identical mesons $\Delta |\mathbf{p}| = ||\mathbf{p}_1| - |\mathbf{p}_2||$,
- (ii) by studying the interference as functions of magnitudes of difference of transverse and longitudinal components of the mesons, $q_t = ||\mathbf{p}_{1t}| - |\mathbf{p}_{2t}||$, and $q_l = ||\mathbf{p}_{1l}| - |\mathbf{p}_{2l}||$,
- (iii) by studying the interference as function of four-momentum transferred squared, $q^2 = -(q_1 - q_2)^2$.

For a coherent source of particle emission, the production probabilities for individual mesons $P(\mathbf{p}_1)$ and $P(\mathbf{p}_2)$ are independent of each other. Whereas, for a chaotic source these probabilities are correlated, and the degree of correlation is measured by a two-particle correlation coefficient defined by,

$$R_2(\mathbf{p}_1, \mathbf{p}_2) = C_2(\mathbf{p}_1, \mathbf{p}_2) - 1 = \frac{P(\mathbf{p}_1, \mathbf{p}_2)}{P(\mathbf{p}_1)P(\mathbf{p}_2)} - 1.$$

$R_2(\mathbf{p}_1, \mathbf{p}_2) = 0$ for a perfectly coherent source, and $R_2(\mathbf{p}_1, \mathbf{p}_2) = 1$ for a fully chaotic source. Experimentally (i) R_2 or C_2 is measured as a function of phase-space variable as mentioned above, (ii) an analytical expression for C_2 is chosen that depends on source dimension R and freeze-out time τ , and (iii) experimental values of C_2 are fitted with that analytical expression. One choice for the analytic form for C_2 is,

$$C_2 = A \left[1 + \lambda e^{-q^2 R^2} \right],$$

where λ is called the chaoticity parameter: $\lambda = 0$ means coherent emission while $\lambda = 1$ signifies a chaotic emission of mesons. To extract the three dimensional information about the source size, multidimensional Gaussian fit has been made to the relative momentum correlations in the sideward, outward and longitudinal directions with corresponding radii ($R_{side}, R_{out}, R_{long}$) serving the role of fit parameters, the choice for C_2 being,

$$C_2 = A \left[1 + \lambda e^{-(q.R)^2} \right].$$

There are however, other choices for C_2 that appropriately incorporate the dynamics of relativistic AB collision.

Some experimental observations on Interferometry

Interferometric measurements on pions and kaons were carried out both at BNL-AGS and CERN-SPS. Experimentally the correlation coefficient C_2 is measured by normalizing the two particle probability function $P(\mathbf{p}_1, \mathbf{p}_2)$, not with respect to single particle probabilities like $P(\mathbf{p}_1)$, $P(\mathbf{p}_2)$. Instead, a two particle probability function that does not contain any BE-correlation, is used. Such an uncorrelated function is obtained by looking at the production probability of two charged mesons with unlike charges, or by detecting two neutral mesons coming from two different events. Results on three dimensional analysis obtained by the WA80 and NA35 collaborations [38] showed that, (i) transverse radii at mid-rapidity increase with centrality of the collision, (ii) source radii for kaons are consistently smaller than those for pions, (iii) larger radii are obtained for larger collision systems, and (iv) the source radii depend on the sum of pair momentum defined by, $p_t = p_{1t} + p_{2t}$. In central Pb+Pb collisions at 158A GeV incident energy, 5 – 7 fm large transverse root mean square (rms) radii of pion source were observed [39]. This is almost twice the geometrical transverse rms dimension of the colliding nuclei. This indicates that the interferometric dimensions represent a later stage of the collision that has undergone an expansion process. Smaller source radii for kaons (in comparison with pions) indicate that kaons probably freeze out of the collision region earlier than the pions. The p_t dependence of source radii indicates the existence of a collective expansion before the freeze out period. At RHIC large source size and longer duration time for particle production are expected to be achieved. Two particle correlations were measured by the STAR and the PHENIX collaborations [40]. Once again in Au+Au collisions at $\sqrt{s_{NN}} = 200$ GeV the pion source size was of the same order of magnitude as the Pb+Pb collisions. The ratio R_{out}/R_{side} is expected to be significantly different from unity for a prolonged source lifetime. But the observations show that $R_{out}/R_{side} \sim 1$. Interferometric results in general are in conformity with an expanding fireball scenario, where local thermal equilibrium and independent longitudinal and transverse motion are assumed.

1.6.5 Strangeness Production

An enhancement in the number of strange quarks and antiquarks can be treated as one of the signals for QGP formation [41]. As one moves from the pre-equilibrium stage to a thermalized plasma which is also chemically equilibrated, interactions among the constituents belonging to different species of particles present within the system take place. For a thermally equilibrated system the energy-momentum gained by one of the constituent particle is compensated by a corresponding loss of the other, so that the overall distribution remains unaltered. For a chemically equilibrated system gain in the number density of one species is balanced by a corresponding loss through some other (reverse, pair production/annihilation processes etc.), so that the number density of each species remains same. Such a thermally and chemically equilibrated state is characterized, respectively, by a temperature T and chemical potential μ . The occupation probabilities for the quarks (antiquarks) are guided by the Fermi-Dirac type of functions, whereas, the same for the gluons are governed by the Bose-Einstein type of distributions. In an early stage of the AB interaction, where the strangeness content is negligibly small, the system is dominated mainly by lighter quarks (u, d), antiquarks (\bar{u}, \bar{d}) and gluons. As thermal and chemical equilibriums are gradually established through interactions among these particles, strange quarks and antiquarks are copiously formed through processes like, (i) $u\bar{u} \rightarrow s\bar{s}$, (ii) $d\bar{d} \rightarrow s\bar{s}$, and (iii) $gg \rightarrow s\bar{s}$, resulting in a change in the overall strangeness content of the plasma. At high collision energy, where the colliding nuclei are substantially transparent to each other, the nuclear fragmentation regions will be well separated from the central baryon free gluonic plasma region, where the net baryon density can be taken as zero, ($\mu_{u,\bar{u}} = \mu_{d,\bar{d}} = \mu_{s,\bar{s}} = 0$). With the help of perturbative QCD, one can estimate the number density of each quark (antiquark) species provided the QGP is sufficiently long lived to reach thermal and chemical equilibrium. It is possible to show that the density of all quarks and antiquarks are nearly same when a temperature T equivalent to the same order of the strange quark effective mass (m_s) is achieved. Under such circumstances enhancement of strange matter is manifested through production of strange mesons (K^\pm, K^0, \bar{K}^0), strange hyperons ($\Lambda, \Sigma, \Xi, \Omega$), and strange antihyperons ($\bar{\Lambda}, \bar{\Sigma}, \bar{\Xi}, \bar{\Omega}$). On the other hand at comparatively lower collision energy (typical of the BNL-AGS energy), there will be enough stopping between the colliding nuclei, leading

to a baryon rich quark matter having nonzero chemical potential for each of its quark constituents restricted by the condition $\mu_{u,d} > \mu_{s,\bar{s}} > \mu_{\bar{u},\bar{d}}$ near the transition temperature. In a baryon rich system strangeness production is enhanced due to Pauli blocking of light quark production. It's known that, the volume swept out by the cross-section of interaction times the relative velocity between two particles gives us the rate of a particular interaction. One can use this fact to determine the chemical equilibration time (τ) to reach from an initial zero strange quark density to a finite equilibrium density say, n_s . The typical time scale within which a heavy-ion interaction takes place is about ~ 10 fm/c. The estimated value of τ is about 10 fm/c if a temperature of 200 MeV is to be reached. Therefore, it may be concluded that the chemical equilibrium may not be achieved at a plasma temperature ~ 200 MeV, but probably at a higher temperature e.g, $\sim 300 - 400$ MeV.

Some experimental observations on strangeness production

Strange quarks and antiquarks produced pairwise, hadronize either through associated production $NN \rightarrow N\Lambda K^+$ or through production of kaon pairs $NN \rightarrow NNK^+K^-$. If the net baryon density is high associated production of Λ is favored, which in comparison to production of kaon pairs also has a lower threshold energy. Thus the K^+/K^- ratio within the mid-rapidity region can be considered as a signature for strangeness enhancement. Large values of K^+/K^- ratio have been reported by the E802 collaboration in Si+Si, Si+Au and Au+Au collisions, respectively, at 14.6, 14.6, 11.7A GeV incident beam energies [42]. The measured K^+/K^- ratio varied between 5 – 7 with little dependence on the number of participating nucleons. There was however variation in the ratio with the beam energy. In a quark clustering scenario a $\bar{u}d$ di-quark in an environment of high baryon content, is more likely to find an \bar{s} and form a $\bar{\Lambda}$, than to find another \bar{u} and form a \bar{p} . Hence the $\bar{\Lambda}/\bar{p}$ abundance ratio can also serve as a sensitive parameter to study strangeness enhancement. The E864 and E878 experiments [43] measured this ratio around $p_t \sim 0$. The ratio was found to be significantly above unity for the most central Au+Pb collisions at 11.5A GeV incident energy. A ratio greater than unity was also obtained in the E917 experiment [44].

At SPS enhanced production of hyperons (Λ, Ξ, Ω) and antihyperons ($\bar{\Lambda}, \bar{\Xi}, \bar{\Omega}$), was observed and the ratio of each strange baryon and its antibaryon was analyzed by the NA36,

WA85 and WA97 collaborations. The enhancement in strange baryon production was found to be larger than antibaryons. This asymmetry is probably due to large net baryon content at the central rapidity region. The WA97 and NA57 experiments were designed to study the production of strange and multistrange particles in Pb+Pb collisions at the SPS. WA97 collected data from p+Be, p+Pb and Pb+Pb collisions at a beam momentum of 158A GeV at the SPS [45]. The Pb+Pb data have been divided into four centrality classes according to the multiplicity of charged particles (n_{ch}). The yield (multiplicity per event) per unit rapidity of the various particles is determined by integrating the invariant cross section over the full p_t range and over one unit of central rapidity centered around the midrapidity ($y_{cms} = 0$). All yields including those of negative particles (mostly π^-) are enhanced. This is the pattern expected for QGP formation.

The STAR Collaboration studied the production of strange and multistrange baryons in Au+Au collisions and pp interactions at $\sqrt{s_{NN}} = 200$ GeV [46]. The Au+Au event sample consisted of 1.5×10^6 central collision triggers and 1.6×10^6 minimum bias triggers. The pp results were obtained from 6×10^6 minimum bias events. Particles were identified through reconstruction of charged daughter decay particles in a TPC. After suitable cuts the mid-rapidity yield, enhancements for Λ , $\bar{\Lambda}$, Ξ^- , $\bar{\Xi}^+$, Ω^- , $\bar{\Omega}^+$ and inclusive p , as a function of participating nucleon number were plotted. A definite enhancement in the yields over that expected from participating nucleon number scaling, was observed for all the particles mentioned. In SPS the difference in the scale of enhancements in baryon and anti-baryon was due to the existence of a net nonzero baryon number. However, at SPS the ratio of anti-baryon yield to baryon yield varied as a function of participating nucleon number. This possibly indicates different production / annihilation mechanisms for (anti)particles at SPS and at RHIC.

1.6.6 Elliptic flow of hadrons

When two nuclei interact centrally there is a cylindrical symmetry in the colliding system. As a result the azimuthal emission of the hadrons produced exhibit more or less a cylindrically symmetric radial flow. For finite impact parameter ($b \neq 0$) this cylindrical symmetry is destroyed and it is reflected in the emission pattern of the final state hadrons. The elastic collisions between the nucleons change the direction of the particles. If these

collisions are sufficiently frequent, pressure builds up and a collective flow occurs preferentially along the direction of the largest pressure gradient. To determine any preferential emission one has to first define a reaction plane constructed by the beam axis and the impact parameter for a particular interaction. At lower energies (a few GeV per nucleon) the centrally produced matter and the participating nucleons try to escape preferentially in an orthogonal direction to the reaction plane, while the spectator nucleons from both the projectile and the target block their path, leading to a so called "squeeze out" effect. At higher energies the passage time of the spectator nucleons is shrunk by the Lorentz factor given approximately by $2R/\gamma_c$, where R is the radius of individual nuclei, and γ_c is the Lorentz factor in the *cms*. The particle production process takes such a time, that the passage time is not completely irrelevant. As a result the centrally produced matter is initially squeezed-out orthogonal to the reaction plane. But with the spectator nucleons escaping from the reaction zone, the block disappears, and the almond shaped geometry of the overlap region (due to finite b) favors central flow parallel to the impact parameter. The orientation of the flow of this matter is decided by the relative strength of the initial compression and the subsequent expansion time. The anisotropic flow is measured by expanding the particles' azimuthal momentum distribution with respect to the reaction plane in terms of a Fourier series, the coefficients v_n of each term in the expansion characterizing the flow. For each event these Fourier coefficients v_n for different harmonics n are calculated as,

$$v_n = \langle \cos n.(\phi - \psi_n) \rangle$$

where ϕ denotes the transverse momentum emission angle of one particle,

$$\phi = \tan^{-1} \frac{p_y}{p_x},$$

and the reaction plane angle ψ_n is estimated on the event-by-event basis. A nonvanishing coefficient of the first harmonic with respect to this plane essentially reflects the directed transverse flow (the so called "bounce-off" effect invented at the Bevalac), and this can be used to determine the reaction plane. Whereas, the second coefficient v_2 of the second harmonic quantifies the elliptic flow [47]. The ellipticity in spatial coordinates comes about because of the asymmetric overlap of the two colliding nuclei in a non-central collision, and from the pressure gradient developed in the almond shaped collision zone. The initial transverse coordinate space anisotropy of the collision zone or eccentricity

$e = \langle (y^2 - x^2)/(y^2 + x^2) \rangle$ is converted, via hadronic or partonic interactions into an azimuthal momentum space anisotropy. Because of a large amount of rescattering, elliptic flow self-quenches during the expansion period of the collision zone. Therefore, in order to achieve relatively large v_2 a fast thermalization is required. Thus elliptic flow carries information about the pressure and hence about the equation of the state as well as the degree of thermalization achieved by the system. Detailed calculations show however that the dependence on the equation of state is rather weak. It has been argued that it is necessary for the pressure to build up at early times to have a maximal effect. What is meant by "early" time however is not immediately obvious. One should keep in mind that the flow takes time to develop, a time typically of the order of the size of the system. Furthermore, it is easy to see that as one decreases the time at which the hydrodynamical motions starts, the pressure increases but that does not lead necessarily to an increase of the flow; indeed the inertia of the hydrodynamical equation increases proportionally to the pressure. In fact detailed calculation shows that no visible variation of v_2 follows when the initial time is changed from 1 to 2 fm/c. Hydrodynamics appears to explain nicely the variation of v_2 with p_t at small p_t ($p_t < 1$ GeV/c) as well as the mass dependence of the effect, provided it takes into account a phase transition from partonic to hadronic degrees of freedom. This sensitivity to the equation of state underlies the importance of elliptic flow for the understanding of hot and dense nuclear matter, including a possible creation of QGP. It has also to be noted that, the flow of heavier particles is less sensitive to the freeze-out temperature, and therefore, in comparison with the lighter particles it directly reflects conditions at the early stage of the collisions.

A distinctively new feature for azimuthal anisotropy stems from the high p_t results offered by the hard scattering AA collisions at RHIC. A colour charge propagating through a colour charged medium suffers induced radiative energy loss in the same way an electrically charged particle loses energy as it traverses an extended electrically charged medium. Due to interference effects the net energy loss within the medium is proportional to the traversed path length square. However, AB collisions do not offer an infinite homogeneous medium, and the above square law has to be modified due to finiteness of medium size as well as fluctuating local energy density. Partons fragment into hadronic jets as the central high-energy density region expands and reaches freeze out temperature.

If now a jet is created near the periphery of the central region, one of the leading partons may escape the colour charged central fireball into free space without much interaction with the medium. Whereas, its opposite side counterpart will have to travel almost the entire extent of the central fireball, thus losing much of its energy which results into the quenching of the associated hadronic jet. Since the energy loss increases with the length of traversed material, one expects this effect to soften the p_t distribution in the direction perpendicular to the collision plane.

Some experimental observations on elliptic flow

The STAR collaboration [48] observed elliptic flows in pion, kaon, proton and lambda spectra. They found that v_2 values are large and are in good agreement with hydrodynamic models for ultra-relativistic heavy-ion collisions. Surprisingly their data also showed that the elliptic flow persists to high momentum and then it saturates. This applies to $\sqrt{s_{NN}} = 130$ GeV as well as for 200 GeV and to all centralities. The flow pattern follows the predictions of hydrodynamics up to about $p_t \approx 2$ GeV/c. Beyond this point hydrodynamics predicts that the curves should continue to rise. In contrast the elliptic flow was found to saturate. Thus, there is some mechanism at high p_t that allows the asymmetry in the emission pattern to persist to the highest measured transverse momenta. This mechanism may be due to partonic energy loss or some other exotic process. However, at $p_t > 6$ GeV/c non-flow effects could have a considerable contribution to the observed v_2 values.

Study of elliptic flow was also performed by the PHENIX Collaboration [49]. The measurements were made at $\sqrt{s_{NN}} = 200$ GeV with the PHENIX detector at the RHIC. Approximately 6.5×10^8 Au+Au and 8.0×10^7 Cu+Cu minimum-bias collisions were analyzed. The differential elliptic flow measurements for charged hadrons were obtained with the reaction plane method. The value of v_2 against p_t was plotted in both Au+Au and Cu+Cu collisions for different centralities. The v_2 values increased as the collisions become more peripheral and as the p_t increased. For each centrality selections these data were tested for the eccentricity scaling by dividing the differential values of v_2 by the v_2 integrated over a p_t range 0.3 – 2.5 GeV/c. The hydrodynamic model predicts that this ratio should be constant with centrality and should be independent of the colliding

system. These scaled values are found to be independent of the colliding system size and show essentially perfect scaling for the full range of centralities. The v_2 are also in accord with the scale invariance of perfect fluid hydrodynamics, which suggests that rapid local thermalization is achieved.

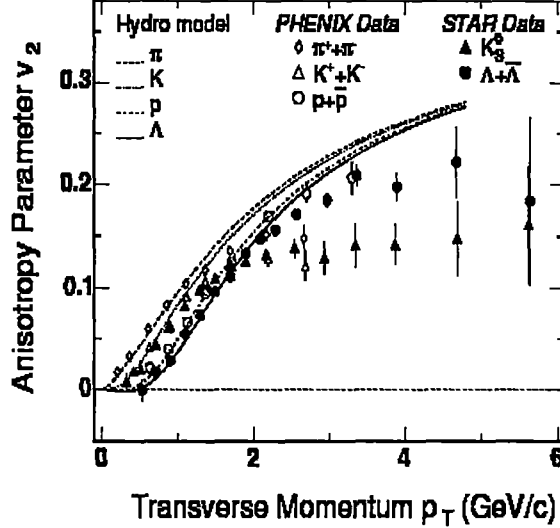


Figure 1.19: Anisotropy parameter v_2 measured in RHIC experiments as a function of transverse momentum p_t .

The elliptic flow of Λ hyperons has been measured by the NA49 experiment in semicentral Pb+Pb collisions at 158A GeV/c [50]. The analyzed sample consists of 3×10^6 semicentral Pb+Pb events with on line trigger selection of the 23.5% most central collisions. The acceptance of Λ hyperons covers the range $p_t \approx 0.4 - 4$ GeV/c and $y \approx -1.5 - +1.0$. The final statistics in Pb+Pb collisions consists of about 10^6 Λ s. The plot of azimuthal distribution of Λ particles with respect to the estimated event plane for real and mixed events and fits of the function in the form of a Fourier series with two parameters v_2 and v_4 . The distributions exhibit a strong correlation for real events and no correlation for mixed events. The correlation significantly increases with transverse momentum and also with impact parameter. The p_t integrated Λ elliptic flow exhibits no significant dependence on rapidity and a weak dependence for protons. The pronounced flatness of $v_2(y)$ suggests that event samples can be directly compared even in different rapidity

ranges as long as Λ -s are measured near midrapidity. The collaboration also measured the p_t dependence of rapidity integrated elliptic flow of Λ -s for two centrality ranges (for $\sigma/\sigma_{tot} = 12.5 - 23.5\%$ and $5.0 - 12.5\%$). They observed that the v_2 parameter significantly increases with transverse momentum - the rise is stronger for more peripheral events. For mid-central collisions NA49 elliptic flow grows linearly with p_t up to ~ 2 GeV/c. The elliptic flow for pions, Λ hyperons and protons are also measured by the NA49 experiment. The elliptic flow grows linearly with p_t for all species but the rise for pions starts from $p_t = 0$ while for protons and Λ s it starts from $p_t = 0.5$ GeV/c. All features observed by the NA49 collaboration are well reproduced by the blast wave parametrization and the hydrodynamic model. The increase of v_2 with p_t is weaker at SPS than at RHIC energy and is significantly overpredicted by the hydrodynamical calculations.

The CERES collaboration [51] measured elliptic flow as a function of p_t of π^\pm and low- p_t protons and Λ and K_S^0 particles from Pb+Au collisions at 158A GeV/c. For the flow analysis, they used 30×10^6 Pb+Au events at 158A GeV/c collected in the year of 2000 data taking period. Of these, 91.2% were triggered on $\sigma/\sigma_{tot} \leq 7\%$, and 8.3% events with $\sigma/\sigma_{tot} \leq 20\%$. Due to small statistics of strange particles, the differential elliptic flow analysis was performed for only two centrality classes. The huge statistics of π^\pm allowed to perform the differential elliptic flow analysis in six centrality bins. They studied the p_t dependences of v_2 for three particle species. An increase of the elliptic flow magnitude vs p_t for all three particle species were observed. The elliptic flow results are compared with the hydrodynamical calculations. The model prediction with the lower freeze-out temperature of $T_f = 120$ MeV overpredicts the data, while rather good agreement can be achieved with a higher freeze-out temperature of $T_f = 160$ MeV (this is however not the preferred value considering the proton p_t spectra). A comparison of the CERES data to results from NA49 at same energy ($\sqrt{s_{NN}} = 17$ GeV) and to STAR results at $\sqrt{s_{NN}} = 200$ GeV is also performed. The NA49 and CERES data are in very good agreement. After rescaling the STAR results to the centrality used in the CERES experiment, the v_2 values measured at RHIC are 15 – 20% higher due to the higher beam energy. From the comparison of the elliptic flow magnitude of the p^\pm , K_S^0 , low momentum protons, and Λ measured by CERES a mass ordering effect is observed. At small p_t up to $p_t \approx 1.5$ GeV/c, $v_2(\Lambda) < v_2(K_S^0) < v_2(p^\pm)$. In high p_t region (above ≈ 2 GeV/c) the

tendency was opposite.

1.6.7 Charged Particle Ratio Fluctuations

According to Jeon and Koch the event by event fluctuations of the ratio of the positively charged and the negatively charged pions $\left(\frac{h^-}{h^+}\right)$ provides a signal of the QGP. The arguments and the methodology are given in their pioneering paper [52], that is summarized below. The idea comes from the fact that in order to detect the colour degree of freedom one generally measures

$$R_{e^-e^+} \equiv \frac{e^-e^+ \rightarrow \text{hadrons}}{e^-e^+ \rightarrow \mu^-\mu^+}.$$

If the fundamental degrees of freedom are hadrons the value of $R_{e^-e^+}$ would have been very different from the simple counting given by,

$$R_{e^-e^+} = n_c \sum_q Q_q^2,$$

where n_c is the number of colour degrees of freedom and Q_q is the charge of each quark flavour. Jeon and Koch suggested that the event-by-event fluctuations of hadron number belonging to different charge signs $\left(\frac{h^-}{h^+}\right)$ can in a similar manner determine whether the underlying degrees of freedom are quarks and gluons or hadrons. They argued that the fluctuation in the net charge depends on the square of the charges of the constituent particles (1/3 for quarks, 0 for gluons, and 1 for hadrons), and hence depends on the phase the hadrons originate from. It is obvious that the ratio $F = Q/N_{ch}$ is a natural choice to measure the net charge fluctuation, where $Q = N_+ - N_-$ is the net charge and $N_{ch} = N_+ + N_-$ is the total charge multiplicity. Here N_{\pm} denotes the positive (negative) multiplicity. However, instead of using F Jeon and Koch used the charge ratio R given by,

$$R = N_+/N_- = \frac{1 + F}{1 - F}.$$

When $\langle N_{ch} \rangle \gg \langle Q \rangle$ one can say that $|F| \ll 1$, as it is the case for high multiplicity AB events. Expanding R in terms of F yields

$$R \approx 1 + 2F + 2F^2,$$

and one can then write

$$\langle \delta R^2 \rangle = \langle R^2 \rangle - \langle R \rangle^2 \approx 4 \langle \delta F^2 \rangle.$$

Using the definition of F one can see that,

$$\langle \delta F^2 \rangle = \frac{\langle Q \rangle^2}{\langle N_{ch} \rangle^2} \left\langle \left(\frac{\delta Q}{\langle Q \rangle} - \frac{\delta N_{ch}}{\langle N_{ch} \rangle} \right)^2 \right\rangle.$$

When the average ratio is very much different from 1, the fluctuation is dominated mainly by the fluctuation in the smaller quantity. In case of relativistic heavy-ion collision it is expected that the fluctuation in F will therefore, be dominated by the fluctuation in Q .

Hence

$$\langle \delta F^2 \rangle \approx \frac{\langle \delta Q \rangle^2}{\langle N_{ch} \rangle^2},$$

and the quantity

$$\langle N_{ch} \rangle \langle \delta R^2 \rangle = 4 \langle N_{ch} \rangle \langle \delta F^2 \rangle \approx 4 \frac{\langle \delta Q \rangle^2}{\langle N_{ch} \rangle^2}$$

has therefore, been considered as the main observable. If the fundamental degree of freedom is a pion gas the value of $\langle \delta Q \rangle^2 / \langle N_{ch} \rangle^2$ is slightly greater than unity and hence the ratio

$$D_{had} \equiv \langle N_{ch} \rangle \langle \delta R^2 \rangle |_{hadron} \approx 4.$$

On the other hand for a QGP the ratio

$$D_{QGP} \equiv \langle N_{ch} \rangle \langle \delta R^2 \rangle |_{QGP} \approx 0.75.$$

It is found that the value D_{QGP} is less than almost by a factor 5 than the value of D_{had} , which one may consider as a suitable signal of QGP formation. Due to several factors the extent of charge fluctuation may either increase or decrease. As for example, hadronization and phase-space cut enhance the ratio D_{had}/D_{QGP} whereas, resonance contributions lower the value of D_{had} .

Some experimental observations on charge fluctuation

STAR Collaboration [53] investigated the charged particle fluctuations in Au+Au collisions at $\sqrt{s_{NN}} = 130$ GeV. Measurements on dynamical fluctuations were performed for inclusive charged particle multiplicities, as well as for identified charged pions, kaons, and protons. They study event-by-event fluctuations of conserved quantities at near-zero rapidity in the center-of-mass rest frame (midrapidity). The data used are from minimum bias and central trigger samples of Au+Au at $\sqrt{s_{NN}} = 130$ GeV acquired by the STAR experiment during the first operation of the relativistic heavy-ion collider. About 1.8×10^5

minimum bias and 8×10^4 central trigger events were used in this analysis. The centrality of the collisions is estimated from the total charged particle track multiplicity detected within the TPC in the η range $\eta \leq 0.75$. Eight contiguous centrality bins based on the fraction of triggered events were used. Specifically, fluctuations in the difference in the number of positively and negatively charged particles (multiplicities) measured within a fixed rapidity range were analyzed. The parameter used for the purpose was,

$$\nu_{\pm} = \left\langle \left(\frac{N_+}{\langle N_+ \rangle} - \frac{N_-}{\langle N_- \rangle} \right)^2 \right\rangle,$$

where N_+ and N_- are multiplicities of positive and negative particles, respectively. The magnitude of the variance (ν_{\pm}) is determined by both statistical and dynamical fluctuations. Statistical fluctuations arise due to the finite number of particles measured, and can be readily calculated based on expectation values for Poisson distributions. The intrinsic or dynamical fluctuations are defined and evaluated as the difference between the measured fluctuations and the statistical limit,

$$\nu_{\pm,dyn} = \nu_{\pm} - \nu_{\pm,st}.$$

STAR Collaboration studied the dynamical fluctuations $\nu_{\pm,dyn}$ of the net charge measured in the η range $|\eta| \leq 0.5$, as a function of the total multiplicity M measured in the η range $|\eta| \leq 0.75$. They obtained the value of dynamical fluctuations of the 5% most central collisions as to $\nu_{\pm,dyn} = -0.00236 \pm 0.00006(st) \pm 0.00012(sys)$. It is found that the dynamical fluctuations are finite and negative which is a clear indication that positive and negative particle production are correlated within the η range considered. One may also observe that the strength of the dynamical fluctuations decreases monotonically with increasing collision centrality. This can be understood from the fact that more central Au+Au collisions involve an increasing number of NN sub-collisions. The two-particle correlations are thus increasingly diluted and the magnitude of $\nu_{\pm,dyn}$ is effectively reduced. The results shows a good agreement with the PHENIX measurements [54]. The results indicate that the dynamical fluctuations for pions are approximately of the same magnitude as for inclusive non-identified charged particles. The dynamical fluctuations of the charged kaons and p , \bar{p} are also finite. Their sizes (absolute value) are in fact larger than the dynamical fluctuations measured for pions and for inclusive non-identified charged particles.

1.7 Particle Density Fluctuations

History shows that the study of fluctuation has often triggered significant advances in physics. Investigation of dynamical fluctuation in the density distributions of particles coming out of high-energy interactions has till date remained one of the most popular tools to study the mechanism of multiparticle production. Efforts have been made to interpret these fluctuations observed within narrow phase-space intervals in AB collisions, in terms of conventional processes like the Bose-Einstein correlation, intranuclear cascading, jet structure, resonances etc., or more exotic process like thermal phase transition. It has been observed that often the produced particles prefer correlated emission. The reason may be a trivial matter of chance, it may be due to the conservation laws associated with kinematic variables, it may be due to some other nontrivial dynamical reason, or it may be a combination of any two and/or all three of the above. Various methods have been devised to separate out the statistical noise arising out of finite number of particles per event from the nontrivial fluctuations arising due to unknown dynamics, if there is any. It would be interesting to identify the origin of the dynamical part of the fluctuation (even through that is speculative in nature), either in terms of any known dynamics or from the perspective of a possible new state such as the QGP. Many particle correlation leads to clustering of particles within narrow regions of a particular phase-space, that would ultimately manifest itself as large fluctuations in the corresponding distribution. The fluctuations may appear either as sharp peaks often called spikes, or as sharp minima called the voids, in the distribution. The existence of spikes may provide crucial information about the substructure in space-time of collision region like, formation of hot spots of hadronic matter. The study of fluctuation is generally carried out in the central particle producing region, because this region carries more information regarding the dynamics of particle production than the other fragmentation regions. In chapter three to five different phenomenological and experimental issues related to the dynamical fluctuation in particle density distribution will be discussed in details. In the following subsections however, a brief review of some of the experimental facts related to this particular topic have been furnished. As far as experimental facts are concerned the discussion is restricted only to some of the AB interactions.

1.7.1 Intermittency

The factorial moment of order q defined for the multiplicity n as

$$f_q = n(n-1) \cdots (n-q+1),$$

is capable of suppressing the Poisson type of statistical noise. Factorial moments of the observed distribution (that contains both a dynamical part and a Poisson type statistical part) are actually equivalent to the ordinary moments of the underlying dynamical part of the distribution, irrespective of its exact analytic form. The importance of factorial moments in analyzing particle distributions with diminishing phase-space interval size was first recognized by Bialas and Peschanski. The technique was then applied to a few very high multiplicity JACEE [55] events initiated by cosmic ray nuclei of extremely high-energy. Bialas and Peschanski [56] also observed that the factorial moments defined for a particular bin (phase-space interval) multiplicity n_m , and normalized by the average bin multiplicity $\langle n_m \rangle$ actually scale with the bin size δX following a power law like,

$$F_q \sim (\delta X)^{-\phi_q},$$

where the exponent $\phi_q (> 0)$ is called the "intermittency index". Normalized factorial moments F_q are particularly sensitive to large density fluctuations at various scales of phase-space interval (bin) size, and they have been found to be very useful to detect large nonstatistical fluctuations as well as the pattern of such fluctuations.

Experimental Results on Intermittency

An analysis on event-to-event fluctuations in hh collisions comparing rapidity distributions of single events with the corresponding sample averaged distribution was performed by Ludlam and Slansky [57]. They observed that the clustering effects in longitudinal phase-space indicate a structured density. After this a series of results confirmed large concentration of particle number in small rapidity regions for single events in cosmic ray experiments, in pp and in pA collisions. The JACEE collaboration [55], the NA22 collaboration [58], the UA5 collaboration [59] have reported high density "spikes" in rapidity space at different resolutions. Using the JACEE data of a single high multiplicity cosmic ray interaction (Si+Ag/Br), the first analysis on intermittency was performed by

Bialas and Peschanski. They were able to show that $\ln \langle F_5 \rangle$ linearly increased with $-\ln \delta\eta$, thus confirming the scaling law. Thereafter, the intermittency analysis had been repeated in different hadronic, leptonic, hA and AB collisions [60]. All experiments confirmed increase in F_q values with diminishing phase-space interval size, though not necessarily always guided by the strict power law proposed by Bialas and Peschanski. The phenomenon is often loosely called 'intermittency', that in case of high-energy interactions is related to an intermittent type dynamical distribution of produced particles.

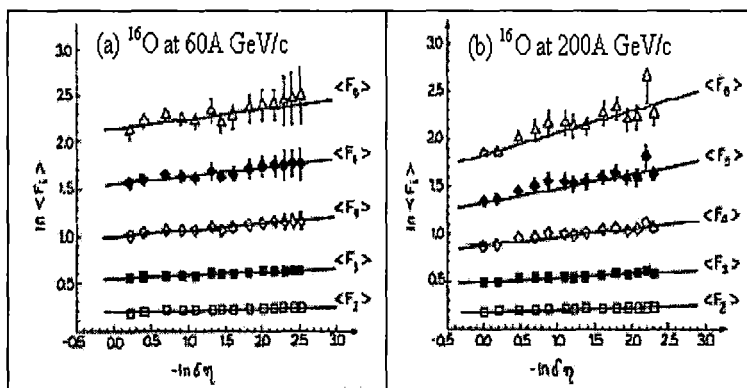


Figure 1.20: First accelerator results on intermittency obtained by the KLM group [61].

The Krakow-Louisiana-Minnesota (KLM) collaboration [61] presented the first experimental evidence for intermittency using accelerator data. The collaboration used nuclear emulsion technique to collect the data. Emulsion pellicles were irradiated by ^{16}O ions at 60A and 200A GeV/c from the CERN-SPS. Fig. 1.20 shows their experimental results, where $\ln \langle F_q \rangle$ values for $q = 2$ to 6 are found to linearly rise with $-\ln \delta\eta$, instead of a flat behaviour that is expected for independent emission. The intermittency indexes increase with increasing order q , and ϕ_q values are larger in 200A GeV/c interactions than those in 60A GeV/c interactions. The EMU01 collaboration [62, 63] also investigated nonstatistical fluctuations in nuclear interactions in terms of intermittency and scaled factorial moment analysis. For this purpose they used emulsion data on ^{16}O and ^{32}S induced interactions at 200A GeV/c from CERN-SPS. Horizontally exposed emulsion pellicles and vertically exposed emulsion chambers were used to collect the data. For all sets of interactions their analysis was confined mainly to the central η -region. The EMU01

collaboration observed that, small intermittency effects were present in one dimensional (η -space) analysis of their AB data. The Monte Carlo code FRITIOF [64], based on a string fragmentation model, could not reproduce the experimentally observed intermittency results. The EMU01 results were also consistent with the relation, $\phi_q = {}^qC_2 \phi_2$, which was another requirement of the scaling law introduced by Bialas and Peschanski. A scaling law like $\phi_2 \sim \langle \rho \rangle^{-1}$ as proposed by Seibert and others [65] was also verified by the EMU01 group for their AB data. The collaboration extended their intermittency analysis to two dimensional (η, φ) space. Though in this case the intermittency effect was found to be stronger, their result on ^{32}S induced interactions was strongly influenced by the γ -conversion [63]. The two dimensional procedure seems to work as a filter for the electron pairs. They concluded that the correlations which gave the largest contributions to the one dimensional moments were not necessarily the same as the one that were contributing to the two dimensional moments.

The WA80 collaboration [66] studied the intermittency phenomenon in very large samples of $^{16}\text{O}+\text{C}$ and $^{16}\text{O}+\text{Au}$ interactions at 200A GeV/c. The data were collected by using Iarocci type streamer tubes, and the analysis were confined to the central η -region ($2.4 < \eta < 4.0$). Centrality of the collision was decided by using a ZDC. Major observations of this experiment were, observation of intermittency effect for produced particles in AB interactions under consideration, higher intermittency indexes for event samples with intermediate value of impact parameter than in the most central collisions, and constancy of $\phi_q/[q(q-1)]$ as required by the scaling law of Bialas and Peschanski.

Sarkisyan et al. [67] used streamer chamber data to study the intermittency effect in C+Cu interactions at 4.5A GeV/c obtained from the JINR Synchrophasotron (Dubna). F_q values for $q = 2 - 8$ were determined. From their analysis on ϕ_q and related fractal parameters, they conjectured occurrence of a nonthermal phase transition during the space-time evolution of the AB collision process. According to their study a transition took place from a 'spin glass' phase where the events are dominated by a few dense particle producing regions, to the normal phase that is populated by a large number of not so dense regions.

Using the EMU01 data on Pb + Pb collision at 158A GeV/c (CERN SPS), Tawfik [68] performed an intermittency analysis in 1-d (η/φ) and 2-d (η, φ) spaces. SFM of order

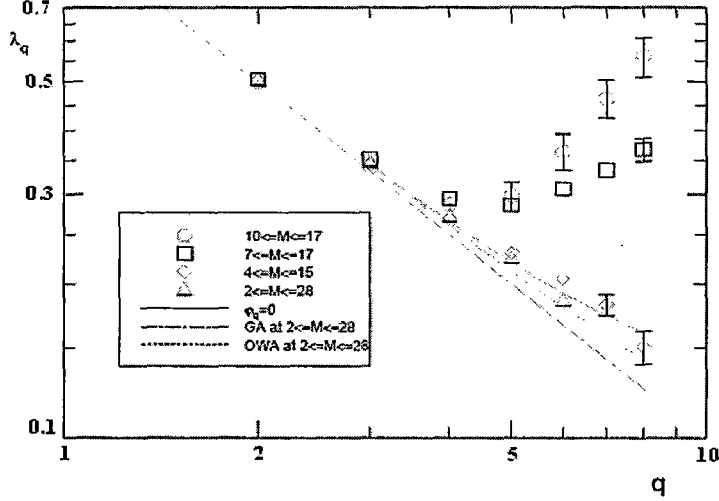


Figure 1.21: Results indicating existence of a mixture of two phases $\lambda < \lambda_c$: normal phase, and $\lambda > \lambda_c$: spin glass phase [67].

$q = 2$ to 6 were obtained as functions of respective phase-space partition numbers M_η , M_φ and $(M_\eta \cdot M_\varphi)$. While in 1-d $2 \leq M_\eta, M_\varphi \leq 30$ in 2-d $2 \leq M_\eta, M_\varphi \leq 11$. F_q values in 2-d analysis increased faster with certain degree of nonlinearity than in the 1-d analysis. Intermittency exponents obtained from 2-d analysis provided a hint of possible thermal phase transition indicating an onset of QGP formation. The indication of such thermal phase transitions however, was not unambiguous. Tawfik and Ganssaugue [69] extended the intermittency analysis to a subsample of very high multiplicity events ($n > 1200$) from the same set of Pb+Pb data and compared the experimental results with the FRITIOF [70], VENUS [71] and RQMD [72] predictions. The 1-d $\eta(\varphi)$ -space was partitioned by a large number $M_\eta(M_\varphi) \sim 10^3$, and an upward exponential bending in the variation of F_q was observed. The simulated values of F_q are consistently lower than the experimental values. However, at the largest partition numbers, the same upward bending could be observed in all three simulated samples, though with varying degree.

1.7.2 Self-affinity

Most of the analysis of factorial moments are generally performed for one dimensional distribution of produced particles, while the real process occurs in a three dimensional

space. In a lower dimensional projection of the actual event an implicit averaging process reduces the extent of fluctuation. In a two dimensional α -model Ochs [73] actually showed that, the effects of intermittency were more prominent in higher dimensions. It was also observed in various experiments that, the power law is not exact in higher dimensions. Moreover, in most of the cases the effect of intermittency has been studied by equally dividing different dimensions of phase-space. But the distributions of particles are not isotropic in each dimension, and hence the scaling should be different in different directions. The scaling behaviour incorporating this kind of unequal partitioning in different directions is known as self-affine rather than self-similar scaling. The self-affine structure of phase-space is characterized by a parameter called the Hurst exponent (H), that connects the partition number in a particular dimension with that in the other. The parameter can be obtained from the observed saturation curves of one dimensional $\ln F_q$ distributions. Only a few works have been reported so far, where evidence of self-affinity in multiparticle production is indicated by the data.

Experimental Results on Self-affinity

The anomalous scaling behaviour of 2-d scaled factorial moments for shower particles produced in AB collisions was studied in detail by the EMU01 collaboration [74], using both minimum bias and central interactions of ^{16}O +emulsion at 60 and 200A GeV/c, ^{32}S +emulsion at 200A GeV/c - both from CERN SPS, and ^{197}Au +emulsion at 11A GeV/c collisions from BNL AGS. They analyzed the experimentally obtained second order SFM with different values of Hurst exponent ($H = 0.8, 1.0, 2.0, 3.0$) in the (η, φ) plane. The variation of $\ln \langle F_2 \rangle$ with respect to $\ln M$ were studied, where M is the 2-d partition number. It can be seen from there investigation that when $H = 1$, the curves bends upward strongly and with increasing value of H this upward bending is weakened. Thus, in order to recover the anomalous scaling of SFM, the phase-space should be divided finer in the longitudinal (η) direction than in the transverse (φ) direction.

Haq et al. [75] investigated the anomalous scaling behaviour of F_2 in (η, φ) plane for shower particles produced in ^{28}Si +emulsion collisions at 14.6A GeV (BNL AGS). The experimental result was compared with the UrQMD generated data. Variation of $\ln \langle F_2 \rangle$ with respect to $\ln M$ was studied with in the region $H = 1.0$ to 3.0. Their investigation

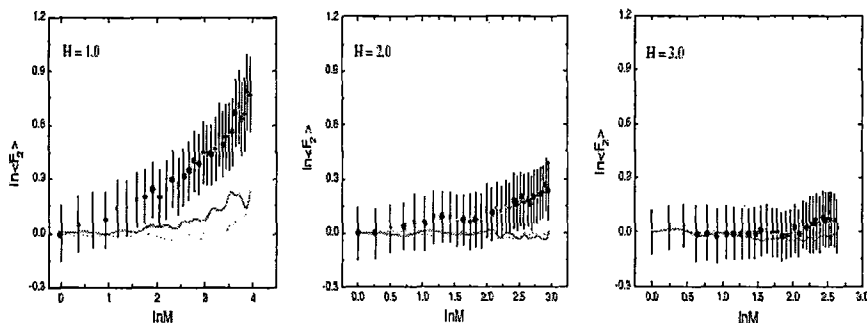


Figure 1.22: Results showing self-affine nature of 2-d intermittency in Si-emulsion interaction at 14.6A GeV/c [75].

shows that, $\ln \langle F_2 \rangle$ versus $\ln M$ plots for the events simulated using UrQMD model consistently lie below the corresponding experimental plots for $H = 1, 1.5$ and 2.0 . For $H = 2.5$ or 3.0 the corresponding separation was not very significant. In order to find out whether the observed behaviour of 2-d second order factorial moment for shower particles is due to interparticle correlation or not, they generated a sample of mixed events of same size and same multiplicity distribution as the experimental one, but without having any interparticle correlation. It was observed that the sample of mixed events also failed to replicate the experimental results. The study on 2-d F_2 for shower particles produced in different AB experiments at CERN SPS and BNL AGS energies showed an upward bending in the variation of $\ln \langle F_2 \rangle$ as a function of $\ln M$. The bending is stronger for heavier colliding system. An AB interaction can be treated as a superposition of many NN collisions. The observations are consistent with the fact that the number of elementary NN collisions is more for heavier colliding nuclei. This upward bending could, however, be removed by choosing different partition along the longitudinal and transverse directions, i.e., the right value of Hurst exponent.

1.7.3 Factorial Correlators

The study of correlation effect provides information on the dynamics of particle production beyond that obtained from single particle inclusive spectra. While the SFM can be used as a measure of local density fluctuations in phase-space, additional information contained in

the correlation between these fluctuations within an event can be extracted by studying the factorial correlators. These correlators are calculated for a particular phase-space interval size and for a pair of nonoverlapping phase-space regions separated by a distance, say D . The normalized correlator is defined as [56],

$$F_{pq} = \frac{\langle n_m^{[p]} n_{m'}^{[q]} \rangle}{\langle n_m^{[p]} \rangle \langle n_{m'}^{[q]} \rangle}.$$

Here n_m and $n_{m'}$ are the number of particles respectively, in the m -th and m' -th intervals each of width $\delta\eta$, and $n_m^{[p]} = n_m(n_m - 1) \cdots (n_m - p + 1)$. According to a simple intermittency model (α -model), F_{pq} depends on D but not on $\delta\eta$ and follows a power law like,

$$F_{pq} \propto D^{-\phi_{pq}},$$

while the exponent ϕ_{pq} follows the relation $\phi_{pq} = pq\phi_{11}$.

Experimental Results on Factorial Correlators

Factorial correlators have been studied in the EMU01 experiment [63] using ^{32}S +emulsion data at 200A GeV/c. Growing correlation with decreasing value of D was observed from their plot of $\ln \langle F_{pq} \rangle$ against $-\ln D$. Islam and Hasan [76] studied the factorial correlators for ^{28}Si +Ag/Br collisions at 14.6A GeV. Their experimental results were compared with the UrQMD generated events. The power-law dependence of $\langle F_{pq} \rangle$ on the correlation length D was established in their data. The slopes (ϕ_{pq}) were observed to increase with the order (p, q) of correlation. In the region $D < 0.5$ the $\langle F_{pq} \rangle$ values were also found to be independent of the phase-space interval size. Such features of the data are in agreement with the random cascading α -model. When UrQMD generated event sample was in terms of $\langle F_{pq} \rangle$, it was found that the model reproduced the bin width independence, but it failed to reproduce the power-law dependence of $\langle F_{pq} \rangle$ on the correlation length D . Finally in this investigation, the validity of the projection independent scaling relation proposed by Peschanski and Seixas [77] confirmed the presence of intermittent type fluctuations in the data without going into higher dimensional analysis.

Ghosh et al. [78] reported a systematic analysis on correlators for charged particles produced in ^{32}S +Ag/Br interactions at 200A GeV/c. They found a linear relationship between $\ln \langle F_{pq} \rangle$ and $-\ln D$ at large D , and concluded that the behaviour of correlated

moments at large D was largely controlled by the long range correlations. The exponents ϕ_{pq} obtained from the linear fit of $\ln \langle F_{pq} \rangle$ and $-\ln D$ with different $\delta\eta$ registered a

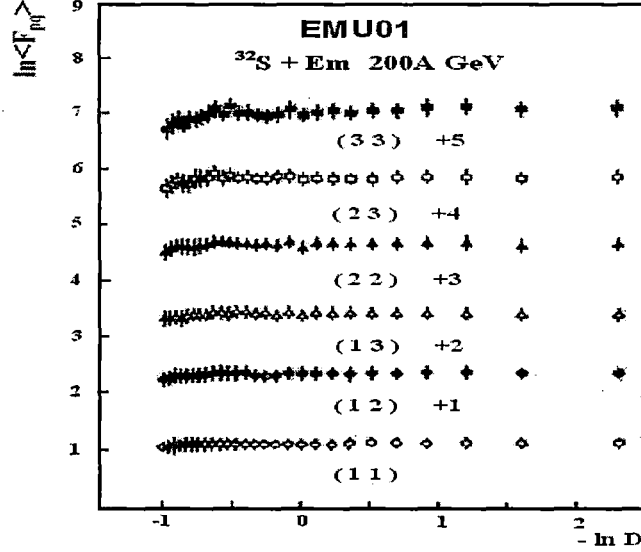


Figure 1.23: EMU01 results on factorial correlators in ^{32}S -Emulsion interaction at 200A GeV/c. For clarity each higher order of F_{pq} has been shifted above the lower one by unit magnitude.

decrease in the exponent value with the decreasing $\delta\eta$. From their measured values of the exponents it was also obvious that for a given bin width $\delta\eta$, the slope values increases with the increase in the product $(p \times q)$. As predicted by the α model they also reported the bin size ($\delta\eta$) independence of the correlators for a fixed D in the region where power law is obeyed. The exponents are expected to follow the relation $\phi_{pq} = \phi_{p+q} - \phi_p - \phi_q = pq\phi_2$, where the first equality sign is due to the α model. This was also confirmed in the investigation. Validity of the dimension independent scaling relation $F_{11}(D) = 2F_2(2D) - F_2(D)$ confirmed the intermittent nature of particle production of their data sample.

1.7.4 Multifractality

With the help of fractal geometry it is possible to mathematically characterize systems that are intrinsically irregular at all scales. The unique property of the fractal structure

is that if a small portion of it is magnified, same complexity or regularity as in the whole system is observed. Fractals fall into two categories - geometrically self-similar or uniform fractals, and nonuniform fractals also called multifractals. The fundamental characteristic of multifractality is that the scaling properties are different in different regions of the system. The idea is therefore to construct a formalism that is able to describe systems with local properties of self-similarity. Unlike geometrical or statistical systems, multiparticle production processes poses a special problem due to finiteness of particle multiplicity in an event. Self-similarity, if existent, therefore, cannot persist indefinitely to finer and finer scales of resolution. For a single event of multiplicity n and for a given $\delta\eta$ one can construct a frequency distribution, which approaches the probability distribution $P(\rho, \delta\eta)$ as $n \rightarrow \infty$. For finite n the frequency distribution and its moments will be subjected to large statistical fluctuations. Event average is therefore recommended. Multifractality concept is understood only to be one probable cause of the observed density fluctuations. The analysis is based on determining the fractal moments also known as frequency moments (G_q) [79, 80]. The moment of order q for an event is defined as,

$$G_q = \sum_{j=1}^M \left[\frac{n_{ij}}{n_i} \right]^q \Theta(n_{ij} - q). \quad (1.8)$$

Here M is the number of intervals into which the entire phase-space has been divided, n_{ij} is the number of particles in the j th bin of i th event, n_i is the total number of particles in the i th event, $[n_i = \sum_{j=1}^M n_{ij}]$, and Θ is a step function which is equal to 1 for $n_{ij} \geq q$ and is equal to 0 for $n_{ij} < q$. Inspired by the theory of intermittency, one can also look into the scaling behaviour of the G-moments in the form,

$$G_q(\delta\eta) \propto (\delta\eta)^{-\tau_q} : (\delta\eta \rightarrow 0).$$

Such a power law dependence typical for fractals cannot be achieved in experiments, as the limit $(\delta\eta \rightarrow 0)$ is admissible only mathematically. One cannot therefore, extract the fractal behaviour in its strict sense. However, significant results can still be obtained around the region of experimental resolution. The multifractal index $\tau(q) = -\partial(\ln G_q)/\partial(\ln M)$, the Lipschitz-Holder exponent $\alpha_q = \partial\tau(q)/\partial q$, and the multifractal spectrum function $f(\alpha_q) = q\alpha_q - \tau(q)$ are some such parameters relevant to multifractal analysis. The generalized fractal dimensions $D_q = \tau(q)^{dyn}/(q-1) = [q\alpha_q - f(\alpha_q)]/[q-1]$ for $q > 2$

can also be extracted experimentally.

Experimental Results On Multifractality

Several experiments have been performed to investigate different aspects of multifractal structure of the underlying dynamical distribution of particle densities. Jain et al. [81] performed their multifractal analysis on the η and φ distributions of charged particles produced in several AB interactions induced by ^{32}S at 200A GeV/c, ^{16}O at 60 and 200A GeV/c, ^{28}Si at 14.5A GeV/c, ^4He at ~ 140 and $\sim 11\text{A}$ GeV, and a proton beam of 800 GeV/c. The experimental results were compared with the VENUS model [71]. Plotting

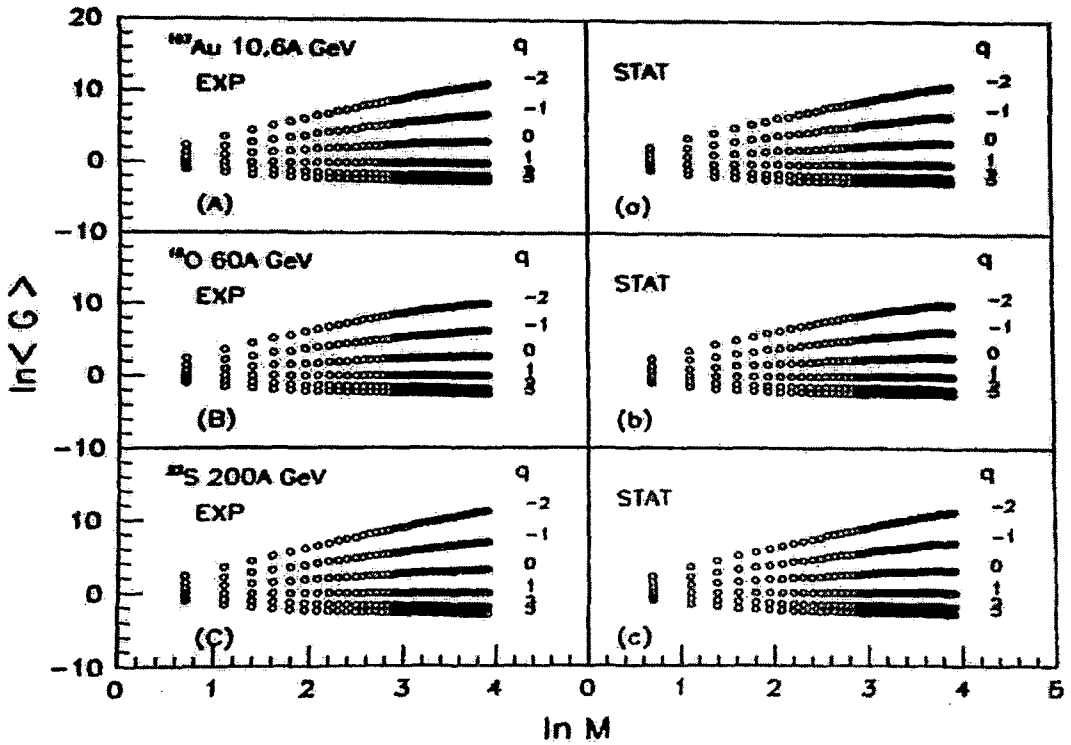


Figure 1.24: Results on multifractal moments obtained by the EMU01 Collaboration [82] on different interactions at SPS energies. Corresponding plots for Monte Carlo generated event sample are also shown.

$\langle \ln G_q \rangle$ against $-\ln \delta\eta$ and $-\ln \delta\varphi$ the power law scaling was verified for all sets of data, and the fractal parameters obtained therefrom showed expected behaviour consistent with the multifractal theory. The multifractal spectrum was wider for the larger

colliding system, while none of them collapsed to a delta function that confirmed the multifractal structure of the dynamical fluctuation. In terms of multifractal analysis no significant difference between the experiment and the VENUS model. Using ^{197}Au , ^{32}S and ^{16}O induced interactions with emulsion nuclei, respectively, at 10.7A GeV, 200A GeV and 60A GeV, the multifractal analysis was performed by the EMU01 collaboration [82]. They also compared their results with Monte Carlo generated samples. They observed that the experimental $\langle G_q \rangle$ and generated $\langle G_q \rangle$ both had very similar forms but still had some differences. They also showed that the behaviour of $\langle \ln G_q \rangle$ and $\ln \langle G_q \rangle$ are different. From their analysis one could see that $\langle G_q \rangle$ did not seem to come only from the contribution of the statistical noise. Their analysis demanded that, the so-called "characteristics for multifractal structure" were obtained for all real data and also for MC data. The behaviour may be described in terms of a purely stochastic model and furthermore the results obtained from real data and MC data were qualitatively same. Thus no definite conclusions on the multifractal structure of particle production in high-energy heavy-ion collisions could be drawn from their analysis.

Sarkisyan et al. [83] reported a fractal analysis of nonstatistical fluctuation in the distribution of produced particles in 4.5A GeV/c C+Ne(Cu) interactions. They used streamer chamber films to collect the data and the exposure was obtained from the JINR at Dubna (Moscow). Both the SFM and the G_q were analyzed to extract fractal parameters and the generalized fractal dimensions D_q . The experimental results on D_q were compared with the predictions of Gaussian approximation, with the assumption of Negative Binomial distribution of multiplicity and prediction of scale invariant branching. As observed in other experiments D_q decreased with increasing q . Multifractal nature of nonstatistical fluctuation was established beyond statistical noise. The authors concluded that their observation was a consequence of nonthermal phase transition in particle production process.

A study of the fractal structure of η distributions of relativistic shower particles produced in $^{28}\text{Si-Ag/Br}$ and $^{12}\text{C-Ag/Br}$ interactions at 4.5A GeV/c was performed by Ahmad and Ahmad [84]. The experimental result was compared with that from events generated by uncorrelated random numbers. While the power law scaling could be verified for both experimental and simulated data, the corresponding fractal parameters behaved differently

in their investigation. Among other parameters the generalized dimensions D_q , which characterize the fractal behaviour, were determined from $\langle G_q \rangle$ values following the relation $D_q = \tau_q/(q - 1)$. It was observed that the D_q values decreased with increasing q and was always less than unity. According to the authors this decreasing trend of D_q indicated multifractality and gave an evidence for the self-similar cascade mechanism in multiparticle production. The measured value of $D_0 = 1$ for different targets implied that there was practically little contribution of empty bins to the analysis.

1.7.5 Takagi's Multifractal Moments

Due to the finiteness in charged particle multiplicity (n_s) of an event, the mathematical limit of phase-space partition number ($M \rightarrow \infty$) can not be realized in practice. Even the step function Θ introduced into the definition of the G_q moments, can not completely remove the saturation effects, particularly at higher $|q|$ values as has already been observed. In an alternative approach, Takagi [85] has suggested a new set of multiplicity moments for $q > 0$ as,

$$T_q(\delta X_\eta) = \ln \sum_{i=1}^{N_{ev}} \sum_{j=1}^M (p_{ij})^q, \quad (1.9)$$

that are not affected by the finiteness of n_s . Here, $p_{ij} (= n_{ij}/K)$ is the normalized density function, K is the total number of particles produced in N_{ev} interactions and n_{ij} is same as Eq. (1.8), when the entire η -space has been divided into M intervals. From the theory of multifractals, $T_q(\delta X_\eta)$ should be a linear function of the logarithm of the resolution $R(\delta X_\eta)$,

$$T_q(\delta X_\eta) = A_q + B_q \ln R(\delta X_\eta), \quad (1.10)$$

where A_q and B_q are constants independent of q . When a linear dependence is observed over a large range of $R(\delta X_\eta)$, following Takagi's method the generalized dimensions can once again be calculated.

Experimental Results On Takagi's Multifractal Moments

Recently Bershanskii suggested that the Bernoulli distribution appears in a natural way when transition from monofractality to multifractality is studied. The following relation for the multifractal Bernoulli function derived by Bershanskii [86] is given by,

$$D_q = D_\infty + C \ln q/(q - 1)$$

where D_q is the generalized dimension of order q and C is a constant. The monofractality to multifractality phase transition corresponds to a gap $C = 0$ to finite nonzero value of C . He also determined the generalized dimensions spectra for ^{32}S -Em interactions at 200 A GeV/c, ^{12}C -Em interactions at 4.5 A GeV and ^{16}O -Em interactions at 60 A GeV [87] and finally obtained a universal value of multifractal specific heat $C \approx 0.25$.

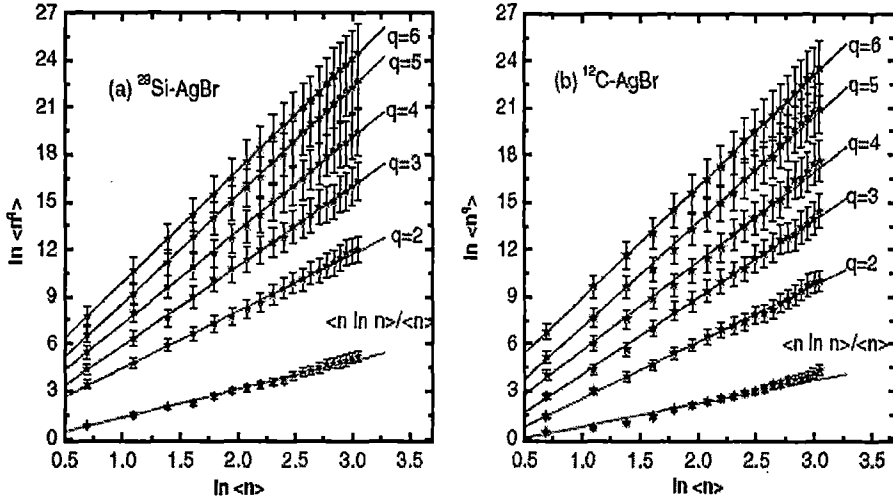


Figure 1.25: Plot of Takagi's multifractal moments in ^{12}C -Em and ^{28}Si -Em collisions at 4.5 A GeV/c [84].

Ahmad et al. [84] applied the Takagi methodology to study the multifractal behaviour of produced particle in ^{12}C -Em and ^{28}Si -Em collisions at 4.5 A GeV/c. Their analysis was confined to the central region ($\eta_{peak} - 1.5 < \eta < \eta_{peak} + 1.5$), which covers most of the produced particles. The values of $\langle n \ln n \rangle / \langle n \rangle$ and $\langle n^q \rangle$ are calculated for each interval. The values of $\ln \langle n^q \rangle$ as a function of $\ln \langle n \rangle$ for different q were plotted for ^{12}C -Em and ^{28}Si -Em collisions and observed that all points clearly follow an excellent linear relation for the whole range of $\langle n \rangle$. The linear behaviour of $\ln \langle n^q \rangle$ with $\ln \langle n \rangle$ in their analysis gives an indication of the fractal structure in multiparticle production in η -space. The values of the slopes, K_q , for ^{12}C -Em and ^{28}Si -Em collisions were calculated. Using the values of K_q they estimates the generalized dimensions D_q , which characterize the fractal behaviour. The values of the generalized dimensions, D_q , for different values of q obtained from Takagi's moment decrease with the increasing order of the moments,

q , and is always less than 1 for all q . The decreasing trend of D_q with increasing q clearly gives an indication of multifractal characteristics, which supports an interpretation in terms of a cascade mechanism in multiparticle production. They also estimated the value of multifractal specific heat using the relation $D_q = D_\infty + C \ln q / (q - 1)$. The observed linear behaviour of D_q with respect to $\ln q / (q - 1)$ indicates good agreement between the experimental data and the multifractal Bernoulli representation.

1.7.6 Erraticity

The erraticity moments $C_{p,q}$ first introduced by Cao and Hwa [88], provide a new technique to investigate both the spatial density fluctuations as well as the event-to-event fluctuations. The method is free from some of the limitations of the scaled factorial moments. The moments $C_{p,q}$ are analytically connected with an entropy index μ_q , a parameter suitable for measuring the chaotic behaviour in the QCD branching process. The entropy index describes the degree of fluctuation of the scaled factorial moments in event space as well as the spatial pattern of the distribution of particles in final states. It also characterizes the degree of fluctuation of the parton multiplicity that initiates the QCD branching. The index μ_q has an added advantage in the sense that it can distinguish a branching process initiated by a quark from that initiated by a gluon. The erraticity moments $C_{p,q}$ is defined as the vertically averaged p -th order moments of the normalized q th order factorial moments i.e.,

$$C_{p,q} = \langle \phi_q^p \rangle_v,$$

where,

$$\langle \phi_q^p \rangle = \frac{F_q^e}{\langle F_q^e \rangle_v},$$

and F_q^e is taken as the horizontally averaged factorial moment for a single event. It should be noted that unlike q , which is always a positive integer, p can be any positive number. If a power law dependence of $C_{p,q}$ on M

$$C_{p,q} \propto M^{\psi_q(p)}$$

is observed, the phenomenon is referred to as erraticity of nonstatistical fluctuation. The exponent $\psi_q(p)$ is called the erraticity index. The slope $\mu_q = \left. \frac{d}{dp} \psi_q(p) \right|_{p=1}$ termed as the entropy index, is an efficient parameter to characterize erraticity. For low multiplicity

hh, hA events the erraticity analysis of gap distribution have also been proposed. In this regard till date very little result exist in the literature.

Experimental Results On Erraticity

Shaoshun and Zhaomin [89] measured the entropy index μ_q for different values of q in case of multiparticle production in pp collisions at 400 GeV/c. Due to nonflatness of the single particle density distribution they used the cumulant variable $\chi(\eta)$ where in $\chi(\eta)$ space the single particle density is uniformly distributed from 0 to 1. They divided the total sample region into M bins and calculate the moments $C_{p,q}(M)$ for $q = 2, 3, 4$, and $p = 0.5 - 2.0$, and $M = 1, 2, \dots, 40$, respectively. The linear fit is performed in a preferred region $M = 5 - 25$ and they estimate the values of μ_q for different values of q . They also compared the values of μ_q with that obtained from Monte Carlo - simulated values of a quark jet and a gluon jet separately at a fixed coupling constant $\alpha_s = 0.05$. It is found that the values of the entropy indexes are quite large and very close to the Monte Carlo simulated values of a quark jet at a fixed coupling constant $\alpha_s = 0.05$. However it is significantly greater than the simulated values of a gluon jet at the same coupling constant $\alpha_s = 0.05$. From the result one may assume that the original parton that initiates the parton shower in 400 GeV/c pp collision is a quark. They also calculated the entropy indexes for different multiplicity region. They found that with increasing average multiplicity the entropy indexes decrease. The experimental results agree with the theoretical predictions. But the experimental results are still significantly larger than the corresponding simulated values based on the assumption of gluon jets. Hence, the reaction may not be dominated by QCD parton showering.

Hasan et al. [91] have studied the fluctuations in the special pattern of the final states of Si-Ag/Br collisions at 14.6A GeV/c by measuring the entropy indexes, as compared to the values from generated uncorrelated events which are also higher in magnitude. Ahmad et al. [92] examined event-by-event fluctuations in factorial moments in terms of erraticity measures are by analysing the experimental data on 4.5A and 14.5A GeV/c ^{28}Si -emulsion interactions. The findings are compared with the predictions of Lund Monte Carlo model, FRITIOF [64]. Values of $C_{p,q}$ moments are calculated for $p = 0.5 - 2.0$, $q = 2, 3, 4$ and $M = 2^k$ where $k = 0, 1, 2, \dots$. The variation of $\ln C_{p,q}$ with $\ln M$ and dependence of Σ_q on $\ln M$ for the experimental data at the two incident energies are studied. It is seen that the

log-log plots of $C_{p,q}$ against M have similar shapes for two data sets under consideration. Trends of the variation of Σ_q with $\ln M$ are also found to be similar for the two data sets.

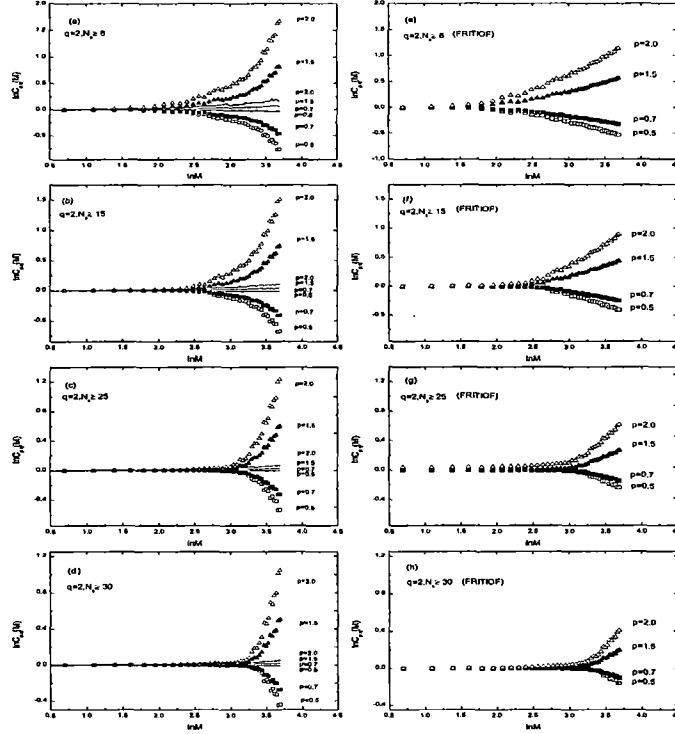


Figure 1.26: Results from erraticity analysis on shower track emission data from ^{28}Si -emulsion interaction at 14.6A GeV/c, along with corresponding FRITIOF prediction.

This, therefore, indicates that erraticity exists in all the cases but with different strength and is, therefore, characterized by different values of entropy index μ_q . As suggested in [89] the value of the entropy index μ_q is evaluated. For investigating the effect of multiplicity n_s on erraticity, $\ln C_{p,q}$ and μ_q are calculated by grouping the interactions on the basis of their n_s values. It is noted that μ_q decreases with increasing $\sqrt{n_s}$ irrespective of the beam energy. This is expected because the fluctuations in the event factorial moments would increase with decreasing particle multiplicity. Furthermore, all the analysis were compared with FRITIOF generated data and noticed that all behaviour are essentially similar. These results, therefore, suggest that the erraticity behaviour observed in Si-emulsion collisions at 4.5 A and 14.5 A GeV/c are in excellent agreement with the corresponding values predicted by the Lund FRITIOF model. A comparison of the results

of the present study with those reported by other workers [93] suggests that the erratic fluctuations observed are rather due to the statistical reasons and there is no unambiguous evidence for the occurrence of dynamical fluctuations. These negative findings provide a positive indication that this approach would be sensitive in extracting the dynamical fluctuations arising due to some new kind of physical phenomena expected in heavy-ion experiments at higher energies with events of higher multiplicities.

Recently the chaotic behaviour of the multiparticle production in high-energy AB collision has been investigated with the help of erraticity analysis using the data of $^{32}\text{S-Ag/Br}$ interaction at 200A GeV/c by Ghosh et al. [90]. They measured the entropy index μ_q in η space for experimental data as well as for randomly generated data in two different process - one from the $C_{p,q}$ moments, and another from the $\Sigma_q = \langle \phi_q(M) \ln \phi_q(M) \rangle$ moments. They also compared their results with the results obtained by Wang et al. [94] for pp collision at 400 GeV/c. Their values of entropy index from $C_{p,q}$ moments are greater for p-p collisions at 400 GeV/c than the $^{32}\text{S-Ag/Br}$ interaction at 200A GeV/c. The same trend is also followed by the entropy index obtained from Σ_q moments. They also reported that the entropy indexes are large signifying chaotic behaviour of the multipion production process in ultra relativistic nuclear interactions. The observed higher value of entropy index for experimental data compare to random data indicates true signals of chaos without any bias of statistical fluctuation. Moreover, it has been also observed that the VENUS [71] model is unable to reproduce such chaotic multiparticle production in $^{32}\text{S-Ag/Br}$ interactions at 200A GeV/c. They also studied the multiplicity dependence of the chaotic behaviour, and found that the chaoticity increased with increasing $\langle n_s \rangle$. They also performed a 2-d erraticity analysis, and found that μ_q in 2-d is almost double of the corresponding 1-d value. They concluded that the 1-d analysis underestimates the fluctuations of spatial patterns, implying the importance of higher dimensional analysis.

1.8 Models of AB interaction

To describe a high-energy heavy-ion interaction many physical mechanisms have to be taken into account. Due to the intrinsic complexities associated with the QCD, nonperturbative effects are to be treated through model calculations. Unfortunately, so far we

do not have any standardized method for the purpose, that describes all stages of space-time evolution process in an AB interaction. A broad classification of the models can however, be made in terms of the emphasis given to a particular stage of the evolution. The hadronic models based on simple superposition of elementary NN interactions, try to simulate the entire history of the space-time evolution. Any deviation from the prediction of a hadronic model should therefore, be interpreted as a collective effect. Models based on parton shower cascade and/or string fragmentation mechanism(s) put emphasis on the initial pre-equilibrium stage of the interaction, where no subsequent equilibration is assumed. Hydrodynamical and/or statistical models on the other hand, mainly describe the thermal/chemical equilibrium stage, a prerequisite for QGP formation. The calculations can however, be extended also to the final freeze out stage. In the following we have briefly reviewed some of the models used to simulate AB interactions at high-energy. As will be seen, the boundary between two different categories is not always very distinct, and often there are cross-overs into each other's domain.

1.8.1 LEXUS

The Linear Extrapolation of Ultrarelativistic Scattering or the LEXUS model [95] belongs to the first category of hadronic models. The extrapolation is based on Glauber's formulation [22], where an AB interaction is looked upon as a superposition of many independent NN interactions in free space. In addition LEXUS also considers that, a collision at an impact parameter b is a sum of independent collisions between rows of nucleons belonging to the colliding nuclei. Two rows collide when the transverse position of the projectile row *w.r.t* the projectile center of mass, and that of the target row *w.r.t* the target center of mass are separated by b . The average number of nucleons in a row at a transverse position \mathbf{s} is obtained from the NN cross section σ_{NN} as,

$$\nu_i = \sigma_{NN} \int dz \rho_i(\mathbf{s}, z) : \quad i = A, B$$

where z is the longitudinal coordinate, and ρ is the baryon density for which a Woods-Saxon type of distribution is used for heavy nuclei, whereas a three parameter Gaussian for light nuclei. Fluctuations in these numbers as well as fluctuations in the number of collisions suffered by any given nucleon in a row are taken into account. The probability

to have exactly m nucleons in a row is obtained by using a binomial distribution with a cut in the upper limit (~ 10 nucleons). Making use of a geometrical overlap function $f(\mathbf{b}) = \int \sigma_{NN}^{-1} d^2s_A \nu_A(\mathbf{s}_A) \nu_B(\mathbf{s}_B)$, the total AB cross section σ_{AB}^{tot} is computed as,

$$\sigma_{AB}^{tot} = \int d^2b \{1 - \exp[-f(\mathbf{b})]\}.$$

LEXUS could well describe global distributions like y and p_t of baryons and y , p_t and multiplicity of (-)ve hadrons at SPS energies. QGP probe like strange particle abundance is not reproduced so well by LEXUS. The treatment can be improved by taking into account the elastic and diffractive dissociation components of NN collision.

1.8.2 Lund Model - Fritiof

During the BNL-AGS and CERN-SPS era, the Lund Monte Carlo Model [96] has been one of the most popular models for AB collisions at high-energy. The computer code FRITIOF [64, 70] is the implementation of the Lund Model. Since the inception of its earliest version 1.6, the code has been modified a number of times, the latest being version 7.0. The model is an extension of the old multiperipheral model and it belongs to the category of string fragmentation, where an AB collision is considered as a superposition of many NN interactions. The model is meant for soft (low p_t) interactions, as bulk of the particles come out with small p_t values. It is assumed that the particle production via hadronic interaction is a two step process - (i) two interacting hadrons are first excited through soft gluon exchange, and (ii) constituents (valence quarks) of the excited hadrons exchange a string of quarks and anti-quarks, from which more hadrons are produced. A string is excited only between the constituents of the same hadron, and there is no net colour exchange between two interacting hadrons. The interacting hadrons (nucleons for AB collision) are assumed to be stretchable only in the longitudinal direction, and they are not excited transversely. The decay of the stretched hadrons may be analyzed in the same way as the fragmentation of a string stretched between a $q\bar{q}$ pair. Representing the energy-momentum of a hadron by its light-cone momenta it can be assumed that, collisions between the hadrons will lead to a flow of their light-cone momenta from one hadron to the other. After each collision a projectile hadron having forward light cone momentum b_+ will transfer an amount Q_+ to one target hadron, and in return the target hadron transfers an

amount Q_- of its backward light-cone momentum a_- to the projectile hadron. Following Feynman's wee parton spectrum the momentum transfer obeys a probability distribution,

$$d^2P \propto \frac{dQ_+}{(Q_+ + \frac{m_b^2}{b_+})} \frac{dQ_-}{(Q_- + \frac{m_a^2}{a_-})}$$

where the mass terms come from the lower limits of the momentum transfer.

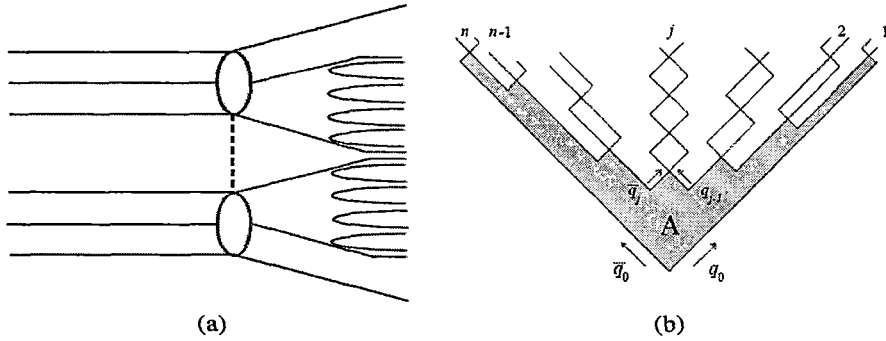


Figure 1.27: The LUND string formation and fragmentation scheme. In (a) note the string being excited between partons of the same hadron. In (b) the space-time trajectories of q and \bar{q} from a string fragmentation have been shown.

For AB collisions a generalization of the above idea is made. An AB interaction is considered as an incoherent combination of a set of many elementary collisions of nucleons of one nucleus with those belonging to the other. A straight line geometry is assumed between the projectile and target nuclei. An incident nucleon impinge upon target nucleons with randomly distributed impact parameter b , which is restricted by a nonzero minimum allowable value. For each NN interaction a Gaussian type of overlapping function $G(b)$ is used. Due to time dilation, fragmentation of an interacting nucleon into any intermediate state, and hence possibility of any intra nuclear cascade is ruled out. Thus a projectile nucleon interacting with ν nucleons inside a target nucleus, will form $\nu + 1$ excited strings. These strings undergo bremsstrahlung radiation, and subsequently fragment into hadrons. The nucleons inside a nucleus (for $A > 16$) follow a Wood-Saxon type of distribution,

$$\rho(\vec{r}) = \frac{\rho_0}{1 + \exp\left(\frac{r - r_0 A^{1/3}}{C_d}\right)}.$$

The radius parameter r_0 has a small A dependence, C_d is the diffuseness parameter, and ρ_0 is a normalization constant. The Lund model has been successful in describing

several global characteristics of multiparticle final states of AB collision at AGS and SPS energies. However, as we shall later see, it fails to account for the small scale structure of phase-space distribution of produced hadrons. On different occasions the prediction of FRITIOF has been compared to our experimental results on ^{32}S induced interactions at 200A GeV/c.

1.8.3 Dual Parton Model

Like the Lund Model (FRITIOF), the Dual Parton Model (DPM) [97] is basically another string fragmentation model. The mechanism of particle production once again is based on the excitation of strings, and their subsequent fragmentation into final state hadrons. In DPM concepts like the Reggeon and the Pomeron are used. The main contribution to hadron production comes from two string events, and in principle multistrings are also feasible. Whereas, in the Lund Model only one string is formed. Moreover, in DPM a string is excited only between the constituents of two different (colliding) hadrons, and therefore, a colour exchange takes place. In this model, a nucleon is considered as composed of a quark and a diquark system. Except that the diquark cannot be annihilated by a quark, the former behaves like an antiquark ! The momentum fraction x_q of a valence quark in a nucleon follows a Field Feynman type of distribution [98],

$$\rho(x_q) \propto x_q^{-1/2} (1 - x_q)^{1.5},$$

whereas that ($x_{qq} = 1 - x_q$) of the diquark system follows,

$$\rho(x_{qq}) \propto (1 - x_{qq})^{-1/2} x_{qq}^{1.5}.$$

An AB collision can be decomposed into a Glauber type of many incoherent NN interactions [22]. A pair of chains (like strings in Lund model) are formed when a valence quark of the incident nucleon interacts with the diquark of the target nucleon, and vice versa. In a second collision the projectile diquark form a chain with the valence quark of the second nucleon, and another chain is formed between one projectile sea quark and the diquark of second target nucleon. Thus the projectile nucleon undergoes n Pomeron exchange in collision with n target nucleons. Each chain gives rise to an independent production of particle. The computer code VENUS [71] based on DPM includes the additional prob-

ability of finding out an antiquark, and its contribution to Pomeron exchange. VENUS made use of deep inelastic experimental data for the momentum distribution of partons.

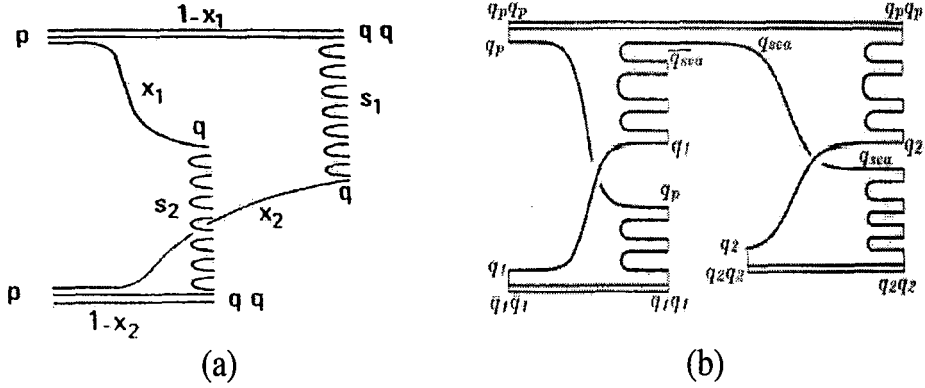


Figure 1.28: String fragmentation in DPM - (a) string formed between a valence quark of the incident nucleon and a diquark of the target nucleon; (b) projectile diquark forms a chain with a sea quark of 2nd target nucleon.

1.8.4 HIJING

The Heavy-Ion Jet Interaction Generator (HIJING) is another Monte Carlo event generator developed for pp, pA, and AB collisions [99]. Salient features of the model can be described in the following manner. HIJING treats an AB collision as a superposition of many binary NN collisions. The impact parameter of each NN interaction is determined by the transverse position of each nucleon generated by the Woods-Saxon density distribution. Diffuse nuclear geometry is used to calculate the impact parameter dependence of the number of inelastic processes. In this scheme multiple soft beam jets are modeled by diquark-quark string excitation and fragmentation along the lines of Lund FRITIOF and DPM. In the HIJING model a diquark is treated as a single entity, and this leads to an average rapidity shift of about one unit in the net baryon distribution. In addition, HIJING also incorporates perturbative QCD adopted in the PYTHIA model of hh interactions [100], and is therefore, capable of describing both soft and hard ($p_t > 2 \text{ GeV}/c$) components of particle production. Hence unlike the Lund model and DPM, HIJING works at the RHIC energy and is expected to work also at the LHC energy. Nuclear

effects like jet quenching and parton shadowing have also been incorporated into this model. A QGP probe like the jet quenching is included to study the dependence of moderate and high p_t observables on an assumed energy loss dE/dx of partons traversing the produced dense matter. Mini jets from produced partons are quenched by losing energy to the wounded nucleons close to their straight line trajectories. An impact parameter dependent parton structure function is introduced to study the sensitivity of observables to nuclear shadowing, especially of the gluon structure functions. To generate the initial phase-space distribution for the parton cascade, the formation time for each parton is determined according to a Lorentzian distribution with a half width $t_f = E/m_t^2$, where E and m_t are the parton energy and transverse mass, respectively. Positions of formed partons are calculated from those of their parent nucleons using straight line trajectories. During the time of formation, partons are considered to be part of the coherent cloud of parent nucleons, and they thus do not suffer rescattering. Once the partons stop interacting, after an additional proper time of about 1.2 fm, they are converted into hadrons according to the HIJING fragmentation scheme.

1.8.5 UrQMD

High-energy nuclear collisions are also investigated in the Ultrarelativistic - Quantum - Molecular - Dynamics (UrQMD) approach [101]. Basically the UrQMD model is a convolution of two different schemes. On one hand, it is a microscopic transport theory of covariant propagation of all hadrons along their classical trajectories, combined with stochastic binary scattering, resonance decay and colour string formation. For this purpose a relativistic Boltzmann equation has to be solved for hadrons in the final stage of the collision. On the other, the model also considers a hydrodynamical evolution of all stages of interaction, formation of a QGP like state, and for that to happen a local thermodynamical equilibrium at the partonic level has to be assumed. The basic input to hadronic transport models is that, a hh interaction would occur if $b < \sqrt{\sigma_{tot}/\pi}$, where total cross-section σ_{tot} depends on isospin of interacting hadrons, their flavour and *cms* energy. Partial cross-sections are also used to compute the relative weights of different channels. The Fermi gas model is utilized to describe the projectile and target nuclei, the initial momentum of each nucleon being randomly distributed between 0 and the

local Thomas-Fermi momentum. Each nucleon is described by a Gaussian shaped density distribution, and the wave function for the nucleus is taken as a product of single nucleon Gaussian functions. In configuration space the centroids of Gaussian are randomly distributed within a sphere, and finite widths of the Gaussian result in a diffused surface region. At low and intermediate energies ($\sqrt{s} < 5$ GeV) the phenomenology of hadronic interactions is described in terms of interactions between known hadrons and their resonances. At higher energies, $\sqrt{s} > 5$ GeV, the excitation of colour strings and their subsequent fragmentation into hadrons dominates the multiple production of particles in the UrQMD model. For AB collisions the soft binary and ternary interactions between nucleons are described by a non-relativistic density-dependent Skyrme potential. In addition, Yukawa, Coulomb and Pauli (optional) potentials are implemented in the model. The potentials allow to calculate the equation of state of the interacting many body system, as long as it is dominated by nucleons. Note that these potential interactions are only used in the model for baryons/nucleons with relative momenta Δp of less than 2 GeV/c. The model should allow for subsequent rescatterings. The collision term in the UrQMD model includes more than fifty baryon species and five meson nonets (45 mesons). This framework allows to bridge with one concise model the entire available range of energies from the Bevalac energy region ($\sqrt{s_{NN}} \sim$ a few GeV) to the RHIC energy ($\sqrt{s_{NN}} = 200$ GeV).

Bibliography

- [1] A comprehensive review of the AGS, SPS era experiments, and an excellent textbook on the subject has been written by C. Y. Wong, *Introduction to high-energy heavy-ion collisions* (World Scientific, Singapore, 1994).
- [2] *Quark matter formation and heavy-ion collisions, Proceedings of Bielefeld Workshop*, ed. M. Jacob and H. Satz (World Scientific, Singapore 1982).
- [3] W. Busza and A. Goldhaber, *Phys. Lett. B* **139**, 235 (1984).
- [4] G. D. Westfall *et al.*, *Phys. Rev. Lett.* **37**, 1202 (1976).
- [5] T. D. Lee, *Rev. Mod. Phys.* **47**, 267 (1975).
- [6] E. Shuryak, *Phys. Rep.* **61**, 71 (1979).
- [7] G. Bertsch and J. Cugnon, *Phys. Rev. C* **24**, 2514 (1981).
- [8] Many aspects of QGP and a review of SPS and RHIC experiments can be found in K. Yagi, T. Hatsuda and Y. Make, *Quark-Gluon Plasma* (Cambridge University Press, New York, 2005).
- [9] A. Chodos, R. L. Jaffe, K. Johnson, C. B. Thorn and V. F. Weisskopf, *Phys. Rev. D* **9**, 3471 (1974)
L. Willets, *Bag Model of Nucleus* (World Scientific, Singapore, 1989).
- [10] Several basic features of high-energy interaction have been lucidly explained by R. A. Salmeron, *Quark-Gluon Plasma*, ed. B. Sinha, S. Paul. and S. Raha (Springer-Verlag, Berlin, 1990).

- [11] I. Otterlund, *Central Heavy-ion Interaction at 15 and 200 GeV - A Comparison: Cosmic and Subatomic Physics Report, LUIP 9012, Invited talk at the International High-density Nuclear Matter* (1990).
- [12] B. Andersson *et al.*, *Phys. Scr.* **34**, 451 (1986).
- [13] Y. Nambu, *Phys. Rev. Lett.* **4**, 380 (1960)
Y. Nambu and G. Jona-Lasinio, *Phys. Rev.* **122**, 345 (1961).
- [14] R. Anishetty, P. Koehler and L. McLerran *Phys. Rev. D* **22**, 2793 (1980).
- [15] G. Baym and S. A. Chin, *Phys. Lett. B* **62**, 241 (1976)
H. Satz, *Ann. Rev. Nucl. Part. Sci.* **35**, 245 (1985)
H. Satz *et al.*, *Z. Phys. C* **38**, 1 (1988).
- [16] S. Z. Belenski and L. D. Landau, *Ups. Fiz. Nauk.* **56**, 309 (1955); *Nuov. Cim. Suppl. II* **3**, 15 (1956).
- [17] J. D. Bjorken, *Phys. Rev. D* **27**, 140 (1983).
- [18] Review of experiments in AGS and SPS era on high-energy heavy-ion collisions can be found in, I. Otterlund, *Ultrarelativistic Nucleus-Nucleus Collisions*, Lectures given at 3rd Hellenic School on Elementary Particle Physics, (Corfu, Greece, 1989).
Physics and Astrophysics of Quark-Gluon Plasma, ed. B. Sinha, D. K. Srivastava and Y. P. Vijoyi, (Narosa, New Delhi, 1998).
- [19] P. V. Ruuskanen, *Nucl. Phys. A* **522**, 255c (1991); *Nucl. Phys. A* **544**, 169c (1992).
- [20] K. Kajantie, J. Kapusta, L. McLerran and A. Mekjian, *Phys. Rev. D* **34**, 2746 (1986).
- [21] S. D. Drell and T. M. Yan, *Phys. Rev. Lett.* **25**, 316 (1970).
- [22] R. J. Galuber, *Lectures on Theoretical Physics*, vol.I, (Interscience, New York, 1959).
- [23] CERES/NA45 Collaboration, G. Agakichiev *et al.*, *Phys. Rev. Lett.* **75**, 1272 (1995);
Nucl. Phys. A **610**, 317c (1996); *Phys. Lett B* **422**, 405 (1998)
B. Lenkeit *et al.*, *Nucl. Phys. A* **661**, 23c (1999).
- [24] NA38 Collaboration, M. C. Abreu *et al.*, *Nucl. Phys. A* **566**, 77c (1994).

- [25] NA50 Collaboration, M. C. Abreu *et al.*, *Nucl. Phys. A* **610**, 404c (1996); *Phys. Lett B* **450**, 456 (1999); *Phys. Lett B* **477**, 28 (2000).
- [26] E. V. Shuryak, *Sov. J. Nucl. Phys.* **28**, 408 (1978)
R. C. Hwa and K. Kajantie, *Phys. Rev. D* **32**, 1109 (1985)
S. Raha and B. Sinha, *Phys. Rev. Lett.* **58**, 101 (1987)
J. Kapusta, P. Lichard and D. Siebert, *Phys. Rev. D* **44**, 2744 (1991)
J. Alam, D. K. Srivastava, B. Sinha and D. N. Basu, *Phys. Rev. D* **48**, 1117 (1993).
- [27] J. Kapusta, P. Lichard and D. Siebert, *Nucl. Phys. A* **544**, 485c (1992).
- [28] HELIOS/NA34 Collaboration, T. Akesson *et al.*, *Z. Phys. C* **46**, 369 (1990).
- [29] WA80 Collaboration, R. Albrecht *et al.*, *Z. Phys. C* **51**, 1 (1991); *Phys. Rev. C* **44**, 2736 (1991); *Nucl. Phys. A* **566**, 61c (1994); *Phys. Rev. Lett.* **76**, 3506 (1996).
- [30] WA98 Collaboration, M. M. Aggarwal *et al.*, *Phys. Rev. Lett.* **83**, 926 (1999); *Phys. Rev. Lett.* **85**, 3595 (2000).
- [31] PHENIX Collaboration, S. S. Adler *et al.*, *Phys. Rev. Lett.* **94**, 232301 (2005).
- [32] T. Matsui and H. Satz, *Phys. Lett. B* **178**, 416 (1986)
T. Matsui, *Z. Phys. C* **38**, 245 (1988).
- [33] NA38 Collaboration, C. Baglin *et al.*, *Phys. Lett. B* **255**, 459 (1991); *Phys. Lett. B* **345**, 617 (1995).
NA51 Collaboration, A. Baldit *et al.*, *Phys. Lett. B* **332**, 244 (1994).
- [34] NA38 Collaboration, C. Baglin *et al.*, *Phys. Lett. B* **262**, 362 (1991).
- [35] G. Goldhaber, S. Goldhaber, W. Lee and A. Pais *Phys. Rev.* **120**, 300 (1960).
- [36] R. Hanbury-Brown and R. Q. Twiss, *Phil. Mag.* **45**, 663 (1954); *Nature* **178**, 1046 (1956).
- [37] G. Cocconi, *Phys. Lett. B* **49**, 459 (1974).

- [38] NA35 Collaboration, A. Bamberger *et al.*, *Phys. Lett. B* **203**, 320 (1988); *Nucl. Phys. A* **498**, 133c (1989).
 WA80 Collaboration T. Peitzmann *et al.*, *Nucl. Phys. A* **498**, 397c (1989).
- [39] NA35 Collaboration, T. Alber *et al.*, *Nucl. Phys. A* **590**, 453c (1995).
 NA49 Collaboration, H. Appelshauser *et al.*, *Eur. Phys. J. C* **2**, 661 (1998).
- [40] STAR Collaboration, C. Adler *et al.*, *Phys. Rev. Lett.* **87**, 082301, (2001).
 STAR Collaboration, J. Adams *et al.*, *Phys. Rev. Lett.* **93**, 012301, (2004).
 PHENIX Collaboration, S. S. Adler *et al.*, *Phys. Rev. Lett.* **93**, 152302, (2004).
- [41] J. Rafelski and B. Muller, *Phys. Rev. Lett.* **48**, 1066 (1982)
 P. Koch, B. Muller and J. Rafelski, J. Rafelski, *Phys. Rep.* **142**, 167 (1986); *Phys. Rep.* **88**, 331 (1988); *Nucl. Phys. A* **544**, 279c(1992).
- [42] E802 Collaboration, T. Abbott *et al.*, *Phys. Rev. Lett.* **64**, 847 (1990)
 L. Ahle *et al.*, *Phys. Rev. C* **60**, 044904 (1999).
- [43] E868 Collaboration, T. Armstrong *et al.*, *Phys. Rev. C* **59**, 2699 (1999).
 E878 Collaboration, M. Bennett *et al.*, *Phys. Rev. C* **56**, 1521 (1997).
- [44] E917 Collaboration, B. B. Back *et al.*, *Phys. Rev. Lett.* **87**, 242301 (2001).
- [45] WA97/NA57 Collaboration, F. Antinori *et al.*, *J. Phys. G* **28**, 1607 (2002).
- [46] STAR Collaboration, C. Adler *et al.*, *Phys. Rev. Lett.* **89**, 092301 (2002).
- [47] A. M. Poskanzer and S. A. Voloshin, *Phys. Rev. C* **58**, 1671 (1998); *Phys. Lett. B* **474**, 27 (2000).
- [48] STAR Collaboration, J. Adams *et al.*, *Phys. Rev. Lett.* **92**, 052302 (2004).
- [49] PHENIX Collaboration, S. S. Adler *et al.*, *Phys. Rev. Lett.* **91**, 182301, (2003).
- [50] NA49 Collaboration, A. M. Poskanzer *et al.*, *Nucl. Phys. A* **661**, 341c (1999).
- [51] CERES Collaboration, J. Milosevic *et al.*, *J. Phys. G* **32**, S97 (2006).
- [52] S. Jeon and V. Koch, *Phys. Rev. Lett.* **85**, 2076, (2000).

- [53] STAR Collaboration, G. D. Westfall *et al.*, *J. Phys. G* **30**, S1389 (2004).
 STAR Collaboration, J. Adams *et al.*, *Phys. Rev. C* **68**, 044905 (2003).
- [54] PHENIX Collaboration, K. Adcox *et al.*, *Phys. Rev. Lett* **89**, 082301 (2002).
- [55] JACEE Collaboration, T. H. Burnett *et al.*, *Phys. Rev. Lett.* **50**, 2062 (1983).
- [56] A. Bialas and R. Peschanski, *Nucl. Phys. B* **273**, 703 (1986); *Nucl. Phys. B* **308**, 857 (1988).
- [57] T. Ludlam and R. Slansky, *Phys. Rev. D* **8**, 1408 (1973).
- [58] NA22 Collaboration, M. Adamus *et al.*, *Phys. Lett. B* **185**, 200 (1987).
- [59] UA5 Collaboration, G. J. Alner *et al.*, *Phys. Rep.* **154**, 247 (1987).
- [60] An excellent review on dynamical fluctuation and scaling laws can be found in E. A. De Wolf, I. M. Dremin and W. Kittel, *Phys. Rep.* **270**, 1 (1996)
 W. Kittel and E. A. De Wolf, *Soft Multihadron Dynamics* (World Scientific, Singapore, 2005).
- [61] KLM Collaboration, R. Holynski *et al.*, *Phys. Rev. Lett.* **62**, 733 (1989); *Phys. Rev. C* **40**, R2449 (1989).
- [62] EMU01 Collaboration, M. I. Adamovich *et al.*, *Phys. Rev. Lett.* **65**, 412 (1990).
- [63] EMU01 Collaboration, M. I. Adamovich *et al.*, *Nucl. Phys. B* **388**, 3 (1992).
- [64] B Nilsson-Almqvist and E. Stenlund, *Comp. Phys. Comm.* **43**, 387 (1987).
- [65] D. Seibert, *Phys. Rev. D* **41**, 3381 (1990).
- [66] WA80 Collaboration, R. Albrecht *et al.*, *Phys. Lett. B* **221**, 427 (1989)
 C. R. Young *et al.*, *Nucl. Phys. A* **498**, 53c (1989).
- [67] E. K. Sarkisyan and G. G. Taran, *Phys. Lett. B* **279**, 177 (1992)
 E. K. Sarkisyan, L. K. Gelovani, G. L. Gogiberidze and G. G. Taran, *Phys. Lett. B* **347**, 439 (1995).
- [68] A. M. Tawfik, *J. Phys. G* **27**, 2283 (2001).

- [69] A. M. Tawfik and G. Ganssauge, arXiv:hep-ph/0012008 v1 (2000).
- [70] H. Pi, *Comp. Phys. Comm.* **71**, 173 (1992)
B. Andersson, G. Gustafson and H. Pi, *Z. Phys. C* **57**, 485 (1993).
- [71] K. Werner, *Phys. Rev. D* **39**, 780 (1989); *Phys. Rep.* **232**, 87 (1993).
- [72] H. Sorge, *Phys. Rev. C* **52**, 3291 (1995).
- [73] W. Ochs *Phys. Lett. B* **247**, 101(1990); *Z. Phys. C* **50**, 339 (1991).
- [74] EMU01 Collaboration, M. I. Adamovich *et al.*, *Z. Phys C* **76**, 659 (1997).
- [75] M. M. Haq, S. Islam and R. Hasan, *J. Phys. G* **30**, 1959 (2004).
- [76] S. Islam and R. Hassan, *J. Phys. G* **34**, 779 (2007).
- [77] R. Peschanski and J. Seixas Report No. CERN.TH 5903/90 unpublished (1990).
- [78] D. Ghosh *et al.*, *Phys. Rev. C* **52**, 2092 (1995).
- [79] R. C. Hwa, *Phys. Rev. D* **41**, 1456 (1990).
- [80] W. Florkowski and R. C. Hwa, *Phys. Rev. D* **43**, 1548 (1991)
C. B. Chiu and R. C. Hwa, *Phys. Rev. D* **43**, 100 (1991).
- [81] P. L. Jain, G. Singh and A. Mukhopadhyay, *Phys. Rev. C* **46**, 721 (1992).
- [82] EMU01 Collaboration, M. I. Adamovich *et al.*, *Europhys. Lett.* **5**, 571 (1998).
- [83] E. K. Sarkisyan, L. K. Gelovani, G. G. Taran and G. I. Sakharov *Phys. Lett. B* **318**, 568 (1993).
- [84] S. Ahmad and M. A. Ahmad, *J. Phys. G* **32**, 1279 (2006).
- [85] F. Takagi, *Phys. Rev. Lett.* **72**, 32 (1994).
- [86] A. Bershadskii, *Phys. Rev. C* **59**, 364 (1999).
- [87] D. Ghosh *et al.*, *Z. Phys. C* **73**, 269 (1997); *Nuov. Cim. A* **110**, 1289 (1997); *Europhys. Lett.* **41**, 371 (1998).

- [88] Z. Cao and R. C. Hwa, *Phys. Rev. Lett.* **75**, 1268 (1995); *Phys. Rev. D* **53**, 6608 (1996); *Phys. Rev. E* **56**, 326 (1997).
- [89] W. Shaoshun and W. Zhaomin, *Phys. Rev. D* **57**, 3036 (1998).
- [90] D. Ghosh, A. Deb, M. Mondal and J. Ghosh, *Phys. Lett. B* **540**, 52 (2002).
- [91] R. Hassan *et al*, *J. Phys. G* **28**, 2939 (2002).
- [92] S. Ahmad *et al*, *J. Phys. G* **30**, 1145 (2004).
- [93] J. Fu *et al*, *Phys. Lett. B* **472**, 161 (2000)
 F. Liu *et al*, *Phys. Lett. B* **516**, 293 (2001)
 Z. Yi-Fei *et al*, *Chin. Phys. Lett.* **18**, 1179 (2001).
- [94] S. Wang *et al*, *Phys. Lett. B* **458**, 505 (1999).
- [95] S. Jeon and J. Kapusta, *Phys. Rev. C* **56**, 468 (1997).
- [96] B. Andersson, G. Gustafson and B Nilsson-Almqvist, *Nucl. Phys. B* **281**, 289 (1987).
- [97] A. Capella, U. Sukhatame, C-I. Tan and J. Tran Thanh Van, *Phys. Lett. B* **81**, 68 (1979)
 A. Capella, U. Sukhatame and J. Tran Thanh Van, *Z. Phys. C* **3**, 329 (1980)
 A. Capella and J. Tran Thanh Van, *Z. Phys. C* **10**, 249 (1981).
- [98] R. D. Field and R. P. Feynman, *Phys. Rev. D* **15**, 2590 (1977);
Nucl. Phys. B **136**, 1 (1978).
- [99] X. N. Wang and M. Gyulassy, *Phys. Rev. D* **50**, 3501 (1991).
- [100] T. Sjostrand, *Comp. Phys. Comm.* **82**, 74 (1993).
- [101] S. A. Bass, A. Dumitru, M. Bleicher, L. Bravina, E. Zabrodin, E. Stoecker and W. Greiner, *Phys. Rev. C* **60**, 021902 (1999)
 S. A. Bass *et al*, *Prog. Part. Nucl. Phys.* **41**, 225 (1998).

Chapter 2

The Emulsion Technique and Data Characteristics

In this chapter, the experimental aspects of the present investigation have been outlined. Salient features of the nuclear emulsion technique have been described in general terms. The optical microscopy, that is so intimately associated with the data acquisition process, has also been briefly discussed. The limitations of this age old technique, as well as its advantages in the perspective of the methods of data analysis adopted subsequently, have been critically scrutinized. A data sample of ^{32}S -Ag/Br interactions at an incident momentum of 200A GeV/c, has been analyzed in the present investigation. Some of the general characteristics of this data sample, that are pertinent to our methods of analysis, have been incorporated for better understanding the issues discussed in subsequent chapters. A data sample generated by the Lund Monte Carlo Code FRITIOF has been used for comparison with the experiment. Gross features of the generated data sample have also been included.

2.1 Nuclear Emulsion Technique

The first use of photographic emulsion to record charged particle tracks was made in 1911, when alpha particles were found to affect silver bromide grains along their paths in such a way as to be later developed to metallic silver [1]. However, it was only around the 1940s that the nuclear emulsion technique matured as an effective and successful tool for research in cosmic ray, nuclear and particle physics. This became possible due to the efforts of firms like the Ilford Ltd. (London), the Kodak Ltd. (New York), and to a great extent due to the contribution of the emulsion research group in the University of Bristol (UK). The usefulness of this technique can be understood from its rich history of being a key detector in discovering several new particles like the charged π -mesons, the charged K -mesons, the Σ^+ and the $\bar{\Lambda}$ baryons etc. In spite of a stiff competition offered by its more prestigious and much costlier large electronic counterparts, even in the recent past the emulsion experiments have contributed significantly in studying different phenomena in high-energy hA and AB interactions. Besides its use in high-energy research, emulsions are currently also being used in medical, biological and geophysical research, in metallurgy and in studying chemically active surfaces. Throughout the world there are several firms and/or institutes who manufacture nuclear research emulsions e.g, the Ilford Ltd. (London), the Eastman Kodak Company (Rochester), the NIKFI Institute (Moscow), the Fuji Films Ltd. (Tokyo) etc. The Ilford G5 type of nuclear emulsion has been used in the present investigation. In the following discussion therefore, if otherwise not mentioned, we shall refer to emulsion characteristics and parameters pertaining only to this particular type. Excellent reviews and texts [2–4] are available on the details of nuclear emulsion technique. However, in the following sections we have tried to summarize its essential features.

2.1.1 Nuclear Emulsion

Any photographic emulsion is basically a dispersion of silver halide crystals within a gelatin matrix. Nuclear emulsions used for recording charged particle tracks consist of silver halide micro-crystals embedded into about equal parts in volume, a matrix material comprising mainly of gelatin and water with a small amount of glycerol and a few other substances. Silver halide, usually in the form of silver bromide crystals, also contains a

small amount of iodine in the crystal lattice. Ionizing (electrically charged) particles, while passing through such emulsions leave behind them silver halide crystals so altered, that upon proper chemical treatment, they appear as a trail of black colloidal grains of metallic silver along the trajectories of the particles. However, compared to the general purpose photographic emulsions the nuclear emulsions have several distinguishing features. In nuclear emulsion plates the photosensitive silver halide material (mostly AgBr) has three to four times more concentration than that in the conventional photographic plates. The nuclear emulsion plates are also made much thicker - a few hundreds to several hundreds of microns as compared to only several microns in case of ordinary photographic plates. The AgBr grains in nuclear emulsion are well separated and are much smaller in size (less than a micron in diameter). Whereas in ordinary photographic plates, the grains are interlocked and the grain diameter can be as large as several microns. Though the silver halide crystals in nuclear emulsion are very uniform in size, it is observed that in any particular sample the grains are actually distributed about a mean value with a small but certain variance in diameter. For Ilford G.5 emulsion the mean grain diameter is $\approx 0.3\mu\text{m}$. However, the mean crystal grain diameters are usually different for different types of emulsions. It is observed that the contrast of nuclear emulsion may be improved if the grains are uniform in size, whereas, the sensitivity goes up with increasing grain size. In nuclear emulsion there are very few crystals that can be developed without exposure to a charged particle.

As mentioned above, thickness of emulsion pellicles (films without any glass plate backing) ranges from $\sim 10^2\mu\text{m}$ to a few millimeters, whereas the length (breadth) usually is a few to several inches. In the present investigation the dimensions of Ilford G5 emulsion pellicles were $18 \times 7.5 \times 0.06 \text{ cm}^3$. The pellicles are mounted on 1.3 mm thick glass plates and their extremely sensitive top surfaces are coated to avoid abrasion marks to be formed. Gelatin is a hygroscopic material and emulsion plates can absorb water from atmosphere. Their volume change with relative humidity shows a hysteresis effect. At around 58% of relative humidity, the volume per unit mass of emulsion during the absorption is found to be equal to that during the desorption process. As far as the composition of emulsion is concerned, it is therefore necessary to refer to the relative humidity value. Each gram of Ilford nuclear emulsion contains 0.83 gm of silver halide and 0.162 gm of gelatine at

58% relative humidity; corresponding volume ratio is about 45 : 55. The percentage of moisture contents by weight in Ilford nuclear emulsions at 20°C at various relative humidities are given below [2] in Table 2.1.

Table 2.1. Moisture content of Ilford emulsion at different relative humidities

Relative humidity	0	30	50	60	70	85
Moisture content	1.41	2.06	2.65	2.95	3.7	5.17

The accepted value of the density of silver halide crystal is ≈ 6.473 gm/cc. The density of supplied emulsion is 1.29 gm/cc at 58% relative humidity, which after drying may rise to 3.83 gm/cc in equilibrium with air at 20°C at 58% relative humidity. In Table 2.2 the chemical composition of Ilford G5 type of emulsion is given [4].

Table 2.2 Composition of standard emulsion

Element	Atomic No. (Z)	Atomic weight (A)	Concentration at 58% R.H.	No. of atoms per cc $\times 10^{20}$	Moles per cc $\times 10^{-3}$
Ag	47	107.88	1.817	101.01	16.764
Br	35	79.916	1.338	100.41	16.673
I	53	129.93	0.012	0.565	0.094
C	6	12.0	0.277	138.30	22.698
N	7	14.008	0.0534	31.68	5.147
S	16	32.06	0.249	1.353	0.216
H	1	1.008	0.074	321.56	53.571
O	8	16.0	0.007	94.97	16.050

The total number of atoms available in emulsion per cc is 7.898×10^{22} , whereas, the total number of electrons available is 1.0446×10^{24} per cc. Taking the nuclear radius parameter $r_0 = 1.2$ fm, the geometrical mean free path of all elements in nuclear emulsion will come out to be ≈ 37 cm. However, as we shall see later this geometrical mean free path is quite different from the interaction mean free path.

2.1.2 Latent Image Formation

The mechanism of developable (usually called 'latent') image formation in nuclear emulsion is essentially the same as that in the ordinary light sensitive photographic plates. But there is a significant difference between the two. In the former case this takes place through ionization of atoms present in the emulsion by electrostatic interaction with the passing charged particles. Whereas, in the latter case this occurs due to emission of photoelectrons by the incident light. The first comprehensive theory of the photolytic process underlying the latent image formation was provided by Gurney and Mott [5]. According to their principle both ionic and electronic conduction contribute during the process of latent image formation. They proposed that, as the incident particle passes through emulsion, photons are absorbed in the silver halide and some electrons are raised to the conduction band. These electrons are allowed to migrate freely until they encounter local minima of potential energy (called sensitivity specks), where they can be trapped. Such local minima are provided by colloidal silver and/or silver sulphide usually located on the crystal surface. The sensitivity specks are now negatively charged and are capable to attract interstitial silver ions (Ag^+) present within the crystal as Frenkel defects, which are free to move through the crystal lattice. The Ag^+ ions are neutralized by capturing the extra electrons and silver specks of sufficiently large size can grow as a stable development (latent image) center. At least three silver atoms adsorbed at the AgBr crystal surface are required to achieve stability. Latent image formation in nuclear emulsion is an inefficient process, particularly for fast moving charged particles. The migration of silver ions through the crystal is considerably slower than that of the electrons. Thus the sensitivity specks acquire negative charges more rapidly than their rate of getting neutralized by Ag^+ ions. Further electron conduction to a particular sensitivity speck is therefore, slowed down. The electrons being raised to conduction band by the moving particle would try to find other points in the crystal, thereby prohibiting any particular speck to grow sufficiently in size as a latent image. The Gurney-Mott theory was later modified by Mitchell and collaborators [6], where conduction of positive holes as well as recombination of holes and electrons were taken into account. However, the details of the theory of latent image formation is not one of the major objectives of the present discussion, and we have preferred to concentrate more on other aspects of the technique.

2.1.3 Emulsion Processing

Once the emulsion pellicles are irradiated by ionizing charged particles, they should be so processed as to be made suitable for scanning and measurement under optical microscopes. This requires the pellicles to undergo through several subprocesses like presoaking, development, stopping, fixing, washing, mounting on glass plates and drying. However, processing emulsion pellicles that are already mounted on glass plates is also very common. Through photographic development the latent images contained in an emulsion are made visible by reduction of silver ions in the silver halide crystals to metallic silver. A developer is usually chosen that reduces the crystals containing a latent image center completely and leaves those not containing a center unchanged. Before development the pellicles are often presoaked in distilled water to facilitate the developer to rapidly diffuse into the emulsion without affecting the actual development. The development time should be sufficient for the crystals with a latent image center to be reduced completely, but not so long that the unexposed crystals are developed. In practice, a certain number of crystals will be developed even though they do not contain a latent image center. These grains, when developed, constitute what is known as fog or background. While developing thick emulsion layers (\sim several hundred microns), care should be taken regarding uniform development with minimum distortion. Techniques like 'temperature development' [7] and 'two bath development' [8] are found useful for uniform development. In the first technique the pellicles may be vertically immersed into the developer at sufficiently low temperature to inhibit its action, and to allow the developer to permeate into the entire bulk of each pellicle from both of its flat (length-breadth) sides. The developer is then slowly warmed and its action starts. In the second technique two developer solutions are employed in two different baths. The first one contains developing agents without any alkali, and the second one containing the same with excess alkali with a high pH environment. Immersing into the first bath will only permit the developing agents to diffuse into the emulsion layers, while in the second bath the actual development takes place. Developer formulations of two reagents from the Ilford Ltd. meant for Ilford G5 emulsions are given in Table 2.3 [9].

After completion of the development stage the developer action should be arrested immediately. For thick emulsions this is done by putting the pellicles into a stop bath that can

reduce their pH value, in conjunction with rapid cooling. An environment of dilute acetic acid ($\sim 1\%$) and a temperature $\sim 5^{\circ}\text{C}$ is suitable for the purpose. Like development, stop bath time also varies with the thickness. Because of high concentration of AgBr in emulsions, and its partial solubility in the developer, a thin film of silver is formed on the surface of the pellicles during development. This surface deposit should be completely removed. This may be done in the stop bath itself with the help of a chamois leather or by finger tips. As the emulsion is in wet condition extreme care should be taken to prevent distortion.

Table 2.3 Developer Formulation

Developer type	Chemical component	Amount
ID-19	Metol	2.2 gm
	Anhydrous Sodium Sulphite	72 gm
	Hydroquinone	8.8 gm
	Anhydrous Sodium Carbonate	48 gm
	Potassium Bromide	4 gm
	Water to make	1 liter
Brussels Amidol	Anhydrous Sodium Sulphite	18 gm
	Potassium Bromide	0.8 gm
	Amidol	4.5 gm
	Boric Acid	35 gm
	Water to make	1 liter

The emulsion should then be fixed. The purpose of fixation is to remove all the residual silver halide, leaving the metallic silver to form the image. If any amount of silver halide is left in the emulsion, it would slowly break into ions and the plate will go brown degrading the quality of the image. The fixing agents most widely used are sodium or ammonium thiosulphate, which form thiosulphate complexes with the silver halide. Silver thiosulphate is soluble in water and so may be removed from the emulsion by washing. It is important to use a fixer that has not been exhausted while processing nuclear emulsions; otherwise some silver halide will remain in the emulsion. To ensure that the entire

silver halide is removed, a fixing time which is twice the time it takes for the emulsion to clear should be allowed. After fixation, the emulsion must be washed very thoroughly in tap water with a final rinse in distilled water to remove all the silver thiosulphate complexes in the emulsion. After washing is completed, the pellicles are mounted on glass plates slightly larger than the size of the pellicles and kept inside a refrigerator until they are set. The glass plates should have grid lines and grid numbers printed on them, so that an event once found out, can easily be relocated later. The glass plates should also have a gelatin coating on them. Drying of emulsion plates is then conducted at around 20°C. A summary of the entire processing procedure for typical 600 μ m thick emulsion is summarized in the following Table [2].

Table 2.4 Processing of 600 μ m thick emulsion

Procedure	Temperature	Time
Presoaking in distilled water	ambient \rightarrow 5°C	100 min
Developer penetration (Brussels Amidol)	5°C	100 min
Dry development	23°C	20 min
Dry cooling	23°C \rightarrow 8°C	5 min
Acid stop bath (1% acetic acid)	5°C	100 min
Removal of surface deposit		
Fixation		
Clearing	5°C	18 hrs
Dilution	5°C	24 hrs
Washing	5°C	24 hrs
Plasticizing solution (10% Ansco Flexiglass)	5°C	30 min
Drying (relative humidity (100% \rightarrow 50%))	5°C	7 days

As gelatin and glycerin are both hygroscopic, the actual thickness and the refractive index of the processed and unprocessed emulsion depends on the surrounding humidity. During

the process of washing, developing and fixing there is a shrinkage in the vertical direction since the other two directions are fixed. Therefore, one has to introduce a shrinkage factor S and multiply the vertical measures to obtain the correct results for any quantitative measurement of grain density, range and angles in emulsion. Generally the shrinkage factor is supplied by the manufacturer of the emulsion plates. The shrinkage factor is defined as $S = T/t$, where T = the thickness of the emulsion layer at the time of exposure and t = that at the time of scanning.

2.1.4 Track Structure

Grain Density: The grain density dn/dx of a track is measured by the number of developed silver grains per unit path length. If the grains are discrete and the upper limit of the grain density is 50 grains per $100\mu\text{m}$ and the lower limit of the grain density is 20 grains per $100\mu\text{m}$ for a relatively low background plate (e.g., less than 4 grains per μm^2) the measurement of dn/dx is not too difficult one. But in actual case there are many blobs of individual grains which can not be resolved. For this purpose a grain count value (n) is assigned to unresolvable grain clumps. Fowler and Perkins considered that $n = 2.4l$, where l is the length of the clump in microns, when the average developed grain diameter is about $0.3 - 0.4\mu\text{m}$. For a particle of mass m , charge ze , and is moving with a velocity $v (= \beta c)$ that is large compared to the velocity of the K -shell electrons of the stopping material, the average restricted energy loss per unit distance is given by [10],

$$-\frac{dE}{dx} = \frac{4\pi z^2 e^4 N Z}{m v^2} \left[\ln \left(\frac{2m v^2}{I} \right) - \ln(1 - \beta^2) - \beta^2 \right], \quad (2.1)$$

where N is the number of atoms per cm^3 of the stopping material (in this case emulsion), Z and I are, respectively, the mean atomic number and ionization potential of the stopping material. It is assumed that there exists a direct proportionality between dE/dx of the particles at various points on their trajectories and the corresponding dn/dx . However, for high dE/dx values this proportionality can no longer remain valid. This is due to the inability of the sensitivity specks of the halide grains to acquire electrons produced in their vicinity by the passage of the charged particle at a sufficiently rapid rate to prevent the formation of a space charge with high electron densities, that ultimately results in an inefficiency of the electron utilization. For specific energy loss below a certain value, the

efficiency of electron utilization in terms of the proportion of electrons contributing to the latent image formation relative to the number initially produced is nearly constant, and this leads to the direct proportionality between dE/dx and dn/dx . For densities above 200 grains per $100\mu\text{m}$ grain saturation occurs, and it is impossible to evaluate dn/dx for such tracks on the basis of grain counts since the proportionality between n and l ceases to hold for such continuous grain distributions. For strongly ionized electrolytes, the potential of an ion cloud surrounding an isolated ion may be taken as $\propto \sqrt{N}$. Since N is proportional to dE/dx , an expression for dn/dx could be obtained in the form [11],

$$dn/dx = c \left[1 - \exp \left\{ -bz (dE/dx)^{\frac{1}{2}} - a^{\frac{1}{2}} \right\} \right]. \quad (2.2)$$

Here 'b' and 'c' are constants that can be experimentally determined for the particular type of emulsion and developing material used, and 'a' is the minimum specific energy loss required to ensure developability of the grains.

Thus one can see that in order to estimate the specific energy loss dE/dx and hence the velocity of the moving charged particle, grain density is a useful parameter. Grain density is mainly determined by counting the number of developed grains within a measured length of the track. It is obvious that the error in measurement is less in case of low grain density. In case of high grain density the error automatically becomes large because the microscope cannot resolve the adjacent and overlapping grains. Sometimes instead of grain density, the blob density (B) is measured. A blob is the resolvable spot in which more than one grains may be present. The estimation of the number of blobs is equivalent to measuring the number of gaps between two blobs. O'Ceallaigh observed that the frequency distribution of the gap length has an exponentially decaying nature [12]. According to Fowler and Perkins [13] the number density of gaps (H) exceeding a value l is given by,

$$H(l) = B \exp(-g.l), \quad (2.3)$$

where the slope parameter g is a measure of the grain density, but cannot be set exactly equal to the true grain density dn/dx . Fowler and Perkins gave another relation as,

$$B = g \exp(-g.\alpha'), \quad (2.4)$$

where α' is a parameter determined by the average developed grain size. From Eq. 2.3 and 2.4 one can determine g as a useful ionizing parameter.

Lacunarity and Opacity: The lacunarity (L) of a track is defined as the fraction of the track made up of gaps, and it can be expressed as,

$$L = \int_0^\infty -l \left(\frac{dH}{dl} \right) dl = \exp(-g \cdot \alpha').$$

Thus one can see that, $g = B/L$, and $\alpha' = -(L/B) \ln L$. For particles with low z and high velocity ($\beta \approx 1$), the restricted energy loss is small, and a simple proportionality like $dE/dx \propto dn/dx$ holds. Assuming $g \approx (dn/dx)$, one may therefore, write

$$z^2 \propto -\ln L. \quad (2.5)$$

One should keep in mind that for a given emulsion α' is constant, and for highly energetic particles variation in β with energy is also not significant. On the other hand the opacity (O) is defined as the fraction of a track made out of blobs, and it is related to lacunarity by the simple relation $O = 1 - L$. Thus the charge of a particle moving at relativistic speed can be determined by measuring its lacunarity or opacity [14]. A high degree of accuracy for such a measurement can be achieved because,

$$\delta z \propto \frac{1}{z} \frac{\delta L}{L},$$

where the error in lacunarity measurement,

$$\delta L = \frac{\sigma_L}{\sqrt{N_c}}$$

is seen to scale with $N_c^{-\frac{1}{2}}$, where N_c is the number of cells of equal length (say S') over which the measurement of L has been made, and one can arbitrarily increase the value of N_c . Here $\sigma_L = \sqrt{\langle L^2 \rangle - \langle L \rangle^2}$ is the variance in L .

Delta rays in Emulsion: Even for a particle moving with relativistic speed ($\beta \approx 1$), the grain density is very high if $z \geq 4$, and the track appears almost as a continuous black filament of silver. For such particles the rate of energy loss may be so large that, secondary electrons are produced with sufficient kinetic energies, and some of these electrons may have observable tracks within emulsion. Such electron tracks are known as the delta rays. The number of delta rays (n_δ) is a function of dE/dx , and the method of delta ray counting can therefore be utilized to determine the charge of a particle, where lacunarity measurement is not possible. The number of such delta rays with energies between W

and $W + dW$ had been calculated as [15],

$$dn_\delta = \frac{2\pi N z^2 e^4}{m_e v^2} \frac{dW}{W} \left[1 - \beta^2 \frac{W}{W_{max}} \right]. \quad (2.6)$$

Here m_e is the electron mass, and

$$W_{max} = \frac{2 m_e c^2 \beta^2 \gamma^2}{1 + 2 \left(\frac{m_e}{m}\right) \gamma + \left(\frac{m_e}{m}\right)^2} \quad (2.7)$$

is the upper energy limit that the electron may have received, and $\gamma [= \sqrt{1 - \beta^2}]$ is the Lorentz factor associated with the moving particle. Whereas, W_{max} depends upon the sensitivity of the emulsion, the lower limit of W that defines a recognizable delta ray in emulsion, depends upon the range energy relation for low velocity electrons, the grain size, the scattering of these electrons, the sensitivity of the emulsion, and upon the criterion to distinguish the delta rays from random background grains. If a grain/blob configuration has to be counted as delta rays, the minimum acceptable track length has conventionally been chosen as $\approx 1.6\mu\text{m}$ measured from the axis of the track of the moving particle. There are other conventions as well e.g., a minimum of four grains in a row. Both conventions give the lower limit of delta ray energy near 10 keV. Integrating dn_δ over dW , one finds that,

$$n_\delta \propto \frac{z^2}{\beta^2}. \quad (2.8)$$

For particles moving with relativistic speed $\beta \approx 1$, and hence the simple proportionality $n_\delta \propto z^2$ can be utilized to determine the charge of such a particle.

Range of a particle: Charged particles suffer collision with the atoms present in the medium through which it traverses, and loses energy as they ionize these atoms. The tracks terminate when the energy of the charged particles become less than the ionization potential of the atoms in the medium. The true range of an ionizing particle can be defined as the distance traveled by the particle with a given velocity v_0 , before it stops within the emulsion. The measurable length of a track, sometimes also called the residual range (R), is the distance along its trajectory from the origin to the last developed silver grain on the track. This gives a measurement of the true range of the particle within a narrow limit. For low energy protons (kinetic energy \ll rest energy) a range-energy relationship like, $R_p = K E_p^n$, has been theoretically obtained and also experimentally verified. Note that R is measured in microns, and E the kinetic energy in MeV. From

the knowledge about specific energy loss (dE/dx) and initial energy (E_0), the range of a particle can be determined as,

$$R(E_0) = \int_0^{E_0} \frac{dE}{dE/dx}.$$

Combining this relation with the expression for dE/dx (Eq. 2.1) one gets,

$$R(E_0) = (m/z^2) f(v_0).$$

In the nonrelativistic limit ($E_0 < mc^2$) the energy ratio of two particles with same v_0 , is same as their mass ratios. In this region for any particle a range-energy relation similar to that of the proton, has been experimentally observed to hold true for any particle. It is therefore, possible to determine the range-energy relation for an arbitrary particle as [16],

$$E = K \left(\frac{m}{m_p} \right)^{(1-n)} z^{2n} R^n, \quad (2.9)$$

where m_p is the proton rest mass, and $K = 0.262$ and $n = 0.575$ are two experimentally obtained parameters. Due to different types of uncertainties and fluctuations, ranges of even monoenergetic particles exhibit straggling. The straggling parameter may be defined as,

$$\Gamma_R = \left(\frac{\pi}{2} \right) \left[\frac{\sum_i^N (R_i - \bar{R})^2}{N} \right]^{\frac{1}{2}}$$

or, as the full width at half maximum of the differential distribution curve of the ranges, that is related to Γ_R as, $\Delta R = 0.94 \Gamma_R$.

Track Width: For high ionization (say $z > 10$), the linear track structure contains little information in terms of grain (or blob) density, and n_s becomes too large to be counted. Under such circumstances, the track width has been found to be a useful parameter to identify the nature of the particle [4]. The track width depends on various factors such as, the type of emulsion, the type of developer used, the particle variables (charge, mass, velocity) etc.. It's also not an easy task to accurately determine the track width and correlate the data with particle identity. Accurate eyepiece micrometers should be used to measure the track width. The track image under high magnification (\sim several thousand times) may be projected, and the area of a particular segment may be determined with a planimeter. The photoelectric opacity may also be used to digitally measure the track width. Experimental data show that the track width increases linearly with particle

charge for $z > 10$. As a track caused by a heavy nucleus/ion reaches towards its end, a thinning down (tapering) of the track is observed due to electron capture, which reduces the effective charge of the nucleus/ion. The length of this tapered portion (L_t) of the track may also be used to find out the atomic number of the particle [17]. An empirical relation like $L_t = C z^\nu$: ($\nu \approx 1$) has been obtained in this connection.

2.2 The Microscopy

A good compound microscope is the main equipment for analyzing the behavior of tracks in emulsion. Emulsion microscopy is significantly different from other microscopy techniques such as those used in biological or material sciences [3, 4]. The horizontal area that has to be scanned is always much larger in size and there is always a greater emphasis on the vertical dimension. Searching for events within a three dimensional space requires fine focus mechanism. The length (or displacement) measuring devices attached to the stage supporting the subject (emulsion) must also possess a high degree of accuracy in all three (two horizontal and one vertical) directions. The stage movement must be very smooth and should be as much noise free as is possible. The most important component of a compound microscope is its objective(s). For minimum spherical aberration, achromatic objective lenses are made using combinations of convex and concave lenses with different refractive indexes and dispersions. The quality of measurement can be improved by creating a homogeneous optical medium. This is achieved by filling up the interstitial space between the objective and the emulsion with a material (often cedar wood oil), that has approximately the same refractive index (≈ 1.52) as that of the glass and gelatin. The resolution of the microscope depends of its numerical aperture. The numerical aperture ($N.A.$) is given by,

$$N.A. = \mu \sin \alpha,$$

where μ is the refractive index and α is the semivertex angle of the light ray cone that a point object extends toward the objective lens aperture. The minimum separation (d) between two adjacent points (not self luminous) that can just be separated is about

$$d \approx \frac{\lambda}{2 \mu \sin \alpha}$$

where λ is the wave length of the light used in air. For dry lenses the $N.A. < 1$, whereas that for wet oil immersion type of objectives can be as high as 1.6. The depth of focus given by,

$$\Delta = \frac{\lambda}{4 \mu \sin^2 \left(\frac{\alpha}{2} \right)}$$

is a vertical length along the axis of the objective over which the sharpness of the visual image remains unchanged. Δ can vary from several microns for dry lenses ($N.A. < 0.25$ or so), to a fraction of a micron for wet lenses ($N.A. > 1$). For rapid scanning the dry lenses with low magnification are useful for rapid scanning, and the wet lenses are more suitable for critically scrutinizing an event and for accurate measurements. The working distance between an oil immersion objective must be of the order of a few mm for thick emulsion plates. Objectives should be parfocally mounted on a turret so that the axis of each lens is aligned to the same position, and each lens focuses at the same depth. A tube length of 160 – 170 mm gives the best image produced by the objective lenses. A two element eyepiece (either Huygen or Ramsden type) consisting of one field lens and one eye lens, may be used to magnify the real image produced by the objective. Now-a-days more complex apochromatic structures are used, that can remove the secondary spectrum from the image and can also eliminate the chromatic effects of spherical aberration. Wide field viewing is an essential feature of nuclear track microscopy. This is limited by the diameter of the binocular eye tube. Binocular tubes with large diameter coupled with wide field ocular lenses are recommended for the purpose. Measurement within the field of view can be made with the help of a micrometer scale (called the graticule), which for a Ramsden type of eyepiece should be placed in front of the field lens. The graticule along with a goniometer can be employed to angle measurements. But such an arrangement is suitable only in those cases, where the tracks are angularly well separated from each other. In $^{32}\text{S-Ag/Br}$ interactions at 200A GeV/c one often encounters very dense jets of produced particles. For such cases one has to move the sample over quite a few number of fields of view, and measure the corresponding displacements using measuring devices attached with the mechanical stage. In all three directions the noise level associated with the stage motion should be as small as a fraction of a micron over a few centimeter of displacement. A microscope that can be used for nuclear track scanning probably desires the following features.

- (a) 100× oil immersion objective with a working distance at least 500μ, 40× oil, 20× dry and a 10× dry objectives.
- (b) A turret mount, co-centered well enough so that the middle of the field of any of the objectives will be found in the field of the 100× objective with a tolerance not more than one thousandth of an inch. Each lens length should be so adjusted that the lenses are parfocal on rotating turret.
- (c) A binocular body with separate focus control of one ocular and sufficient range of interocular distance. Parallel eye tubes are preferred.
- (d) Standard wide field oculars (10×, 15×).
- (e) A goniometer for the dominant eye ocular with a graticule of good quality.
- (f) A condensing lens with an numerical aperture of at least 1.25 and possibly another long working distance with an numerical aperture of about 1.00.
- (g) A mechanical stage of sufficient area with sufficiently long stage motion along either of the perpendicular directions in the horizontal plane for the largest plate to be scanned.

2.2.1 Counting and statistics

In an emulsion experiment counting is as important as measurement. The emulsion provides discrimination between various sorts of events as well as different types of tracks emanating from an event. Events and tracks belonging to different categories should be properly counted. The ionization of a track may be measured by counting the number of grains or blobs over a particular length of the track (say 100 μm). Delta rays over a similar length interval may be counted to help identify the charge of the particle producing a track. Energy spectra are determined by counting the number of tracks within particular range intervals. Angular distributions are determined by counting the number of tracks in prescribed angular intervals. Prong numbers are counted to measure the excitation energy of an event. Therefore, in order to find out the reliability of the collected data, a practical knowledge of counting statistics is required. Three standard statistical distribution functions are often used for this purpose [4]. The Poisson distribution is given by,

$$P(n, \langle n \rangle) = \frac{\langle n \rangle^n e^{-\langle n \rangle}}{n!} \quad (2.10)$$

where $P(n)$ is the probability of occurrence of exactly n counts in a fairly large number of trials. The Poisson distribution is often used to describe the distribution of a random uncorrelated variable. The variance $\sigma^2 = \langle n^2 \rangle - \langle n \rangle^2$ of a Poisson distributed quantity is equal to the average $\langle n \rangle$. If in a trial the probability of occurrence is finite (say q), the probability for a count n in m number of trials is described by the Binomial distribution,

$$P(n, m, \langle n \rangle) = \frac{m!}{n!(m-n)!} \left(1 - \frac{\langle n \rangle}{m}\right)^{m-n} \left(\frac{\langle n \rangle}{m}\right)^n. \quad (2.11)$$

The Binomial distribution under special conditions reduces to a Poisson distribution. For Binomial distribution the average count is $\langle n \rangle = mq$, and the variance is $\sigma^2 = \langle n \rangle (1 - \langle n \rangle / m)$. For large $\langle n \rangle$ and m the Binomial expression converges to the Normal or Gaussian distribution,

$$P(n, \langle n \rangle, \sigma) = \frac{\exp[-(n - \langle n \rangle)^2 / 2\sigma^2]}{\sigma\sqrt{2\pi}}. \quad (2.12)$$

The mean absolute deviation (μ) of n from $\langle n \rangle$ is given by $\mu = \sigma\sqrt{2/\pi} = 0.7979\sigma$. In counting measurement this as convenient a measure of the statistical spread of the data as the standard deviation (σ). The probable error (ϵ) is estimated from $\epsilon = 0.6745\sigma$.

Besides counting it is also often necessary to fit a set of data with a particular trend line. The Pearson's product moment correlation co-efficient (r), also known as the co-efficient of determination, is an indicator of how closely the estimated values corresponding to a particular trend line match with a set of data [18]. For a set of known pairs of variables $(x_i, y_i) : i = 1, \dots, N$, the co-efficient is defined as,

$$r = \frac{N(\sum x_i y_i) - (\sum x_i)(\sum y_i)}{\sqrt{[N \sum x_i^2 - (\sum x_i^2)][N \sum y_i^2 - (\sum y_i^2)]}}, \quad (2.13)$$

where N is the total number of data points. r is a dimensionless index and can range from +1.0 (a perfect positive linear correlation) to -1.0 (a perfect negative linear correlation). On the other hand $r = 0$ would indicate absence of any such correlation. The r^2 value may be interpreted as the proportion of variance in the dependent variable y_i that can be attributed to the variance in the independent variable x_i . For a straight line fit to the data $r^2 = 1.0$ means no discrepancy between observed and expected values. Another measure of discrepancy between observed and expected values (say frequency) is given by

the χ^2 statistic defined as,

$$\chi^2 = \sum_{i=1}^N \frac{(exp_i - obs_i)^2}{exp_i} \quad (2.14)$$

where exp_i (obs_i) denotes the expected (observed) frequencies, and $N = \sum obs_i = \sum exp_i$ denotes the total frequency. In case of dependent variables other than frequencies the formula may be modified as,

$$\chi^2 = \sum_{i=1}^N \frac{(exp_i - obs_i)^2}{\sigma_i^2} \quad (2.15)$$

where σ_i denotes the standard deviation in i th observed value. $\chi^2 = 0$ means a perfect agreement between the observed and expected values. The no. of degrees of freedom (*dof*) is determined by the no. of data points, the no. of parameters involved in the expected distribution (function), and any other condition imposed on the data. The χ^2/dof value is used to estimate the goodness of a fit at a particular level of confidence.

2.2.2 Geometric Measurements in Emulsion

All the geometric measurements should be made with a full knowledge of the distortion effects of emulsion. The geometric measurements consist of determining the coordinates of points in a suitable coordinate system, measurement of distances between two points, measurement of area and volume, measurement of projected and space angles, measurement of deviation of a track from a straight line, measurement of angular (spatial) distributions etc. For geometric measurements, it is essential that the eyepiece graticule has engraved on it a scale that divides the useful field diameter into equal parts (say 100). The useful field diameter is perhaps 50 – 70% of the extreme field diameter. At a magnification of 1000, one division of the graticule usually is in order of magnitude of $1\mu\text{m}$. The coordinates of a point in the field can then be measured with a standard deviation of less than a micron. One can at first choose an arbitrary point as the origin of the coordinate system that can easily be relocated later. For example in case of an interaction, the point of interaction can serve the purpose. One can then easily measure the x and y coordinates of any point in the horizontal plane with respect to the origin. The z coordinate is determined by the vertical displacement of the stage (and hence the emulsion plate) between the positions of two points having same x and y coordinates. This displacement of course

must be corrected by the emulsion shrinkage factor as has been mentioned earlier.

The angle of dip (δ) of a linear track segment is given by $\tan \delta = S \Delta z / L_{xy}$, where Δz is the measured vertical difference between two points on the track segment under consideration, and L_{xy} is the length of the track projected between these two points on the horizontal ($x - y$) plane. It has been implicitly assumed that the refractive index of the oil commonly employed for oil immersion objectives is very close to the refractive index of the developed emulsion and the glass plate. For dry objectives the real depth should be corrected by the refractive index of the with respect to that of the emulsion. The space angle also called the emission angle (θ), between two tracks may also be measured by the simple coordinate method. If two tracks are characterized by direction cosines (l_1, m_1, n_1) and (l_2, m_2, n_2), respectively, then θ is given by,

$$\cos \theta = l_1 l_2 + m_1 m_2 + n_1 n_2. \quad (2.16)$$

If all three coordinates of any two points on a track are given by (x_1, y_1, z_1) and (x_2, y_2, z_2) , the direction cosines are obtained as,

$$l = \frac{(x_1 - x_2)}{[(x_1 - x_2)^2 + (y_1 - y_2)^2 + (z_1 - z_2)^2]^{1/2}},$$

$$m = \frac{(y_1 - y_2)}{[(x_1 - x_2)^2 + (y_1 - y_2)^2 + (z_1 - z_2)^2]^{1/2}},$$

$$n = \frac{(z_1 - z_2)}{[(x_1 - x_2)^2 + (y_1 - y_2)^2 + (z_1 - z_2)^2]^{1/2}}.$$

Thus in order to find out the emission angle of any secondary track coming out of an interaction, it is necessary to find out the direction cosines of the incident projectile track as well as those of the secondary track. The azimuthal plane is defined as a plane perpendicular to the direction of motion of the projectile nucleus. The track direction projected in this plane with respect to some reference direction may be defined as the azimuthal angle (φ) of a track (measured counterclockwise). If the projectile direction is absolutely coinciding with one of the horizontal displacement directions of the stage (say x -direction), then

$$\varphi = \tan^{-1} \left(\frac{\Delta z}{\Delta y} \right).$$

If the projectile direction is not completely coinciding with the x -direction of the stage motion, then φ for a particular track may be measured by setting the corresponding quantity for the projectile track to be equal to zero.

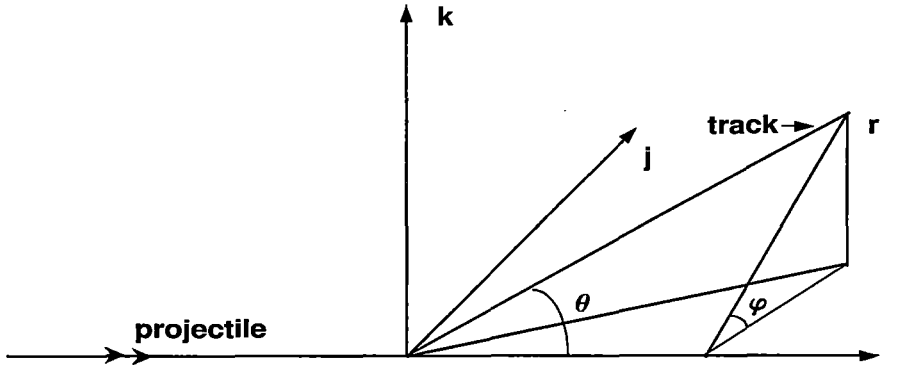


Figure 2.1: Schematic description of secondary track geometry with respect to a primary projectile track.

The track geometry has been schematically represented in Fig. 2.1. Due to scattering the track of a charged particle may not always be straight. Therefore, it is convenient to break up the track into M number of essentially straight segments, and the residual range of the particle may be determined from the relation,

$$R = \sum_{i=1}^M [(x_i - x_{i-1})^2 + (y_i - y_{i-1})^2 + S^2 (z_i - z_{i-1})^2]^{1/2},$$

where S is the shrinkage factor along the vertical (here z) direction. For mounted plates generally no shrinkage factor is associated along either of the horizontal directions.

In high energy heavy-ion interactions the number of secondary particles per event is very large. Therefore, in order to get sufficient spatial separation between two adjacent tracks, it may be necessary to displace the stage to such a large distance, that the point of interaction is far beyond the field of view containing the interaction vertex. There is every chance that the particle under consideration will suffer from Coulomb scattering and will deviate from its original direction. The problem is more acute in the forward direction, that is densely populated by jets of particles. Under such situations one may have to take help of a nearby projectile track located within the same field of view, that is essentially moving parallel to the projectile track under consideration. It is to be noted that if the projectile tracks are close to each other, they will experience almost identical distortions in the emulsion. Heavy-ion interactions are rich sources of highly energetic photons. These photons may interact with the nuclear field available in the emulsion

medium itself and produce e^-e^+ pairs. The angular separations between the electron and positron tracks are often very small and it is therefore, often extremely difficult to identify them as two separate tracks. Moreover, if the $\gamma \rightarrow e^-e^+$ conversion takes place near the interaction vertex, then it is also very likely to confuse the e^-e^+ tracks as originating from the interaction vertex. When the coordinates of points are recorded at a large distance from a particular interaction vertex, there may be interference with the tracks coming from other interaction points. These problems can be solved by recording the coordinates of several points on a single track, and through a reconstruction program obtain the best fitted straight line for them, and also to check whether or not that straight line is passing through the coordinates of the interaction vertex.

Momentum Measurement: A charged particle moving through matter experiences frequent small deflections due to elastic scattering with the Coulomb field offered by the atomic nuclei present in the medium. The probability for a particular deflection is given by Rutherford's scattering formula - small angular deviations occur with high frequency. The distribution follows a Gaussian pattern with the mean at zero. The theoretical treatment suitable for comparison with experiment suggests the mean absolute angular deflection $\langle \phi \rangle$ to be measured. For convenience of measurement ϕ is considered as the projected angle on a plane of the space angle, and its mean value is given by [19],

$$\langle \phi \rangle = \sqrt{\overline{\phi^2}} = \frac{2 z e^2 (Z^2 N d)^{1/2}}{p \cdot \beta} \left[\ln \left(\frac{\phi_{max}}{\phi_{min}} \right) \right]^{1/2}, \quad (2.17)$$

where N = number of atoms per unit volume in emulsion, z = atomic number of the particle, p = momentum of the particle in MeV/c, β = velocity of the particle in the unit of c while traversing a path length = d , Z = the average atomic number of the atoms present in the medium, and ϕ_{max} (ϕ_{min}) = the maximum (minimum) value of the projected angle in the plane of the initial particle trajectory. Following a method suggested by Fowler [20], the mean absolute scattering angle $\langle \phi \rangle$ can be determined. In this method the plate is placed on the mechanical stage of the microscope in such a way that the track is approximately parallel to the abscissa of the stage, say x -axis. The co-ordinates (x_0, y_0) of an arbitrary point on the track are measured. The plate is then displaced by a distance equal to the cell length d along x -direction, and the ordinate y_1 of the point is determined by means of an eyepiece scale. The measurement should be performed under high magnification (e.g., 2500 \times), and the ordinary eyepiece scale is

commonly replaced by a flair micrometer, which is capable of reading distances within a few hundreds of micron. Once again the stage is moved through the standard distance d , and the ordinate y_2 is recorded. The operation is repeated several times along the length of the track. The absolute value of the second differences taken irrespective of the sign $D_k = |y_{k+2} - 2y_{k+1} + y_k|$ of successive such measurements are determined. The mean absolute value between successive chords of length d corrected for stage noise and cell length $\langle D \rangle = \sum_k^n D_k/n$ gives a measure of the scattering parameter,

$$\langle \phi \rangle = \frac{\langle D \rangle}{d} (180/\pi) \quad (2.18)$$

from which $p\beta/z$ in MeV/c can be evaluated. If $\langle \phi \rangle$ is to be a meaningful quantity, then in a given cell length d of the track, the energy loss is considered negligible.

2.2.3 Scanning in Emulsion

In a scanning program events of certain types are sought in a systematic way. Area (more specifically volume) scanning of a plate is usually done in strips approximately equal in width to a side of an inscribed square within the field of view. During the process the focal surface is continually shifted to sweep up and down from the surface of the emulsion to that of the glass by rotating the fine focus control, while observing events successively coming into and going out of the view. One such elementary motion down or up can be termed as scanning traverse. For high efficiency the field may be divided into a number of sufficiently small separate areas, so that the entire volume can be covered as the traverse is made. The field is not shifted until a particular volume has been completely searched. Generally area scanning is performed under either of the following two circumstances, (i) when events of a certain type within a given volume of emulsion are to be found, and (ii) if the situation demands a representative sample of events. Preliminary volume scanning may be performed under a total magnification of $300 - 400\times$ ($15\times$ ocular and $20\times$ dry objective, or $10\times$ ocular and $40\times$ oil immersion objective). The collected data can be finally refined under $1500\times$ total magnification ($15\times$ ocular and $100\times$ oil immersion objective). As high multiplicity events easily catch human eyes, with volume scanning it's seldom possible to get an unbiased sample of events. For that purpose the technique of along the track scanning is preferred. In this technique each

projectile track is carefully followed from the leading edge of a plate along its length until the projectile interacts or leaves the plate. Just like in the case of volume scanning, in this case too preliminary scanning may be performed under $300 - 400\times$ total magnification, but the final selection of events has to be done under $1500\times$ total magnification. It is a tiresome and time consuming process, and it requires a lot of concentration on the part of a scanner, and accuracy of experimental results depends largely on the experience and skill of the observer. To avoid individual bias counter checking of the same data sample by independent observers is recommended. Through along the track scanning it is possible to acquire a sample of events with minimum bias.

2.3 Advantages and Disadvantages of Emulsion Technique

One of the main advantages of nuclear emulsion is that it serves as a detector of charged particles as well as it provides different targets like H, C, O, N, Ag, and Br nuclei of varying mass numbers. As far as high energy interactions are concerned, information regarding target nucleus mass (size) dependence can therefore be obtained. Nuclear emulsion has the capacity to detect all charged particles coming out of an interaction. Thus nuclear emulsion is one of the very few detectors that have 4π acceptance. However, the detection efficiency may not be equally good in all directions. Particularly the efficiency is not very good along the vertical (along the thickness of the plate) direction. Due to a high medium density, the stopping power and therefore, the probability of interaction between a projectile particle and a target nucleus is high in case of nuclear emulsion. As a detector nuclear emulsion is less costly, light and can be handled very easily. The nuclear emulsion is also a very useful detector in cosmic ray experiments. As it can register all the charged particles with energy from very low up to the relativistic limit, and because the sensitivity of nuclear emulsion lasts for a few weeks, all charged particles within a sufficiently long time span can therefore be recorded. Therefore, it is suitable for balloon flight and satellite experiments. Nuclear emulsion permanently registers the trajectory of charged particles and tracks belonging to different types of particles have their own characteristic appearances. Hence if need arises, they can be distinguished from one another with a

little extra effort. In nuclear emulsion neutral particles can also be indirectly identified, as and when they interact with the nuclei present within the medium and produce tracks of charged particles. Nuclear emulsion has a large operating range with respect to temperature - from the temperature of liquid helium up to the boiling point of water. The most striking advantage of nuclear emulsion is its high spatial resolution. For conventional horizontally irradiated stacks of emulsion plates (or pellicles), in spite of multiple Coulomb scattering and distortion effects an accuracy of 0.1 unit of pseudorapidity can be achieved. If distributions of produced particles are to be analyzed in narrow intervals of pseudorapidity space, this unique feature makes the emulsion as competitive a detector as its large and much more costly electronic counterparts.

The nuclear emulsion has also quite a few limitations. One can not distinguish between the sign of a charge unless a magnetic field is applied. But it is difficult to get the magnetic field penetrate into the emulsion material, hence to produce enough curvature in the track of a relativistic particle to identify its charge. The tracks formed in emulsion are relatively small and hence they can be studied only under a microscope with high magnification. This makes the data acquisition process a tedious and time consuming one. For AB interactions where a few hundreds of particles are produced per event, the time taken to build up a statistics of an acceptable size is typically of the order of a few years. Moreover, till date human eyes remain most suitable for tasks like counting and identification of events and tracks. Therefore, the collected data can never be fully free from personal bias and errors. However, such limitations can be reduced through counter checking by more than one independent observers. Measurement of energy, momentum and mass of a particle in emulsion is so cumbersome and time consuming that such a proposition is often considered as impractical, and for routine investigations they are almost never undertaken. The sensitivity and the thickness of emulsion pellicles are affected by factors like temperature, humidity, age etc.. Unless proper care is taken in this regard, such factors induce extra errors in measured values. Because the identification of target fragments is often extremely difficult, and sometimes even impossible, therefore, in this technique its often impossible to exactly identify the target nucleus of an interaction. However, as later mentioned, there are ways by which one can make a gross distinction between the light group (H,C,N,O) and heavy group (Ag,Br) of target nuclei.

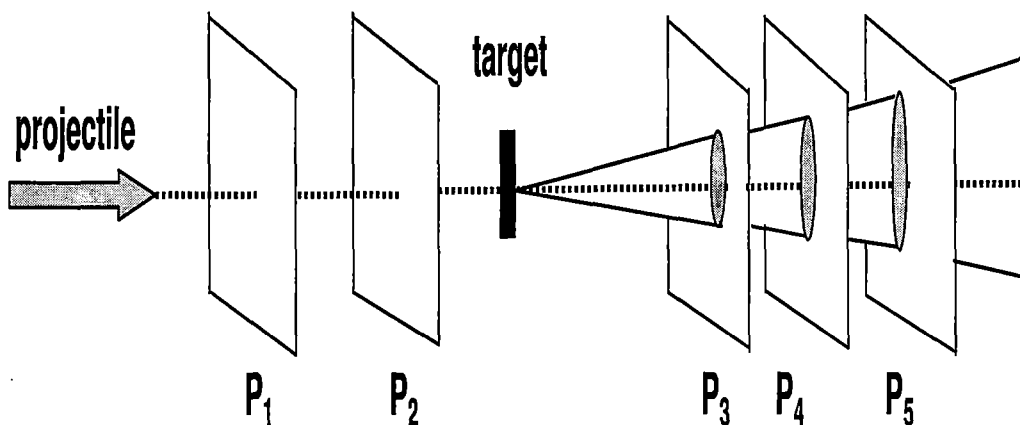


Figure 2.2: Schematic description of an emulsion chamber set up. P_1, P_2, P_3 etc. represent the emulsion coated plastic plates.

In the recent past instead of standard stacks of emulsion pellicles, the emulsion chamber arrangement has been used in several emulsion experiments [21]. In this technique, thin plastic (acrylic or polystyrene) plates of typical dimension $10 \times 10 \times 0.1 \text{ cm}^3$, coated on both sides with emulsion layers are used. The thickness of emulsion coating is of the order of $2 - 3 \times 10^2 \mu\text{m}$. These emulsion plates are separated by honeycomb paper spacers with a few $2 - 3 \times 10^2 \mu\text{m}$ thick metal targets (e.g, Pb or Au) placed in between. The incident beam travels perpendicularly through the arrangement, mostly through empty space. As the tracks travel mostly through empty space they suffer much less multiple Coulomb scattering. The position coordinates of the tracks are measured in the emulsion-air and emulsion-plastic interfaces with respect to other primary beam tracks. This substantially reduces the distortion effect. Thus in the chamber technique an accuracy of 0.01 pseudorapidity unit can be achieved. Because of the novel design of the emulsion chamber, it is possible to separate out all the tracks coming from an interaction, as they can be followed over as large a distance as several centimeters. However, there are a few disadvantages of this technique as well. Only area scanning (to be explained later) is possible in this technique, and an event sample with minimum bias can not be obtained. Another disadvantage is that the particles moving in the backward direction can not be traced, thereby limiting the pseudorapidity acceptance of the system. However, the central particle producing region can still be covered.

2.4 General Characteristics of the Data

In an emulsion experiment (Expt. no. EMU08) performed by the Buffalo group, Ilford G5 type nuclear photographic emulsion pellicles were horizontally exposed to a beam of ^{32}S nuclei at an incident momentum of 200A GeV/c obtained from the Super Proton Synchrotron (SPS) at CERN, Geneva [22]. The ^{32}S beam flux was 10^3 particles per square centimeter, and as mentioned before, the dimension of the emulsion plates at the time of exposure was $18 \times 7.5 \times 0.06 \text{ cm}^3$. The emulsion plates were scanned along the track with the help of Leitz Metalloplan microscopes under a total magnification of $300\times$ by two independent observers, so that the bias in event detection can be minimized. Periplan eyepieces ($10\times, 15\times$) in conjunction with ($10\times, 0.30$) dry, ($20\times, 0.50$) dry, ($40\times, 0.70$) oil immersion, and ($100\times, 1.32$) oil immersion objectives were used. Figures within each bracket denote respectively, the magnification and the *N.A.* of the lens system. The accuracy of coordinate measurement was $1\mu\text{m}$ along the horizontal ($x - y$) directions and $0.5\mu\text{m}$ along the vertical (z) direction. If an interaction has occurred within $20\mu\text{m}$ of either the top (emulsion-air) or bottom (emulsion-glass) surface, it has not been taken into account. Angle measurement of tracks becomes difficult for such events located near the interface of two different medium. Due to the same reason events occurring within 4 mm of the leading edge of the plate have also been excluded, as such regions are often plagued by severe distortion. A total path length of 127.38 mt was followed, within which a total number of 1354 inelastic ^{32}S -emulsion interactions were found. This resulted in an interaction mean free path $\lambda = 9.41 \pm 0.26 \text{ cm}$, that is related to the total cross-section through $\sigma_{S-Em} = 1/N \lambda$, and the value is $\sigma_{S-Em} = 1150 \pm 34 \text{ mb}$. Recall that the no. of scattering centers (N) present in emulsion is 7.898×10^{22} per cc (Table 2.2). After finding out a primary interaction induced by the incoming ^{32}S projectile, the number of secondary tracks in an event belonging to each category was counted. According to the emulsion terminology, tracks coming out of an interaction can be classified into four categories namely, the shower tracks, the gray tracks, the black tracks and the projectile fragments.

1. The shower tracks are created by singly charged particles moving at relativistic speed ($\beta \approx 0.7$). This category mainly comprises of particles produced in a high-energy interaction, most of which are charged π mesons. The total number of shower tracks in an event

is denoted by n_s . The ionization of shower tracks $I \leq 1.4 I_0$ where I_0 is the minimum ionization in emulsion. For the Ilford G5 type of plates used in the present investigation this value is $I_0 = 20$ grains per $100\mu\text{m}$.

2. The gray tracks are generally due to the protons that have directly participated in an interaction, and are knocked out from the target nuclei. They usually fall within an energy range of 30 – 400 MeV. The ionization of these tracks is $1.4 I_0 < I \leq 6.8 I_0$. The range of a gray track is > 3 mm in emulsion, and the particle velocity is within $0.3c - 0.7c$. A few percent of the gray tracks may also be due to the slow moving mesons. The number of gray tracks in an event is denoted by n_g .

3. Black tracks are due to the slow moving heavy target fragments emitted by the remaining part of the excited target nucleus after an interaction has taken place. The process is similar to the evaporation of a heated liquid drop. These tracks have ionization $I > 6.8 I_0$, range less than 3 mm in emulsion, and for a black track caused by a proton the velocity $< 0.3c$. The corresponding kinetic energy is less than 30 MeV. The number of black tracks in an event is denoted by n_b .

4. The projectile fragments are the spectator parts of the incoming projectile nucleus. They remain confined within an extremely narrow forward cone of small semi-vertex angle (θ_f), that depends on the momentum of the incoming nucleus. The tracks are very straight as they suffer very small Coulomb scattering. According to a simple Fermi gas model of a nucleus, the Fermi energy of a nucleon is given by,

$$E_f = \frac{\hbar^2}{2m_p} \left(\frac{3}{2} \pi^2 n_p \right)^{2/3},$$

where m_p and n_p are, respectively, the nucleon mass and nucleon number density. Numerically E_f is estimated as 21 MeV, and the corresponding Fermi momentum $p_f \approx 200$ MeV/c. For a nucleus having 200A GeV/c incident momentum, $\theta_f = 1$ mrad. In an event n_{pf} denotes the number of projectile fragments of charge $z \geq 2$ falling within this cone.

The sample of inelastic interactions can be classified into two different categories namely, the electromagnetic dissociation (ED) events and the nuclear events. Extremely strong electromagnetic fields offered by the target nuclei causes ED of the projectile nuclei. The impact parameter (b) for such an interaction \geq sum of radii of the target and projectile. Such events typically consist only of projectile fragments [23]. Barring the ED events, rest of the events in the sample may be considered as nuclear interactions. After eliminat-

ing the ED events as well as the ^{32}S -H interactions, the mean free path for other nuclear interactions came out as $\lambda_{nuc} = 11.01 \pm 0.32$ cm. The no. of H-atoms present in emulsion is 3.2156×10^{22} per cc. If this no. is subtracted from the total no. of scattering centers per cc. then the cross-section comes out as, $\sigma_{nuc} = 1940 \pm 57$ mb. From simple geometric considerations of a participant spectator model [24] the nuclear cross-section is given by,

$$\sigma_{nuc}^{th} = \pi r_0^2 [A^{1/3} + B^{1/3} - \delta]^2. \quad (2.19)$$

With projectile mass no. $B = 32$, and excluding the contribution from H-nuclei the weighted average target mass no. of emulsion $A = 48.39$. This gives us $\sigma_{nuc}^{th} = 1904.3$ mb., where $\delta = 0.83$ and $r_0 = 1.3$ fm. have been used.

The nuclear interactions can also be subdivided into peripheral (large b) and central (small b) collisions by looking at their respective shower multiplicities. The number of heavy tracks in an event (n_h) is given by, $n_h = n_b + n_g$. By putting a condition on the number of these heavy target fragments like, $n_h \geq 8$ with at least one fragment of $Z \geq 2$ per event, it can be ensured that a subsample consisting only of ^{32}S -Ag/Br interactions are taken into account. The events with $n_h < 8$ can either be an Ag/Br, or a H/C/N/O interaction. A further restriction on the number of spectator projectile fragments in an event $n_{pf}(z \geq 2) = 0$, enabled us to choose only those interactions for which total fragmentation of the incident ^{32}S nuclei have taken place. Assuming each ^{32}S -Ag/Br interaction as an entirely incoherent set of 32 independent NN collisions, the total center of mass (cm) energy $\sqrt{s} \approx 620$ GeV. On the other hand, if the ^{32}S nucleus interacts as a single coherent object (see section 1.3.4) with an Ag ($A = 108$) or a Br ($A = 80$) nucleus, then the corresponding center of mass energy will, respectively be $\sqrt{s} \approx 1145$ GeV or $\sqrt{s} \approx 984$ GeV. The actual center of mass energy is perhaps somewhere in between the two extreme cases mentioned above, because (i) neither all interactions between two nuclei are coherent, and (ii) nor in a mixed sample of central and semicentral interactions, where the impact parameter does not have a fixed value, all nucleons belonging to the target and projectile nuclei always directly participate in the interactions. However, the purpose of quoting the above values of \sqrt{s} is only to give an idea about the (cm) energy scale at which particle production is taking place, and not to determine the exact degree of coherence.

After counting measurements are completed, the emission angle (θ) and the azimuthal

angle (φ) of each track with respect to the incident projectile track were measured. This has been done by using $100\times$ oil immersion objectives and at a total magnification of $1500\times$. As mentioned in section 1.2, the rapidity variable previously defined as,

$$y = \frac{1}{2} \ln \frac{E + p_l}{E - p_l}, \quad (2.20)$$

additive under Lorentz boost, can be used to locate a particle in a one dimensional phase space. Here E and p_l are, respectively, the energy and longitudinal component of linear momentum of the particle. The pseudorapidity variable,

$$\eta = -\ln \tan \frac{\theta}{2}, \quad (2.21)$$

is a convenient replacement of the rapidity variable, where energy and/or momentum measurements are difficult as it is the case for emulsion experiments, and where in comparison with the total energy the rest energy of a particle can be neglected, as it is the case for most of the charged mesons produced in high-energy interactions. The resolution in η as a function of θ is given by,

$$\delta\eta = -\frac{1}{\sin \theta} \delta\theta.$$

So, at small angles only a small error in θ can ensure a good resolution in η . Together with the azimuthal angle (φ), the pseudorapidity (η) variable constitutes a two-dimensional phase space. Distribution of both η and φ for all shower tracks in our event sample have been obtained in terms of the respective density functions namely, $\rho(\eta) = N_{ev}^{-1}(dn_s/d\eta)$ and $\rho(\varphi) = N_{ev}^{-1}(dn_s/d\varphi)$. $N_{ev} = 200$ is the total number of events in the sample. The η -distribution has been fitted with a Gaussian function like,

$$\rho(\eta)d\eta = \rho_0 \exp \left[-\frac{(\eta - \eta_0)^2}{2\sigma_\eta^2} \right] d\eta, \quad (2.22)$$

where ρ_0 is the peak density, η_0 is the peak position and σ_η is the standard deviation of the Gaussian distribution. The experimental histogram and the fitted Gaussian curve are both plotted in Fig. 2.3(a). One can see that, the Gaussian function well describes the η -distribution. Values of the fit parameters of the Gaussian curve along with average no. of each category of tracks in the event sample are given in Table 2.5. One similar plot for the φ -distribution can be seen in Fig. 2.3(b). Within statistical uncertainties $\rho(\varphi)$ is found to be uniformly distributed in between $\varphi = 0 - 360$ degree. The dips near $\varphi = 90^\circ$

and 270° are to be noted. Most probably they are due to inefficient recording of shower tracks in directions vertical to the emulsions plates, and exactly toward or away from the direction of vision.

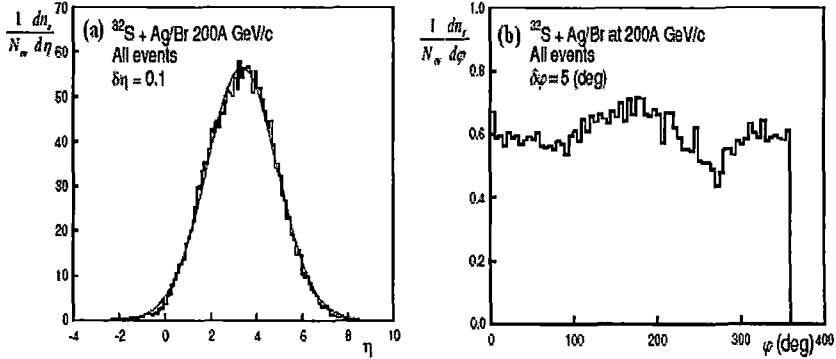


Figure 2.3: (a) Pseudorapidity η and (b) azimuthal angle φ distribution of shower tracks emanating from ^{32}S -Ag/Br interactions at 200A GeV/c.

The no. density of shower tracks in the central pseudorapidity region is a good measure of the centrality of the collision. Following a method suggested by Wong [25], an estimate of the average impact parameter (\bar{b}) for the sample of events used in the analysis can be obtained. In this method the peak value of the pseudorapidity density of produced charged particles in AB collision at an impact parameter b , and at a particular incident momentum per nucleon, is related to the same density for pp interaction at the same momentum by the following formula,

$$\left. \frac{dn_{AB}}{d\eta} \right|_{peak} \approx 1.28 \frac{AB}{A^{2/3} + B^{2/3}} \frac{1}{1 + a(A^{1/3} + B^{1/3})} \exp(-b^2/2\beta^2) \left. \frac{dn_{pp}}{d\eta} \right|_{peak} \quad (2.23)$$

In pp interaction at laboratory momentum 200 GeV/c ($\sqrt{s} = 19.4$ GeV), the peak density of particles = 1.38 [26]. A and B are the mass no. of the interacting nuclei, and a ($= 0.09$) is a parameter obtained by linearly fitting $dn_{ch}/d\eta$ against $B^{1/3}$ for different AB collisions at 200A GeV/c [25]. In our case $B = 32$, whereas the weighted average mass no. of target Ag or Br nuclei $A \approx 94$. Putting these values in Eq. (2.23) one can determine the factor $\exp(-b^2/2\beta^2)$. In the above formula, $\beta^2 = \beta_A^2 + \beta_B^2 + \beta_p^2$, $\beta_A = r_0 A^{1/3}/\sqrt{3}$, $\beta_B = r_0 B^{1/3}/\sqrt{3}$, $r_0 (= 1.05 fm)$ is the radius parameter and $\beta_p (= 0.68 fm)$ is a

thickness parameter for NN collision. Substituting these values in Eq. (2.23) an estimated average value of the impact parameter (\bar{b}) for a sample of events can be obtained. The impact parameter values for our sample and subsample of events are quoted in Table 2.5. It should be noted that in obtaining \bar{b} the rapidity distribution is replaced by the η distribution. However, at high energies they do not differ significantly from each other. The value of impact parameter obtained in this manner may not be treated as an exact one. It only gives us a rough idea about the average centrality of the event sample used. While investigating issues like dynamical fluctuation, it is imperative to restrict all other trivial sources of fluctuation originating from widely varying collision geometry or widely fluctuating no. of particles from one η bin to the other. The contribution from fluctuating geometry is marginal to our results, because a high value of average shower multiplicity and total fragmentation of the incident projectile in all events substantially restrict the range of b . The geometry dependence of the colliding system can be better understood if the sample is partitioned based on shower multiplicities. Three subsamples, almost equal in size, have been obtained in this way with the criteria, $n_s < 175$, $175 \leq n_s \leq 275$ and $n_s > 275$. For each subsample the average multiplicity of each category of tracks has been determined and quoted in Table 2.5. The η distribution for each subsample has also been obtained and fitted with the respective Gaussian functions. The fit results are also presented in Table 2.5. With increasing $\langle n_s \rangle$, a shift in η_0 towards lower value is to be noted. This probably is an outcome of more stopping of the projectiles by the target nuclei with increasing centrality. The \bar{b} values are also computed for each set of data, and included in the same Table. As expected, there is a mark decrease in \bar{b} value with increasing $\langle n_s \rangle$. The energy density in the central η region can now be estimated keeping two points in mind: (i) the sample with $n_s > 275$ has the highest centrality, and one may assume that the overlapping area (\mathcal{A}) between ^{32}S projectile and Ag/Br target is almost equal to the geometrical area of a ^{32}S nucleus; (ii) one has also to remember that the production of neutral π mesons in any high energy interaction is as abundant as either of their charged varieties. Therefore, while using Bjorken's formula $N_{ev}^{-1} (dn_s/d\eta)$ has to be replaced by,

$$N_{ev}^{-1} (dn_{all}/d\eta) = 1.5 N_{ev}^{-1} (dn_s/d\eta). \quad (2.24)$$

Keeping these two factors in mind and putting $\langle m_t \rangle = \sqrt{m^2 + \langle p_t \rangle^2} \approx 0.38$ GeV, and the proper formation time $\tau_0 = 1$ fm/c into,

$$\epsilon = \frac{\langle m_t \rangle}{\tau_0 \mathcal{A}} \left. \frac{dn_{all}}{d\eta} \right|_{\eta=\eta_0}, \quad (2.25)$$

one gets, $\epsilon \approx 1.3$ GeV/fm³. Note that even for the subsample with highest no. of produced particles, the value is equal to just about the threshold required for the onset of a QGP like state, which according to the lattice QCD calculations is \sim a few GeV/fm³ [27].

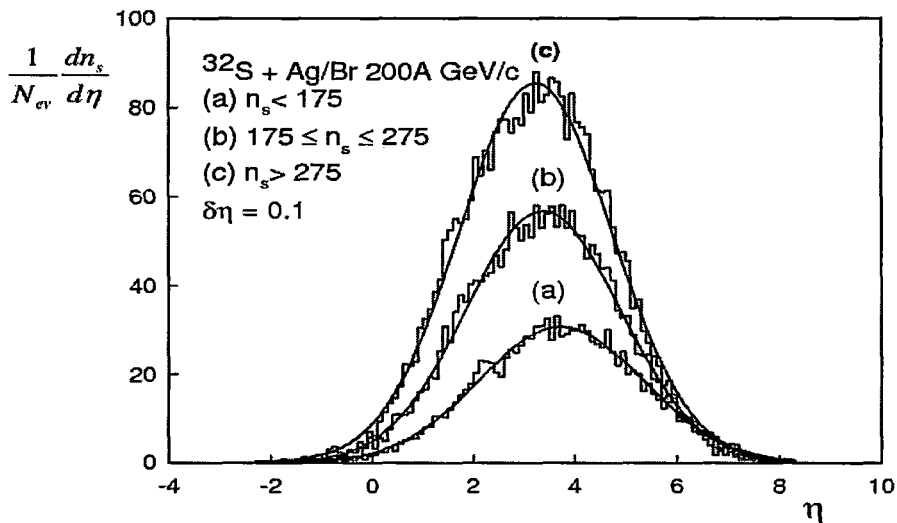


Figure 2.4: Pseudorapidity η distribution of shower tracks when the entire event sample has been divided into three subsamples.

As mentioned earlier, the experimental results have also been compared with those obtained by analyzing events generated with the computer code FRITIOF based on Lund Monte Carlo model [28] for high energy AB interactions. The model assumes that, as two nucleons collide with each other particle production takes place through the creation of longitudinally excited strings between the constituents of the same nucleon. The strings subsequently fragment, and new hadrons originate. An AB collision is considered to be a combination of multiple collisions between the nucleons belonging to one nucleus with those of the other. A large sample (7×10^4) of ^{32}S -emulsion events has been generated

using the Lund Monte Carlo Code FRITIOF, where the proportional abundance of different categories of target nuclei present in the emulsion material (Table 2.2) has been taken into account.

Table 2.5 Gross features of the ^{32}S -Ag/Br data sample. Standard errors are quoted within first brackets.

Event sample	No. of events	$\langle n_s \rangle$	$\langle n_g \rangle$	$\langle n_b \rangle$	η_0	ρ_0	σ_η	\bar{b} fm
All	200	217.79 (6.16)	4.66 (0.23)	8.99 (0.35)	3.37 (0.008)	56.34 (0.26)	1.55 (0.008)	3.77
$n_s < 175$	71	123.24 (3.83)	2.75 (0.35)	6.31 (0.68)	3.72 (0.01)	30.69 (0.21)	1.62 (0.01)	5.34
$175 \leq n_s \leq 275$	65	215.35 (3.77)	6.02 (0.97)	11.82 (0.96)	3.37 (0.01)	56.71 (0.34)	1.53 (0.01)	3.75
$n_s > 275$	64	319.94 (3.88)	6.31 (0.36)	9.92 (0.48)	3.23 (0.01)	85.44 (0.52)	1.51 (0.01)	2.10

From the generated sample a ^{32}S -Ag/Br subsample has been so filtered out that it has the same multiplicity distribution of produced particles as the corresponding shower track multiplicity distribution of the experimental data set. The size of generated event sample is ten times as large as the experimental one. Event samples have also been simulated by generating (pseudo) random numbers. In this case the phase space variables associated with each shower track (η , φ) have been replaced by a pair random numbers. The sample size is once again ten times the size of the experimental one, and the shower multiplicity distribution is same as the experimental one. While generating the random numbers, independent emission of particles has been assumed with no correlation whatsoever between these particles being produced.

Bibliography

- [1] M. Reingamum, *Z. Physik.* **12**, 1076 (1911).
- [2] A. Beiser, *Rev. Mod. Phys.* **24**, 273 (1952).
- [3] C. F. Powell, P. H. Fowler, and D. H. Perkins, *The Study of Elementary Particles by Photographic Method* (Pergamon, Oxford), NY (1959).
- [4] W. H. Barkas, *Nuclear Research Emulsions, Vol. I and II* (Academic Press, New York 1963).
- [5] R. W. Gurney and N. F. Mott, *Proc. Roy. Soc. (London)* **A164**, 151 (1938).
- [6] J. W. Mitchell, *Phil. Mag.* **40**, 249 (1949); *ibid*, **40**, 667 (1949).
- [7] C. C. Dilworth, G. P. S. Occhialini, and R. M. Payne, *Nature* **163**, 102 (1948).
- [8] M. Blau and J. A. De Felice, *Phys. Rev.* **74**, 1198 (1948).
- [9] Ilford Fact Sheet, <http://www.illfordphoto.com> (2005).
- [10] M. S. Livingstone and H. A. Bethe, *Rev. Mod. Phys.* **9**, 245 (1937).
- [11] M. Blau, *Phys. Rev.* **75**, 279 (1949)
M. Morand and L. van Rossum, *Fundamental Mechanisms of Photographic Sensitivity*, ed. J. W. Mitchell, (Butterworths Scientific Publications, London, 1951).
- [12] C. O'Ceallaigh, *Nuov. Cim. Suppl.* **12**, 412 (1954).
- [13] P. H. Fowler and D. H. Perkins, *Phil. Mag.* **46**, 587 (1955).
- [14] M. A. Bloomer, H. H. Heckman, and Y. J. Karant, *Nucl. Instrum. Methods* **215**, 247 (1983).

- [15] N. F. Mott, *Proc. Roy. Soc. (London)* **124**, 425 (1929)
 B. Rossi, *High Energy Particles* (Prentice Hall, Englewood Cliffs, New Jersey, 1952).
- [16] C. M. G. Lattes, G. P. S. Occhialini and C. F. Powell, *Proc. Phys. Soc. (London)* **61**, 173 (1948).
- [17] P. Freier, E. J. Lofgren, E. P. Ney, and F. Oppenheimer, *Phys. Rev.* **74**, 1818 (1948).
- [18] M. R. Spiegel *Theory and Problems of Statistics*, (McGraw-Hill Book Co., UK, 1988).
- [19] E. J. Williams, *Phys. Rev.* **58**, 292 (1940).
- [20] P. H. Fowler, *Phil. Mag.* **41**, 169 (1950).
- [21] I. Otterlund, *3rd Hellenic School on Elementary Particle Physics*, (Corfu, Greece, 1989)
 S. Garpman *et al.*, *Nucl. Instrum. Methods* **A269**, 134 (1988).
- [22] G. Singh, K. Sengupta and P. L. Jain, *Phys. Rev. Lett.* **61**, 1073 (1988)
 P. L. Jain, K. Sengupta and G. Singh, *Phys. Rev. C* **44**, 844 (1991).
- [23] G. Singh, K. Sengupta and P. L. Jain, *Phys. Rev.* **41**, 999 (1990).
- [24] G. D. Westfall *et al.*, *Phys. Rev. C* **19**, 1309 (1979).
- [25] C. Wong, *Introduction to High-Energy Heavy-ion Collisions*, (World Scientific, Singapore, 1994).
- [26] M.J. Tannenbaum, *Quark-Gluon Plasma* eds. B. Sinha, S. Paul and S. Raha, (Springer Verlag, Berlin, 1990).
- [27] F. Karsch, *Proceedings of Quark Matter '01 Conference*, (Stony Brook, USA, 2001),
Nucl. Phys. A **698**, 199c (2002).
- [28] B. Andersson, G. Gustafsson, and B. Nilsson-Almqvist, *Nucl. Phys.* **B281**, 289 (1987)
 B. Nilsson-Almqvist and E. Stenlund, *Comp. Phys. Commun.* **43**, 387 (1987).

Chapter 3

Intermittency in $^{32}\text{S-Ag/Br}$ interaction at 200A GeV/c

The nature of dynamical fluctuation in the density distribution of singly charged particles produced in $^{32}\text{S-Ag/Br}$ interactions at an incident momentum of 200A GeV/c, has been investigated. The data were collected with the help of nuclear photographic emulsion technique. Different statistical methods of multiplicity moments have been used to analyze this data in terms of the intermittency and fractal properties. The analysis have been performed both in one and two dimensional phase-space distributions. Wherever possible, our experimental results have been compared with the results obtained in similar other heavy-ion induced experiments, as well as with those obtained from simulated events. The investigation shows presence of weak intermittency in one dimension (1-d), which is consistent with self-similarity of the fluctuations. In two dimension (2-d), a kind of anisotropy in the distributions between longitudinal and transverse phase-space variables has been observed. This indicates that, self-affinity rather than self-similarity in the distributions, is responsible for the observed anisotropic behavior. From the analysis of the factorial correlators and oscillatory multiplicity moments, presence of a few particle short ranged correlation has also been established. In almost all cases, the simulated interactions failed to replicate the experimental results.

3.1 Introduction

The single particle phase-space distribution of charged particles produced in a high-energy interaction exhibits rapid fluctuations that contain spikes as well as dips. Such fluctuations have two different origins. One comes from the statistical noise due to finite multiplicity of particles in an event, and the other comes from some nontrivial dynamical reason that can not be directly measured in an experiment. When the density function is averaged over an entire sample of events, the effect of statistical noise can be substantially reduced. But at the same time the dynamical part of these fluctuations is also averaged out, resulting in a smooth distribution of the final state hadrons. The method of analyzing multiparticle data underwent a paradigm shift when Bialas and Peschanski first suggested that, the particle density function should be examined locally within narrow regions of phase-space [1], and they themselves applied the technique of scaled factorial moment (SFM) on the now famous JACEE events induced by ultra high-energy cosmic ray nuclei [2]. The SFMs of integer order were found to depend on the phase-space resolution obeying a power law scaling behaviour. Such a scaling behaviour of the SFM has since then been known as 'intermittency'. During last two decades or so, the topic has generated quite a significant amount of research interest within and beyond the high-energy physics community, and a whole range of new issues related to the complex process of multiparticle production have opened up. Experiments have been performed with different types of colliding particles that also involve widely varying values of collision energy. Various other methods have been proposed to identify the extent and nature of fluctuations, so that the mechanism of particle production can be understood within the framework of existing models. A large section of these techniques is based on the notion that, the density distribution of produced particles has a self-similar or fractal nature, that may have resulted due to some kind of scale invariant dynamics. Similar to the SFM, several other moments of density distribution have been found to depend on the phase-space interval size obeying different types of power laws, that indicates possibility of a fractal structure in the underlying distribution. Efforts have been made to interpret the observed scale invariance of moments of particle density distribution in terms of the random cascading model, phase transition or more conventional mechanisms like the cluster production or Bose-Einstein correlation etc. Both the experimental and phenomenological status of the subject has been compre-

hensively reviewed by De Wolf, Dremin and Kittel [3].

In this chapter we are going to present an analysis of a data set on the angular emission of singly charged secondary particles produced in central and semicentral $^{32}\text{S-Ag/Br}$ interactions at an incident momentum of 200 A GeV/c. Centered around two basic ideas of self-similarity and self-affinity of density fluctuation, the scaling behaviour of different types of multiplicity moments as functions of phase-space interval size, has been examined. As far as possible, efforts have been made to correlate the results obtained from different techniques of data analysis. For the purpose of comparison, whenever felt necessary, references of similar other heavy-ion induced experiments have been made. Results obtained by analyzing simulated $^{32}\text{S-Ag/Br}$ events at the same incident momentum and having identical multiplicity distribution as the experimental one, have been incorporated. The major objectives of the present investigation are, (i) to study the intermittency phenomenon of multiparticle production in 1-d and 2-d, (ii) to examine whether the intermittency is a result of self-similarity or self-affinity in the branching (cascading) process, (iii) to compare the experimental results with at least one of the extensively used models of particle production in high-energy AB interactions, and lastly (iv) to identify the influence of particle correlation in the observed intermittent behaviour.

3.2 Methodology and Results

As mentioned above, a high-energy AB interaction contains rapidly fluctuating particle density in different regions of phase-space, that gets smoothed out when averaged over many events. In Fig. 3.1(a) and (b) the η distribution of two high multiplicity $^{32}\text{S-Ag/Br}$ interactions at 200A GeV/c incident momentum, with interval size $\delta\eta = 0.2$ have been schematically presented. In Fig. 3.1(c) and (d) the same plots are made with a reduced interval size, $\delta\eta = 0.1$, and the extent of fluctuations drastically increases. The presence of both peaks and dips has been highlighted by drawing Gaussian fits to the data. When averaged over many events, these local fluctuations are smoothed out, as can be seen from the plot of $N_{ev}^{-1} (dn_s/d\eta)$ against η in Fig. 2.3(a). Distribution of these local densities $dn_s/d\eta$ obtained from individual events can be found in Fig. 3.2(a) and (b). These

distributions correspond only to the central particle producing region, respectively, to $\eta_0 \leq \eta < \eta_0 + 1$ and $\eta_0 - 1 < \eta \leq \eta_0$, where η_0 is the peak position of the Gaussian fit shown in Fig. 2.3(a), and the density values are obtained with $\delta\eta = 0.2$. In these diagrams $dn_s/d\eta$ values as large as ~ 150 can be observed.

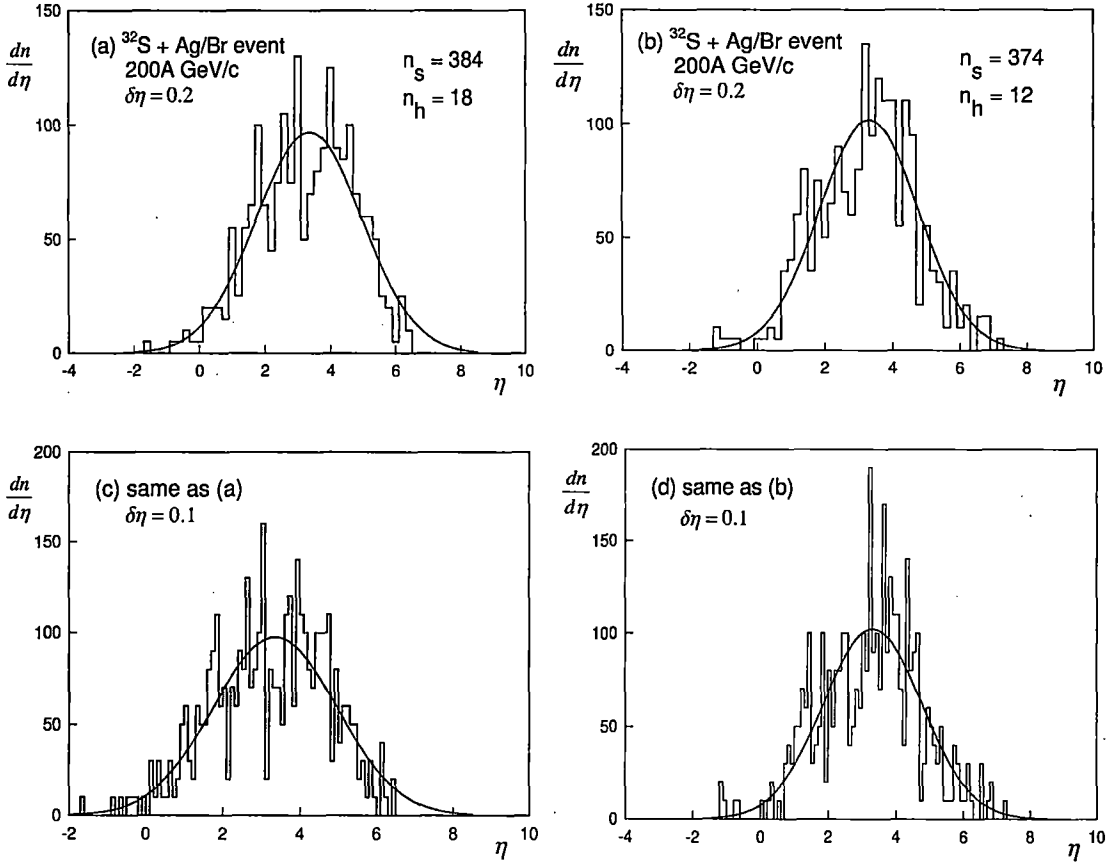


Figure 3.1: Pseudorapidity distribution of shower tracks of two high multiplicity ^{32}S -Ag/Br events. (a) and (b) with $\delta\eta = 0.2$; (c) and (d) with $\delta\eta = 0.1$. Note how the fluctuation increases with decreasing bin size. Solid curves represent Gaussian fits to the data.

Dynamical fluctuation of produced particles can be analyzed in terms of the factorial moments (f_q). The q -th order (q is a positive integer) factorial moment is defined as,

$$f_q = n_j (n_j - 1) \dots (n_j - q + 1),$$

where n_j is the particle number falling in the j th phase-space interval of an event. The entire range of phase-space say (ΔX) , has been divided into M intervals of equal size say $\delta X = \Delta X/M$. If the phase-space distribution $P(n)$ of the particle multiplicity (n) is considered as a convolution of a dynamical part $D(\xi)$ and a Poisson type statistical part,

$$P(n) = \int dt \frac{t^n e^{-t}}{n!} D(t),$$

then summing over n the event averaged factorial moment $\langle f_q \rangle$ is given by,

$$\langle f_q \rangle = \sum_q \frac{n!}{(n-q)!} P(n) = \int dt t^q D(t).$$

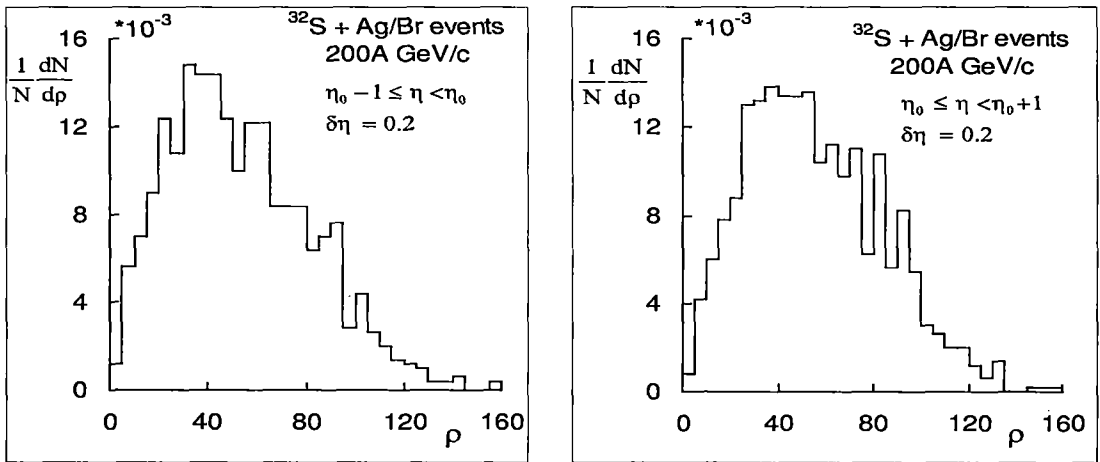


Figure 3.2: Distribution of local density of particles produced in ^{32}S -Ag/Br interactions at 200A GeV/c. The η range and size of $\delta\eta$ are shown in each diagram.

Hence one can see that the event averaged factorial moment is nothing but the simple moment of the corresponding dynamical part of the phase-space distribution, irrespective of the exact analytical form of the dynamical component. Thus $\langle f_q \rangle$ are capable of suppressing the Poisson type statistical noise, which the ordinary moments can not. This kind of noise suppression is not possible, (i) if n does not tend to ∞ , or (ii) the statistical part is not of Poisson type. Fortunately in our sample of high-energy AB collision, $n \rightarrow$ a large value, and the Poisson nature of statistical fluctuation in bin multiplicity could also be confirmed by generating random numbers. Note that bins only with $n_j \geq q$ contribute to f_q , but f_q is not sensitive to the position of the bin. However, in the case of AB collision

where average multiplicity is large, many bins contribute if the order is not too large or the bin width is not too low. Hence the bin position is not so important. f_q can not only measure large scale fluctuations, but as we shall find later, they can also provide information about the pattern of these fluctuations. The f_q values can be normalized (or scaled) by the global average multiplicity of particles ($\langle n_s \rangle$ in the present case), and such a normalized moment is called the SFM. Averaged over an event sample, the SFM of order q is denoted by $\langle F_q \rangle$ and is therefore, defined as [1],

$$\langle F_q \rangle_h = \frac{1}{N_{ev}} \sum_{i=1}^{N_{ev}} M^{q-1} \sum_{j=1}^M \frac{n_{ij}(n_{ij}-1)\dots(n_{ij}-q+1)}{\langle n_s \rangle^q}, \quad (3.1)$$

where

$$\langle n_s \rangle = \frac{1}{N_{ev}} \sum_{i=1}^{N_{ev}} n_s,$$

and n_{ij} is the number of particles falling into the j th such interval of the i th event. In the above definition of $\langle F_q \rangle_h$, the so called 'horizontal' averaging method has been adopted. The SFM defined in this way is sensitive to the shape of the single particle distribution, and it further depends on the correlation between different phase-space intervals. The problem of shape dependence can be solved either by applying the Fialkowski correction factor [5] given by,

$$R_F(q, M) = \frac{1}{M} \sum_{j=1}^M M^q \frac{\langle n_j \rangle^q}{\langle n_s \rangle^q} : \quad \langle n_j \rangle = \frac{1}{N_{ev}} \sum_{i=1}^{N_{ev}} n_{ij},$$

or by replacing the phase-space variable (say η) with a cumulative variable X_η defined as [6],

$$X_\eta = \left[\int_{\eta_{min}}^{\eta} \rho(\eta) d\eta \right] / \left[\int_{\eta_{min}}^{\eta_{max}} \rho(\eta) d\eta \right].$$

Here, $\eta_{min}(\eta_{max})$ is the minimum (maximum) value of η , and $\rho(\eta)$ is the single particle density function in terms of η . Irrespective of the basic phase-space variable from which it is derived, the X distribution is always uniform within $0 \leq X \leq 1$. Though our entire analysis on multiplicity moments will henceforth be preformed by considering X_η and/or X_φ as the phase-space variables, we shall continue to call the corresponding space either the η -space or the φ -space. The problem of correlation between different intervals can be eliminated by considering the so called 'vertical' averaging of the SFM that is locally

normalized by the average bin multiplicity. They carry information about the event space fluctuations within each interval, and are defined as,

$$\langle F_q \rangle_v = \frac{1}{M} \sum_{m=1}^M \frac{1}{N_{ev}} \sum_{i=1}^{N_{ev}} \frac{n_{ij}(n_{ij} - 1) \dots (n_{ij} - q + 1)}{\langle n_j \rangle^q}. \quad (3.2)$$

In case of particle production the term 'intermittency' is not used in the strict hydrodynamical sense from where the word has been coined, but it refers only to a scale invariance of the SFM with decreasing size of the phase-space interval δX , abiding a power law such as,

$$\langle F_q(\delta X) \rangle \propto (\delta X)^{-\phi_q} : \quad \delta X \rightarrow 0. \quad (3.3)$$

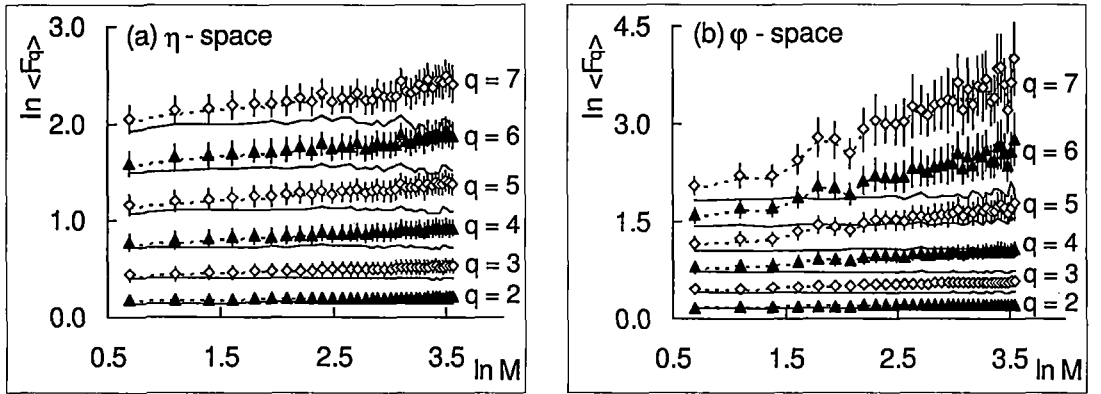


Figure 3.3: Variation of SFM of different orders with phase-space partition number. In both (a) and (b) the points represent experimental values of horizontally averaged moments, and the dotted lines are obtained by connecting the experimental values of vertically averaged moments. Whereas in (a) the solid lines are obtained by joining the FRITIOF simulated values of horizontally averaged SFM, in (b) the solid lines correspond to those obtained by generating random numbers.

In Fig. 3.3(a) our results on intermittency analysis in the η -space have been graphically plotted along with the corresponding FRITIOF predictions. The error bar associated with each experimental $\langle F_q \rangle_h$ value is merely of statistical origin. They have been estimated by assuming that F_q for each event is an error free quantity, and thus the correlation between different phase-space intervals has been ignored. The average multiplicity for the present sample of events is substantially high, and therefore, this simplification in error estimation is not going to significantly influence our results [7]. Both the horizontally and

vertically averaged SFM have been calculated with respect to the uniformly distributed cumulative variable X_η , and for any q no significant difference in the values from two different averaging methods could be seen. For all orders linear rise in $\ln \langle F_q \rangle$ values with increasing $\ln M$ as given by Eq. (3.3), can be observed in our experimental results. This trend is missing in the corresponding FRITIOF predictions. Similar plot in the φ -space can be found in Fig. 3.3(b). Due to conservation of linear momentum, particles tend to move in opposite directions in a plane transverse to the incident projectile direction. Due to this effect $\langle F_q \rangle$ values obtained for small values of partition number in the φ -space, do not follow the same linear trend as that in the large M region, where such effects of kinematic conservation laws get reduced. Therefore, in this case for each q , the first four experimental data points corresponding to the smaller values of M (< 6) have been excluded from the process of straight line fit. SFM values have also been computed by generating random numbers distributed uniformly over an interval of $(0, 1)$, and for comparison these values are incorporated in Fig. 3.3(b). As expected, the $\langle F_q \rangle$ values obtained from random numbers do not exhibit any rise. They remain more or less uniformly distributed with decreasing bin size.

The exponents ϕ_q , called intermittency indices, possess positive values, and each should be a constant for any given order q . These indices are obtained from the slopes of best fitted straight lines of $\ln \langle F_q \rangle$ vs. $\ln M$ data. For both η and φ -spaces, the experimentally obtained intermittency indices are given in Table 3.1. Values of Pearson's r^2 coefficient [8], showing goodness of linearity in the $\ln M$ dependence of $\ln \langle F_q \rangle$, are also given in Table 3.1. In almost all cases the r^2 values are close to +1, confirming the validity of the power law scaling behavior of the SFM as given in Eq. (3.3). In φ -space the intermittency indexes are consistently higher than those in η -space, indicating that in our case intermittency analysis is not independent of the phase-space variable considered. At this point it should be mentioned that, for a given order the data points in Fig. 3.3 are highly correlated, because the SFM are computed for the same sample of events with differing bin size. The error estimation of ϕ_q is therefore, an extremely different task. For this purpose we have adopted the method of simulating several independent event samples, each of same size and having identical multiplicity distribution as the experimental one, and have obtained ϕ_q for each such sample [9]. The errors associated with the ϕ_q values

shown in Table 3.1 are nothing but the standard deviation of different ϕ_q values obtained from ten such independently simulated event samples,

$$\sigma(\phi_q) = \sqrt{\langle \phi_q^2 \rangle - \langle \phi_q \rangle^2},$$

where $\langle \rangle$ indicates averaging over the number of event samples generated. The FRITIOF code has been used for the η -space, whereas random numbers have been used for the φ -space. As neither the FRITIOF nor the random number generated samples can account for the dynamical intermittency effect, the errors evaluated through this indirect method are obviously underestimated.

Table 3.1 Intermittency indices for experimental and simulated data sets along with Pearson's r^2 values indicating the goodness of fit.

Order	η - space		φ - space	
	ϕ_q	r^2	ϕ_q	r^2
q=2	0.013 \pm 0.003	0.982	0.014 \pm 0.0006	0.967
q=3	0.032 \pm 0.003	0.977	0.044 \pm 0.002	0.972
q=4	0.056 \pm 0.007	0.961	0.099 \pm 0.005	0.967
q=5	0.082 \pm 0.013	0.937	0.201 \pm 0.011	0.946
q=6	0.112 \pm 0.021	0.905	0.371 \pm 0.021	0.915
q=7	0.138 \pm 0.033	0.865	0.607 \pm 0.039	0.888

Due to intermixing of many sources of particle production, the intermittency indexes ϕ_q in $^{32}\text{S-Ag/Br}$ interactions at 200A GeV/c are smaller than those in the leptonic [10] and hadronic collisions [7] at comparable energies, but they are comparable to similar AB experiments [11]. To examine whether or not the observed intermittency effect is exclusively a result of the contribution from lower order correlation functions, the normalized exponents

$$\zeta_q = \phi_q / \binom{q}{2}, \quad (3.4)$$

with $q \geq 2$ are evaluated. True three particle correlation in terms of these normalized slopes can be written as,

$$\zeta_q^{(3)} = (q-2)\zeta_3 - (q-3)\zeta_2. \quad (3.5)$$

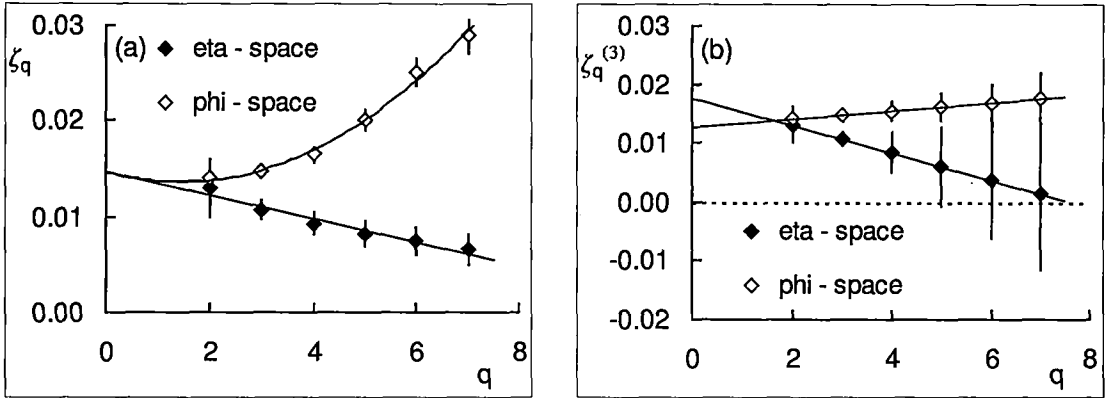


Figure 3.4: Normalized intermittency exponents plotted against q for the experimental data. The straight lines and the quadratic curve are best fit to data.

Variation of both types of experimentally obtained normalized exponents against q are graphically represented in Fig. 3.4(a) and (b), respectively for η -space and φ -space. A linear variation of ζ_q with q can be observed for the η -space, whereas, in the φ -space the behavior is not linear. In neither case normalized slopes are independent of q . The difference in behaviour in η and φ -spaces can also be seen from the variation of $\zeta_q^{(3)}$ with q , while one decreases with q , the other increases. From this analysis it can not be unambiguously concluded that all correlations for $q \geq 4$, particularly in the φ -space, can be explained only in terms of two and three-particle correlations.

The order (q) dependence of intermittency index ϕ_q can be further used to look into different probable mechanisms of particle production. It has been pointed out that, intermittency as scale invariance of SFM may be observed either due to a branching process, or due to some kind of phase transition [12]. Whereas, multiplicative cascade models based on the branching process exhibit a multifractal structure, a second order phase transition as another possible mechanism of particle production, will lead to monofractal pattern in the fluctuation of final state particles. Multifractality, as a possible reason for intermittency, is connected to an infinite number of anomalous dimensions $d_q (= D - D_q)$, which are again directly related to the intermittency indexes ϕ_q as,

$$d_q = \phi_q / (q - 1). \quad (3.6)$$

Here D_q is the generalized q th order Renyi dimension, and D is the ordinary topological dimension of the space into which the fractal objects are embedded. For a self-similar

cascade mechanism the probability density distribution is obtained by using the Levy stable law, that is characterized by a Levy stability index μ considered to be a measure of the degree of multifractality. Under the Levy-law approximation [14], the ratio of anomalous dimensions is expected to follow a relation like,

$$\frac{d_q}{d_2} = \frac{1}{2^\mu - 2} \frac{(q^\mu - q)}{(q - 1)}. \quad (3.7)$$

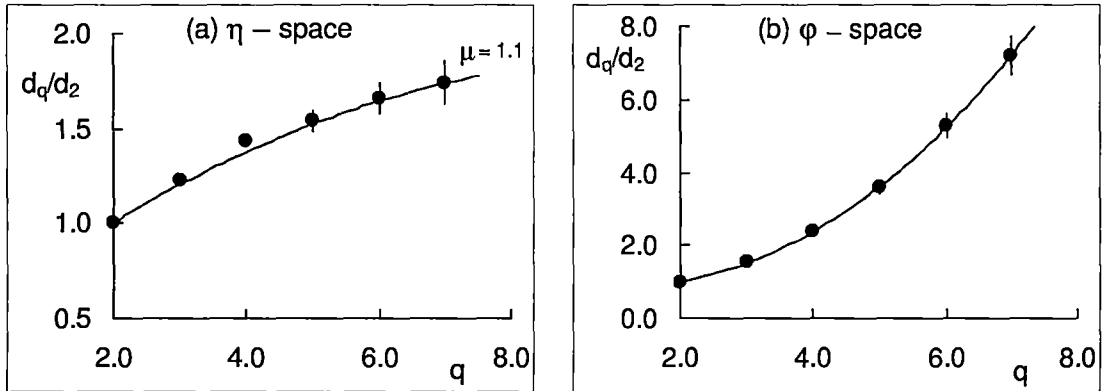


Figure 3.5: (a) Plot of $\frac{d_q}{d_2}$ against q in η -space. The solid line represents corresponding values of $\frac{d_q}{d_2}$ obtained from Eq. (3.7) with $\mu = 1.1$. (b) Plot of $\frac{d_q}{d_2}$ against q in φ -space. The solid line has been drawn just to guide the eye.

In Fig. 3.5 our results on the anomalous dimensions obtained from intermittency analysis have been graphically shown. Whereas, in η -space the ratio d_q/d_2 slowly increases with q , the same in φ -space clearly exhibits a quadratic increase. The behaviour of anomalous dimensions in φ -space is not in conformity with the prediction of Levy-law. Therefore, the Levy index is obtained only for the η -space and it came out to be $\mu = 1.1$. This value is less than a previously obtained value ($\mu = 1.6$) in high-energy pA and heavy-ion interaction [12], but is still within the limit allowed by the Levy-law $0 \leq \mu \leq 2$, and is indicative of a wild singularity in the multifractal structure. The spiky structure of density distribution of particles can be also examined with the help of a set of bunching parameters [13]. In this approach, higher order bunching parameters can be expressed in terms of the lower order parameters, resulting in a linear expression like,

$$d_q = d_2 (1 - r) + \frac{q}{2} d_2 r. \quad (3.8)$$

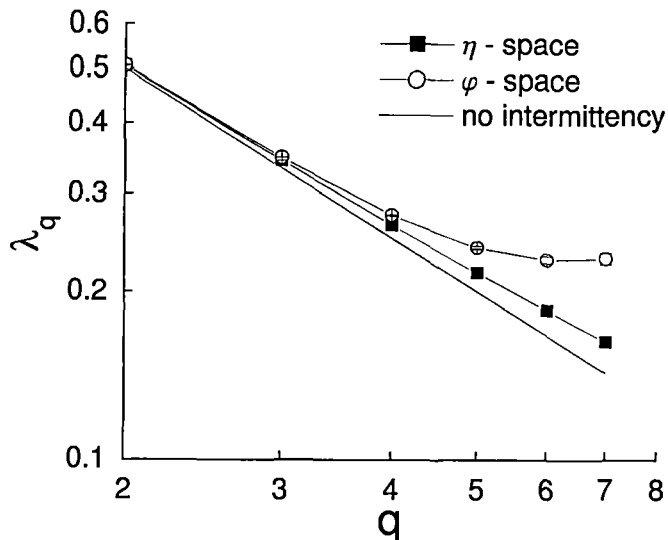


Figure 3.6: Plot of λ_q against q . The no-intermittency line corresponding to $\phi_q = 0$ has also been shown.

A nonzero value of the slope r implies a multifractal behaviour, and in η -space it came out to be $r = 0.383 \pm 0.015$. Note that if $\mu = 0$, $d_q = d_2$, and the multifractal behaviour reduces to a monofractal behaviour. It has been mentioned earlier that, such a condition would have indicated in favour of a possible phase transition, which the intermittency analysis of present set of heavy-ion data does not. It is probably still worthwhile to give a closer look into this aspect and examine different possibilities for the observed intermittency. On the basis of the Ginzburg-Landau (GL) theory it has been predicted that [15], a thermal phase transition may be a reason for intermittency, where a universal parameter ν describes the variation of d_q as,

$$\frac{d_q}{d_2} = (q - 1)^{(\nu-1)}. \quad (3.9)$$

In the present case it has been found that, $\nu = 1.327 \pm 0.009$ for the η -space. In comparison with other heavy-ion results, within statistical errors ν in the present experiment is closer to the universal value $\nu = 1.304$, as it should be for all systems describable by the GL theory [3]. However, because d_q values are obtained from ϕ_q , and the errors in ϕ_q are underestimated as they do not contain any contribution from the dynamical fluctuation, therefore, one should be extra cautious while trying to draw any conclusion about the

underlying physical process. Occurrence of a nonthermal phase transition is another possibility, where intermittency can be observed as a result of a parton-shower cascading process, and different phases can coexist if the function,

$$\lambda_q = \frac{\phi_q + 1}{q}, \quad (3.10)$$

exhibit a minimum at a certain critical value $\lambda_q = \lambda_c$ [16]. Behaviour of λ_q as a function of q has been presented in Fig. 3.6, where no such minimum can be observed. Small deviations of experimental results from the 'no intermittency' line ($\phi_q = 0$) indicate only a presence of weak intermittency in the one dimensional analysis of our data. It may be noted however, that the deviation is larger in φ -space than in the η -space.

3.2.1 Intermittency in 2-d

In 1-d the intermittency effect has not been found to be very prominent. The SFM technique can therefore be extended to the two dimensional ($\eta - \varphi$) plane, to examine whether or not the so called 'projection effect' is responsible for the observed weak intermittency in 1-d. The entire range of each cumulant variable $0 \leq X_\eta, (X_\varphi) \leq 1$, has been partitioned into M_1 intervals of equal size, resulting in a total of $M = (M_1)^2$ such intervals of the 2-d plane. Making use of Eq. (3.1) the SFM are now evaluated. In Fig. 3.7 these 2-d moments have been plotted against the partition number M . The variation of $\ln \langle F_q \rangle$ in 2-d is clearly not linear over the entire range of $\ln M$. For each q an upward bending in the variation of $\ln \langle F_q \rangle$ with $\ln M$ can be seen. For $q = 4$ and 5 probably due to finite shower multiplicity, one can see saturation effects in large $\ln M$ region. In 2-d partition most of the events do not contribute to F_6 or F_7 . Therefore, these moments have not been calculated. Obtaining ϕ_q from such nonlinear dependence does not carry any meaning, as the value will depend on the region where the linear fit has been performed. However, within a restricted $\ln M$ region (for $400 \geq M \geq 64$), linear fit of the data has resulted in the following indexes, $\phi_2^2 = 0.075 \pm 0.003$, $\chi^2(dof) = 0.17(11)$; $\phi_3^2 = 0.384 \pm 0.038$, $\chi^2(dof) = 0.79(11)$; $\phi_4^2 = 1.03 \pm 0.17$, $\chi^2(dof) = 2.27(11)$; $\phi_5^2 = 1.56 \pm 0.29$, $\chi^2(dof) = 4.48(11)$. The superscript 2 associated with each ϕ_q denotes the dimensionality of phase-space. The ratio of 2-d and 1-d intermittency exponents for $q = 2$ is, $\phi_2^2/\phi_2 \approx 6$, which is consistent with the previously obtained results from similar heavy-ion experiments [11]. On the other hand,

in contrast to the finding of [11], the ratio ϕ_q/ϕ_2 in the present case is not found to be a dimension independent quantity.

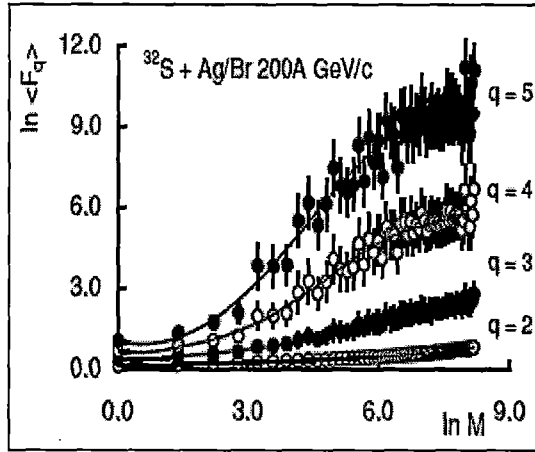


Figure 3.7: Plot of 2-d SFM of different order against phase-space partition number. The lines are drawn to guide the eye.

The issue of electron pairs produced through γ -conversion or otherwise, as being responsible for the observed intermittency effect has been addressed by the EMU01 collaboration. In a 1-d intermittency analysis of ^{32}S -Emulsion data they have found that, the contribution of electron pairs do not significantly influence the observed intermittency effects, whereas in 2-d their intermittency signal is hidden in the background from γ -conversion [9]. Most of the electron pair tracks in EMU01 experiment with vertically irradiated emulsion films have originated from their Au-foil targets. We would like to mention that in the present case, Ag ($Z = 47$) or Br ($Z = 37$) nuclei have the highest atomic no. among the target nuclei. Even their Z -values are smaller than Au ($Z = 79$). Therefore, the rate of γ -conversion, which is a function of Z^2 , would be considerably smaller in our case. Moreover, the electron pair tracks produced through γ -conversion, emanate not from the interaction vertex, but are produced at a distance from the vertex after traveling through certain radiation lengths. While scanning horizontally exposed plates, with experienced eye such tracks can be distinguished from the tracks coming out of the point of interaction, and have therefore, been excluded from our consideration of shower tracks. Such a process of filtering out electron pair tracks is difficult in horizontally exposed emulsion

films. It would not be improper to mention that, as observed in a different occasion by the same collaboration [21], the nuclear effects on intermittency can certainly be a topic of investigation, irrespective of their physical origin.

It has been argued that [17], multiparticle production in high-energy interactions is an anisotropic process. Whereas, the longitudinal momenta can vary over a wide range, the transverse momenta are limited within a short range of values with a universal average of $\langle p_t \rangle \approx 0.35 \text{ GeV}/c$ only. The observed nonlinearity in the 2-d analysis of SFM is a result of this asymmetry. If a QGP like state is formed in an AB collision, their will not be any elementary NN collision, and the entire AB system will thermalize to melt into a unique system. Under such a situation upward bending of the 2-d SFM may not be observed. But under ordinary circumstances, an AB collision can be looked upon as a superposition of many elementary NN collisions, η centers of which are generally distributed over the η -axis. When the entire η range $\Delta\eta(= \eta_{max} - \eta_{min})$ of each NN interaction is divided into M equal partitions, the effective bin size for the AB process actually becomes $< \Delta\eta/M$. Because of the restriction $0 \leq \varphi \leq 2\pi$ the situation in φ -space is different. Hence the usual practice of dividing a 2-d anisotropic phase-space into subcells of equal size, a method compatible to the self-similar fractal property, will not result into same scaling behaviour of the SFM in the longitudinal (η) as well as in the transverse (φ) directions [18]. When the pattern of fluctuations scale in different ways in different directions of phase-space, it is a characteristic of a self-affine fractal, rather than a self-similar one. This kind of self-affinity in nonstatistical fluctuation can be investigated by shrinking the phase-space interval size in two anisotropic independent directions in different ways, e.g.,

$$\begin{aligned} M_\varphi = M_\eta^H : \quad M_\eta = 2, 3, \dots, 60; \quad H < 1.0 \\ M_\eta = M_\varphi^{(1/H)} : \quad M_\varphi = 2, 3, \dots, 60; \quad H > 1.0. \end{aligned} \quad (3.11)$$

Here M_η (M_φ) is the partition number of the η (φ) space. The new parameter H is called the Hurst exponent, and it is a measure of the self-affine property of the fractal structure. Eq. (3.11) suggests that for $H < 1.0$ the η -space is partitioned into finer intervals, whereas, for $H > 1.0$ the φ -space is partitioned into finer intervals. Obviously if one sets $M_\eta = M_\varphi = M$, the 2-d phase-space is shrunk self-similarly. It is also obvious that, both M_η and M_φ can not be integers, and at least one of them is only a positive real number, say $M = N + a$, where N is an integer and $0 \leq a < 1$. As any one of the 1-d

space is divided into M cells of width $\delta X = 1/M$, N such cells and a smaller one of width a/M are obtained. Replacing M by N in Eq. (3.1) and ignoring the contribution of the smaller cell that is positioned either in front of or after these N cells, one can obtain the SFM in a similar manner as has been done before.

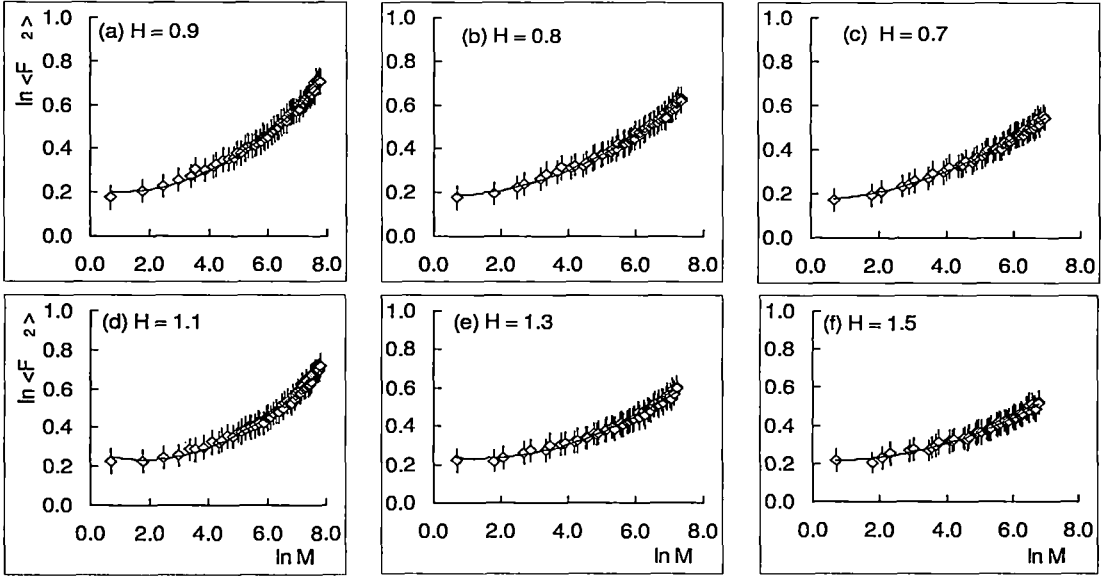


Figure 3.8: Plot of anomalous SFM of order 2 against phase-space partition number in 2-d. The lines represent best fitted quadratic function $f(\xi) = a\xi^2 + b\xi + c$ of the data.

How the self-affine SFM of second order for different values of H depends on M , has been graphically shown in Fig. 3.8. Whereas Fig. 3.8(a) to 3.8(c) correspond to real M_φ and integer M_η i.e., $H < 1.0$, Fig. 3.8(d) to 3.8(f) correspond to the $H > 1.0$ case. In each case, experimental points are fitted with a quadratic function like $f(\xi) = a\xi^2 + b\xi + c$, and the values of the fit parameters along with the $\chi^2(dof)$ values showing goodness of fit are presented in Table 3.2. From Fig. 3.8 as well as from the parameter values given in Table 3.2, one can see that, as H deviates more and more from unity, the non-linearity slowly disappears straightening out the $\ln M$ dependence of $\ln \langle F_2 \rangle$. As H becomes substantially different from unity ($H \approx 0.5$), growing discontinuities in the variation of self-affine $\langle F_2 \rangle$ are observed. In a similar heavy-ion induced experiment [21] anomalous scaling of SFM was better observed in finer resolutions of η -space than in the φ -space. In

contrast to that, in the present case no such preference of any of the phase-space variables over the other can be established. However, the analysis confirms anisotropy between the distributions of produced particles along the longitudinal variable (η) and the transverse one (φ).

Table 3.2 Values of fit parameters of experimental anomalous moments of $q = 2$ with a quadratic function $f(\xi) = a\xi^2 + b\xi + c$, along with the χ^2 and number of degrees of freedom showing goodness of fit.

Value of Hurst exponent	Value of a	Value of b	χ^2 (d.o.f)
H = 0.6	0.0058 ± 0.00048	0.0107 ± 0.0041	1.893 (57)
H = 0.7	0.0069 ± 0.00042	0.0062 ± 0.0038	1.349 (57)
H = 0.8	0.0089 ± 0.00046	$- 0.0071 \pm 0.0044$	2.055 (57)
H = 0.9	0.0108 ± 0.00052	$- 0.0224 \pm 0.0053$	3.259 (57)
H = 1.1	0.0131 ± 0.00057	$- 0.0487 \pm 0.0059$	3.514 (57)
H = 1.2	0.0116 ± 0.00058	$- 0.0377 \pm 0.0057$	2.797 (57)
H = 1.3	0.0098 ± 0.00052	$- 0.0249 \pm 0.0049$	1.947 (57)
H = 1.4	0.0092 ± 0.00057	$- 0.0199 \pm 0.0052$	1.996 (57)
H = 1.5	0.0076 ± 0.00052	$- 0.0088 \pm 0.0046$	1.501 (57)

It should be pointed out that, the methodology to examine self-affinity in phase-space structure, as described in [19] is based on the assumption that, both the probability density and the dynamical fluctuation are uniformly distributed in phase-space. Nonuniformity in either of these distributions may lead to a discontinuity in the variation of the self-affine SFM [20]. Making use of the cumulant variables (X_η, X_φ) the first condition could be achieved in the present case, whereas, the second one could not be achieved as the frequency distributions of the SFM values are nonuniform. Therefore, it can influence our result. Necessary corrective measure as suggested in the case of NA22 results [20], has been employed for $q = 2$ by introducing a correction factor $R(x)$ as,

$$F_2 = \frac{1}{R(x)} \frac{1}{N_{ev}} \sum_{i=1}^{N_{ev}} \frac{1}{N} \sum_{j=1}^N \frac{n_{ij}(n_{ij} - 1)}{\langle n \rangle^2}. \quad (3.12)$$

Here $\langle n \rangle$ is calculated by excluding the contribution of the bin of width a/M . With two integers N' and M' , a correction matrix is then introduced as the ratio of the SFM averaged only over N'/M' part of the entire 2-d space,

$$C(N', M') = \frac{\frac{1}{N_{ev}} \sum_{i=1}^{N_{ev}} \frac{1}{N'} \sum_{j=1}^{N'} \frac{n_{ij}(n_{ij}-1)}{\langle n \rangle^2}}{\frac{1}{N_{ev}} \sum_{i=1}^{N_{ev}} \frac{1}{M'} \sum_{j=1}^{M'} \frac{n_{ij}(n_{ij}-1)}{\langle n \rangle^2}}. \quad (3.13)$$

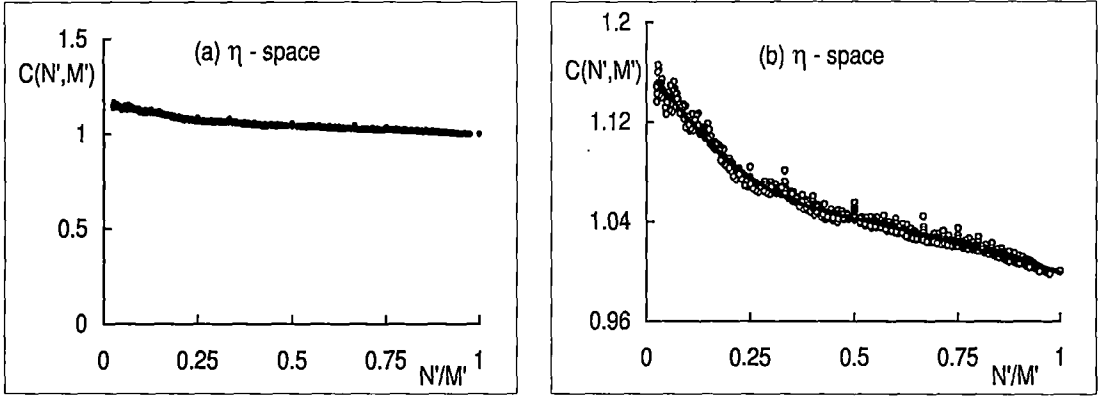


Figure 3.9: Plot of correction factor $C(N', M')$ as a function of N'/M' . Notice the change in scale in two diagrams. Solid curve in (b) represents interpolated polynomial fit.

A plot of this correction matrix for noninteger partition of η -space has been shown in Fig. 3.9. In Fig. 3.9(a) the scale along the abscissa is considerably shrunk and the variation appears as almost linear with a small ($-$)ve gradient. When the same plot is made with an enlarged scale one gets an actual feeling of how nonlinear is the change of $C(N', M')$ with N'/M' . $C(N', M')$ is then supposed to be approximately equal to $R(x)$ if the integers N' and M' are chosen in such a way that,

$$\frac{N'}{M'} \approx \frac{N}{M} = x. \quad (3.14)$$

The factor $R(x) = R(N/M)$ is thereafter, obtained with the help of a polynomial (degree 6) interpolation of the variation of $C(N', M')$ against N'/M' . The solid curve shown in Fig. 3.9(b) represents this polynomial fit of the data. In Fig. 3.10 plots of self-affine SFM $\ln \langle F_2 \rangle$ at $H = 0.5$ have been shown both before and after making use of the correction factor $R(x)$. Standard errors are associated with the uncorrected data points.

Unfortunately, as one can see from Fig. 3.10 the technique [20] has been found to be inadequate to remove the discontinuities in the variation of $\ln \langle F_2 \rangle$.

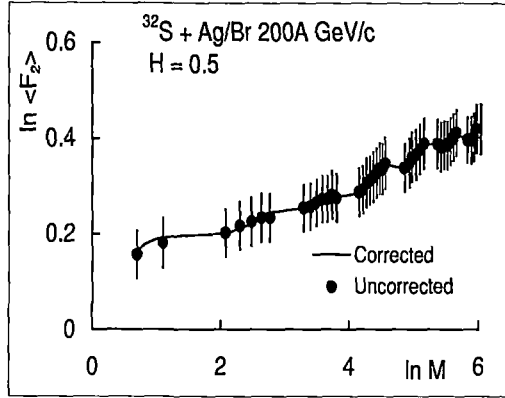


Figure 3.10: Plot of anomalous $\ln \langle F_2 \rangle$ against phase-space partition number in 2-d for $H = 0.5$. Solid circles represent uncorrected values, and the continuous curve has been drawn by joining the corresponding corrected values.

3.2.2 Factorial Correlators

Dynamics of particle production beyond that obtained from the single particle inclusive spectra, can be investigated by studying the correlation effects. Whereas, the SFM can be used as a measure of local density fluctuations, the two-fold factorial moments or the factorial correlators [1] denoted by F_{pq} , can extract additional information on the bin to bin correlation between these fluctuations within an event [9, 22]. The factorial correlators are calculated for each combination of nonoverlapping pair of bins (jj') separated by a fixed distance D . For the sake of statistics they are then averaged over all such combinations of bins. The correlators are defined as,

$$\tilde{F}_{pq} = \frac{\langle n_j^{[p]} n_{j'}^{[q]} \rangle}{\tilde{F}_p \tilde{F}_q}. \quad (3.15)$$

Here, $n_j^{[q]} = n_j(n_j - 1) \dots (n_j - q + 1)$, $\tilde{F}_q = \langle n_j^{[q]} \rangle$, and $n_j(n_{j'})$ is the number of particles in the $j(j')$ th bin. As $p \neq q$, \tilde{F}_{pq} as defined in Eq. (3.15) is not symmetric. They are therefore, symmetrized as

$$\langle F_{pq} \rangle = (\tilde{F}_{pq} + \tilde{F}_{qp})/2. \quad (3.16)$$

According to a simple intermittency model (α -model) [1], F_{pq} should depend on the correlation distance D but not on the interval size δX_η say, and should follow a power law like,

$$\langle F_{pq} \rangle \propto (\Delta X_\eta / D)^{\phi_{pq}}, \quad (3.17)$$

as $1/D$ approaches a large value.

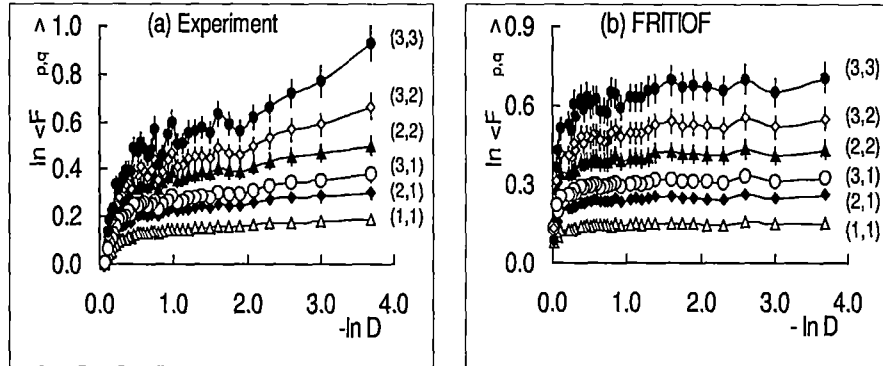


Figure 3.11: Plot showing dependence of factorial correlators of different ordered against correlation length. Points represent experimental values in η -space. In each case only the last six points have been used to fit straight lines to data and obtain the exponents. The lines are drawn to guide the eye.

In Fig. 3.11 the experimental results as well as the FRITIOF simulated results on F_{pq} in η -space, have been graphically presented for several different combinations of p and q . For each such combination the experimental points show that, as $-\ln D$ increases, there is a rapidly growing correlation at the beginning of the curve, a saturation next, and again a moderate linear rise at the end. On the other hand for the simulated event sample, with increasing $-\ln D$ hardly any variation in the values of $\ln F_{pq}$ can be found. The variation of experimental $\ln F_{pq}$ with $-\ln D$ is not linear, and the exponents ϕ_{pq} have been obtained by fitting straight lines to the data only in the large $-\ln D$ region, a region that corresponds to short range correlation. The values of ϕ_{pq} and r^2 have been incorporated in Table 3.3 for the experiment as well as for the FRITIOF simulated data. Negligibly small values of ϕ_{pq} for the simulated data shows that, the model can not reproduce the experimentally observed correlations. According to the α -model and the

log-normal approximation, the exponents should follow a relation like,

$$\phi_{pq} = \phi_{p+q} - \phi_p - \phi_q = pq \phi_{11}. \quad (3.18)$$

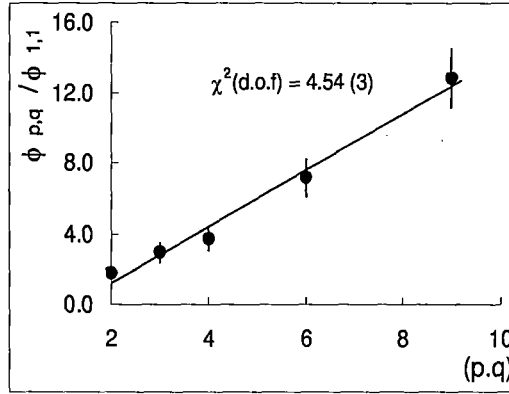


Figure 3.12: Plot of $\phi_{p,q}/\phi_{1,1}$ against $(p \cdot q)$ in η -space according to the predictions of α -model. The solid line is the best fitted straight line to the experimental values.

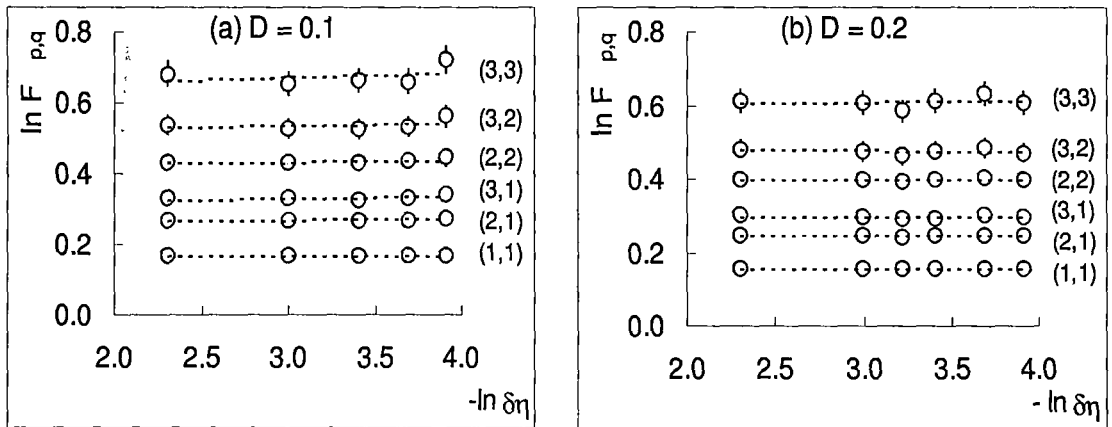


Figure 3.13: Plot showing independence of factorial correlators with respect to phase-space partition size δX_η at fixed D . The dashed lines are best fitted straight lines to the data.

The values of ϕ_{pq}/ϕ_{11} should therefore, linearly rise with the product $(p \cdot q)$. Such a plot has been given in Fig. 3.12 for the experimentally obtained values only. Another

prediction of the α -model is that, for a fixed D the correlators should be independent of δX . This aspect can be verified from Fig. 3.13, where graphical plot of $\ln F_{pq}$ for several different values of δX_η and at a fixed $D(= 0.1, \text{ and } 0.2)$, have been shown both for the experiment and for the FRITIOF. Within errors the δX_η independence of F_{pq} has been established. It has to be mentioned that, such a property does not only hold for the α -model, but is a feature of any model that takes short range correlation into consideration [23]. Overall, the study shows presence of short range correlation in our heavy-ion data, and gross features of the experimental observations are consistent with predictions of α -model. Most of the long range correlations have probably been smeared out due to intermixing of many sources of particle production.

Table 3.3. Values of exponents of factorial correlators of different orders both for the experiment and FRITIOF simulated events, along with the Pearson's r^2 co-efficient showing goodness of linearity.

Values of (p,q)	Experiment		FRITIOF	
	$\phi_{p,q}$	r^2	$\phi_{p,q}$	r^2
(1,1)	0.0152 ± 0.0019	0.9433	0.0047 ± 0.0012	0.6589
(2,1)	0.0272 ± 0.0038	0.9270	0.0087 ± 0.0018	0.7549
(3,1)	0.0447 ± 0.0061	0.9317	0.0126 ± 0.0028	0.8202
(2,2)	0.0562 ± 0.0066	0.9477	0.0171 ± 0.0021	0.8235
(3,2)	0.1086 ± 0.0090	0.9733	0.0291 ± 0.0044	0.8459
(3,3)	0.1946 ± 0.0096	0.9904	0.0395 ± 0.0053	0.8731

3.2.3 Oscillatory Multiplicity Moments

The effect of multiparticle correlation over and above any trivial background effect can also be studied with the help of normalized factorial cumulant moments (K_q) [24]. These moments provide a measure of genuine higher order correlation beyond the lower one, and they are defined as,

$$K_q = F_q - \sum_{j=1}^{q-1} \binom{q-1}{j-1} F_{q-j} K_j, \quad j = 2, 3, \dots \quad (3.19)$$

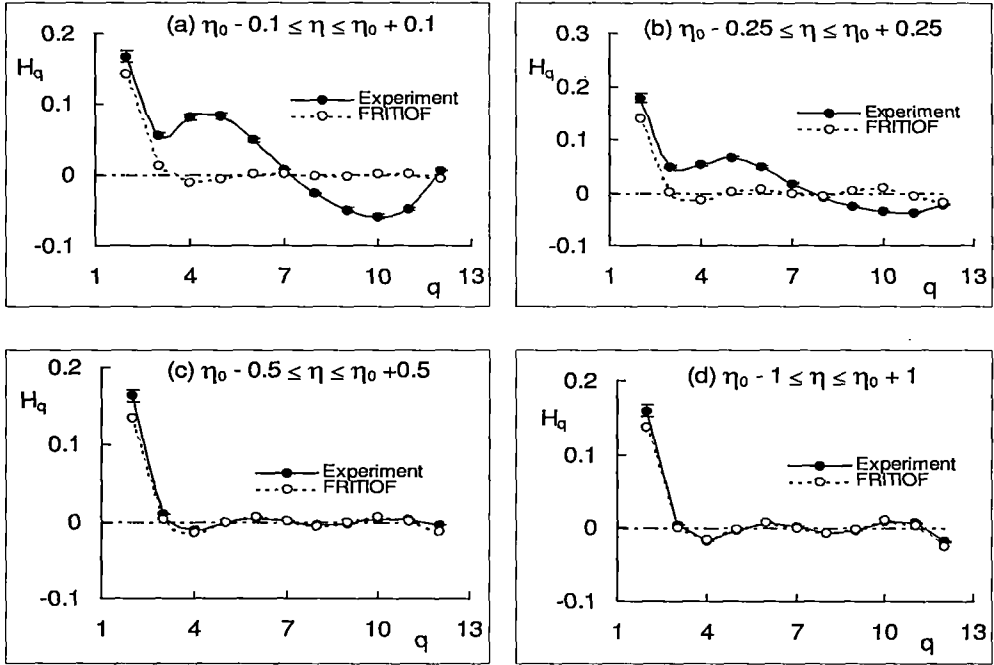


Figure 3.14: Plot of oscillatory multiplicity moments H_q against q at different η intervals indicated in the diagrams. Note how the experimental results coincide with the FRITIOF prediction with increasing η_{cut} .

For a Poisson distribution $K_1 = 1$ and $K_q = 0$ for $q > 1$. Nonzero value of K_q (for $q \geq 2$) indicates presence of two or more particle correlation in the inclusive density distribution of produced particles. It has been predicted by a parton shower cascade model based on QCD, that the K_q moments would oscillate irregularly around the zero value with increasing order q . Both F_q and K_q have strong energy and order dependence. Sometimes, a new set of normalized cumulant moments is introduced as,

$$H_q = K_q / F_q, \quad (3.20)$$

where such dependences are partially canceled. H_q reflects genuine q -particle correlation integral relative to the global correlation integral. In the cases of high-energy e^+e^- , hh and hA interactions, oscillatory behaviour of H_q with increasing q has been experimentally confirmed [25]. Whereas, for e^+e^- and hh interactions the oscillatory behavior has been attributed to the multicomponent structure of the particle production process, in the hA case the result has been explained in terms of a leading particle cascade model. In all

cases for each participating particle either a negative binomial, or a modified negative binomial multiplicity distribution, or both has been successfully used. In the present case of $^{32}\text{S-Ag/Br}$ interactions, the variation of H_q moments with order q has been graphically presented in Fig. 3.14, for the experiment as well as for the FRITIOF data. Several η intervals like $(\eta_0 - \eta_{cut}) \leq \eta \leq (\eta_0 + \eta_{cut})$ with $\eta_{cut} = 0.1, 0.25, 0.5$ and 1.0 , each centered about η_0 have been chosen to examine the jet structure in central particle producing region. One can see that, in narrow intervals ($\eta_{cut} = 0.1, 0.25$) the experimental results are significantly different from the FRITIOF results. The extent of oscillation, particularly in the high q region is much larger for the experiment than it is for the FRITIOF. This is indicative of different characteristics of the jet structure between the experimental and simulated data. Unlike the hh and hA cases the oscillation, though present in our AB experimental result, is not always about $H_q = 0$, but in the small q (< 7) region it is above the $H_q = 0$ line. The FRITIOF on the other hand exhibits only a small oscillation with increasing q . As the η interval size is increased, at ($\eta_{cut} = 0.5$, and 1.0) probably due to intermixing from different particle producing regions, the correlation effects are washed out, and the experimental result starts to coincide with the simulated result showing only a little or no oscillation. Only a sharp fall around $q = 2 - 4$ is prominently visible in each of these diagrams.

3.3 Discussion

An analysis of spatial distribution of shower tracks in central and semicentral $^{32}\text{S-Ag/Br}$ interactions at 200A GeV/c has been presented above. Multiplicity moments related to the intermittency phenomenon, with varying phase-space interval size have been evaluated. The results show presence of weak intermittency in the one dimensional distributions of singly charged produced particles. The intermittency results however, are not independent of the choice of phase-space variable. Even the weak intermittency effect in η -space can not be explained with the Lund Monte Carlo code FRITIOF, and in the φ -space the same could not be reproduced by assuming independent emission of particles based on random number generation. Fluctuations in the density distribution of like sign charged particles in small intervals of phase-space can be explained in terms of Bose-Einstein (BE)

correlation, i.e., interference among identical particles emitted by an extended coherent source. For shower tracks, created by both positive and negative charges (mostly pions), the increase of SFM with decreasing interval size shows a small but significant effect beyond the BE correlation effect. Lower value of intermittency indexes in experiments involving higher mass number or energy of the incident nucleus have been explained in terms of intermixing of more sources of particle production within the collision region. A close scrutiny of the experimentally obtained ϕ_q values does not allow us to draw any strong conclusion regarding any definite mechanism underlying the observed weak intermittency effect. On the one hand, absence of any noticeable prominent minimum in the λ_q vs. q plot does not necessarily indicate that, there exist a mixture of two phases - one normal with a large number of small peaks and shallow dips, and the other a spin glass with a small number of sharp peaks and deep valleys. Thus the present observation hardly corroborates the proposition that, the observed intermittency effect results due to presence of a mixture of two states like those mentioned above, as has been suggested and observed in the JINR data [27]. On the other hand, the Ginzburg-Landau parameter $\nu = 1.327 \pm 0.009$ with some degree of uncertainty in its error, is different from the universal value $\nu = 1.304$ necessary for a second order QCD phase transition to take place. Even if there is any phase transition, in the present case it has to be non-thermal type as a greater than unity Levy index ($\mu = 1.1$) indicates. However, a hierarchical relation between the SFMs has been established, that indicates some kind of interdependence between the correlation functions of different order. Also a multifractal structure of the particle density function in 1-d has also been established from the study of the anomalous dimensions [26].

Intermittency analysis in 2-d shows much stronger effect with an upward nonlinear bending in the SFM variation with decreasing interval size. The 2-d result confirms that in 1-d, intermittency effect is substantially shadowed due to projection effect. In the midst of all confusion regarding the exact reason, probably a scale invariant cascade mechanism in 2-d remains the only viable alternative as responsible for the intermittency phenomenon in the present case. An anisotropy between the phase-space distributions along longitudinal (η) and transverse (φ) directions has been found in our data. This lead us to conclude that, the intermittency is a result of self-affinity rather than a self-similarity in the par-

ticle distribution. Study of factorial correlators shows presence short range bin to bin correlation, that is consistent with the predictions of a simple α -model. Once again the observed correlation could not be accounted for by the FRITIOF prediction. Result on oscillatory multiplicity moments (H_q) confirms presence of true higher order ($q \geq 2$) correlation in our $^{32}\text{S-Ag/Br}$ data, that can not be reproduced by the FRITIOF. It also shows that, such correlation effects are more prominent in narrow phase-space intervals. With growing phase-space interval size the correlation effects are neutralized, and ultimately the experimental results coincide with the FRITIOF simulated results.

Bibliography

- [1] A. Bialas and R. Peschanski, *Nucl. Phys. B* **273**, 703 (1986)
A. Bialas and R. Peschanski, *Nucl. Phys. B* **308**, 857 (1988).
- [2] JACEE Collaboration, T. Burnett *et al.*, *Phys. Rev. Lett.* **50**, 2062 (1983).
- [3] E. A. De Wolf, I. M. Dremin, and W. Kittel, *Phys. Rep.* **270**, 1 (1996)
W. Kittel and E. A. De Wolf, *Soft Multihadron Dynamics*, (World Scientific, Singapore, 2005).
- [4] B. Andersson, G. Gustafson, and B. Nilsson-Almqvist, *Nucl. Phys. B* **281**, 289 (1987).
B. Nilsson-Almqvist and E. Stenlund, *Comp. Phys. Commun.* **43**, 387 (1987).
- [5] K. Fialkowski *et al.*, *Acta Phys. Pol. B* **20**, 639 (1989).
- [6] A. Bialas and M. Gazdzicki, *Phys. Lett. B* **252**, 483 (1990).
- [7] I. V. Ajinenko *et al.*, *Phys. Lett. B* **222**, 306 (1989)
N. M. Agababyan, *et al.*, *Phys. Lett. B* **382**, 305 (1996).
- [8] M. R. Spiegel *Theory and Problems of Statistics*, (McGraw-Hill Book Co., UK, 1988).
- [9] EMU01 Collaboration, M. I. Adamovich *et al.*, *Nucl. Phys. B* **388**, 3 (1992).
- [10] B. Buschbeck, R. Lipa and R. Peschanski, *Phys. Lett. B* **215**, 788 (1988)
W. Braunschweig *et al.*, *Phys. Lett. B* **231**, 548 (1988)
I. Derado, G. Jansco, N. Schmitz and P. Stopa *Z. Phys. C* **47**, 23 (1990)
- [11] KLM Collaboration, R. Holynski *et al.*, *Phys. Rev. Lett.* **62**, 733 (1989)
KLM Collaboration, R. Holynski *et al.*, *Phys. Rev. C* **40**, 2449 (1989)
EMU01 Collaboration, M. I. Adamovich *et al.*, *Phys. Rev. Lett.* **263**, 539 (1991).

- [12] W. Ochs, *Phys. Lett. B* **247**, 101 (1990)
W. Ochs, *Z. Phys. C* **50**, 339 (1991).
- [13] S. V. Chekanov and V. I. Kuvshinov, *Acta Phys. Pol. B* **25**, 1189 (1994).
- [14] Ph. Brax and R. Peschanski, *Phys. Lett. B* **253**, 225 (1991).
- [15] R. C. Hwa and M. T. Nazirov, *Phys. Rev. Lett.* **69**, 741 (1992).
- [16] A. Bialas and K. Zalewski, *Phys. Lett. B* **238**, 413 (1990).
- [17] L. Van Hove, *Phys. Lett. B* **28**, 429 (1969).
- [18] Y. Wu and L. Liu, *Phys. Rev. Lett.* **70**, 3197 (1993).
- [19] L. Liu, Y. Zhang and Y. Wu, *Z. Phys. C* **69**, 323 (1996).
- [20] C. Gang, L. Liu and G. Yanmin, arxiv:hep-ph/9812329v1 (1998).
- [21] EMU01 Collaboration, M. I. Adamovich *et al.*, *Z. Phys. C* **76**, 659 (1997).
- [22] NA22 Collaboration, V. V. Aivazyan *et al.*, *Phys. Lett. B* **258**, 487 (1991).
EMC Collaboration, I. Derado *et al.*, *Z. Phys. C* **54**, 357 (1992).
D. Ghosh *et al.*, *Phys. Rev. C* **52**, 2092 (1995).
- [23] E. A. De Wolf, *Proceedings of the Ringberg Workshop on Multiparticle Production*
eds. Hwa R C *et al.*, 222 (World Scientific, Singapore, 1992)
- [24] P. Carruthers, H. C. Eggers and I. Sarcevic, *Phys. Lett. B* **254**, 258 (1991).
P. Carruthers, H. C. Eggers and I. Sarcevic, *Phys. Rev. C* **44**, 1629 (1991).
- [25] I. M. Dremin, *Phys. Lett. B* **313**, 209 (1993)
N. Suzuki, M. Biyajima, G. Wilk and Z. Wlodarczyk, *Phys. Rev. C* **58**, 1720 (1998).
- [26] M. K. Ghosh, A. Mukhopadhyay and G. Singh, *J. Phys.*, **G 32**, 2293 (2006).
- [27] E. K. Sarkisyan, L. K. Gelovani, G. L. Gogiberidze, and G. G. Taran, *Phys. Lett. B*
347, 439 (1995).

Chapter 4

Multifractality in ^{32}S -Ag/Br interaction at 200A GeV/c

The multifractal structure of nonstatistical fluctuations in the phase-space distribution of singly charged particles produced in ^{32}S -Ag/Br interactions at an incident momentum of 200A GeV/c has been investigated. Various parameters related to multifractality have been obtained by analysing the data. Besides obtaining the fractal dimensions and a smooth multifractal spectrum, the experimental results have also been used to determine universal parameters like the Levy index, and the multifractal specific heat. The experimental results have been compared with those obtained from an event sample simulated by the Lund Monte Carlo code FRITIOF.

4.1 Introduction

We have already seen that the single particle distribution of secondary charged particles produced in a $^{32}\text{S-Ag/Br}$ interaction at 200A GeV/c, exhibits rapid fluctuations containing both sharp peaks and deep valleys in the phase-space density (dn_s/dX) values. It has also been mentioned that, these fluctuations result both from the statistical noise due to finite multiplicity of particles in an event, as well as from some dynamical reason that is not directly accessible to any experiment. The extent of such fluctuations depends on the resolution at which the density distribution is analyzed. Effects of statistical noise can be substantially reduced by taking an average over a large number of events. While doing so, unfortunately the dynamical components too are averaged out resulting in a smooth distribution of final state hadrons, as can be found in Fig. 2.3. Making use of suitable data analysis techniques characteristics of the dynamical component can still be investigated, and the mechanism of multiparticle production can be explored within the framework of existing models. One such set of techniques is based on the notion that the density fluctuations have self-similar multifractal property, that probably is an outcome of some kind of scale invariant dynamics. The fluctuation properties can be quantified by evaluating appropriate multifractal moments of the distribution, and by examining how they depend on the phase-space interval size, say δX . It has been suggested in theory [1–3] and observed in experiments [4–8] that, self-similarity in density fluctuations should lead to a power law scaling behaviour of δX dependence of the multifractal moments. Such scaling laws can further be utilized to extract universal fractal properties of the underlying distribution and its fluctuation. Efforts have been made to interpret the observed scale invariance in terms of random cascading model, phase transition or more conventional phenomenon like the Bose-Einstein correlation; but each with limited degree of success. Both the experimental and phenomenological status of the subject have been comprehensively reviewed in [9].

In Chapter III dynamical fluctuations have been analyzed in terms of the intermittency phenomenon. In this technique the scaled factorial moments (SFMs) of different order are evaluated. In one dimension the event space averaged SFM $\langle F_q \rangle$ of order q has been found to scale with δX following

$$\langle F_q \rangle \propto \delta X^{-\phi_q}, \quad (4.1)$$

where ϕ_q is called the intermittency index. This self-similarity of fluctuations in the density of produced particles down to the experimental resolution indicates that, fractal structures are involved in the process of particle emission. Though the SFMs are very efficient to suppress Poisson type noise; they do suffer from a few limitations as well. For example, the order q must always be a positive integer - it can neither be a fraction nor a negative number. The SFM provides information only about the peaks in particle density, but the technique is not suitable for analyzing the dips or valleys in the distribution. It's therefore quite natural to extend the scope of investigation beyond intermittency, to verify a probable existence of interrelated fractal characteristics in the already used ^{32}S -data, and also to find out interpretation of the intermittency parameters in terms of the fractal parameters. In this chapter we have therefore, presented some results on multifractal analysis of the density fluctuation of singly charged produced particles in ^{32}S -Ag/Br interactions at 200A GeV/c. In particular, the scaling behaviour of multifractal moments as functions of δX has been examined by using two different techniques [1, 11, 12] to be described later. Results obtained from these two different formalisms have been compared to the extent possible. ^{32}S -Emulsion interactions at 200A GeV/c have been simulated by using the computer code FRITIOF based on the Lund Monte Carlo model [13] on high energy AB interaction. Results obtained by analyzing a sample of FRITIOF generated ^{32}S -Ag/Br events, having identical multiplicity distribution of produced particles as the experimental one, have been compared with experimental results. The main objectives of this chapter are therefore, (i) to establish the presence of multifractal characteristics in the experimental data beyond those arising from trivial statistical noise, (ii) to extract relevant fractal parameters that can help develop future models of particle production, (iii) to see whether or not FRITIOF can reproduce the experimentally observed results, and finally (iv) to examine how the results obtained from two different multifractal techniques adopted in this investigation, agree or disagree with each other.

4.2 Hwa's Multifractal Moments

Scale invariance of fluctuations in the density distribution of final state hadrons, as observed from the intermittency analysis of the present set of data [10] indicates that, with

the help of fractal geometry it may also be possible to characterize the distribution. According to the theory of multifractality the number density of final state hadrons should scale with the phase-space partition size, and the scaling properties should be different in different regions of phase-space. Unlike a geometrical or a statistical system, multi-particle production process possesses special problems, the most obvious one being the finiteness of average shower track multiplicity $\langle n_s \rangle$. For finite $\langle n_s \rangle$ the frequency distribution and its moments are subjected to large statistical fluctuations. As the bin size gets smaller, the problem of statistical noise arising out of growing presence of empty bins requires special attention. The multifractal moment (G-moment) of order q , also known as the frequency moment, is defined for an event as

$$G_q = \sum_{j=1}^M (p_j)^q = \sum_{j=1}^M \left(\frac{n_j}{n_s} \right)^q, \quad (4.2)$$

where q is any (+)ve or (-)ve real number, when the entire phase-space interval, say ΔX , has been divided into M equal intervals and n_j is the number of particles in j th such interval. In the above expression two points are to be noted, (i) the summation runs only over nonempty intervals ($n_j \neq 0$) allowing negative values of q , and (ii) for finite n_s , however large, p_j can not represent the true probability, but at the best may be called a relative frequency. For negative q the G-moments are capable of providing information about dips in the phase-space distribution.

By definition, a fractal dimension D_F relates the mass element (δm) of an object having fractal characteristics to its size, say δl , through

$$\delta m \sim [\delta l]^{D_F}.$$

For ordinary objects D_F equals the topological dimension D of the supporting space, whereas for fractal objects they do not. At small δl the probability $p(\delta l)$ to be within a hypervolume may be assumed to scale with its size,

$$p(\delta l) \propto [\delta l]^{D_F} : \quad D_F = \text{constant},$$

and therefore, for a fractal object the mean q th order moment should abide by,

$$\langle p(\delta l)^q \rangle \propto [\delta l]^q D_F.$$

In the theory of multifractal structure of particle distribution this notion of fractal theory has been generalized as,

$$G_q = \sum_{j=1}^M p_j^q(\delta X) = \langle p_j^{q-1}(\delta X) \rangle \propto (\delta X)^{\tau(q)}, \quad (4.3)$$

where $\tau(q) = (q-1)D_q$ and D_q is called the Renyi dimension. In stead of fractal dimension, a multifractal may also be characterized by a spectral function. Each phase-space interval has its own δX dependence. If all singularities associated with a particular scaling index α (may be termed as the local mass dimension in the sense, $p_j(\delta X) \sim (\delta X)^\alpha : \delta X \rightarrow 0$) are grouped together to form a fractal subset $S(\alpha)$, then the number of intervals to fill up $S(\alpha)$ may be assumed to increase with decreasing δX as,

$$M_\alpha(\delta X) \sim (\delta X)^{-f(\alpha)},$$

where $f(\alpha)$ is the fractal dimension for $S(\alpha)$. Since each $S(\alpha)$ is associated with a particular α the summation in G_q over j may be replaced by,

$$\sum_{j=1}^M \rightarrow \int d\alpha \rho(\alpha) (\delta X)^{-f(\alpha)},$$

where $\rho(\alpha)$ is some weight factor whose exact analytic form is not very important. Thus at small δX ,

$$G_q \propto \int d\alpha \rho(\alpha) (\delta X)^{-f(\alpha)+q\alpha},$$

and the dominant contribution comes from the region where the exponent is small. For each q , the minimum in the exponent occurs at a particular α say at $\alpha = \alpha_q$, that may be determined by setting,

$$\begin{aligned} \frac{d}{d\alpha} [q\alpha - f(\alpha)] &= 0, \\ \frac{d^2}{d\alpha^2} [q\alpha - f(\alpha)] &< 0. \end{aligned}$$

Therefore, it suffices to evaluate the integral at or around α_q , when

$$\frac{d}{d\alpha_q} f(\alpha_q) = q \quad \text{and} \quad \frac{d^2}{d\alpha^2} f(\alpha_q) < 0.$$

From Eq. (4.3) we therefore get,

$$\alpha_q = d\tau(q)/dq$$

and

$$\tau(q) \approx q\alpha_q - f(\alpha_q).$$

The effect of empty bins has been taken care of by defining a modified form of the multifractal moment for a single event as [11],

$$G_q = \sum_{j=1}^M \left[\frac{n_{ij}}{(n_s)_i} \right]^q \Theta(n_{ij} - q). \quad (4.4)$$

Here n_{ij} is the number of particles in the j th bin of the i th event, $(n_s)_i$ is the total number of particles in the i th event, $[(n_s)_i = \sum_{j=1}^M n_{ij}]$, and Θ is a step function for integer as well as fractional q as defined in [11]. As mentioned above in the theory of fractals, if self-similar dynamical component is present in the density fluctuation, the G-moments should exhibit a scaling behaviour like,

$$G_q(\delta X_\eta) \propto M^{-\tau(q)} : \delta X_\eta \rightarrow 0. \quad (4.5)$$

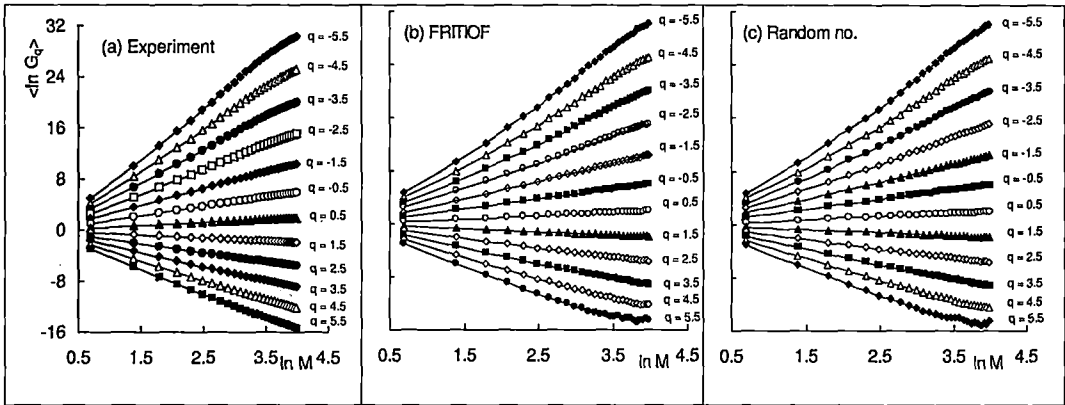


Figure 4.1: Variation of G-moments with phase-space partition number for $^{32}\text{S-Ag/Br}$ interaction at 200A GeV/c - (a) Experiment, (b) FRITIOF and (c) Random number. In all diagrams the continuous lines are drawn simply by joining the points.

Here $\tau(q)$ may be called the mass exponent. As long as M remains finite, the limit $\delta X_\eta \rightarrow 0$ can not actually be reached and, therefore, the fractal behaviour can not be extracted in its strict sense. However, by examining the scaling properties of the G-moments in a region where δX_η is of the order of the phase-space resolution permitted by the experiment, significant results can still be obtained. Taking the vertical average of

G-moments over the sample of events under consideration, one can determine the event space average of the mass exponent as,

$$\langle \tau(q) \rangle = - \frac{\partial(\langle \ln G_q \rangle)}{\partial(\ln M)}. \quad (4.6)$$

The methodology summarized above and as described in [1, 2, 11] allows us to determine various parameters related to multifractal characteristics of density fluctuation. Values of $\langle \ln G_q \rangle$ for different q have been graphically plotted against $\ln M$ in Fig. 4.1. The experimental results, the FRITIOF simulated results and the results obtained by random number generation are shown separately. In general, for all three sets of data $\langle \ln G_q \rangle$ linearly depends on $\ln M$ in accordance with Eq. (4.5), increasing for $q < 0$ and decreasing for $q > 1$. However, in the large $\ln M$ region saturation effects, due to finiteness of $\langle n_s \rangle$, are visible particularly at high $|q|$. Following Eq. (4.6) the $\langle \tau_q \rangle$ values can be determined for each q from the best linear fit of the $\ln M$ dependence of $\langle \ln G_q \rangle$.

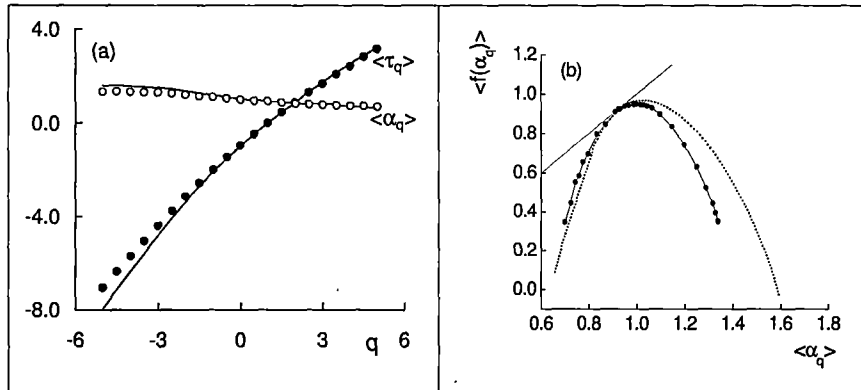


Figure 4.2: (a) Event averaged mass exponents $\langle \tau_q \rangle$ and Lipschitz-Holder exponents $\langle \alpha_q \rangle$ against q for $^{32}\text{S-Ag/Br}$ interaction at 200A GeV/c. Data points represent the experimental values and the lines represent the corresponding FRITIOF predictions. (b) Multifractal spectral function for both the experiment and FRITIOF. The solid curve with points represents experimental results and the dotted curve represents the FRITIOF prediction. The straight line represents $\langle f(\alpha_q) \rangle = \langle \alpha_q \rangle$.

The event space averaged multifractal spectral function

$$\langle f(\alpha_q) \rangle = q \langle \alpha_q \rangle - \langle \tau(q) \rangle,$$

is introduced through a Legendre transform with the help of Lipschitz-Holder exponent α_q , that is defined as,

$$\langle \alpha_q \rangle = \partial \langle \tau(q) \rangle / \partial q.$$

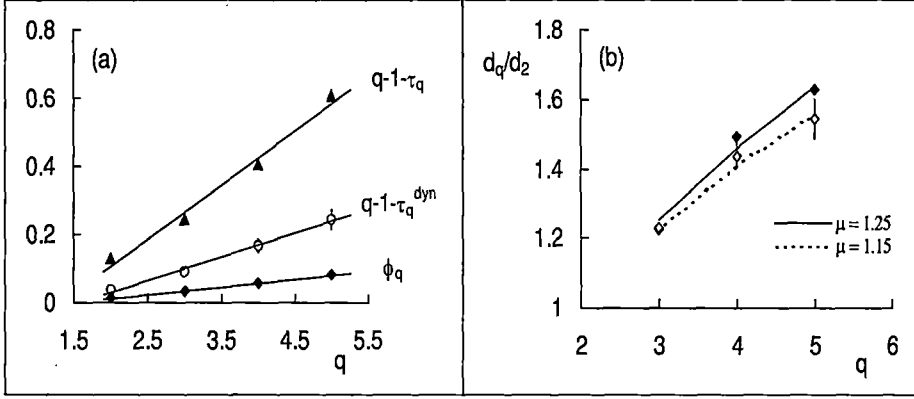


Figure 4.3: (a) Experimental values of the intermittency indices (ϕ_q), $(q - 1 - \langle \tau(q) \rangle)$ and $(q - 1 - \langle \tau(q) \rangle^{dyn})$ are plotted against q for $^{32}\text{S-Ag/Br}$ interaction at 200A GeV/c. The straight lines are best linear fit to data. (b) Experimental values of d_q/d_2 obtained both from SFM (solid diamonds) and G-moments (open diamonds) are plotted against q . The continuous (solid and dotted) lines represent the corresponding Levy law prediction using Eq. (4.11).

Since a derivative is involved, it is necessary to determine $\langle \alpha_q \rangle$ for small incremental changes in q , especially in the neighbourhood of $q = 0$, where $\langle f(\alpha_q) \rangle$ has its maximum. In Fig. 4.2(a) we have shown how $\langle \tau_q \rangle$ and $\langle \alpha_q \rangle$ values for the experimental and FRITIOF data vary with q . Unlike in the case of intermittency analysis [10], we do not see any significant difference between the experimental and simulated results from multifractal analysis. A smooth and stable multifractal spectral function $\langle f(\alpha_q) \rangle$ has been obtained both for the experiment and for the FRITIOF. Both of them are plotted against $\langle \alpha_q \rangle$ in Fig. 4.2(b), and both satisfy the general characteristics [1, 3] such as, (i) $\langle f(\alpha_q) \rangle$ is a function of $\langle \alpha_q \rangle$ that is concave downwards, (ii) has a peak at $\langle \alpha_0 \rangle$, and (iii) the straight line $\langle f(\alpha_q) \rangle = \langle \alpha_q \rangle$ tangentially touches both the spectra around $\langle \alpha_1 \rangle$, because $\langle f(\alpha_1) \rangle = \langle \alpha_1 \rangle$ and $\langle f'(\alpha_1) \rangle = 1$. The region above the $\langle f(\alpha_q) \rangle = \langle \alpha_q \rangle$ line corresponds to an unphysical region. The fact that a wide distribution in $\langle f(\alpha_q) \rangle$ and not a delta function peaked around α_0 has been

obtained, confirms multifractal nature of the density fluctuation in each case. The left and right sides of the spectrum correspond, respectively, to the dense and sparse regions of density distribution. Both experimental and simulated maximum values of $\langle f(\alpha_q) \rangle$ are very close to unity, indicating that the empty bin effect particularly in the higher resolution region, is marginal in the present case. The FRITIOF simulated spectrum is wider than the experimental one. For a $p\bar{p}$ interaction similar feature has been observed while UA1 data were being compared with GENCL and PYTHIA predictions [4]. In the case of AB interactions multifractal characteristics were observed both in the experimental data as well as in the Monte Carlo predictions based on a simple stochastic model [8]. As the average number of charged particles in our event sample is finite, the G_q moments contain statistical contribution (G_q^{st}), that can be determined by distributing n_s particles of an event randomly within $0 \leq X_\eta \leq 1$. In the process short range correlation among the particles, if any, is destroyed. The dynamical contribution (G_q^{dyn}) can then be extracted after eliminating the statistical one. In [11] it has been shown that, for a trivial dynamics the dynamical part of $\langle \tau_q \rangle$, denoted by $\langle \tau(q) \rangle^{dyn}$, should be equal to $(q - 1)$. Therefore, any deviation in $\langle \tau(q) \rangle^{dyn}$ from $(q - 1)$ should be read as a contribution from nontrivial dynamical contribution. Allowing all three G-moments namely G_q , G_q^{st} and G_q^{dyn} to obey their respective power laws, the following relation can be obtained,

$$\langle \tau(q) \rangle^{dyn} = \langle \tau(q) \rangle - \langle \tau(q) \rangle^{st} + q - 1. \quad (4.7)$$

whereas, the intermittency index ϕ_q introduced in Eq. (4.1), can also be connected to $\langle \tau(q) \rangle^{dyn}$ as [11],

$$\langle \tau(q) \rangle^{dyn} - q + 1 \approx -\phi_q. \quad (4.8)$$

For comparison, ϕ_q values obtained previously from intermittency analysis [10] for the same set of experimental data along with the $(q - 1 - \langle \tau(q) \rangle)$ and $(q - 1 - \langle \tau(q) \rangle^{dyn})$ values obtained from the present analysis, are plotted together against q in Fig. 4.3(a). One can see that the ϕ_q values differ from the respective $(q - 1 - \langle \tau(q) \rangle^{dyn})$ values only to a small extent. The difference in their values may probably be attributed to the different ways of defining SFM and G-moment. The generalized Renyi dimensions denoted by D_q , are directly related to the intermittency indexes as,

$$D_q = 1 - \frac{\phi_q}{(q - 1)}. \quad (4.9)$$

Therefore, in view of Eq. (4.8) one can also set,

$$D_q \approx \frac{\langle \tau(q) \rangle^{dyn}}{(q-1)}. \quad (4.10)$$

On the other hand, the anomalous dimensions are defined as

$$d_q = D - D_q,$$

where D is the topological dimension of the supporting space. For one dimensional analysis $D = 1$. One of the properties of universal multifractals is that, they can be classified by a parameter μ ($0 \leq \mu \leq 2$) called the Levy index, that indicates the degree of multifractality as well as estimates the cascading rate in self-similar branching process [15]. The Levy index (μ) can also be utilized to decipher possible mechanism of particle production. Such a characterization of multifractality is possible if the underlying density distribution can be described by a Levy stable law. Under a Levy law approximation, using anomalous dimensions one can determine the value of μ from the following relation [16],

$$\frac{d_q}{d_2} = \frac{1}{2^\mu - 2} \frac{q^\mu - q}{q - 1}. \quad (4.11)$$

In Fig. 4.3(b) experimentally obtained values of d_q/d_2 obtained both from the exact [10] and the approximate values of ϕ_q [Eq. (4.8)], have been plotted together against q . Corresponding d_q/d_2 values evaluated by using Eq. (4.11) have also been incorporated in the same diagram in the form of continuous lines. The lines correspond, respectively, to $\mu = 1.15$ for the exact values of ϕ_q and to $\mu = 1.25$ for the approximate values. If μ were equal to 2, the Levy distribution would have transformed into a Gaussian one. Under this condition one expects minimum fluctuation in the self-similar branching processes. On the other hand, for $\mu = 0$, d_q/d_2 values become independent of order. This corresponds to mono-fractals and maximum fluctuation, and might therefore, be a signal of second order phase transition. Neither of the above conditions is satisfied by the μ values obtained in the present investigation. One can see that, the present values obtained from two different sets of parameters, are very close to each other. The fact that $\mu > 1.0$, indicates presence of wild singularities arising out of non-Poisson like fluctuations in the density distribution. As far as mechanism of particle production is concerned, this condition also indicates that, in the present case of $^{32}\text{S-Ag/Br}$ interactions there may be a non-thermal

phase transition during the cascading process. On the other hand, a value of $0 < \mu < 1.0$ would have indicated soft bound singularities, that can be related to a thermal phase transition interspersed in the cascading process. It should however be mentioned that, the present values of Levy index are less than a previously obtained value ($\mu = 1.6$) based on a set of combined data on AB, pA, e^+e^- and μp interactions [16], but are well within the limit allowed by the Levy law description, and do not necessarily warrant a thermal phase transition to occur during particle production.

4.3 Takagi's Multifractal Moments

As mentioned above, due to the finiteness in charged particle multiplicity (n_s) of an event, the mathematical limit of phase-space partition number ($M \rightarrow \infty$) can not be realised in practice. Even the step function Θ introduced into the definition of the G_q moments, can not completely remove the saturation effects, particularly at higher $|q|$ values as has already been observed. In an alternative approach, Takagi [12] has suggested a new set of multiplicity moments for $q > 0$ as,

$$T_q(\delta X_\eta) = \ln \sum_{i=1}^{N_{ev}} \sum_{j=1}^M (p_{ij})^q, \quad (4.12)$$

that are not affected by the finiteness of n_s . Here, $p_{ij} (= n_{ij}/K)$ is the normalized density function, K is the total number of particles produced in N_{ev} interactions and n_{ij} is same as Eq. (4.4), when the entire X_η space has been divided into M intervals. Takagi's method is based on two assumptions, (i) the density function ρ is uniform over the phase-space interval considered, and (ii) the multiplicity distribution P_n does not depend on the location of the interval δX_η - both found to be valid in the present case where X_η has been used as phase-space variable. According to the theory of multifractals, $T_q(\delta X_\eta)$ should be a linear function of the logarithm of the resolution $R(\delta X_\eta)$,

$$T_q(\delta X_\eta) = A_q + B_q \ln R(\delta X_\eta), \quad (4.13)$$

where A_q and B_q are constants independent of q . When a linear dependence like that of Eq. (4.13) is observed over a large range of $R(\delta X_\eta)$, following Takagi's method the generalized dimensions can once again be calculated,

$$D_q = B_q/(q - 1). \quad (4.14)$$

For $q = 1$, one may either take the appropriate limit [17], or can consider the entropy function defined as,

$$S(\delta X_\eta) = - \sum_{i=1}^{N_{ev}} \sum_{j=1}^M p_{ij} \ln p_{ij}, \quad (4.15)$$

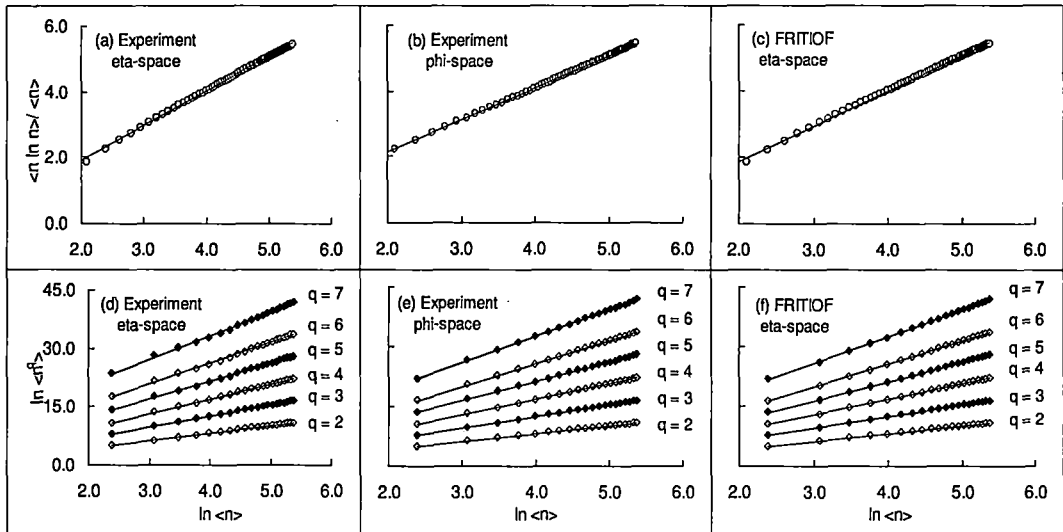


Figure 4.4: Plot of Takagi's multifractal moments for ^{32}S -Ag/Br interaction at 200A GeV/c. In all diagrams the straight lines represent best linear fit to data.

and look for a dependence of this quantity like,

$$S(\delta X_\eta) = -D_1 \ln R(\delta X_\eta) + \text{constant}, \quad (4.16)$$

where D_1 is called the information dimension. If the number of events N_{ev} is large one has,

$$\sum_{i=1}^{N_{ev}} \sum_{j=1}^M (p_{ij})^q = \langle n^q \rangle / (K^{q-1} \langle n \rangle), \quad (4.17)$$

where average bin multiplicity $\langle n \rangle = K / (M \cdot N_{ev})$, and therefore,

$$\ln \langle n^q \rangle = A_q + [(q-1)D_q + 1] \ln(\delta X_\eta) \quad (4.18)$$

for the simplest choice of $R(\delta X_\eta) = \delta X_\eta$. Replacing δX_η with $\langle n \rangle$, the generalized dimensions can now be obtained following the relations,

$$\ln \langle n^q \rangle = A_q + [(q-1)D_q + 1] \ln \langle n \rangle \quad (4.19)$$

for $q \geq 2$. For $q = 1$,

$$\langle n \ln n \rangle / \langle n \rangle = C_1 + D_1 \ln \langle n \rangle . \quad (4.20)$$

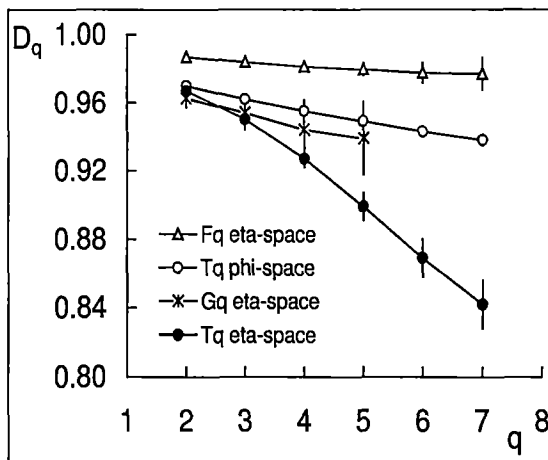


Figure 4.5: Experimental values of the generalised dimensions D_q for $^{32}\text{S-Ag/Br}$ interaction at 200A GeV/c. Solid lines are drawn to guide the eye.

Proceeding in the same way as [12], for a symmetric interval about the central value $X_\eta = 0.5$ of the distribution, values of $\langle n \ln n \rangle$ and $\ln \langle n^q \rangle$ are calculated with increasing width of the interval. Our results on Takagi's method of multifractal analysis have been graphically shown by plotting $\langle n \ln n \rangle / \langle n \rangle$ against $\ln \langle n \rangle$, in Fig. 4.4(a)-(c), respectively for the experimental values in η and φ -space and the FRITIOF prediction in η -space. From the slopes of best linear fit to data values of the information dimension (D_1) have been obtained respectively as, $D_1 = 0.973 \pm 0.0014$, 0.972 ± 0.002 and 0.979 ± 0.002 . Values of generalized dimensions for $q \geq 2$ have been obtained from the best linear fit of $\ln \langle n^q \rangle$ values against $\ln \langle n \rangle$ as shown in Fig. 4.4(d)-(f). For comparison in Fig. 4.5, D_q values of different orders obtained from Takagi's generalized moments are plotted against $q (\geq 2)$ together with those obtained from the intermittency indexes (ϕ_q) and from the dynamical part of Hwa's multifractal mass exponents $\langle \tau(q) \rangle^{dyn}$, respectively, making use of Eq. (4.9) and (4.10). With increasing q in general we find a monotonous decreasing trend in the D_q values. However, the D_q values from Takagi's method exhibit steepest fall, whereas those obtained from the intermittency indices decrease at the slowest rate. Probably because of the different ways of defining the multifractal T-moments, and

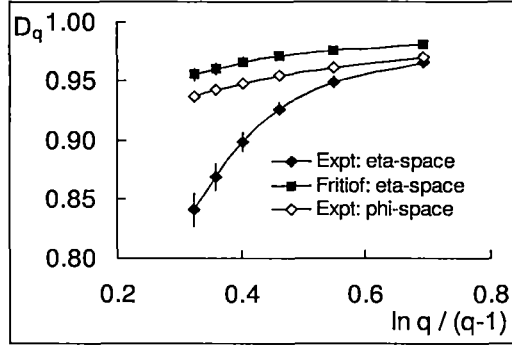


Figure 4.6: Graph to determine the multifractal specific heat for $^{32}\text{S-Ag/Br}$ interaction at 200A GeV/c, from the D_q values obtained by using Takagi's method. The experimental data points in η -space are simply connected by a continuous line, whereas, for both the FRITIOF prediction in η -space and the experimental data points in φ -space, the straight lines represent best linear fit.

due to the reason that in Takagi's method no attempt has been made to separate the non-statistical contribution from the statistical one, in this case at large q the D_q values differ significantly from those obtained from the SFMs and G-moments. However, for a simple Poissonian multiplicity distribution within a given interval δX_η , the D_q values would all have been equal to unity. Any deviation in their values from 1.0 would thus provide us with a measure of nonstatistical fluctuation. This has been found in all the methods described above for characterizing multifractality in density fluctuations. On the basis of the fact that, only Bernoulli type of fluctuations are responsible for a transition from monofractality to multifractality, Bershadskii [18] gave a thermodynamic interpretation of the observed results in terms of a constant specific heat C ,

$$D_q = D_\infty + \frac{C \ln q}{q-1}. \quad (4.21)$$

A monofractal to multifractal phase transition corresponds to a jump in the value of C from $C = 0$ to a nonzero finite positive value. By plotting D_q against $\ln q / (q - 1)$ we can therefore, obtain the value of specific heat from the slope of the best linear fit. Such a plot can be found in Fig. 4.6 both for the experiment and FRITIOF simulated values. In X_η space a strict linearity is not seen over the entire range of q under consideration, and a linear fit in the range $q = 2$ to 5 resulted into $C = 0.329 \pm 0.061 \approx \frac{1}{3}$. On the other hand best linear fit of FRITIOF data in X_η space over $q = 2$ to 7 results in $C = 0.066 \pm 0.009$,

which is much smaller than the corresponding experimental value. On the other hand, in X_φ space linear fit once again over the entire range of q ($= 2$ to 7) gave us a much smaller value of C ($= 0.086 \pm 0.008$). The C value in X_φ space is significantly smaller than a previously obtained value ($C = \frac{1}{4}$) based on an analysis in the azimuthal angle space of similar ^{32}S -ion induced experiment at same incident energy [19]. As a probable reason for this discrepancy, it may be pointed out that the analysis presented in [19] has been performed over a set of events with minimum bias, that possesses a much wider range of impact parameter values, and also has a much smaller average value of shower multiplicity as well as smaller statistics than the present set of experimental data. Our value of C in φ -space is also smaller than the predictions of another analysis ($C = 0.56$) on simulated high multiplicity single jet events in the azimuthal angle space [20].

4.4 Discussion

Observations of the present investigation can be summarized in the following way. From the above analysis of angular distribution of produced particles in ^{32}S -Ag/Br interactions at 200A GeV/c, multifractal characteristics of the density fluctuation over and above that coming from trivial statistical noise, have been established. Results obtained from two different methods of analysis, one prescribed by Hwa [1–3, 11] and the other by Takagi [12], are more or less consistent with each other. However, multifractal nature of the density fluctuation has also been observed in the FRITIOF simulated data. This is in contrast to our previous investigation of intermittency phenomenon for the same set of experimental data [10], where FRITIOF failed to reproduce the experimental observations. The SFM contains information on particle correlation, that has not been taken into account in the present version of FRITIOF. Hence the discrepancy with the experiment has been found. Using Hwa's methodology, not only have we obtained important multifractal parameters like the generalised Renyi dimensions (D_q) and stable multifractal spectrum $f(\alpha_q)$, but also we have been able to determine the Levy index that measures the degree of multifractality for the present set of data on AB interactions. Our value of μ (≈ 1.2) is consistent with the Levy law description of density distribution of produced charged particles, and also indicates a non-thermal phase transition during particle production. The Takagi's

methodology, perceived to be a better tool of analysis than Hwa's G-moments, once again has been able to establish the multifractal characteristics and yields generalised dimensions. The experimental D_q values obtained from Takagi's method differ significantly from unity with increasing q , whereas, the corresponding FRITIOF values are always very close to unity, which is the topological dimension of the supporting space. The multifractal specific heat, which again is a measure of the degree of multifractality, came out to be higher in pseudorapidity space than the universal value $C = \frac{1}{4}$ for moderate and very heavy-ion interactions, as claimed in [18]. The difference in bias while choosing each experimental data set, should be kept in mind while comparing such parameter values obtained from different investigations. A small FRITIOF simulated value of C indicates that, though multifractal characteristics are present also in the simulated events, the extent of multifractality is smaller than that of the experimental one. In the azimuthal angle space, in contrast to some previous observations, present value of C came out to be substantially smaller.

We would like to point out that several measures can be taken, to enable us in future to make stronger conclusions. First of all, fractal structures present in higher dimensions is a worthwhile topic of future investigation. Often self-similar multifractal characteristics of geometrical objects disappear in their lower dimensional projection, and therefore, stronger indication of multifractality is expected in a higher dimensional analysis. The influence of collision geometry can be another aspect that requires special attention, when a much larger statistics is available. This requires partitioning the data set into several subsets, each with a narrow range of shower multiplicity. Performing similar multifractal analysis for each such subset, variation with $\langle n_s \rangle$ (a measure of impact parameter of collision) can be examined. The fact that FRITIOF simulated events also exhibit multifractality while it fails to do so in the case of intermittency, is a major point of concern. More sophisticated methods of analysis are therefore necessary, where the structure obtained from trivial backgrounds can be properly accounted for. The generalized dimensions obtained from Takagi's methodology are significantly different in the higher q region, from similar values obtained from the SFM and G-moment analysis of data. This discrepancy probably arises because, in Takagi's method the issue of eliminating statistical noise has not yet been addressed.

Bibliography

- [1] R. C. Hwa, *Phys. Rev. D* **41**, 1456 (1990).
- [2] W. Florkowski and R. C. Hwa, *Phys. Rev. D* **43**, 1548 (1991).
- [3] C. B. Chiu and R. C. Hwa *Phys. Rev. D* **43**, 100 (1991).
- [4] UA1 Collaboration, C. Albajar, *et al.*, *Z. Phys. C* **56**, 37 (1991).
- [5] I. Derado, R. C. Hwa, G. Jansco and N. Schmitz *Phys. Lett. B* **283**, 151 (1991).
- [6] R. K. Shivpuri and V. Anand, *Phys. Rev. D* **50**, 287 (1994).
- [7] E. K. Sarkisyan, L. K. Gelovani and G. G. Taran, *Phys. Lett. B* **302**, 331 (1993).
- [8] EMU01 Collaboration, M. I. Adamovich *et al.*, *Europhys. Lett.* **44**, 571 (1998).
- [9] E. A. De Wolf, I. M. Dremin and W. Kittel, *Phys. Rep.* **270** 1 (1996); W. Kittel and E. A. De Wolf, *Soft Multihadron Dynamics*, (World Scientific, Singapore), (2005).
- [10] M. K. Ghosh, A. Mukhopadhyay and G. Singh, *J. Phys. G: Nucl. Part. Phys.* **34**, 177 (2007).
- [11] R. C. Hwa and J. Pan, *Phys. Rev. D* **45**, 1476 (1992).
- [12] F. Takagi *Phys. Rev. Lett.* **72**, 32 (1994).
- [13] B. Anderson, G. Gustavson and B. Nilsson-Almqvist, *Nucl. Phys. B* **281**, 289 (1987)
B. Nilsson-Almqvist and E. Stenlund, *Comp. Phys. Commun.* **43**, 387 (1987).
- [14] A. Bialas and M. Gradzicki *Phys. Lett. B* **252**, 483 (1990).
- [15] Ph. Brax and R. Peschanski, *Phys. Lett. B* **253**, 225 (1991).

- [16] W. Ochs *Phys. Lett. B* **247**, 101 (1990).
W. Ochs *Z. Phys. C* **50**, 339 (1991).
- [17] H. G. E. Hentschel and I. Procaccia *Physica D* **40**, 435 (1983).
- [18] A. Bershadskii, *Phys. Rev. C* **59**, 364 (1999).
- [19] D. Ghosh *et al.*, *Z. Phys. C* **73**, 269 (1997).
- [20] S. K. Nayak and Y. P. Vijoyi *Phys. Lett. B* **367**, 386 (1996).

Chapter 5

Erraticity in ^{32}S -Ag/Br interaction at 200A GeV/c

Spatial fluctuations as well as event-to-event fluctuations are investigated in terms of the erraticity moments of pseudorapidity distribution of singly charged particles produced in ^{32}S -Ag/Br interactions at 200A GeV/c. A generalized scaling law, similar to those for the scaled factorial moments and the multifractal moments, has been observed also for the erraticity moments. The erraticity parameters have been extracted by analyzing the experimental data. These parameters can serve a very useful purpose for future model calculations on soft multiparticle dynamics, that takes into account all possible sources of fluctuation. The experimental results have been compared with the prediction of Lund Monte Carlo code FRITIOF on corresponding high energy AB interaction. The model failed to reproduce any of the present experimental observations. The erraticity technique for phase-space gaps between produced particles has also been applied to the present set of data. In this regard only the experimental results have been presented. The observations from both methods of analysis are consistent with their respective expectations.

5.1 Introduction

It is generally believed that, particles belonging to the final states of high energy AB interactions may be an outcome of some kind of phase transition e.g, from the quark-gluon plasma to the normal hadronic state of matter. As a result, one can expect various time integrated patterns of clusters within narrow regions of phase-space, as well as sharp voids in the phase-space distribution. Such unusually large local fluctuations in particle densities observed in the JACEE events [1] indicated that, the fluctuations were not merely statistical artifacts. In their pioneering work Bialas and Peschanski [2] showed that, if these fluctuations were Poisson distributed, sample averaged factorial moments $\langle F_q \rangle$ of order q (a positive integer) becomes equal to the average of ordinary moments C_q of the corresponding dynamical distribution, irrespective of the nature of the latter. Bialas and Peschanski also showed that $\langle F_q \rangle$ anomalously scales with diminishing size of the phase-space variable. This scaling behaviour technically termed as the "intermittency", has so far been extensively and successfully studied in many high energy experiments [3–6]. Efforts have been made to interpret these fluctuations not only in terms of phase transition, but also in terms of more conventional phenomena like, production of shock waves, Bose-Einstein correlation, or simple cascading effects [7]. Though the factorial moments are capable of filtering out the dynamical part of spatial fluctuation, it should however be noted that when averaged over a large sample of events, they may lose information on the variation of such spatial fluctuations from event to event. For example, creation of an exotic state like the quark-gluon plasma (QGP) may result in large spatial fluctuations only in some of the events, and not in the entire event sample under consideration. In the process of averaging, information on such large fluctuations may be smoothed out. Moreover, these moments are incapable to locate the position of a spike or a sharp void in an event. When the study is made over a limited region of phase-space, and only a few phase-space intervals contribute to the final value of the moment because of the finite multiplicity in an event, very little information about that event is contained in the value of $\langle F_q \rangle$. Therefore, it becomes imperative to study the fluctuation of single event factorial moments as well.

Recently, a few alternative methods have been suggested to overcome the above mentioned limitations of $\langle F_q \rangle$, and this has sparked some interest to investigate the event-to-event

fluctuation of particle distribution. Cao and Hwa [8, 9] have proposed a scheme to investigate the event-to-event fluctuation of single event factorial moments $\langle F_q^e \rangle$ with the help of a new set of moments, called the "erraticity" moments $C_{p,q}$ where p is any positive number. The method as indicated by the authors is free from the limitations of the scaled factorial moments as described above, and therefore is a useful technique for investigating the chaotic behavior of multiparticle production in high energy collisions. The erraticity moments, which also scale with phase-space partition size obeying a generalized power law, can be related to several parameters, one of which is an entropy index μ_q that can adequately determine the chaotic nature of spatial fluctuation in event space, and it also characterizes the degree of fluctuation of the parton multiplicity that initiates QCD branching processes. Positive non-vanishing value of μ_q denotes a wide distribution of $\langle F_q^e \rangle$, and this implies that the spatial fluctuations are unpredictable from event to event. All events in a sample may have started with same initial conditions, but during the collision process each event may have evolved with a different strength of dynamical fluctuation. Thus such chaotic behaviour may be attributed to different dynamical fluctuation strength in different events. If the analysis can be performed with a cut on the transverse momentum p_t of produced particles, it can also be checked whether the observed chaotic behavior is an outcome of some kind of phase transition or not. As was pointed out in [8], to describe the chaotic behavior of particle production in high energy interactions these entropy indices are as effective as the Lyapunov exponents are for a classical deterministic nonlinear system, and nonvanishing positive values of μ_q can be used as a criterion for this purpose. The index μ_q has an added advantage in the sense that, it can distinguish a branching process initiated by a quark from that initiated by a gluon. If the entropy index is of high value, the initial parton responsible for a branching process can be identified as a quark, though in such a case no quantitative criterion for how large or small the value should be, has yet been decided. The scaling behaviour of erraticity moments has so far been verified in several high energy hadronic and nuclear interactions [10, 11, 13, 14], but the reason for such chaotic nature of fluctuation in event space is far from clear. Thus the problem has to be investigated by comparing experimental results with model calculations with probable mechanisms of particle production as input. While in case of hadronic interactions such comparisons do exist in literature

[9–12], for high energy AB interactions it is virtually nonexistent.

In another method, the erraticity moments of phase-space variable gaps are computed [15] to study the event-to-event fluctuation. To some extent this method is complementary to that suggested in [8, 9]. In an event occurrence of large spikes in an event will naturally be accompanied with large gaps as a compensating feature to result in a finite multiplicity in that event. As far as mechanism of particle production is concerned, often these gaps contain more information than the spikes. When the average multiplicity per event is high, $C_{p,q}$ is more suitable; on the other hand if the average multiplicity of produced particles is small, or the analysis is made in such a restricted region of phase-space that the average multiplicity is not too large, the method of phase-space gaps is a useful tool to investigate the chaotic behavior. This method has also been tested for AB and hh interactions [11, 13, 16] though a complete analysis of all gap moments, can not be found in any of these works. In this chapter we have also incorporated a study on the moments of gap distribution of produced charged particles in $^{32}\text{S-Ag/Br}$ interactions at 200A GeV/c. Objectives of the present work are therefore, (i) to comprehensively investigate the erraticity characteristics of particle production in $^{32}\text{S-Ag/Br}$ interactions at 200A GeV/c, (ii) to compare the experimentally obtained results with those obtained from the LUND Monte-Carlo model for high-energy AB interaction FRITIOF [17], as well as in some cases with those obtained by generating simple random numbers, and (iii) to analyze the same data on $^{32}\text{S-Ag/Br}$ interaction in terms of erraticity of gap distribution.

5.2 Erraticity of particle distribution

The methodology used to analyze distribution of produced particles in terms of "erraticity", has been discussed in details elsewhere [8, 9]. Here we are presenting a short account of the same technique for the sake of completeness without any claim for originality. The single event factorial moment F_q^e of order q (essentially a positive integer) is defined as,

$$F_q^e = \frac{\frac{1}{M} \sum_{m=1}^M n_m (n_m - 1) \cdots (n_m - q + 1)}{(\bar{n}_m)^q}, \quad (5.1)$$

where $\bar{n}_m = M^{-1} \sum_{m=1}^M n_m$ is the average bin multiplicity in that event when the entire phase-space interval ΔX has been divided into M equal intervals. If X is a cumulant variable [18], then $\delta X = M^{-1}$ is the bin size. F_q^e fluctuates from event to event and the

degree of fluctuation can be estimated from the probability distribution $P(F_q^e)$ over all events. For this purpose, a new moment for the single event is introduced as,

$$\Phi_q = \frac{F_q^e}{\langle F_q^e \rangle}$$

that is normalized by $\langle F_q^e \rangle$ - the event space (vertical) average of F_q^e , and is determined from the distribution $P(F_q^e)$.

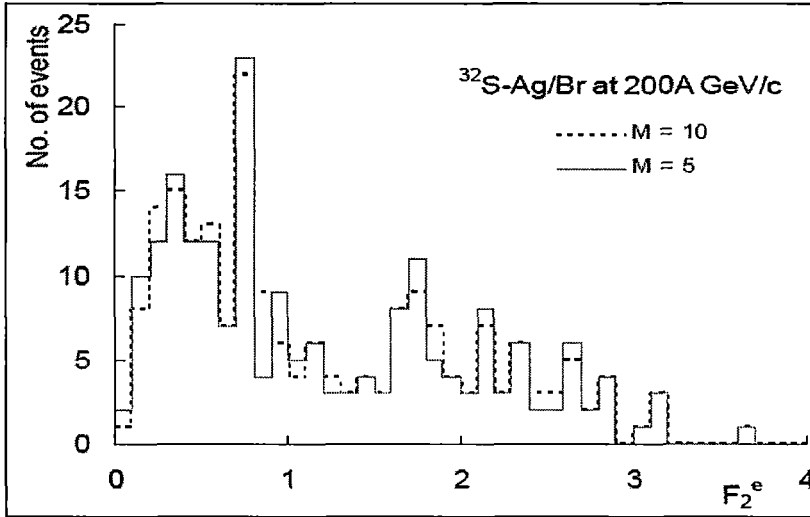


Figure 5.1: Distribution of single event SFM of second order F_2^e for all 200 events in the sample of $^{32}\text{S-Ag/Br}$ interaction at 200A GeV/c.

One can now define the vertically averaged p^{th} -order moment of the normalized q^{th} -order factorial moment as,

$$C_{p,q} = \langle \Phi_q^p \rangle$$

where the $\langle \dots \rangle$ sign once again denotes an averaging over the event space, and p can be any number. Note that $C_{p,q}$ is not the pq th order moment of multiplicity, but is the erraticity moment that measures event-to-event fluctuation of F_q^e . If now one observes $C_{p,q}$ to follow a generalized power law like

$$C_{p,q} \propto M^{\psi_q(p)}, \quad (5.2)$$

the phenomenon is then referred to as the erraticity of nonstatistical fluctuation, and $\psi_q(p)$ is called the erraticity exponent. If the spatial pattern never changes from event-to-event, $C_{p,q} = 1$ and $\psi_q(p) = 0$ for all M, p and q . Large $\psi_q(p)$ is associated with more erratic fluctuation of the spatial distribution of particles. The slope,

$$\mu_q = \left. \frac{d}{dp} \psi_q(p) \right|_{p=1} \quad (5.3)$$

termed as the entropy index, is an efficient parameter to characterize erraticity. We can also determine an entropy like quantity Σ_q directly from Φ_q as,

$$\Sigma_q = \langle \Phi_q \ln \Phi_q \rangle \quad (5.4)$$

that can be used to find out the entropy index from another relation,

$$\mu_q = \frac{\partial \Sigma_q}{\partial \ln M} \quad (5.5)$$

provided $C_{p,q}$ exhibits an exact scaling behavior as in Eq. (5.2). On the other hand, if $C_{p,q}$ does not obey an exact scaling behavior like Eq. (5.2), one may take the liberty of introducing a more general form of power law behavior,

$$C_{p,q}(M) \propto g(M)^{\bar{\psi}(p,q)} \quad (5.6)$$

where $g(M)$ is a function of M . Even if such a relation is only approximately valid for a common $g(M)$ but for all p and q , one can express Σ_q as,

$$\Sigma_q(M) \propto \bar{\mu}_q \ln g(M), \quad (5.7)$$

where

$$\bar{\mu}_q = \left. \frac{d}{dp} \bar{\psi}_q(p) \right|_{p=1} \quad (5.8)$$

Under such circumstances we also expect a linear dependence of Σ_q on Σ_2 . The slope for such dependence is denoted by,

$$\omega_q = \partial \Sigma_q / \partial \Sigma_2 \quad (5.9)$$

and it automatically follows that,

$$\bar{\mu}_q = \bar{\mu}_2 \omega_q \quad (5.10)$$

It should be noted that, $\bar{\mu}_q$ and the previously introduced entropy parameter μ_q are entirely different quantities, and therefore they can not be compared with each other.

5.3 Results on Erraticity of particle distribution

In Fig. 5.1 the frequency distributions of single event factorial moments F_2^e computed in η space have been shown for $M = 5$ and 10 for $^{32}\text{S-Ag/Br}$ interactions. For a particular M , the entire range of F_2^e values is divided into a number of smaller groups. These frequency distributions are obtained by plotting the number within each such group against the corresponding F_2^e range. Though majority of the F_2^e values are found to be confined within a limited range, a significant number of large F_2^e values are also encountered in the distribution. It is these fluctuations, that can be quantified in terms of the erraticity moments and erraticity parameters related to the chaotic behaviour of multiparticle production dynamics. In Fig. 5.2 (a) - (e) the experimentally obtained erraticity moments on $^{32}\text{S-Ag/Br}$ interaction are graphically plotted as functions of $\ln M$ for $q = 2$ to 6, and for $p = 0.5, 0.9, 1.2, 1.4,$ and 1.6 . Corresponding FRITIOF predictions are shown in Fig. 5.2(f) - (j). From these diagrams the following points may be noted. As the relevant erraticity parameters can all be derived from the variation pattern of the erraticity moments in the neighbourhood of $p = 1$, the analysis has been performed and the graphs are drawn only around that region. In general a nonlinear dependence of $\ln C_{p,q}(M)$ on $\ln M$ can be observed, a feature that is more prominent for moments with $p < 1$ than for moments with $p > 1$. For larger values of order of spatial fluctuation i.e., $q = 5$ or 6 and for $p > 1$, saturation effects in $\ln C_{p,q}(M)$ values can be seen in the higher $\ln M$ region both for the experimental and simulated data sets. This feature can be attributed to the finiteness in particle number per event. With increasing M lesser number of events contribute to the moments of higher order. A few kinks can also be found in these plots, which probably are results of fluctuations in particle number with changing interval size in a particular event. This effect can be substantially reduced by accumulating larger statistics. However, on an average a heavy-ion event has larger shower multiplicity than a hadronic interaction at same energy, and therefore, in a heavy-ion event the bin-to-bin fluctuation of multiplicity is not so large as a hadronic event. For each q , the standard statistical errors due to event-to-event fluctuation of the scaled factorial moments are computed, and these errors are graphically shown only for the highest and the lowest values of p . For the FRITIOF generated events the pattern of variation of $\ln C_{p,q}(M)$ on $\ln M$ is more or less similar to that of the experiment, but the magnitudes of erraticity moments are always significantly

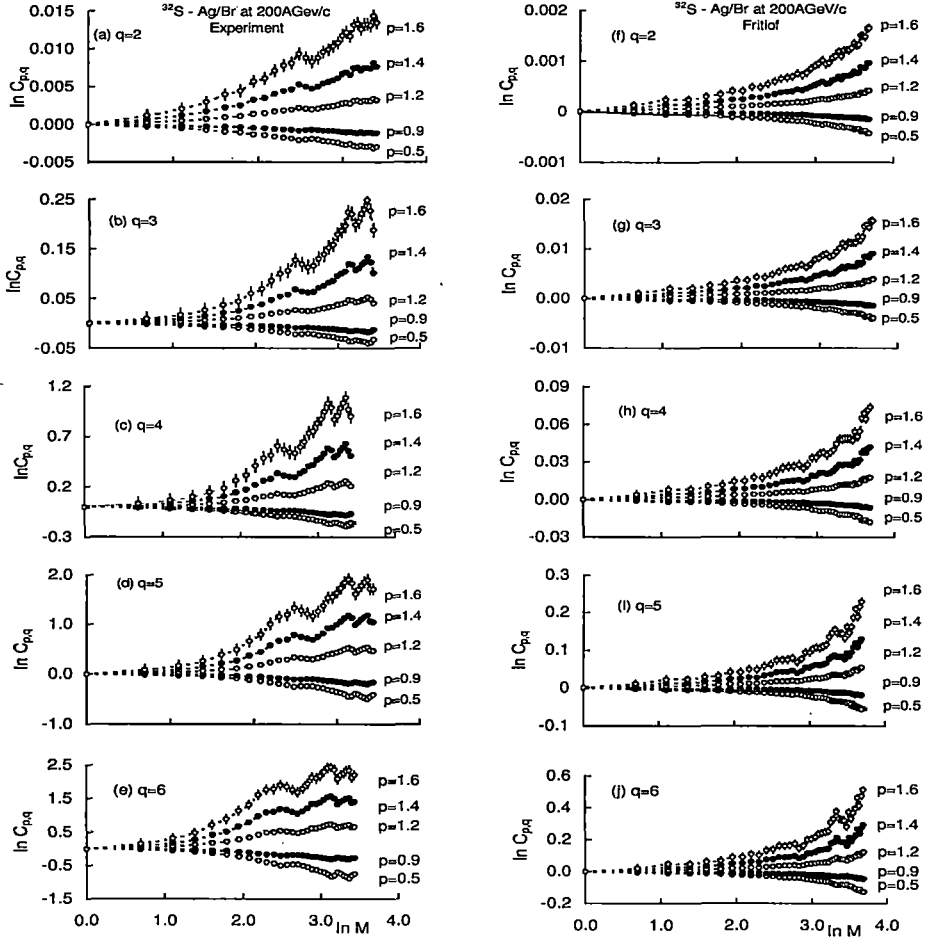


Figure 5.2: Erraticity moments $C_{p,q}$ plotted against phase-space partition number M . Whereas, (a)-(e) show experimental results, in (f)-(j) corresponding FRITIOF predictions are graphically presented.

and consistently less than in the experiment. In our work a generalized scaling form as given by Eq. (5.6) has been used. It was emphasized by Cao and Hwa [9] that, a common function $g(M)$ may not always best represent the variation of $C_{p,q}(M)$ with M for all p and all q . As a possible functional form for $g(M)$, they suggested $\ln g(M) = (\ln M)^b$, and as a consequence $\ln C_{p,q}$ for $q > 2$ will automatically be linear against $\ln C_{2,2}$. The best linear dependence of $\ln C_{2,2}$ on $\ln g(M)$ can be obtained by adjusting the value of b . In case of ^{32}S -Ag/Br interactions this has been achieved with $b = 2.08$ for the experiment, with $b = 3.06$ for the FRITIOF, and $b = 3.60$ for the random number generated sample.

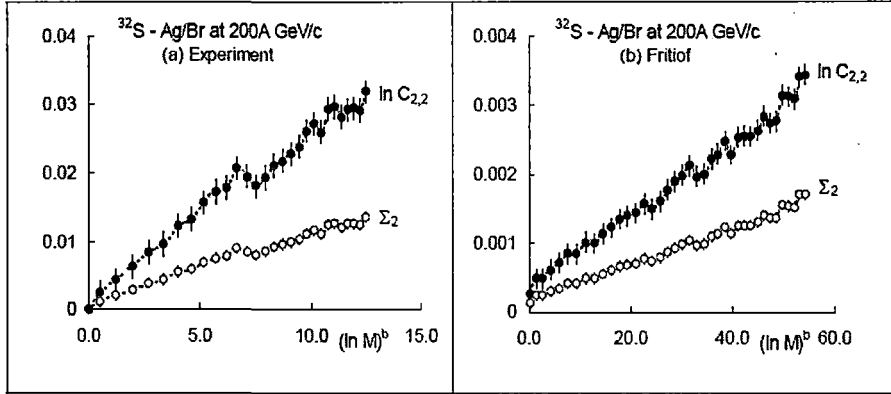


Figure 5.3: Generalized scaling of $C_{2,2}$ with respect to M . The entropy like quantity Σ_2 has also been included in the diagrams - (a) The experimental result, (b) the FRITIOF prediction. The scale difference between (a) and (b) is to be noticed.

In Fig. 5.3(a) and (b) results of the best linear fit of the experimental data sets, and the corresponding FRITIOF predictions are graphically plotted. From Eq. (5.6) one can readily see that, the slope of the linear variation of $\ln C_{2,2}$ on $\ln g(M)$ gives the value of the erraticity parameter $\bar{\psi}_2(2)$. In the present case the values are, $\bar{\psi}_2(2) = 2.91 \times 10^{-3} \pm 7.2 \times 10^{-5}$ for the experiment, $\bar{\psi}_2(2) = 5.3 \times 10^{-5} \pm 9.9 \times 10^{-7}$ for the FRITIOF, and $\bar{\psi}_2(2) = 2.9 \times 10^{-5} \pm 1.2 \times 10^{-6}$ for the random number.

As mentioned above, instead of using $\ln M$ one can as well use $\ln C_{2,2}$ as the independent variable, and hence can obtain a linear dependence of $\ln C_{p,q}$ on $\ln C_{2,2}$. Such plots for the experimental data set can be found in Fig. 5.4(a) - (e) for $q = 2$ to 6, and for $p = 0.5, 0.9, 1.2, 1.4$ and 1.6. Corresponding FRITIOF results are shown in Fig. 5.4 (f) - (j). For experiment the linear dependence of $\ln C_{p,q}$ on $\ln C_{2,2}$ is acceptable until $q = 4$. At $q = 5$ and 6, early saturation effects are observed in $\ln C_{p,q}$ against $\ln C_{2,2}$ plot on experiment. In these cases for all q linear dependence of $\ln C_{p,q}$ on $\ln C_{2,2}$ has been obtained only within a limited region, e.g., $0.01 < \ln C_{2,2} < 0.02$. Corresponding range of phase-space partition number would be from $M = 10$ to 25. In all these cases the Pearson's r^2 values obtained for the best linear regression between the independent and the dependent variables are close to 0.9 to ensure a reasonably good linear dependence between these variables. The FRITIOF diagrams however shows more linearity over an

wider range of $\ln M$, q and p in the variation of $\ln C_{p,q}$ against $\ln C_{2,2}$.

$$C_{p,q} \propto (C_{2,2})^{\chi(p,q)}$$

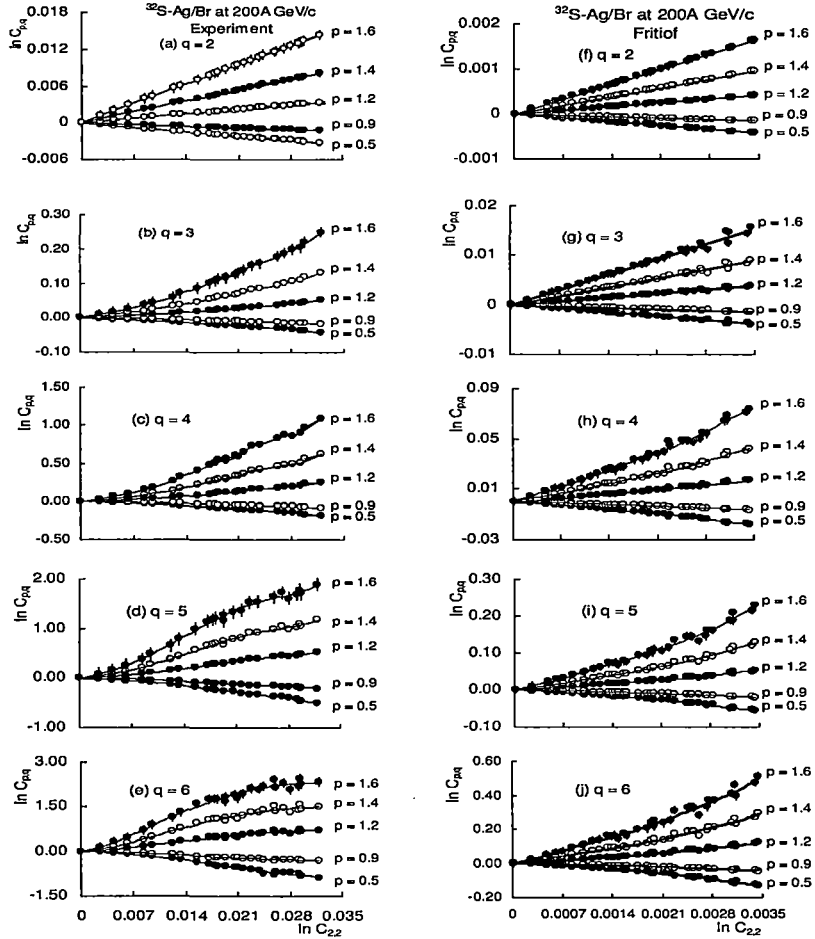


Figure 5.4: $\ln C_{p,q}$ plotted against $\ln C_{2,2}$: (a)-(e) experiment, (f)-(j) FRITIOF. For experiment the expected linearity holds good for low q while saturation crops up at $q = 5, 6$. No such saturation effect is observed for the FRITIOF result.

Therefore, one can conclude that a scaling behaviour like, is obeyed by the erraticity moments. For each q and for different p values, the exponent $\chi(p, q)$ are obtained from the best linear dependence of $\ln C_{p,q}$ against $\ln C_{2,2}$, and thereafter these values are fitted with a quadratic function of p like,

$$\chi(p, q) = \alpha_q p^2 + \beta_q p + \gamma_q. \quad (5.11)$$

A plot showing such variations of $\chi(p, q)$ on p along with the best fitted quadratic functions are presented in Fig. 5.5. Derivatives the quadratic functions at $p = 1$ namely,

$$\chi_q' = \left. \frac{d}{dp} \chi(p, q) \right|_{p=1}$$

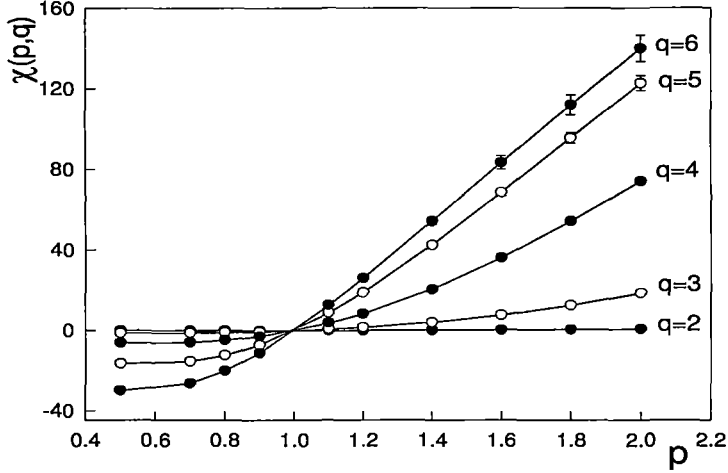


Figure 5.5: Erraticity parameter $\chi_{p,q}$ plotted against p . The solid curves are best fitted quadratic function given in Eq. (5.11)

provide us with another erraticity parameter χ_q' , values of which are listed in Table 5.1. Using the following relation we are now in a position to derive the entropy index $\bar{\mu}_q$,

$$\bar{\mu}_q = \bar{\psi}_2(2)\chi_q'. \quad (5.12)$$

The values of $\bar{\mu}_q$ calculated through Eq. (5.10) and (5.12) are both included in Table 5.1. As has been pointed out in the methodology section, making use of Eq. (5.10) one can derive the $\bar{\mu}_q$ values in another way. Keeping in mind that $\ln g(M) = (\ln M)^b$, and setting the values of b as obtained before, a linear dependence of Σ_2 against $\ln g(M)$ can also be obtained. Along with $\ln C_{2,2}$ the Σ_2 values are also plotted against $\ln g(M)$ in Fig. 5.3(a) and (b) for $^{32}\text{S-Ag/Br}$ experimental data set and for the corresponding FRITIOF data set. The slope of the best fitted straight line directly gives us μ_2 . As expected, Σ_q should linearly rise with Σ_2 . Graphical plots showing variation of Σ_q against Σ_2 is presented in Fig. 5.6(a) and (b). Slopes of the best fitted straight lines (ω_q) obtained from these graphs were used to derive $\bar{\mu}_q$ from Eq. (5.10). The values of ω_q and $\bar{\mu}_q$ are also incorporated

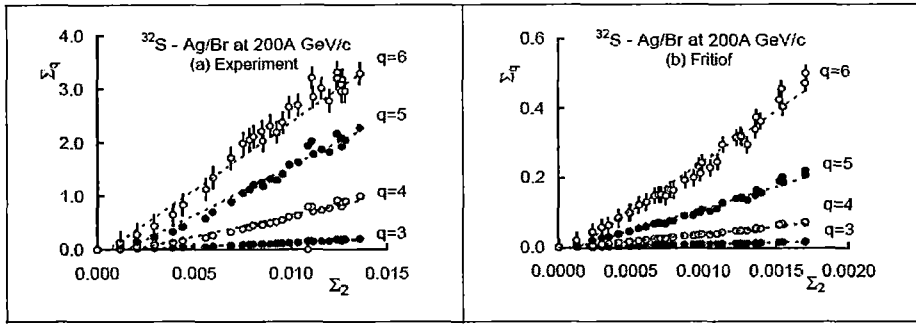


Figure 5.6: Linearity between $\Sigma_q : q \geq 3$ and Σ_2 is schematically presented - (a) Experiment, and (b) FRITIOF.

into Table 5.1. In Fig. 5.7(a) - (d) all erraticity parameters namely, χ'_q , ω_q and $\bar{\mu}_q$ have been graphically plotted against q for all three data sets i.e., experimental, FRITIOF and random number. For the FRITIOF and random number generated events, the variation

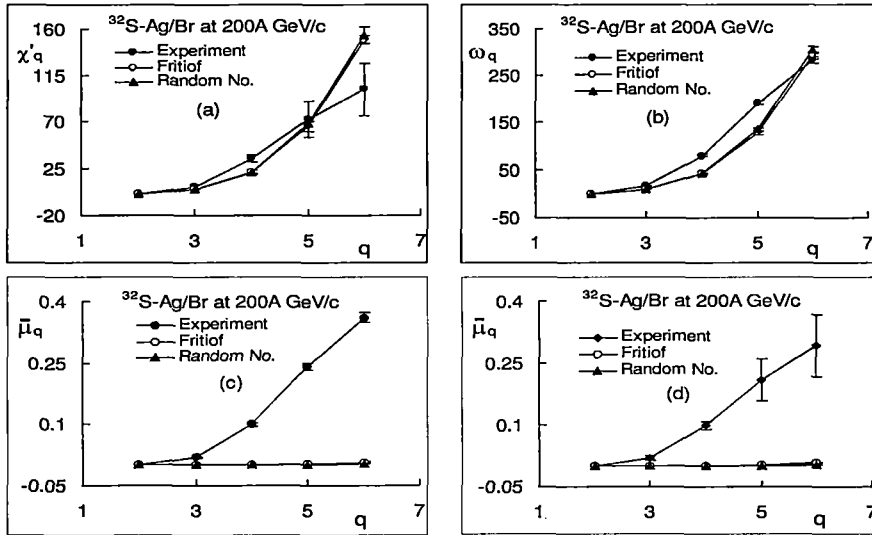


Figure 5.7: Erraticity parameters for the experimental data set as well as for the FRITIOF generated data set are plotted against order q .

patterns of all erraticity parameters are more or less similar. As expected the experimental results exhibit different trends. A closer look into these graphs shows that the

χ'_q and ω_q values for both kind of generated data increase systematically with q , whereas corresponding experimental values after showing a similar initial trend, differ significantly from the generated results at $q = 6$. On the other hand ω_q which increases systematically for all data sets, again shows significant difference between experimental and generated results at $q = 4$ and 5. Large differences can be observed in the variation of the entropy index $\bar{\mu}_q$ with q between the generated data and the experimental data. Values of

Table. 5.1. Erraticity parameters in $^{32}\text{S-Ag/Br}$ interactions at 200A GeV/c. $\bar{\mu}_q$ values presented in the third row are based on Eq. (5.10), whereas those in the fourth row are computed by Eq. (5.12).

Parameter	Experiment	FRITIOF	Random number
χ'_2	0.437 ± 0.054	0.497 ± 0.003	0.492 ± 0.006
χ'_3	7.06 ± 1.74	4.76 ± 0.11	4.66 ± 0.171
χ'_4	33.98 ± 3.17	21.61 ± 1.38	21.64 ± 2.10
χ'_5	72.26 ± 17.37	65.47 ± 4.95	67.74 ± 7.13
χ'_6	101.07 ± 25.68	149.50 ± 3.89	154.00 ± 7.81
ω_2	1.00	1.00	1.00
ω_3	15.55 ± 0.54	9.48 ± 0.09	9.37 ± 0.11
ω_4	79.63 ± 3.33	42.42 ± 0.77	43.08 ± 0.73
ω_5	191.20 ± 5.00	127.70 ± 3.00	134.90 ± 2.91
ω_6	282.70 ± 7.53	292.40 ± 7.60	305.00 ± 7.24
$\bar{\mu}_2$	0.00126 ± 0.000029	0.000026 ± 0.00000049	0.000014 ± 0.00000056
$\bar{\mu}_3$	0.0195 ± 0.0008	0.00025 ± 0.0000052	0.000134 ± 0.0000054
$\bar{\mu}_4$	0.10 ± 0.0048	0.00112 ± 0.000029	0.00062 ± 0.000026
$\bar{\mu}_5$	0.24 ± 0.0084	0.00336 ± 0.0001	0.00193 ± 0.000086
$\bar{\mu}_6$	0.36 ± 0.0125	0.00769 ± 0.00025	0.00437 ± 0.0002
$\bar{\mu}_2$	0.00127 ± 0.00016	0.000026 ± 0.00000051	0.000014 ± 0.00000061
$\bar{\mu}_3$	0.0205 ± 0.0051	0.00025 ± 0.0000056	0.000136 ± 0.0000074
$\bar{\mu}_4$	0.099 ± 0.0095	0.00115 ± 0.000042	0.00063 ± 0.000066
$\bar{\mu}_5$	0.21 ± 0.051	0.00347 ± 0.00016	0.00197 ± 0.00022
$\bar{\mu}_6$	0.293 ± 0.075	0.00793 ± 0.00018	0.0045 ± 0.00029

entropy indexes obtained from the FRITIOF and random number generated samples change similarly, showing marginal rise in their values with increasing q . The experimentally obtained values of $\bar{\mu}_q$ for the ^{32}S experimental event sample systematically increase with q , and they are consistently higher than the corresponding simulated values for almost all $q (> 2)$. Within statistical uncertainties values of $\bar{\mu}_q$ calculated in two different ways quite i.e., either using Eq. (5.10) or (5.12), reasonably agree with each other.

5.4 Erraticity of gap distribution

In the erraticity analysis of gap distribution, an event with n produced particles is considered. The gap (x_i) between two neighbouring particles (in our case the shower tracks), is defined as the difference in their cumulative variables $X(\eta)$ in the same event,

$$x_i = X_{i+1} - X_i, \quad i = 0, 1, 2, 3 \dots, n.$$

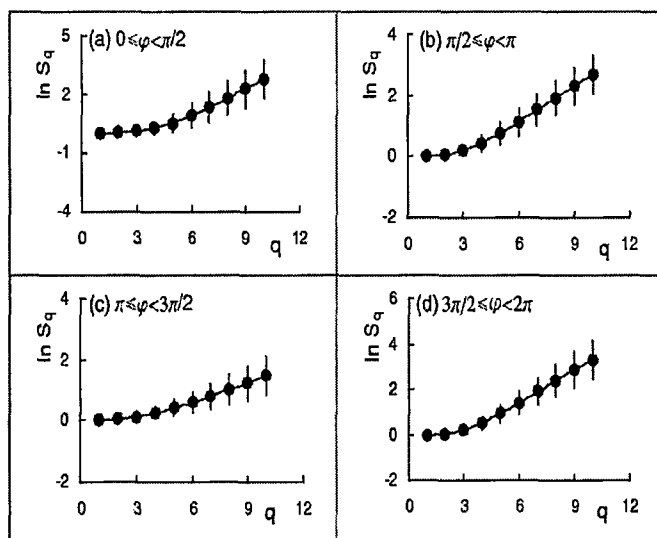


Figure 5.8: S_q moments plotted as functions of q in all four φ quadrants. The solid curves represent quadratic functions like Eq. (5.20).

Note that $X_{i+1} > X_i$, $\sum_0^n x_i = 1$, whereas, $X_0 = 0$ and $X_{n+1} = 1$ are the boundaries. For a single event two gap moments G_q and H_q are defined, respectively as,

$$G_q = \frac{1}{n+1} \sum_{i=0}^{i=n} (x_i)^q, \quad (5.13)$$

and

$$H_q = \frac{1}{n+1} \sum_{i=0}^{i=n} (1-x_i)^{-q}, \quad (5.14)$$

where $n \geq q+1$. These moments provide us with a quantitative characteristic of a single event. Here the order of the moment q is an integer, and it is clear that G_q is always less than unity whereas, H_q is always greater than unity. As the moments G_q and H_q fluctuate from event to event, Hwa and Zhang [15] proposed to consider the sample averaged quantities s_q and σ_q as,

$$s_q = -\langle G_q \ln G_q \rangle, \quad (5.15)$$

and

$$\sigma_q = -\langle H_q \ln H_q \rangle, \quad (5.16)$$

to characterize the event-to-event fluctuation of these quantities. In defining s_q and σ_q the statistical fluctuations are not excluded. The contribution from statistical fluctuations can be minimized by eliminating them in the following manner. One may calculate,

$$s_q^{st} = -\langle G_q^{st} \ln G_q^{st} \rangle,$$

and

$$\sigma_q^{st} = -\langle H_q^{st} \ln H_q^{st} \rangle,$$

where G_q^{st} and H_q^{st} are obtained using Eq. (5.13) and Eq. (5.14) from a purely statistical distribution i.e, when all n particles in an event are randomly distributed in X -space within a limit of $0 \leq X \leq 1$. The multiplicity distribution of the random number generated sample within the phase-space interval under consideration, should match with that of the experiment. Finally one defines two moments of gap distribution, normalized by the respective statistical contributions as,

$$S_q = \frac{s_q}{s_q^{st}}, \quad \text{and} \quad \Sigma_q = \frac{\sigma_q}{\sigma_q^{st}}. \quad (5.17)$$

These moments indicate how much s_q and σ_q stand out above the corresponding statistical contributions. One can also calculate the deviation of G_q and H_q from the respective event sample averaged quantities $\langle G_q \rangle$ and $\langle H_q \rangle$, and another set of moments \bar{s}_q and $\bar{\sigma}_q$ are defined as a measure of such deviations in the following manner,

$$\bar{s}_q = -\left\langle \frac{G_q}{\langle G_q \rangle} \ln \frac{G_q}{\langle G_q \rangle} \right\rangle \quad (5.18)$$

and

$$\bar{\sigma}_q = - \left\langle \frac{H_q}{\langle H_q \rangle} \ln \frac{H_q}{\langle H_q \rangle} \right\rangle. \quad (5.19)$$

These moments can once again be normalized by the corresponding statistical contributions as,

$$\bar{S}_q = \frac{\bar{s}_q}{\bar{s}_q^{st}}, \quad \text{and} \quad \bar{\Sigma}_q = \frac{\bar{\sigma}_q}{\bar{\sigma}_q^{st}},$$

respectively, to provide another set of erraticity moments of gap distribution.

5.5 Results on Erraticity of Gap Distribution

As mentioned above, the erraticity analysis of gaps provides information, that is complementary to the analysis of spikes in the phase-space distribution. But gap analysis is not very effective for events with very high multiplicity. For heavy-ion interaction in most cases the event multiplicity is high. Therefore, one needs to make a severe cut on the domain of analysis, so that the average multiplicity under consideration is never too large. In the present case the analysis has been performed in a central particle producing region given by, $\eta_0 - 1 \leq \eta \leq \eta_0 + 1$. The peak of a Gaussian fit to the experimental η distribution of shower tracks occurs at $\eta_0 = 3.37$. The phase-space domain has further been reduced by partitioning the φ space into four quadrants namely, (i) $0 \leq \varphi < \pi/2$, (ii) $\pi/2 \leq \varphi < \pi$, (iii) $\pi \leq \varphi < 3\pi/2$, and (iv) $3\pi/2 \leq \varphi < 2\pi$. After η cut the average shower multiplicity $\langle n_s \rangle$ in each of these quadrants came out, respectively to be (i) 25.37 ± 0.84 , (ii) 26.65 ± 0.98 , (iii) 26.43 ± 1.00 , (iv) 25.89 ± 0.94 - values that are not too large to make the gap analysis ineffective. Values of the cumulative variable $X(\eta)$ for the shower tracks have been obtained belonging to each quadrant separately. The results of erraticity analysis on gap distribution of shower tracks from $^{32}\text{S-Ag/Br}$ interactions at 200A GeV/c starts with a graphical representation of the S_q moments. In Fig. 5.8 the $\ln S_q$ values have been plotted against q for all four quadrants of azimuthal angle φ , and for $q = 2$ to 10 in each case. The error associated with each data point is statistical in nature. They are computed by following standard methods with an assumption that, unlike the SFM or multifractal moments no $X(\eta)$ subinterval is considered to compute the single event G_q . Therefore, it is a number with very small statistical error. Though the experimentally obtained values of S_q are associated with large statistical errors, one

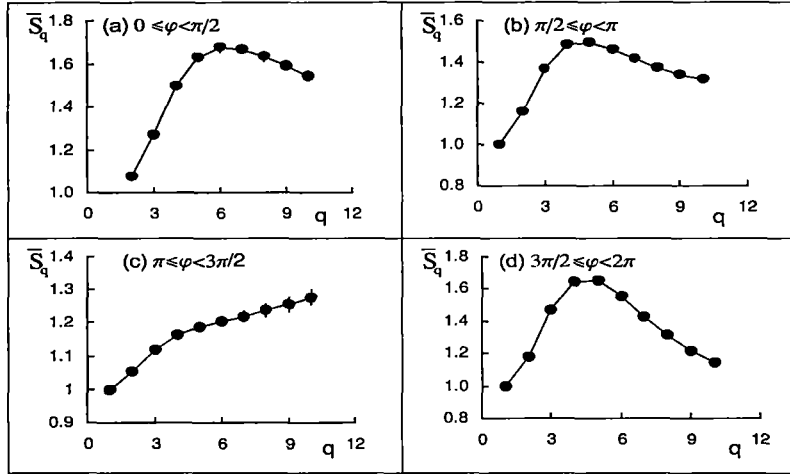


Figure 5.9: \bar{S}_q moments plotted against q in all four φ quadrants. Note that except $q = 2$ the moments are always significantly different from unity. The errors (statistical) are often too small to show, and the solid curves are drawn to guide the eye.

can see from the graphs that, with increasing q the $\ln S_q$ values are deviating more and more from zero. The change in $\ln S_q$ with q has been parameterized by using a quadratic form, for $2 \leq q \leq 10$. The values of α , β and γ along with the Pearson's r^2 co-efficients are listed in Table 5.2, showing that the fit is reasonably good in each case. In Fig. 5.9 the \bar{S}_q moments are plotted against q for all four quadrants of φ for $q = 2$ to 10. One can see that the \bar{S}_q values always deviate from unity beyond statistical uncertainties, which are always very small in this case. The variation of \bar{S}_q with q does not follow any unique pattern. While for the first, second and fourth quadrants maxima in \bar{S}_q occur around $q = 4$ to 6, in the third quadrant only a monotonic rise of \bar{S}_q with increasing q can be seen.

$$\ln S_q = \alpha + \beta q + \gamma q^2, \quad (5.20)$$

Fig. 5.10 shows the graphical plots of erraticity moments Σ_q against q for all four quadrants of azimuthal angle and for $q = 1$ to 10. Like S_q in this case also large statistical errors can be seen, particularly in higher q region. The variation of Σ_q with q has been parameterized in the same way as has been done in the case of S_q using Eq. (5.20). The values of the parameters as well as the r^2 values are given in Table 5.2. One can see that in this case also the fit of a quadratic curve to experimental data has always been good.

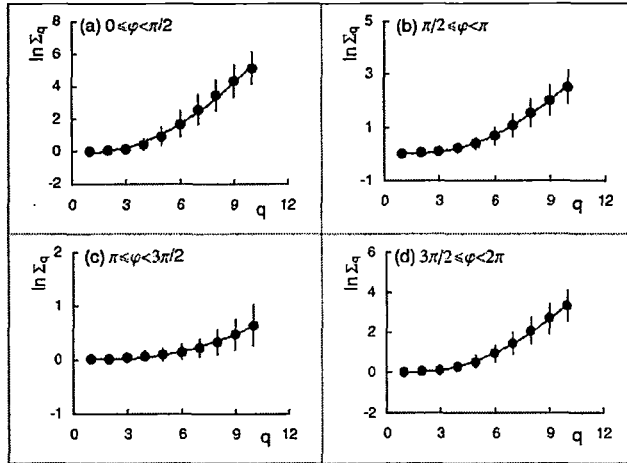


Figure 5.10: Gap distribution moments Σ_q plotted against q in four φ quadrants. The solid curves represent a quadratic function like in Eq. (5.20).

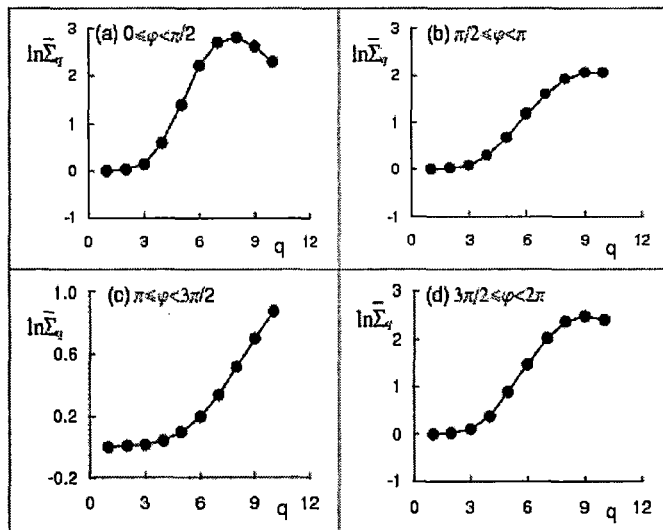


Figure 5.11: Gap distribution moments $\bar{\Sigma}_q$ plotted against q in four φ quadrants. The solid curves are drawn to guide the eye.

In Fig. 5.11 the last set of erraticity moments $\bar{\Sigma}_q$ has been graphically represented by plotting $\ln \bar{\Sigma}_q$ against q for $q = 1$ to 10, and for each of the four quadrants of φ . Once again no definite pattern in the variation of these moments is observed, except the fact

that in the region $1 \leq q \leq 7$, the increase of $\ln \bar{\Sigma}_q$ with q in each quadrant is quadratic in nature. Once again like in the case of \bar{S}_q , very small statistical errors are associated with $\ln \bar{\Sigma}_q$ values.

Table. 5.2. Fit results from Eq. (5.20) for two sets of erraticity moments of gap distribution.

Moment	$\Delta\varphi$	α	β	γ	r^2
S_q	$0 \leq \varphi < \pi/2$	-0.07 ± 0.09	-0.03 ± 0.03	0.03 ± 0.003	0.998
	$\pi/2 \leq \varphi < \pi$	-0.40 ± 0.10	0.16 ± 0.04	0.15 ± 0.03	0.998
	$\pi \leq \varphi < 3\pi/2$	-0.14 ± 0.02	0.06 ± 0.01	0.01 ± 0.0007	1.000
	$3\pi/2 \leq \varphi < 2\pi$	-0.54 ± 0.15	0.22 ± 0.06	0.02 ± 0.005	0.997
Σ_q	$0 \leq \varphi < \pi/2$	-0.05 ± 0.02	-0.10 ± 0.08	0.06 ± 0.007	0.994
	$\pi/2 \leq \varphi < \pi$	0.13 ± 0.04	-0.13 ± 0.02	0.04 ± 0.001	0.999
	$\pi \leq \varphi < 3\pi/2$	0.07 ± 0.02	-0.05 ± 0.01	0.01 ± 0.001	0.994
	$3\pi/2 \leq \varphi < 2\pi$	0.13 ± 0.06	-0.15 ± 0.03	0.05 ± 0.002	0.998

5.6 Discussion

The erraticity analysis shows signature of chaotic behaviour of spatial fluctuation in multi-particle production mechanism in $^{32}\text{S-Ag/Br}$ interactions. Substantial amount of event-to-event fluctuations of factorial moments are observed in the experiments. The fluctuations resulted in a power law scaling variation of the erraticity moments $C_{p,q}$ and Σ_q . Results of FRITIOF and random number generated data sets significantly differ from the corresponding experimental one. We therefore, conclude that the entropy index μ_q is the most suitable parameter to compare experimental results with model predictions, as it amply reflects the inadequacy of the model prediction in our case. Neither an independent emission model, nor a string fragmentation mechanism of particle production can account for the variation of μ_q for the present set of data. While effects of two-particle correlation have been taken into consideration in the FRITIOF, such effects can not completely account for the outcome of heavy-ion interactions. Therefore, it is not surprising that a smooth model like the FRITIOF also fails to predict the observed event-to-event fluctuation of scaled factorial moments, as in this regard no dynamical input has been

introduced into the code. Consequently the FRITIOF predictions are similar to those obtained from random numbers. This suggests that the QCD branching processes associated with particle production are more chaotic for the experiment than for both of the corresponding generated data sets. Observed fluctuations of scaled factorial moments need to be addressed with new physics as input. Experimental values of the erraticity parameters given in Table 5.1 may be used for this purpose. On the other hand, in the present case experimental values of μ_q are significantly smaller than those involving hadrons and nucleons [10, 11, 13]. This indicates that there is more fluctuation in the distribution of F_q^e over event space for the present set of experimental data, than in any other hadronic or nuclear collision investigated so far. Since the emulsion data do not allow us to make a transverse momentum p_t cut in the η distribution of produced particles, at this stage it is not possible to decide whether or not some kind of phase transition is responsible for the observed fluctuations.

The analysis on gap distribution of shower tracks emitted from $^{32}\text{S-Ag/Br}$ interactions at 200A GeV/c shows that, event-to-event fluctuation of gap moments G_q and H_q , exists over the corresponding statistical contribution. The conclusion is based on the fact that, all entropy like erraticity parameters suggested by Hwa and Zhang [15] namely, S_q , \bar{S}_q , Σ_q and $\bar{\Sigma}_q$ deviate significantly from unity beyond their standard errors. In general the erraticity moments behave in a more or less similar way in all four quadrants of the azimuthal angle within the central η region. In view of comparatively smaller errors associated with \bar{S}_q and $\bar{\Sigma}_q$, we conclude that in the present case these parameters provide a better measure of erraticity than S_q or Σ_q . It should be noted that, \bar{S}_q and $\bar{\Sigma}_q$ contain information about how much the gap moments, G_q and H_q deviate from their average values $\langle G_q \rangle$ and $\langle H_q \rangle$, respectively. The other two parameters S_q and Σ_q have been found to increase with increasing q , showing a quadratic variation in each case. The exact nature of these variations or the exact values of fit parameters α , β and γ are not much important. It would however be interesting to compare the present experimental results on erraticity analysis of gap distribution of produced charged hadrons with those obtained from other experiments, as well as with the results from event sample generated by computer codes based on some realistic model on relativistic heavy-ion interactions, that takes into account all possible sources of fluctuations. As far as erraticity of rapidity

gaps is concerned, event generators like PYTHIA or ECOMB underestimate the experimental on hadronic interactions, even after the Bose-Einstein correlation has been taken into account as a possible source of dynamical fluctuation. Such a comparison is yet to be made in case of heavy-ion interactions, where the collision mechanism is much more complex involving a large number of hadrons, and the number of participating nucleons being dependent on the collision geometry. By choosing only those interactions where complete break-up of the projectile nucleus has taken place, an effort has certainly been made in the present investigation to restrict the collision geometry within a certain limit as can be seen above, from the estimated average value of the impact parameter for the event sample.

Bibliography

- [1] JACEE Collaboration, T. H. Burnett *et al.*, *Phys. Rev. Lett.* **50**, 2062 (1983).
- [2] A. Bialas and R. Peschanski, *Nucl. Phys. B* **273**, 703 (1986); **308**, 857 (1988).
- [3] B. Buschbeck, R. Lipa, and R. Peschanski, *Phys. Lett. B* **215**, 788 (1988)
W. Braunschweig *et al.*, *Phys. Lett. B* **231**, 548 (1988).
- [4] I. Derado, G. Jansco, N. Schmitz, and P. Stopa, *Z. Phys. C* **47**, 23 (1990).
- [5] NA22 Collaboration, I.V. Ajinenko *et al.*, *Phys. Lett. B* **222**, 306 (1989).
- [6] KLM Collaboration, R. Holynski *et al.*, *Phys. Rev. Lett.* **62**, 733 (1989)
EMU-01 Collaboration, M. I. Adamovich *et al.*, *Phys. Lett. B* **263**, 539 (1991); *Nucl. Phys. B* **388**, 3 (1992).
- [7] R. C. Hwa, *Phys. Lett. B* **201**, 165 (1988)
I. M. Dremin, *JETP Lett.* **30**, 152 (1980); *Sov. Jr. of Nucl. Phys.* **33**, 726 (1981)
W. Ochs and J. Wosiek, *Phys. Lett. B* **214**, 617 (1988)
B. Andersson, P. Dahlquist and G. Gustafson, *Phys. Lett. B* **214**, 604 (1988)
B. C. Chiu and R. C. Hwa, *Phys. Lett. B* **236**, 466 (1990)
E. A. De Wolf and W. Kittel, *Soft Multihadron Dynamics* (World Scientific, Singapore, 2005).
- [8] Z. Cao and R.C. Hwa, *Phys. Rev. Lett.* **75**, 1268 (1995); *Phys. Rev. D* **53**, 6608 (1996);
Phys. Rev. E **56**, 326 (1997).
- [9] Z. Cao and R.C. Hwa, *Phys. Rev. D* **61**, 074011 (2000).
- [10] EHS/NA22 Collaboration, M.R. Atayan *et al.*, **HEN 450** (2003).

- [11] W. Shaoshun and W. Zhaomin, *Phys. Rev. D* **57**, 5 (1998).
- [12] F. Jinghua, W. Yuanfang and L. Lianshou, *HZPP-9903*, (1999)
F. Jinghua, L. Lianshou and W. Yuanfang, *HZPP-9901*, (1999).
- [13] D. Ghosh *et al.*, *Phys. Lett. B* **540**, 52 (2002).
- [14] M. K. Ghosh and A. Mukhopadhyay, *Phys. Rev. C* **68**, 034907 (2003).
- [15] R. C. Hwa and Q. Zhang, *Phys. Rev. D* **62**, 014003 (2000).
- [16] EHS/NA22 Collaboration, M.R. Atayan *et al.*, *HEN* **449** (2003).
- [17] B. Anderson, G. Gustafson and B. Nilsson-Almqvist, *Nucl. Phys. B* **281**, 289 (1987)
B. Nilsson-Almqvist and E. Stenlund, *Comp. Phys. Comm.* **43**, 387 (1987).
- [18] A. Bialas and M. Gazdzicki, *Phys. Lett. B* **252**, 483 (1990).

Concluding Remarks

The general conclusions that one can draw from both theoretical and experimental pursuit in high-energy heavy-ion research for over three decades, can now be briefly summarized. Finite temperature lattice QCD has confirmed that for vanishing baryon density, at a critical temperature $T_c \approx 150 - 180$ MeV, strongly interacting matter undergoes a transition from a medium of colour singlet hadronic constituents to one of deconfined coloured quarks and gluons [1]. The transition turns a hadronic state of spontaneously broken chiral symmetry, into one where this symmetry is restored (QGP). Experimental evidences on high-energy AB collisions suggest that the onset of deconfinement starts at low SPS energies [2]. An initial energy density $\epsilon_i \approx 250$ GeV/fm³ could possibly be reached at the moment of maximum nuclear overlap in central $^{197}\text{Au}+^{197}\text{Au}$ collisions with $\sqrt{s_{NN}} = 200$ GeV at the RHIC. The corresponding value for central $^{208}\text{Pb}+^{208}\text{Pb}$ collisions at LHC would be around $\epsilon_i \approx 7500$ GeV/fm³. One can compare these values with the critical energy density required for a QCD phase transition, which is $\epsilon_c \approx 1 - 10$ GeV/fm³. It is expected that at such high energies, relativistic hydrodynamics can describe the space-time evolution of AB collision. Typical expected values for different stages of space-time evolution of AB collisions are about 0.1 – 0.3 fm for the pre-equilibrium stage, about 1 – 5 fm for the plasma phase, and 20 – 40 fm for the freeze out stage [3]. As far as QGP is concerned it would not be improper to say that, a QGP like state has perhaps already been created. However, only at the LHC energy such a state is expected to be sufficiently dense and long lived, so that its existence can be identified without any ambiguity. In the following subsections we have tried to briefly outline the lessons we have learned from the experiments performed during the AGS - SPS era, from those in the RHIC, and from our own investigation in one of the SPS experiments on dynamical fluctuation of produced charged particles.

AGS - SPS lessons: The major findings of the experiments performed using BNL-AGS and CERN-SPS facilities can be summarized in the following way [4, 5].

1. The initial energy densities measured in different AGS and SPS experiments lie somewhat within the range of $\epsilon_i \approx 1 - 3.5 \text{ GeV/fm}^3$, a value exceeding the threshold of deconfinement. As expected ϵ_i has been found to increase with the centrality of the collision. The apparent temperature obtained from the transverse mass distributions of different hadrons, appeared to increase with the particle mass. Such observation allows us to determine the freeze out temperature and transverse flow velocity. At SPS in Pb+Pb collisions, it was found that freeze out takes place at about 140 MeV, and the central region is expanding at about half the velocity of light.
2. The observed dilepton invariant mass spectrum in the region between ϕ and J/ψ mesons showed an excess over the cocktail of different known lepton pair production processes. Such excess has been attributed to thermal emission, only a small fraction of which actually originates in the hot early stage of the evolution. It does not necessarily require a QGP scenario to explain the experimental results in this regard. Some photon excess over that coming from known hadronic decays have been observed. The interpretation still remains an open issue.
3. J/ψ production has been found to be suppressed in different light and heavy-ion induced experiments. The suppression always increases with centrality of the collision. In central Pb-Pb collision at the SPS an additional anomalous suppression has been observed. This observation is probably the first signal for colour deconfinement through parton condensation, which does not require any thermalization.
4. Hadron abundances showed expected enhancement in strangeness production. The enhancement increases with the strangeness content of the particles. The yield per unit rapidity per participant relative to the corresponding pA yields has been found to be ≈ 15 times larger in central Pb+Pb collisions for $\Omega^-, \bar{\Omega}^+ : |S| = 3$. No model could explain the full spectrum of abundance of different strange hadrons.
5. Results on HBT correlation study did not show the expected increase of source radii with increasing collision energy. The source radius is essentially determined by the initial nuclear size and is independent of collision energy. From AGS to SPS and from Au+Au

to Pb+Pb, in contrast to larger expected values $R_{side} \approx R_{out} \approx 5 - 6$ fm has been found. As H. Satz pointed out [4], at SPS the colour deconfinement seems to occur at the beginning of the collision evolution, and thermalization along with collective behaviour at the end. For QGP formation we need both to occur at the early stage of collision.

RHIC lessons: The matter created at the RHIC behaves almost like a perfect fluid, low on its viscosity. The RHIC data also conclusively indicated occurrence of a striking set of new phenomena. Some of the major observations of RHIC experiments are once again summarily furnished below [5, 6].

1. Transverse momentum spectra of hadrons of different species showed interesting features. The \bar{p} yield is comparable to the p yield, and the yield ratio seems to be constant up to $p_t \sim 4$ GeV/c. Both the p and \bar{p} yields are comparable to the π yield at and around $p_t \sim 2$ GeV/c. For $p_t > 2$ GeV/c a significant fraction of total particle yield comes from baryons.

Besides the above, strong suppression in different hadronic p_t spectra has been observed in central Au+Au collisions at RHIC. The invariant differential cross-section scaled with the average number of binary NN collisions and the corresponding NN cross-section, differ significantly from unity in central AA collisions. The observation is consistent with the predicted energy loss of the parent light quarks and gluons due to induced gluonic radiation, when they traverse the dense coloured medium.

2. An elliptic flow resulting from a pressure gradient developed in the almond shaped collision zone is another interesting phenomenon observed in the RHIC. The data showed an evidence of fast thermalization, a critical pre-requisite of QGP formation, is achieved. A common collective flow velocity was observed for hadrons of different species. The observation is consistent with a perfect fluid model [7].

3. Another exciting phenomenon observed in the RHIC was the suppression of back to back jet-like correlation. In contrast to the observations from d+Au and pp collisions, the away side dihadron azimuthal correlation at $\Delta\varphi \approx \pi$ disappears in central Au+Au collisions. Such a conical configuration may be an outcome of fast jet movements in a fluid medium, where either Mach type or Cerenkov type shock waves are generated. The structure of the away side azimuthal correlation is consistent not only with conical emis-

sion, but also with other interpretations.

4. RHIC results obtained from Au+Au collisions at $\sqrt{s_{NN}} = 200$ GeV on the dynamical fluctuation of net electrical charge of a particular hadron species (say pion) show a strong dependence on the centrality of the collision. Lattice QCD calculations predict an enhanced charge fluctuation for hadronic phase, and a suppression of the same in QGP phase. The measured values of fluctuation are larger than the predicted value from charge conservation, and they are close to the prediction of a resonance gas picture. From top SPS energy to RHIC, the extent of dynamical net charge fluctuation remains essentially unaltered with collision energy. Thus significant suppression in the net charge fluctuation is yet to be observed. Higher order moments of net charge distribution may yield significant results.

5. The J/ψ suppression at RHIC was expected to be larger than that observed in the SPS. Experimentally no additional suppression could be found. Two possible interpretations for this can be given - (i) regeneration of bound charm pairs during the late expansion stages that experience large production of charmness at high density, and (ii) the observed suppression in the SPS is probably a result of screening of higher mass resonances like the ψ' , χ_c . One will have to wait for the LHC results to confirm one possibility or the other.

In RHIC experiments it has thus been demonstrated that in comparison to elementary NN collision, in AA collision there exists a universal suppression of high p_t hadron production, which indicates the presence of a dense colour deconfined medium. The azimuthal asymmetry occurring as a result of opposite side jet quenching mechanism, can be utilized to verify the QCD law on energy loss of leading partons in a deconfined medium [8].

Lessons from the Present Investigation: The present analysis of a sample of central and semi-central $^{32}\text{S-Ag/Br}$ events at 200A GeV/c, shows several interesting features on dynamical fluctuation of produced charged particles within limited phase-space intervals. From the three different statistical methods adopted in our investigation namely intermittency, multifractality and erraticity, major observations of our analysis have once again been briefly discussed below.

Presence of weak intermittency, beyond a simple Bose-Einstein type of correlation between like sign charged particles, has been established. The computer code FRITIOF based on the Lund string fragmentation model on AB collision, could not account for the observed effect. Presence of higher order (more than two particle) correlation could be found from our result on normalized exponents. The factorial correlator analysis shows that the bin to bin correlations are short ranged. A critical examination of the intermittency index leads to conclude that, (i) it's neither necessary to invoke a QCD second order phase transition nor to assume an intermixing of different phases to interpret the observed behaviour, and (ii) probably there has not been a Landau-Ginzburg type of phase transition either [9]. Another important result of the present investigation is the Levy index ($\mu \approx 1.2$), that not only indicates presence of non-Poisson type wild singularities in the phase-space distribution of produced particles, but also characterizes a hierarchical pattern between correlations of successive order. The intermittency phenomenon is not dimension independent. An extension of the technique to 2-d revealed stronger intermittency effects. In stead of the originally proposed self-similar nature of dynamical density fluctuation [10], the observed behaviour of SFM in 2-d has been interpreted in terms of self-affinity. This is a consequence of anisotropy in distributions along different (η and φ) directions. Using a Hurst parameter the extent of anisotropy could be reduced with unequal partitioning of phase-space interval in different directions. Exact reasons for the observed dynamical fluctuations are not clear from the above analysis. As mentioned above, some of the possibilities can be excluded. Whereas, a few other like the intranuclear cascade mechanism or the non-thermal phase transition, or both, can be put in a conjectural form as possible mechanisms behind the observed behaviour of our data [11]. In intermittency analysis there is enough evidence of multifractal structures being involved in the spatial distribution of shower tracks in our event sample. When subjected to specific multifractal methods of analysis, the $^{32}\text{S-Ag/Br}$ data show expected behaviour. A multifractal spectrum, the anomalous Renyi dimensions, and the multifractal specific heat are some of the major outcomes of the analysis. The multifractal specific heat obtained from our analysis though reinforces the idea of multifractality in particle density distribution, it does not possess the same universal value as claimed in [12]. The event space fluctuation of SFM has been studied with the help of erraticity technique applied to

the η distribution as well as X_η gap distribution. The results are qualitatively consistent with the expectation and they are also in agreement with other results on AB collision. All erraticity parameters are obtained, most important of which is the entropy index $\bar{\mu}_q$. A smooth model like the FRITIOF code fails to replicate the experimental results on erraticity.

While looking for dynamical fluctuations in narrow phase-space regions several precautions should be taken. As has been pointed out in [9] the causes that can influence our result, are either automatically taken care of in the emulsion technique itself, or they are accommodated in our bias of event sample and methods of analysis. The emulsion technique does not allow us to determine the p_t and charge values of produced particles. These factors desisted us to draw strong conclusions from the analysis of our data. However, there are a few scopes of improvement (which is always there!), that can be taken up in future investigations. One can accumulate a larger statistics and study the effect of centrality of collision by extending the analysis to smaller subsamples of events (see Chapter 2) of differing $\langle n_s \rangle$ values. One can also use other event samples and event generators e.g., UrQMD, and compare their predictions with those of the present data set.

Bibliography

- [1] F. Carsch, *Nucl. Phys. A* **698**, 199c (2002).
- [2] M. Gazdziński and M. I. Gorenstein, *Acta Phys. Pol. B* **30**, 2705 (1999).
- [3] K. Geiger, *Quark-Gluon Plasma 2*, ed. R. C. Hwa, (World Scientific, Singapore, 1995).
- [4] H. Satz, *Talk given in Quark Matter 2002*, (Nantes, France, 17-24 July 2002), *Nucl. Phys. A* **715**, 3 (2003).
- [5] K. Yagi, T. Hatsuda and Y. Make, *Quark-Gluon Plasma* (Cambridge University Press, New York, 2005).
- [6] C. Pajares, *Talk given in Quark Confinement and Hadron Spectrum VII Conference*, (Ponta Delgada, Azores, Portugal, 2007).
- [7] R. Lacey, *Nucl. Phys. A* **774**, 199 (2006).
- [8] R. Stock, *Talk given in Quark Matter 2004*, (Oakland, California, USA 2004), *J. Phys. G* **30**, S633 (2004).
- [9] E. A. De Wolf, I. M. Dremin, and W. Kittel, *Phys. Rep.* **270**, 1 (1996)
W. Kittel and E. A. De Wolf, *Soft Multihadron Dynamics*, (World Scientific, Singapore, 2005).
- [10] A. Bialas and R. Peschanski, *Nucl. Phys. B* **273**, 703 (1986)
A. Bialas and R. Peschanski, *Nucl. Phys. B* **308**, 857 (1988).
- [11] W. Ochs, *Z. Phys. C* **50**, 339 (1991).
- [12] A. Bershanskii, *Phys. Rev. C* **59**, 364 (1999).

